Fortschritt-Berichte VDI

VDI

Reihe 3

Verfahrenstechnik

Dipl.-Ing., Ingénieur de l'Ecole Centrale Paris Jürgen Stoll, Köln

Nr. 836

Molecular Models for the Prediction of Thermophysical Properties of Pure Fluids and Mixtures

Fortschritt-Berichte VDI

Reihe 3

Verfahrenstechnik

Dipl.-Ing., Ingénieur de l'Ecole Centrale Paris Jürgen Stoll, Köln

Nr. 836

Molecular Models for the Prediction of Thermophysical Properties of Pure Fluids and Mixtures

VDI Verlag

Stoll, Jürgen
Molecular Models for the Prediction of Thermophysical Properties of Pure Fluids and Mixtures
Fortschr.-Ber. VDI Reihe 3 Nr. 836. Düsseldorf: VDI Verlag 2005.
250 Seiten, 72 Bilder, 38 Tabellen.
ISBN 3-18-383603-3, ISSN 0178-9503,
€ 73,00 / VDI-Mitgliederpreis € 65,70.

Keywords: Molecular models – Molecular simulation – Prediction – Thermophysical properties – Vapor-liquid equilibria – Pure fluids – Dipolar – Quadrupolar – Methanol – Mixtures

Process engineers can expect reliable support from thermophysical properties predicted by molecular simulation using accurate molecular models. For engineering tasks, such molecular models of 80 pure fluids, like carbon dioxide, oxygen, ethane, halogens, alternative refrigerants, ethylene oxide and methanol, and of 45 binary mixtures of these components are developed. The pure fluid models are based on the two-centre Lennard-Jones potential model with embedded point dipole, point quadrupole, or point charges. The models are efficiently parametrized by a new methodological approach. Comparison to experimental data of vapor-liquid equilibria and further thermophysical properties demonstrates the excellent accuracy and predictive power of these pure fluid models. It is shown, that the present molecular models of mixtures predict vapor-liquid equilibria more reliably than, for example, the Peng-Robinson equation of state. Excellent agreement with experimental vapor-liquid equilibria is obtained with a binary interaction parameter in the Lorentz-Berthelot combining rules conve-niently adjusted to a single experimental state point. Quantitative predictions of vapor-liquid equilibria of five ternary mixtures are obtained from direct application of the present molecular models of binary mixtures. This molecular models can be applied to the investigation of further molecular phenomena, like diffusion in zeolites.

Die Reihen der FORTSCHRITT-BERICHTE VDI:

1 Konstruktionstechnik/Maschinenelemente
2 Fertigungstechnik
3 Verfahrenstechnik
4 Bauingenieurwesen
5 Grund- und Werkstoffe/Kunststoffe
6 Energietechnik
7 Strömungstechnik
8 Mess-, Steuerungs- und Regelungstechnik
9 Elektronik/Mikro- und Nanotechnik
10 Informatik/Kommunikation
11 Schwingungstechnik
12 Verkehrstechnik/Fahrzeugtechnik
13 Fördertechnik/Logistik
14 Landtechnik/Lebensmitteltechnik
15 Umwelttechnik
16 Technik und Wirtschaft
17 Biotechnik/Medizintechnik
18 Mechanik/Bruchmechanik
19 Wärmetechnik/Kältetechnik
20 Rechnerunterstützte Verfahren (CAD, CAM, CAE, CAP, CAQ, CIM, . . .)
21 Elektrotechnik
22 Mensch-Maschine-Systeme

D 93 (Diss. Universität Stuttgart)

Als Manuskript gedruckt. Printed in Germany.
ISSN 0178-9503
ISBN 3-18-383603-3

Vorwort

Die vorliegende Arbeit entstand während meiner Tätigkeit als wissenschaftlicher Mitarbeiter von Herrn Prof. Dr.-Ing. Hans Hasse am Institut für Technische Thermodynamik und Thermische Verfahrenstechnik (ITT) der Universität Stuttgart. Herr Prof. Dr.-Ing. Hans Hasse hat diese Arbeit angeregt und in allen Phasen mit großem Interesse begleitet. In unseren regelmäßigen Diskussionen hat er mit seinem wertvollen Erfahrungsschatz und seinem unterstützenden fachlichen Rat entscheidend zum Gelingen dieser Arbeit beigetragen, wofür ich ihm herzlich danke. Ebenso danke ich ihm für das mir entgegengebrachte Vertrauen und die mir wie selbstverständlich eingeräumten Freiheiten, mit denen er ein für die Erstellung dieser Arbeit sehr motivierendes Umfeld geschaffen hat.

Herrn Prof. Dr. phil. Johann Fischer danke ich für die freundliche Übernahme des Korreferats und die kritische Durchsicht der Ergebnisse. Mein besonderer Dank gilt Herrn Prof. Dr. phil. Johann Fischer auch für die anregenden fachlichen Diskussionen während der Erstellung dieser Arbeit.

Weiterhin gilt mein herzlicher Dank Herrn Dr.-Ing. Jadran Vrabec, der mit großem Engagement die Arbeitsgruppe Molekulare Simulation am Institut leitet und die vorliegende Arbeit tatkräftig unterstützt hat. Durch unsere tägliche Zusammenarbeit und seine stete Diskussionsbereitschaft übermittelte er mir sein wertvolles Fachwissen, das für das Gelingen der vorliegenden Arbeit unverzichtbar war.

Der Deutschen Forschungsgemeinschaft danke ich für die Förderung dieser Arbeit im Rahmen des Sonderforschungsbereichs 412 "Rechnergestützte Modellierung und Simulation zur Analyse, Synthese und Führung verfahrenstechnischer Prozesse" an der Universität Stuttgart.

Bei meinen ehemaligen Kollegen in der Arbeitsgruppe Molekulare Simulation, Herrn Dr. rer. nat. Matthias Kettler und Herrn Dr. Sergej Lishchuk, möchte ich mich bedanken für zahlreiche Diskussionen. Ihr Fachwissen über molekulare Simulation ist in diese Arbeit mit eingeflossen.

Herrn Dr.-Ing. Martin Wendland und Herrn Dr. rer. nat. Matthias Mecke möchte ich für ihre Bereitschaft zum Gedankenaustausch danken, mit dem sie diese Arbeit unterstützt haben.

Herrn Dr. Tamás Kristóf danke ich für seine Simulationsarbeit an der Universität Veszprem, mit der er die Arbeiten über die Modellierung von Methanol in einer entscheidenden Phase unterstützt hat.

All den hier namentlich nicht aufgeführten Mitarbeiterinnen und Mitarbeitern des Höchstleistungsrechenzentrums der Universität Stuttgart möchte ich an dieser Stelle für die jahrelange sehr gute Zusammenarbeit danken.

Ohne die Unterstützung meiner ehemaligen Kolleginnen und Kollegen am ITT und vieler Studenten, die sich für molekulare Simulation begeisterten, wäre diese Arbeit nicht möglich gewesen. Insbesondere gilt Thorsten Schnabel mein aufrichtiger Dank; er hat die umfangreichen Simulationsarbeiten über Kältemittel und Methanol durchgeführt und

hat mit dem Ausbau der Rechnerinfrastruktur am Institut diese Arbeit entscheidend unterstützt. Weiterhin bedanke ich mich bei Andreas Linhard, der als wissenschaftliche Hilfskraft mit seinem herausragenden Fachwissen über Numerik das in dieser Arbeit verwendete effiziente Werkzeug zur Parametrierung quadrupolarer und dipolarer Fluide aus seiner Feder fließen ließ. Des weiteren möchte ich mich bei Tobias Günther bedanken, der für seine Diplomarbeit die umfangreiche Modellierung quadrupolarer Mischungen bearbeitet hat. Er hat damit einen sehr wichtigen Beitrag zu dieser Arbeit geleistet. Matthias Gloede danke ich für seinen Einfallsreichtum und sein Durchhaltevermögen bei der Optimierung des Modells für Ethylenoxid im Rahmen seiner Studienarbeit. Jiong Fang hat als wissenschaftliche Hilfskraft alle Phasen der vorliegenden Arbeit begleitet, wofür ich ihm aufrichtig danke. In seiner Studienarbeit hat er die anspruchsvolle Erweiterung des hier verwendeten Modellierungsansatz auf dipolar-quadrupolare Modellfluide bearbeitet. Martin Tenzer, Andreas Büchler und Elyas Sheik danke ich für ihren engagierten Einsatz und ihr selbständiges Arbeiten als wissenschaftliche Hilfskräfte bei weiteren umfangreichen Simulationsarbeiten. Außerdem danke ich Veronika Wetter für ihre Unterstützung bei den Simulationsarbeiten über quadrupolare Modellfluide. Bei Gaurav Kedia möchte ich mich für seine Sorgfalt und Zuverlässigkeit beim Durchführen von Simulationen und Berechnungen mit der Peng-Robinson Zustandsgleichung sowie bei der Bearbeitung und Pflege der zahlreichen Abbildungen bedanken.

Bei allen ehemaligen Kolleginnen und Kollegen am Institut bedanke ich mich herzlich für die angenehme, freundschaftliche Atmosphäre. Durch den guten Zusammenhalt und unsere gemeinsamen Unternehmungen hat die Arbeit am ITT viel Spaß gemacht. Stellvertretend möchte ich hier Dr.-Ing. Jadran Vrabec, Petra Genske, Dr. rer. nat. Michael Maiwald, Dr.-Ing. Sascha Grob, Thorsten Schnabel und Thomas Grützner nennen.

Nicht zuletzt möchte ich meinen Eltern für ihr Verständnis und ihre stets liebevolle Unterstützung danken; sie hielten mir auch dann den Rücken frei, wenn die Moleküle wochenlang, scheinbar unzähmbar aus der Reihe tanzten und viel Einsatz einforderten.

Köln, im März 2005

Jürgen Stoll

Contents

List of Symbols

A	arbitrary thermophysical property
ΔA	difference of property A
a	coefficient of linear fit
a	component index
a	component in mixture
a	distance
a^t	model parameter in transformed model parameter space
a'	component with spherical molecules
a'	index for component with spherical molecules
a''	component with non-spherical molecules
a''	index for component with non-spherical molecules
B	second virial coefficient
b	coefficient of linear fit
b	component index
b	component in mixture
C	constant for reaction field calculations
C	inertia parameter ascribed to volume
C_1	coefficient for saturated densities correlations
C_2'	coefficient for saturated liquid density correlation
C_3'	coefficient for saturated liquid density correlation
C_2''	coefficient for saturated vapor density correlation
C_3''	coefficient for saturated vapor density correlation
c	component in mixture
c	constant for global correlation
c	number of all intermediate states of fluctuating particle
c	short-cut notation for cosine
c_1	coefficient for vapor pressure correlation
c_2	coefficient for vapor pressure correlation
c_3	coefficient for vapor pressure correlation
d	number of data points
E	energy
e	electronic charge $e = 1.60218 \cdot 10^{-19}$ C
F	Helmholtz free energy
$\mathcal{F}$	weighted fitness function
f	number of molecular degrees of freedom
f	scaling factor for gradual insertion
f_i	intermediate state i of fluctuating particle
f_ε	relation of Lennard-Jones energy parameters
f_σ	relation of Lennard-Jones size parameters
G	Gibbs free energy

g	pair distribution function in terms of relative configurational phase space variables
$g_{(2)}$	pair distribution function in terms of configurational phase space variables
H	enthalpy
$\mathcal{H}$	*Hamiltonian*
h	molar enthalpy
h	Planck's constant $h = 6.626076 \cdot 10^{-34}$ Js
Δh_V	molar enthalpy of vaporization
I	ideal term
I	molecular moment of inertia
i	elementary function index
i	molecule index
i	property index
i	state point index
j	elementary function index
j	*model parameter index*
j	molecule index
k	counting index
k	elementary function index
k	interaction site index
k	molecule index
k_B	Boltzmann's constant $k_B = 1.38066 \cdot 10^{23}$J/K
k_{ij}	binary parameter
L	elongation
ℓ	compact notation for reduced elongation L^*
l	geometry parameter of molecular model
m	*model parameter*
m	molecular mass
m	number of components
m^{PC}	parameter for PC-SAFT equation of state
N	number of molecules
N_0	number of spherical molecules
N_2	number of symmetric linear molecules
N_3	number of asymmetric molecules
$N_1, \ldots, N_m$	numbers of molecules of components $1, \ldots, m$
$n_1, \ldots, n_m$	indices for numbers of molecules of components $1, \ldots, m$
n	exponent of repulsive term of Lennard-Jones potential
n	*number of model parameters*
n	number of state points
P	polarity representing point dipole or point quadrupole
p	pressure
p_σ	vapor pressure

Q	partition function
Q	quadrupole momentum
Q_{xx}, Q_{yy}, Q_{zz}	elements of diagonalized quadrupole tensor
$\bar{Q}$	partition function independent of the factorial of number of molecules
Q^{*2}	parameter for BACKONE equation of state
q	compact notation for reduced squared quadrupole momentum Q^{*2}
q	point charge
q	quaternion
R	ideal gas constant $R = 8.31451\text{J}/(\text{mol K})$
R	ideal term for chemical potential of non-spherical molecules
r	distance
r_c	cut-off radius
r_{isjk}	distance of interaction site s on molecule i and interaction site k on molecule j
$\delta r_{\max}$	maximum translational displacement
s	interaction site index
T	temperature
T_0	parameter for BACKONE equation of state
t	time as integration variable
U	internal energy
δU	change of internal energy
u	pair potential
u	internal energy per molecule
u	interaction energy of a dipole and an electrical field
V	volume
V_0	reference volume
v	molar volume
v_a	partial molar volume of component a
δV	volume displacement
$\delta V_{\max}$	maximum volume displacement
w	virial
w	weight
x	coordinate of interaction site in molecular model
x	mole fraction
x	mole fraction of liquid phase
x	space coordinate
y	coordinate of interaction site in molecular model
y	mole fraction of vapor phase
y	space coordinate
Z	compressibility
z	space coordinate

α	coefficient for global correlation
α	parameter for BACKONE equation of state
α	polarizability
α_{CH_3-O-H}	bond angle methylene group – oxygen – hydrogen in methanol molecule
β	coefficient for global correlation
β	inverse temperature $\beta = 1/(k_B T)$
β_T	isothermal compressibility
Γ	phase space
γ	coefficient for global correlation
$\gamma^c_{a'}$	phase space variables of an added molecule of species a'
$\gamma^c_{a''}$	phase space variables of an added molecule of species a''
γ^c_{ia}	configurational phase space variables of molecule i of component a
γ^c_{ja}	configurational phase space variables of molecule j of component a
γ^c_{jb}	configurational phase space variables of molecule j of component b
γ^c_{1a}	configurational phase space variables of molecule 1 of component a
γ^c_{2a}	configurational phase space variables of molecule 2 of component a
γ^c_{1b}	configurational phase space variables of molecule 1 of component b
γ^c_{12aa}	relative configurational phase space variables of molecules 1 and 2 of component a
γ^c_{11ab}	relative configurational phase space variables of molecules 1 of components a and b
γ_{ij}	relative angle of precession between molecules i and j
δ	Dirac δ-function
δA	statistical uncertainty of property A
$\overline{\delta A}$	mean relative deviation of property A
$\lvert\delta A\rvert$	relative deviation of property A
ε	Lennard-Jones energy parameter
ε_0	permittivity of the vacuum $\varepsilon_0 = 8.85419 \cdot 10^{-12}\ \mathrm{C^2/(Nm^2)}$
ε^{PC}	parameter for PC-SAFT equation of state
ε_s	relative permittivity
η	binary interaction parameter
θ	angle of nutation
Λ	thermal de Broglie wave length
μ	chemical potential
μ	dipole momentum
$\tilde{\mu}$	chemical potential $\tilde{\mu} = \mu/(k_B T)$
μ_a	chemical potential of component a
μ^q	dipole momentum of a set of point charges
ξ	binary interaction parameter
ξ	elementary function for global correlation
Π	a priori transition probabilities
ρ	charge density

ρ	molar density
ρ	normalized weighting probability density
ρ_0	parameter for BACKONE equation of state
σ	Lennard-Jones size parameter
σ	standard deviation
σ^{PC}	parameter for PC-SAFT equation of state
τ	time
τ_x, τ_y, τ_z	x-, y-, z-component of torque vector
χ	elementary function for global correlation
ψ	elementary function for global correlation
ψ	interaction energy of one molecule with all other molecules
Ω	total orientational integral
ω	acentric factor
ω_x, ω_y, ω_z	rotational velocity around x-, y-, z-axis
$\delta\omega_{\max}$	maximum angular displacement

Vector, Matrix, and Tensor Properties

$\boldsymbol{A}$	rotation matrix
$\boldsymbol{E}^{\mathrm{RF}}$	reaction field vector
$\boldsymbol{e}$	unit vector
$\boldsymbol{F}$	force
$\boldsymbol{I}$	tensor of molecular momenta of inertia
$\boldsymbol{M}$	vector of model parameters
$\boldsymbol{q}$	quaternion vector
$\boldsymbol{r}_c$	cut-off radius
$\boldsymbol{r}_i$	position vector of molecule i
$\boldsymbol{r}_{ij}$	distance vector of centers of mass of molecules i and j ($\boldsymbol{r}_{ij} = \boldsymbol{r}_i - \boldsymbol{r}_j$)
$\boldsymbol{r}_{is}$	position vector of site s on molecule i
$\Delta\boldsymbol{r}_{is}$	position vector of site s on molecule i relative to center of mass of molecule i
$\boldsymbol{r}_{jk}$	position vector of site k on molecule j
$\Delta\boldsymbol{r}_{jk}$	position vector of site k on molecule j relative to center of mass of molecule j
$\boldsymbol{r}_{isjk}$	distance vector of interaction site s on molecule i and interaction site k on molecule j
$\delta\boldsymbol{r}$	translational displacement vector
$\boldsymbol{s}$	vector in model parameter space
$\boldsymbol{t}$	vector in model parameter space
$\boldsymbol{v}$	translational velocity vector
$\boldsymbol{x}$	mole fractions
$\boldsymbol{x}$	mole fractions of liquid phase
$\boldsymbol{y}$	mole fractions of vapor phase

ρ	position vector scaled by box length
τ	torque vector
ω_i	rotational velocity of molecule i
ω_{12aa}	relative orientational phase space variables of molecules 1 and 2 of component a
ω_{11ab}	relative orientational phase space variables of molecules 1 of components a and b
$\delta\omega$	angular displacement vector

Subscript

0	reference property
0	*initial value*
96	Lennard-Jones-9-6 potential function
246	Lennard-Jones-24-6 potential function
2CLJ	two-center Lennard-Jones
2CLJD	two-center Lennard-Jones plus point dipole
2CLJQ	two-center Lennard-Jones plus point quadrupole
LJ	Lennard-Jones
$n6$	Lennard-Jones-n-6 potential function
a	related to component a
a'	related to component with spherical molecules
a''	related to component with non-spherical molecules
$a\backslash i$	molecule i of component a is omitted
$a\backslash ij$	molecules i and j of component a are omitted
app	approximation
b	related to component b
$b\backslash j$	molecule j of component b is omitted
CH_2	related to CH_2-group in molecule
CH_3	related to methylene group in methanol
CH_3-O	related to distance of methylene group and oxygen atom in methanol
c	property at the critical point
cor	data from correlation
D	point dipole
E	excess
ens	*ensemble*
est	estimated
Ethylene	*related to ethylene*
exp	experimental data
H	related to hydrogen atom in molecule
i	related to molecule i
ia	related to molecule i of component a
ij	related to molecules i and j

is	related to interaction site s on molecule i
j	related to molecule j
ja	related to molecule j of component a
jb	related to molecule j of component b
jk	related to interaction site k on molecule j
$isjk$	related to interaction site s on molecule i and interaction site k on molecule j
max	maximum
N	related to N molecules
$N+1$	related to $N+1$ molecules
$N-1$	related to $N-1$ molecules
NpT	related to NpT ensemble
NVT	related to NVT ensemble
O	related to oxygen atom in molecule
O – H	related to distance of oxygen atom and hydrogen atom in methanol
O_2	related to oxygen
opt	resulting from optimization
other	from other authors
pT	depending on pressure and temperature
Q	point quadrupole
Tx	at specified temperature and mole fraction
s	specified
sim	data from molecular simulation
xx, yy, zz	moment of inertia referred to molecular principal axis x, y, z
μVT	related to μVT ensemble
τ	time

Superscript

a	related to component a
b	related to component b
ab	related to unlike interaction of molecules of components a and b
b	in molecular body-fixed principal axis coordinates
c	configurational
EF	electrical field
id	ideal
LJ	interaction of Lennard-Jones sites
LR	long range correction
l	liquid phase
l1	liquid phase 1
l2	liquid phase 2

QQ	interaction of point quadrupoles
$Q\mu$	interaction of point quadrupole and point dipole
Qq	interaction of a point quadrupole and a set of point charges
q	related to a set of point charges
qQ	interaction of a set of point charges and a point quadrupole
qq	interaction of sets of point charges
$q\mu$	interaction of a set of point charges and a point dipole
RF	reaction field
res	residual
rot	related to rotational degrees of freedom
s	*in space-fixed coordinates*
scal	scaled
t	model parameters in transformed model parameter space
tot	total
tr	related to translational degrees of freedom
v	vapor phase
$\mu\mu$	interaction of point dipoles
μQ	*interaction of point dipole and point quadrupole*
μq	interaction of a point dipole and a set of point charges
μRF	interaction of point dipole and reaction field
$*$	reduced property
$'$	property in saturated liquid state
$''$	property in saturated vapor state

Abbreviations

1CLJ	one-center Lennard-Jones
1CLJD	one-center Lennard-Jones plus point dipole
1CLJQ	one-center Lennard-Jones plus point quadrupole
2CLJ	two-center Lennard-Jones
2CLJD	two-center Lennard-Jones plus point dipole
2CLJQ	two-center Lennard-Jones plus point quadrupole
exp.	experimental data
n.a.	no data available
PR EOS	Peng-Robinson equation of state
sim.	data from molecular simulation

Abstract

In chemical engineering, the knowledge on thermophysical properties of mixtures is important for the design and optimization of processes. As the experimental data base is often narrow, methods are required that predict thermophysical properties quantitatively. Usually, equations of state or G^E models are used for that purpose. They are known as excellent correlation tools, but they lack in predictive power and hold only little promise for further improvement.

It is shown in the present work, that molecular modeling and simulation is an alternative modeling approach for pure fluids and mixtures with excellent predictive power and high potential for further development. For that purpose, molecular models of 78 pure fluids, like nitrogen, oxygen, ethane, carbon monoxide, carbon dioxide, halogens, and alternative refrigerants, were developed on the basis of the two-center-Lennard-Jones model fluids with point quadrupole (2CLJQ) or point dipole (2CLJD). A new parametrization approach based on global correlations of the vapor-liquid equilibria of these model fluids allowed the efficient development of these molecular models. The vapor-liquid equilibrium data of the 2CLJQ/2CLJD model fluids used for the development of the global correlations were calculated by means of molecular simulation. The 2CLJQ/2CLJD models yield typical relative deviations from experiment of $\pm 0.5\%$ for the saturated liquid densities, about $\pm 4\%$ for the vapor pressures, and $\pm 3\%$ for enthalpies of vaporization. They are essentially more accurate than existing molecular models from the literature. Also in homogeneous fluid states far away from the vapor-liquid equilibria, they describe thermophysical properties with good accuracy. More elaborate Lennard-Jones based molecular models of ethylene oxide and methanol, were developed.

These compatible models of real pure fluids were applied straightforwardly for the modeling of 45 binary interactions of unlike molecules in real fluid mixtures. Unlike Lennard-Jones interactions were described with the Lorentz-Berthelot combining rules. Purely predictive simulation results with these combining rules showed, that these molecular models predict vapor-liquid equilibria of real mixtures more reliably than the Peng-Robinson equation of state. The molecular models describe vapor-liquid equilibria of real mixtures quantitatively, when a binary interaction parameter is used in the Lorentz-Berthelot combining rules, that was adjusted by a simple method to a single experimental equilibrium pressure for each mixture modeled here.

These molecular models of binary interactions of unlike molecules were used in the present work for the quantitative prediction of vapor-liquid equilibria of five ternary mixtures. They describe vapor phase compositions and saturated liquid and vapor densities more reliably than the Peng-Robinson equation of state.

The results of the present work show, that the newly developed molecular models of real pure fluids and mixtures offer a high potential for further application.

Kurzfassung

Für die Auslegung und Optimierung verfahrenstechnischer Prozesse werden thermophysikalische Stoffdaten von Mischungen benötigt. Da häufig nur eine schmale experimentelle Datenbasis vorliegt, werden Methoden benötigt, die eine quantitative Stoffdatenvorhersage ermöglichen. Hierfür werden üblicherweise Zustandsgleichungen oder G^E-Modelle verwendet, die zwar sehr gute Korrelationswerkzeuge sind, aber Schwächen bei der Stoffdatenvorhersage zeigen. Das Entwicklungspotenzial dieser Ansätze erscheint ausgereizt.

In der vorliegenden Arbeit wird gezeigt, dass molekulare Modellierung und Simulation ein alternativer Modellierungsansatz für fluide Reinstoffe und Mischungen mit sehr guten Vorhersageeigenschaften und hohem Entwicklungspotenzial ist. Hierfür wurden für 78 unpolare, quadrupolare und multipolare Reinstoffe, wie zum Beispiel Stickstoff, Sauerstoff, Ethan, Kohlenmonoxid, Kohlendioxid, Halogene, und alternative Kältemittel, molekulare Modelle auf Basis der Zwei-Zentren-Lennard-Jones Modellfluide mit Punktquadrupol (2CLJQ) bzw. Punktdipol (2CLJD) entwickelt. Ein neuer, auf globalen Korrelationen der Dampf-Flüssigkeits Gleichgewichte dieser beiden Modellfluide beruhender Parametrierungsansatz ermöglichte die effiziente Modellentwicklung. Die für die Entwicklung der Korrelationen benötigten Dampf-Flüssigkeits Gleichgewichte der Modellfluide wurden mit molekularer Simulation berechnet. Typische relative Abweichungen dieser Modelle von experimentellen Daten liegen bei ±0.5% für Siededichten, bei etwa ±4% für Dampfdrücke und bei ±3% für Verdampfungsenthalpien. Sie sind wesentlich genauer als Modelle aus der Literatur. Auch im einphasigen fluiden Zustandsgebiet weit außerhalb des Nassdampfgebiets beschreiben diese Modelle Stoffeigenschaften mit guter Genauigkeit. Für Ethylenoxid und Methanol wurden aufwändigere Lennard-Jones-basierte Modelle entwickelt.

Mit diesen kompatiblen Modellen realer Reinstoffe wurden 45 Modelle binärer Wechselwirkungen ungleicher Moleküle in realen Mischungen entwickelt. Ungleiche Lennard-Jones-Wechselwirkungen wurden mit den Lorentz-Berthelot Kombinationsregeln berechnet. Rein prädiktive Simulationen mit diesen Kombinationsregeln zeigten, dass diese molekularen Modelle Dampf-Flüssigkeits Gleichgewichte realer Mischungen zuverlässiger vorhersagen als die Peng-Robinson Zustandsgleichung. Eine quantitative Beschreibung der Dampf-Flüssigkeits Gleichgewichte realer Mischungen ist möglich mit einem binären Wechselwirkungsparameter in den Lorentz-Berthelot Kombinationsregeln, der für jede der hier modellierten Mischungen mit einer einfachen Methode an einen experimentellen Gleichgewichtsdruck angepasst wurde.

Diese molekularen Modelle binärer Wechselwirkungen ungleicher Moleküle wurden in der vorliegenden Arbeit zur quantitativen Vorhersage der Dampf-Flüssigkeits Gleichgewichte von fünf ternären Mischungen verwendet. Im Vergleich zur Peng-Robinson Zustandsgleichung beschreiben die molekularen Modelle die Dampfzusammensetzung sowie die Siede- und Taudichten deutlich zuverlässiger.

Die Ergebnisse der vorliegenden Arbeit zeigen, dass die neu entwickelten molekularen Modelle realer Reinstoffe und Mischungen für weitere Anwendungen geeignet sind.

1 Introduction

1.1 Molecular Based Methods in Chemical Engineering?

With the evolution of new technologies in the 21st century, ranging from biotechnology, material science, and nanotechnology to pharmacogenomics and molecular design of drugs and specialty chemicals, chemical engineering faces new challenges. For the exploitation of the tremendous market potential of these technologies, chemical engineers need to rapidly design and optimize processes for the efficient on-demand production of an increasing number of tailored substances. On that background, molecular based methods, like molecular simulation or computational chemistry, gain importance and acceptance in industrial applications [43, 135] and will, as indispensable tools, accompany the methods conventionally used in chemical engineering [102]. This development requires an extension and a relocation of the foci of chemical engineering research and education, that will be characterized by increasing interdisciplinarity. The benefits gained from molecular based methods in chemical engineering will reward these efforts [77, 205]. Various examples for the successful application of such methods in chemical industry exist [69, 102].

The advantages of the application of molecular based methods in chemical engineering are twofold. The insights into the micro- and nanoworld gained from such methods allow a deeper understanding of phenomena on the molecular level, for example the adsorption of reactants on catalyst surfaces or the hindered diffusion of reaction educts and products in zeolites [69]. Such knowledge helps to optimize macroscopic processes at their very roots. The second advantage is related to the paramount importance of the availability of reliable data on thermophysical properties of mixtures for process engineering [138], where, in particular, phase equilibrium data, or more detailed, vapor-liquid equilibrium data, are broadly needed. Due to the high costs of experimental laboratory work, the prediction of thermophysical properties of mixtures on a narrow experimental data base has always been a very important issue for practicing engineers. Conventionally, equations of state, like the Peng-Robinson or the Soave-Redlich-Kwong equations of state, or models of the Gibbs free energy G^E [349], are used for the correlation of experimental data of mixtures, however, they are known to lack often in predictive power and hold little promise for further improvements. Therefore, the low-cost but reliable prediction of thermophysical properties is still a demanding problem. In this context, the broader substitution of laboratory experiments by the application of computer power for the reliable molecular based pseudo-experimental prediction of physical and thermophysical properties of new substances will be an important cost saving factor for more accurate and faster process design in future [102].

The present work focusses on the prediction of thermophysical properties of pure fluids and mixtures by means of molecular simulation [3, 114], which is at present the most important molecular based method that combines high potential for further development, flexibility, and – very important for practical applications – reasonable computational ef-

fort, cf. for example [50, 69, 134, 135] for overviews. Classical statistical thermodynamics is used to obtain various thermophysical properties from molecular simulation: for example vapor-liquid equilibria (cf. the remainder of this work for references), solubilities [1, 172], or diffusion coefficients [447]. Moreover, molecular simulation is applicable to the investigation of molecular scale phenomena, like the structure and thermodynamics of nitrogen clusters [335], the properties of vapor-liquid interfaces of real fluids [199, 269, 272, 427], nucleation [171, 200], thermophysics in nanostructures [215, 257, 443], or even mechanical slide friction [213], to cite only some.

In addition to molecular simulation, further important molecular based methods are the COSMO-RS method [177, 178, 179], and Car-Parrinello methods [35, 43].

In the COSMO-RS method the energetic pairwise interactions of molecular surface elements are described by means of surface charge density distributions of the pure fluids obtained from unimolecular – and therefore fast – quantum chemical electronic-structure calculations using the continuum solvation model. Typically, density functional theory is used for these quantum chemical calculations. Based on this information, the COSMO-RS method allows predictions of a multitude of thermophysical properties of mixtures by means of very fast unidimensional Boltzmann statistics [84, 85]. The low computational effort, that allows bridging between molecular based methods and process simulation [58, 102], the general applicability to different kinds of mixtures, and the predictive results of the COSMO-RS method are appealing. The drawback of the method is, that configurational effects are treated only conventionally like in G^{E}-models.

Car-Parrinello methods [35, 43] combine quantum chemical methods based on density functional theory with molecular dynamics simulation. This approach predicts, at least in principle, all kinds of molecular interactions, adjustable parameters are not necessary. However, compared to molecular simulation, the computational effort is exceedingly high for Car-Parrinello methods, even though only comparably simple quantum mechanical approaches are used, which, furthermore, can lead to considerable errors in the prediction of molecular interactions.

In contrast to the Car-Parrinello approach, molecular simulation uses semiempirical potential functions, hereafter also called molecular models, to model molecular interactions. This approach allows simulations with an acceptable computational effort, but, as mentioned above, requires the parametrization of the molecular models.

The careful parametrization of molecular models of pure fluids is of key importance for obtaining quantitative thermophysical properties from molecular simulation. Excellent molecular models of pure fluids are a prerequisite for accurate modeling of mixtures. Various methods for the optimization of model parameters were developed, cf. Chapter 5 and the references in Appendix I, but, in general, the fine tuning of model parameters remains a time consuming task. In many recent studies, quantum chemistry was applied for more efficient model parametrization, cf. examples in Chapter 4. Quantum chemistry is typically used for the specification of Coulomb charges in molecular models, or for the

parametrization of elaborate potential functions, that are not conveniently transferable to mixtures. More research work on the application of quantum chemistry to model parametrization is needed. The literature survey in Chapter 4 shows, that there is still a lack of molecular models of pure fluids and mixtures, that hinders the exploration of molecular simulation in industry.

1.2 Contributions of the Present Work

The two principal goals of the present work were: firstly, to develop efficiently quantitative molecular models of a large number of pure fluids, secondly, to apply these pure fluid models to modeling of mixtures.

Usually, molecular models are developed individually for each real fluid. This approach is time consuming and only efficient for complex fluids. An alternative route was followed in the present work. It allowed the efficient development of state-independent, simple but accurate and compatible molecular models of 78 low-molecular fluids, most of which are important in industrial applications. These models can directly be used for modeling of mixtures. The basic idea of this route is the modeling of classes of real fluids with similar shapes and polarities by classes of simple physically meaningful molecular models. This approach is particularly well adapted to the optimization of molecular models with low number of adjustable model parameters.

In the present work, the class of unpolar or quadrupolar fluids (23 fluids) and the class of multipolar fluids (55 fluids) were modeled. The latter have, apart from their molecular dipole moment, also higher molecular polar momenta. Typical quadrupolar fluids are nitrogen, oxygen, ethane, carbon dioxide, or halogens, whereas carbon monoxide or alternative refrigerants are typical multipolar fluids. For the modeling of these fluids two three-site model classes based on the two-center Lennard Jones model (2CLJ) with embedded non-polarizable point quadrupole (2CLJQ) or non-polarizable point dipole (2CLJD) were used. The class of 2CLJQ models was used for the modeling of quadrupolar fluids. For the modeling of multipolar fluids, the 2CLJD and 2CLJQ model classes were used. Unpolar fluids were modeled without polarity. In reduced properties both model types have only two parameters, the reduced elongation, i.e. the distance of the Lennard-Jones interaction sites, and the reduced quadrupole or dipole momentum. This allows carrying out comprehensive studies of the thermodynamic properties, like vapor-liquid equilibria, of the model classes. Moreover, these models permit the use of simple combining rules in the modeling of mixtures, and they reduce the computation time in computer simulations considerably.

Correlations of vapor-liquid equilibria of the 2CLJQ and 2CLJD model fluids were developed as functions of the model parameters on the basis of comprehensive vapor-liquid equilibrium data from molecular simulation generated in this work. These empirical correlations were used for fitting of the model parameters to experimental vapor-liquid

equilibrium data. This is a new approach which made it possible to find parameters for a large number of real fluids.

Apart from this new optimization approach based on model classes, a way to determine parameters of more specialized molecular models is discussed in the present work and used for developing models of ethylene oxide and methanol.

The present molecular models of pure fluids were used as a basis for the development of molecular models of 45 real mixtures. This work is the broadest application of molecular simulation to the quantitative description of thermophysical properties of real pure fluids and mixtures presently available. For all mixtures modeled here, an adjustable binary interaction parameter in the energetic part of the modified Lorentz-Berthelot combining rules is used for improved accuracy. This binary parameter accounts for polarization effects between unlike molecules and can be adjusted efficiently by a simple method developed in the present work.

The present work is structured as follows: in Chapter 2 the theoretical background of the molecular simulation methods applied here is briefly described, in Chapter 3 the results of the comprehensive investigation of the vapor-liquid equilibria of the 2CLJQ/2CLJD model fluids are presented and the development of the empirical correlations is described, in Chapter 4 the new molecular models for fluid classes are discussed, in Chapter 5 the optimization of the molecular models of ethylene oxide and methanol is described, and in Chapter 6 results from molecular modeling of real binary and ternary mixtures are compared to those from equations of state. In Chapter 7 the present work is summarized and an outlook on future work on the development of quantitative molecular models is given.

In the present work, answers are given to the following questions: Which depth of molecular modeling is required for the accurate description of thermophysical properties of real quadrupolar and multipolar fluids? Are state-independent models sufficient for that purpose? Are such models predictive? Should molecular polarizability be modeled explicitly? How do effective molecular models perform in the modeling of real mixtures, where polarization occurs? How does molecular simulation compare to conventional methods?

The many positive results shown in the subsequent chapters underline, that comparatively simple state independent molecular models are sufficiently accurate to yield a close-to-experiment description and prediction of thermophysical properties of pure fluids and mixtures.

2 Molecular Simulation

In this chapter, the theoretical background of the molecular simulation methods applied in the present work is outlined. After a short description of the modeling of molecular interactions by means of semiempirical, effective pair potentials in Chapter 2.1, the calculation of averages of thermophysical properties from molecular simulation is sketched in Chapter 2.2. In Chapter 2.3 the two molecular simulation methods used in the present work – molecular dynamics and Monte Carlo – are explained. In Chapter 2.4, expressions of the chemical potential and the partial molar volume are derived from partition functions, and two methods used in the present work for the calculation of these properties in molecular simulations – test particle insertion and gradual insertion – are described. Chemical potentials and partial molar volumes are needed for the NpT+Test Particle Method and the Grand Equilibrium Method, cf. Chapter 2.5, that were used in the present work for the calculation of vapor-liquid equilibria.

The assumptions adopted throughout this work are: rigidity of the molecules, i.e. internal degrees of freedom are not modeled explicitly; classical approximation, i.e. the molecules are considered as particles and their translational and rotational motion is described by classical equations of motion; only pairwise additive potentials are considered; the energetic contributions from different types of interactions simply add up, i.e. no cross effects are considered.

2.1 Models of Molecular Interactions

Interaction energies between molecules stem from electrostatic and magnetic interactions of the molecular charge clouds and nuclei. Usually, models of molecular interactions only describe interactions resulting from electrostatics, as they are about four orders of magnitude higher than the magnetic interactions [132]. Therefore, only molecular interactions resulting from electrostatics are considered in the present work.

Molecular interactions resulting from electrostatics can be separated into different contributions. At large intermolecular distances, dispersive and electrostatic multipolar interactions can be distinguished. The latter ones are caused by permanent molecular charge distributions. At small distances, molecular interactions are repulsive due to charge cloud overlaps. Furthermore, strong, highly directional, short-ranged hydrogen bond interactions may occur.

In the present work, dispersive and repulsive molecular interactions at interaction site distance r are modeled with the Lennard-Jones pair potential function [132]

$$u^{\mathrm{LJ}} = 4\varepsilon \left[\left(\frac{\sigma}{r}\right)^{12} - \left(\frac{\sigma}{r}\right)^{6} \right]. \tag{1}$$

In Equation (1) the physical r^{-6}-term describes dispersive interactions at long range, the empirical r^{-12}-term describes repulsive interactions at short range.

Electrostatic multipolar interactions of molecules can be described by the interactions of sets of point charges, which are used for modeling methanol in the present work. The arrangement of the point charges describes the molecular multipole momenta of the methanol molecule. Furthermore, the point charges model hydrogen bonding of methanol molecules. In order to decrease the number of model parameters, it is often more convenient to model molecular electrostatic multipoles by point multipoles. In the present work, non-polarizable point dipoles and axial point quadrupoles are used for modeling the electrostatic interactions of 78 quadrupolar or multipolar fluids. The pair potentials for mutual interactions of point charges, point dipoles, and point quadrupoles are given in Appendix A.

In the present work, molecular models are constructed by additive superposition of Lennard-Jones interaction sites and point charge, point dipole or point quadrupole interaction sites located within the Lennard-Jones site structure.

2.2 Averages of Thermophysical Properties

A fluid bulk phase of m components in a defined macroscopic state, for example at given Volume V and temperature T, is modeled here as a system with a very large number N of rigid spherical or non-spherical molecules

$$N = \sum_{a=1}^{m} N_a, \tag{2}$$

wherein the index a counts the m components. The interactions of the molecules are described by model potentials. For these N molecules, a multitude of more or less probable microscopic states are allowed, that all represent the same macroscopic state. Statistical thermodynamics allows to deduce macroscopic thermophysical properties of this fluid bulk phase, such as internal energy or pressure, as averages of the ensemble of the accessible microscopic states. As example, the NVT-ensemble with specified number of molecules, volume, and temperature is used here.

In the classical limit, a microscopic state of the N molecules in the NVT-ensemble is described by their spatial positions and translational impulsions, and, in the case of non-spherical molecules, also by their orientations and angular momenta. These form altogether a single point in the phase space Γ_{NVT}. It is convenient to split up the phase space Γ_{NVT} into the ideal phase subspace $\Gamma^{\mathrm{id}}_{NVT}$ of translational impulsions and angular momenta, and into the configurational phase subspace $\Gamma^{\mathrm{c}}_{NVT}$ of positions and orientations.

Any thermophysical property A depends on the microscopic state variables of the N molecules and can be written as sum of an ideal contribution A^{id}, that depends only on variables in $\Gamma^{\mathrm{id}}_{NVT}$, and a configurational contribution A^{c}, that depends only on the variables in $\Gamma^{\mathrm{c}}_{NVT}$

$$A\left(\Gamma_{NVT}\right) = A^{\mathrm{id}}\left(\Gamma^{\mathrm{id}}_{NVT}\right) + A^{\mathrm{c}}\left(\Gamma^{\mathrm{c}}_{NVT}\right). \tag{3}$$

As a multitude of microscopic states are allowed, the thermophysical property A fluctuates. Its macroscopic average can be expressed either as time average [148]

$$\langle A\rangle_\tau = \lim_{\tau\to\infty}\frac{1}{\tau}\int_0^\tau \left[A^{\mathrm{id}}\left(\Gamma^{\mathrm{id}}_{NVT}(t)\right) + A^{\mathrm{c}}\left(\Gamma^{\mathrm{c}}_{NVT}(t)\right)\right] dt \tag{4}$$

$$= \langle A^{\mathrm{id}}\rangle_\tau + \langle A^{\mathrm{c}}\rangle_\tau, \tag{5}$$

or as ensemble average

$$\langle A\rangle_{\mathrm{ens}} = \int_{\Gamma^{\mathrm{id}}_{NVT}} A^{\mathrm{id}}\left(\Gamma^{\mathrm{id}}_{NVT}\right)\rho^{\mathrm{id}}\left(\Gamma^{\mathrm{id}}_{NVT}\right) d\Gamma^{\mathrm{id}}_{NVT} + \int_{\Gamma^{\mathrm{c}}_{NVT}} A^{\mathrm{c}}\left(\Gamma^{\mathrm{c}}_{NVT}\right)\rho^{\mathrm{c}}\left(\Gamma^{\mathrm{c}}_{NVT}\right) d\Gamma^{\mathrm{c}}_{NVT} \tag{6}$$

$$= \langle A^{\mathrm{id}}\rangle_{\mathrm{ens}} + \langle A^{\mathrm{c}}\rangle_{\mathrm{ens}}. \tag{7}$$

Equations (5) and (7) are equivalent according to the theorem of ergodicity [410]. In Equation (5) $\Gamma^{\mathrm{id}}_{NVT}(t)$ and $\Gamma^{\mathrm{c}}_{NVT}(t)$ are the trajectories of the N molecules system in the two phase subspaces. In Equation (7) $\rho^{\mathrm{id}}(\Gamma^{\mathrm{id}}_{NVT})$ and $\rho^{\mathrm{c}}(\Gamma^{\mathrm{c}}_{NVT})$ are normalized weighting probability densities for the microscopic states [3]. Due to the equivalence of Equations (5) and (7), the average is generally noted without index

$$\langle A\rangle \equiv \langle A\rangle_\tau \equiv \langle A\rangle_{\mathrm{ens}}. \tag{8}$$

For example, the macroscopic average of the internal energy is, cf. [141],

$$\langle U\rangle = \langle U^{\mathrm{id}}\rangle + \langle \sum_{i=1}^{N-1}\sum_{j=i+1}^{N} u^{\mathrm{c}}_{ij}\left(\Gamma^{\mathrm{c}}_{NVT}\right)\rangle, \tag{9}$$

and the macroscopic average of the pressure is, cf. [141],

$$\langle p\rangle = \langle p^{\mathrm{id}}\rangle - \langle \frac{1}{3V}\sum_{i=1}^{N-1}\sum_{j=i+1}^{N} \boldsymbol{r}_{ij}\frac{\partial u^{\mathrm{c}}_{ij}\left(\Gamma^{\mathrm{c}}_{NVT}\right)}{\partial \boldsymbol{r}_{ij}}\rangle, \tag{10}$$

wherein the second term on the right side is the configurational contribution to the internal energy U^{c} (Equation (9)) and the configurational contribution to the pressure p^{c} (Equation (10)).

In Equations (9) and (10) $u^{\mathrm{c}}_{ij}\left(\Gamma^{\mathrm{c}}_{NVT}\right)$ is the potential interaction energy between molecules i and j.

According to the theorem of equipartition of the kinetic energy [266], the temperature T of the m-component mixture with N molecules is related to the average of the kinetic energy U^{id} of the N molecules, that depends only on variables in $\Gamma^{\mathrm{id}}_{NVT}$

$$T = \frac{2}{(3N_0 + 5N_2 + 6N_3)\,k_{\mathrm{B}}}\langle U^{\mathrm{id}}\left(\Gamma^{\mathrm{id}}_{NVT}\right)\rangle, \tag{11}$$

wherein N_0 is the number of spherical molecules, N_2 is the number of symmetric linear molecules, and N_3 is the number of asymmetric molecules. The potential degrees of freedom are fully accessible at the temperatures studied in the present work. Internal degrees of freedom like vibration and bending are not included in the modeling. In Equation (11), the kinetic energy U^{id} of the N molecules is

$$U^{\mathrm{id}}\left(\Gamma^{\mathrm{id}}_{NVT}\right) = U^{\mathrm{id,tr}}\left(\Gamma^{\mathrm{id,tr}}_{NVT}\right) + U^{\mathrm{id,rot}}\left(\Gamma^{\mathrm{id,rot}}_{NVT}\right) \tag{12}$$

$$= \frac{1}{2}\sum_{i=1}^{N_0} m_i \boldsymbol{v}_i^2 + \frac{1}{2}\sum_{j=1}^{N_2}\left[m_j \boldsymbol{v}_j^2 + \left(I_{xxj}\omega_{xj}^2 + I_{yyj}\omega_{yj}^2\right)\right] + \frac{1}{2}\sum_{k=1}^{N_3}\left[m_k \boldsymbol{v}_k^2 + \left(I_{xxk}\omega_{xk}^2 + I_{yyk}\omega_{yk}^2 + I_{zzk}\omega_{zk}^2\right)\right]. \tag{13}$$

Partition functions and their relation to averages of thermophysical properties are explained in Chapter 2.4.1.

2.3 Molecular Simulation Methods

Molecular simulation is used in the present work for estimating averages of configurational contributions to macroscopic thermophysical properties of model bulk fluids. For adequate estimation of configurational contributions, molecular simulation methods must ensure that primarily the most probable configurations are sampled efficiently according to their weighting probabilities during the simulation. These configurations contribute most significantly to the configurational parts of thermophysical properties.

For that purpose, two principal approaches exist, that were both applied in the present work: molecular dynamics simulation and Monte Carlo simulation [3, 114]. These methods generate new configurations of the molecules in different ways. The Monte Carlo method subsequently generates a new configuration on the basis of a present configuration, so that the configurations are elements of a Markov chain [3, 410]. Results from Monte Carlo simulations are estimates for ensemble averages according to Equation (7). In contrast, molecular dynamics simulations solve Newton's equations of motion and thus yield the trajectory of the configurations. They yield, hence, estimates for time averages according to Equation (5).

Prior to a closer description of these methods, some concepts common to both methods are outlined.

Due to computational costs, molecular simulations of bulk fluids for obtaining thermodynamic properties are typically restricted to approximately 1,000 molecules. This number, though essentially lower than the some 10^{23} molecules in real bulk fluids, is yet sufficient for obtaining results with accuracies suitable for engineering applications, if periodic boundary conditions are applied to the cubic simulation volume of finite size, usually called simulation box. Periodic boundary conditions discharge the simulation from border

influences by turning the small model system to a quasi-infinite one and are, hence, the basic concept that allows to estimate bulk phase thermodynamics from simulations of small model systems.

As a consequence of the finite size of the simulation box, molecular interactions can only be evaluated explicitly within a cut-off sphere. In the present work, the cut-off sphere is centered on the center of mass of each molecule, i.e. center-of-mass cut-off was chosen. With center-of-mass cut-off the interactions between the sites on two molecules are only evaluated, if the distance of the two molecular centers of mass is within the cut-off sphere of radius r_c, otherwise the two molecules do not interact. The interactions of the molecules within the cut-off sphere with the fluid outside the cut-off sphere must not be neglected. Under the assumption, that the fluid outside the cut-off sphere is homogeneous and isotropic, long-range corrections are taken into account. Details on long-range corrections are given in Appendix A.

In the present work, molecular simulations were started from a cubic face-centered lattice arrangement of the N molecules. In the case of molecular dynamics simulations, translational and rotational velocities are randomly ascribed, the total translational and rotational momenta are set to zero.

Molecular dynamics simulation

Molecular dynamics simulations are based on Newton's classical equations of motion of rigid bodies. The forces and torques on molecules resulting from molecular interactions are evaluated and used to describe the translational and rotational motion of the molecules. By their nature, the laws of dynamics ensure that configurations with high weighting probabilities occur preferably.

The translational and rotational motions of the molecules are conveniently described with reference to their center of mass. With $\boldsymbol{F}_i^{\mathrm{tot}}$ being the sum of all forces exerted on molecule i, the translational motion of the center of mass of this molecule, located at $\boldsymbol{r}_i$, is governed by Newton's law

$$\boldsymbol{F}_i^{\mathrm{tot}} = m_i \ddot{\boldsymbol{r}}_i, \tag{14}$$

wherein m_i is the mass of molecule i.

A symmetric linear molecule i has two rotational degrees of freedom. In that case, the Euler equations in the molecular body-fixed (superscript "b") principal axis system centered in the molecule's center of mass are

$$\boldsymbol{\tau}_i^{\mathrm{b,tot}} = \boldsymbol{I}_i \dot{\boldsymbol{\omega}}_i^{\mathrm{b}}, \tag{15}$$

wherein $\boldsymbol{\tau}_i^{\mathrm{b,tot}}$ is the sum of all torques exerted on molecule i and $\boldsymbol{I}_i$ is the diagonalized tensor of the molecular momenta of inertia. For asymmetric molecules with three rotational axis, the Euler equations extend to

$$\tau_{xi}^{\mathrm{b,tot}} = I_{xxi} \dot{\omega}_{xi}^{\mathrm{b}} - \left(I_{yyi} - I_{zzi}\right) \omega_{yi}^{\mathrm{b}} \omega_{zi}^{\mathrm{b}}, \tag{16}$$

$$\tau_{yi}^{\mathrm{b,tot}} = I_{yyi}\dot{\omega}_{yi}^{\mathrm{b}} - (I_{zzi} - I_{xxi})\,\omega_{xi}^{\mathrm{b}}\omega_{zi}^{\mathrm{b}}, \tag{17}$$

$$\tau_{zi}^{\mathrm{b,tot}} = I_{zzi}\dot{\omega}_{zi}^{\mathrm{b}} - (I_{xxi} - I_{yyi})\,\omega_{xi}^{\mathrm{b}}\omega_{yi}^{\mathrm{b}}. \tag{18}$$

Molecular forces and torques relevant for the present work are given in Appendix A.

As exclusively compact rigid molecules without internal degrees of freedom are considered in the present work, quaternions $\boldsymbol{q}_i = (q_{0i}, q_{1i}, q_{2i}, q_{3i})$ can advantageously be used for describing the spatial orientations of each molecule i [3]. They satisfy the constraint

$$\sum_{k=0}^{3} q_{ki}^2 = 1. \tag{19}$$

Compared to rotation algorithms based on Euler angles, quaternion based rotation algorithms have the advantage to be free of singularity traps and are therefore implemented more conveniently [3]. During molecular dynamics simulations torques are evaluated in the space-fixed coordinate system (superscript "s"). For the evaluation of Equations (15) and (18) they must be transformed to molecular body-fixed principal axis coordinates. For that purpose the quaternion-based rotation matrix $\boldsymbol{A}_i$, defined for molecule i as, cf. [3],

$$\boldsymbol{A}_i = \begin{pmatrix} q_{0i}^2 + q_{1i}^2 - q_{2i}^2 - q_{3i}^2 & 2\,(q_{1i}q_{2i} + q_{0i}q_{3i}) & 2\,(q_{1i}q_{3i} - q_{0i}q_{2i}) \\ 2\,(q_{1i}q_{2i} - q_{0i}q_{3i}) & q_{0i}^2 - q_{1i}^2 + q_{2i}^2 - q_{3i}^2 & 2\,(q_{2i}q_{3i} + q_{0i}q_{1i}) \\ 2\,(q_{1i}q_{3i} + q_{0i}q_{2i}) & 2\,(q_{2i}q_{3i} - q_{0i}q_{1i}) & q_{0i}^2 - q_{1i}^2 - q_{2i}^2 + q_{3i}^2 \end{pmatrix} \tag{20}$$

is used, so that

$$\boldsymbol{\tau}_i^{\mathrm{b,tot}} = \boldsymbol{A}_i \boldsymbol{\tau}_i^{\mathrm{s,tot}}. \tag{21}$$

Solving Equations (15) and (18) in a quaternion based algorithm requires that the time derivatives of the quaternions be coupled to the angular velocities according to the following equation, cf. [3],

$$\begin{pmatrix} \dot{q}_{0i} \\ \dot{q}_{1i} \\ \dot{q}_{2i} \\ \dot{q}_{3i} \end{pmatrix} = \frac{1}{2} \begin{pmatrix} q_{0i} & -q_{1i} & -q_{2i} & -q_{3i} \\ q_{1i} & q_{0i} & -q_{3i} & q_{2i} \\ q_{2i} & q_{3i} & q_{0i} & -q_{1i} \\ q_{3i} & -q_{2i} & q_{1i} & q_{0i} \end{pmatrix} \begin{pmatrix} 0 \\ \omega_{xi}^{\mathrm{b}} \\ \omega_{yi}^{\mathrm{b}} \\ \omega_{zi}^{\mathrm{b}} \end{pmatrix} \tag{22}$$

The translational equations of motion, cf. Equation (14), were solved numerically with a Gear predictor-corrector integrator [125] of fifth order, whereas a fourth order Gear predictor-corrector integrator was used for solving the rotational equations of motion, cf. Equations (15), (18) and (22). A detailed description of the Gear predictor-corrector integrator is available in [338].

Thermostating in molecular dynamics simulations in the NpT-ensemble was assured by isokinetic scaling of translational and angular velocities [139]. With T being the specified

temperature, the scaling expressions for the velocities of each molecule i stem from the theorem of equipartition of the kinetic energy and write as

$$\boldsymbol{v}_i^{\text{scal}} = \boldsymbol{v}_i \left[\frac{3NT}{\sum_{j=1}^{N} m_j \boldsymbol{v}_j^2} \right]^{1/2} \tag{23}$$

for the translational velocities of all molecules,

$$\boldsymbol{\omega}_i^{\text{scal}} = \boldsymbol{\omega}_i \left[\frac{2N_2T}{\sum_{j=1}^{N_2} \left(I_{xxj}\omega_{xj}^2 + I_{yyj}\omega_{yj}^2 \right)} \right]^{1/2} \tag{24}$$

for the angular velocities of the N_2 symmetric linear molecules, and

$$\boldsymbol{\omega}_i^{\text{scal}} = \boldsymbol{\omega}_i \left[\frac{3N_3T}{\sum_{j=1}^{N_3} \left(I_{xxj}\omega_{xj}^2 + I_{yyj}\omega_{yj}^2 + I_{zzj}\omega_{zj}^2 \right)} \right]^{1/2} \tag{25}$$

for the angular velocities of the N_3 asymmetric molecules. After each integration time step, the translational and angular velocities are scaled according to Equations (23) to (25).

Molecular dynamics simulations in the NpT-ensemble were barostated according to a method suggested by Andersen [4]. For that purpose, an equation is introduced, that allows fluctuations of the volume V of the simulation box

$$\ddot{V} = (p - p_s)/C, \tag{26}$$

wherein p is the pressure due to the actual microscopic state, p_s is the specified pressure, and C is an inertia parameter ascribed to the volume of the simulation box. Equation (26) assures that the time average of the pressure $\langle p \rangle_\tau$ equals the specified pressure p_s. A Gear predictor-corrector integrator of fifth order was used for solving Equation (26) numerically.

The introduction of Equation (26) requires the use of center-of-mass vectors scaled to the edge length of the simulation box of volume V

$$\boldsymbol{\rho}_i = \frac{\boldsymbol{r}_i}{V^{1/3}}. \tag{27}$$

Then, as shown in [3], for molecular dynamics NpT-simulations the translational equations of motion, cf. Equation (14), transform to

$$\ddot{\boldsymbol{\rho}}_i = \frac{\boldsymbol{F}_i^{\text{tot}}}{m_i V^{1/3}} - \frac{2}{3}\dot{\boldsymbol{\rho}}_i \frac{\dot{V}}{V}. \tag{28}$$

After each integration time step, a new configuration is obtained, that contributes to the calculation of the averages of the considered thermophysical properties.

Monte Carlo simulation

Monte Carlo simulations are carried out by stochastic generation of molecular configurations, that are accepted or rejected according to criteria based on energy changes. Thermostating is no issue in Monte Carlo simulations, as temperature is a given simulation parameter. Moreover, the absence of dynamics in this simulation method allows unphysical moves.

Monte Carlo simulations are organized in loops, that are comparable to integration time steps in molecular dynamics simulations. Within one Monte Carlo loop, a sequence of configurational changes is processed. Configurational changes are, for example, translational and rotational moves of the molecules, fluctuations of the volume of the simulation box for NpT-simulations, and insertion and deletion of molecules for simulations in the grand canonical μVT-ensemble, cf. Chapters 2.4.1 and 2.5.2. The implementation of the gradual insertion method, cf. Chapter 2.4.2, in Monte Carlo simulations requires further types of changes in the Monte Carlo loops, like changes of size or geometrical structure of molecules.

The Metropolis algorithm, the basic Monte Carlo algorithm for efficient, non-biased generation of configurations, is described here briefly.

If a new configuration shall be generated by a translational move of a molecule, among all N molecules one molecule i is selected at random. Then, molecule i is displaced from its location $\boldsymbol{r}_i$ to another location $\boldsymbol{r}_i + \delta\boldsymbol{r}$, where the displacement vector $\delta\boldsymbol{r}$ is chosen randomly with equal probability for all three space directions, and $|\delta\boldsymbol{r}| \leq \delta r_{\max}$. With δU being the change of energy between the present configuration and the configuration resulting from the suggested displacement of molecule i, this translational move of molecule i is accepted with the probability

$$\min\left(1, \exp(-\beta\delta U)\right). \tag{29}$$

A completely analogous scheme, where orientations are considered instead of locations, applies to the generation of new configurations by rotational moves of molecules. It is important, that the angular displacement $\delta\boldsymbol{\omega}$, with $|\delta\boldsymbol{\omega}| \leq \delta\omega_{\max}$, for molecule i results from a random choice with equal probability for all orientations, that is from unbiased orientational random sampling on a unit sphere. In the present work, the orientation of linear molecules in Monte Carlo simulations was described by means of a single unit vector per molecule. Orientational moves of these unit vectors were performed according to an algorithm described in [3]. The orientations of asymmetric molecules were described by means of quaternions, that can be sampled uniformly according to an efficient algorithm suggested by Vesely [409].

Controlled fluctuations of the volume of the simulation box allow the barostating of Monte Carlo simulations. For that purpose, a new volume $V + \delta V$ is chosen, wherein δV is a random fluctuation of volume, with $|\delta V| \leq \delta V_{\max}$. With δU being the change of energy between the configuration at present volume V and the configuration at suggested

volume $V + \delta V$, this volume fluctuation is accepted with the probability

$$\min\left(1, \exp\left[-\beta\left(\delta U + p_s \delta V - N k_B T \ln\left((V + \delta V)/V\right)\right)\right]\right), \tag{30}$$

wherein p_s is the specified pressure.

The choice of the maximum displacements δr_{max}, $\delta \omega_{max}$, and δV_{max} influences the efficiency of phase space sampling during a Monte Carlo simulation. It is generally advised to choose values for these displacements that allow acceptance rates for each move type of about 50 %.

The probabilities that control the calling of the various move types are generally selected in such a way as to try N translational moves, $(f^{rot}/3)N$ rotational moves (f^{rot} is the number of rotational degrees of freedom per molecule), and one volume fluctuation for NpT-simulations within one loop.

Results from molecular simulation show fluctuations. In the present work, statistical uncertainties of simulation data were determined with the block-averaging method proposed by Fincham et al. [107], cf. also [135] and [3]. Statistical uncertainties of properties calculated from simulation results, for example vapor pressure or saturated densities, were determined with the error propagation law.

2.4 Chemical Potential and Partial Molar Volume

The NpT+Test Particle Method, cf. Chapter 2.5.1, and the Grand Equilibrium Method, cf. Chapter 2.5.2, applied in the present work for the calculation of vapor-liquid equilibria, require the chemical potentials μ_i and, in the case of mixtures, the partial molar volumes v_i of each component in the two phases considered in equilibrium.

Various methods were suggested for the calculation of the chemical potential, or, more general, of the free energy, cf. [114] for an overview, and [23, 25, 32, 63, 146, 182, 216, 322] for recent works on this subject. Among these methods, the test particle insertion method, cf. [435] for the NVT ensemble and [358] for the NpT ensemble, and, in some cases, the computationally more elaborate gradual insertion method [241, 242, 243, 276, 300, 356, 420] were used in the present work. Apart from the chemical potentials, both methods allow obtaining the partial molar volumes from the same molecular simulation without further computational effort.

For the derivation of the expressions for the chemical potentials and the partial molar volumes of each component in a multicomponent mixture in the NpT-ensemble the partition function Q_{NpT} of this ensemble is needed, cf. Chapter 2.4.1. In Chapter 2.4.2, after the derivation of the expressions for the chemical potentials and the partial molar volumes, the test particle insertion method and the gradual insertion method are described.

2.4.1 Partition Functions

All thermophysical properties of a statistical ensemble are related to the partition function of that ensemble. These relations are shown here exemplarily for the average internal energy and the average pressure of the NVT-ensemble. Based on the NVT-partition function, the partition function of the NpT-ensemble with specified pressure p and temperature T for the N molecules is described. The NpT-partition function is needed for the derivation of the expressions for calculating the chemical potentials and the partial molar volumes in Chapter 2.4.2. As the Grand Equilibrium Method applied in the present work for the calculation of vapor-liquid equilibria of mixtures is based on quasi grand-canonical simulations, cf. Chapter 2.5.2, the partition function of the grand-canonical μVT-ensemble with specified chemical potentials μ_i, volume V, and temperature T is also described here.

NVT-ensemble

In the classical limit, the NVT-partition function for the m-component mixture introduced in Chapter 2.2 is

$$Q_{NVT} = \frac{1}{\prod_{a=1}^{m} N_a! \cdot h^{f_a N_a}} \int_{\Gamma_{NVT}} e^{-\beta \mathcal{H}(\Gamma_{NVT})} \prod_{a=1}^{m} d\Gamma_{a,NVT}, \tag{31}$$

wherein a is the component index, f_a is the number of degrees of freedom of a molecule of species a, $\mathcal{H} = U^{\mathrm{id}} + U^{\mathrm{c}}$ is the Hamiltonian of this system, and

$$\beta = 1/(k_{\mathrm{B}} T) \tag{32}$$

is the inverse temperature. Γ_{NVT} represents all phase space variables of the m-component mixture, $\Gamma_{a,NVT}$ are the phase space variables of the N_a molecules of component a. The division by the factorials of N_a accounts for the indistinguishability of the molecules belonging to component a. The division by the powers of h is due to the constraints of Heisenberg's uncertainty principle and makes the partition function dimensionless. The potential energy U^{c} contains additive contributions from Lennard-Jones interactions and from interactions of point dipoles, point quadrupoles, and point charges.

The Hamiltonian allows to divide the partition function into an ideal and a configurational contribution. For that purpose, the components are separated into species a' with spherical molecules and species a'' with non-spherical molecules. Spherical molecules of species a' have $f_{a'}^{\mathrm{tr}}$ translational degrees of freedom and non-spherical molecules of species a'' have $f_{a''}^{\mathrm{tr,rot}}$ translational and rotational degrees of freedom, hence they contribute in different ways to the partition function. With this distinction, Equation (31) can be separated

$$Q_{NVT} = \prod_{a'} Q_{a',NVT}^{\mathrm{id}} \cdot \prod_{a''} Q_{a'',NVT}^{\mathrm{id}} \cdot Q_{NVT}^{\mathrm{c}}, \tag{33}$$

with the ideal contributions $Q^{\mathrm{id}}_{a',NVT}$ and $Q^{\mathrm{id}}_{a'',NVT}$ of each component

$$Q^{\mathrm{id}}_{a',NVT} = \frac{V^{N_{a'}}}{N_{a'}! \cdot h^{f^{\mathrm{tr}}_{a'} N_{a'}}} \int_{\Gamma^{\mathrm{id}}_{a',NVT}} e^{-\beta U^{\mathrm{id,tr}}_{a'}\left(\Gamma^{\mathrm{id}}_{a',NVT}\right)} d\Gamma^{\mathrm{id}}_{a',NVT}, \tag{34}$$

$$Q^{\mathrm{id}}_{a'',NVT} = \frac{V^{N_{a''}}}{N_{a''}! \cdot h^{f^{\mathrm{tr,rot}}_{a''} N_{a''}}} \int_{\Gamma^{\mathrm{id}}_{a'',NVT}} e^{-\beta U^{\mathrm{id,tr,rot}}_{a''}\left(\Gamma^{\mathrm{id}}_{a'',NVT}\right)} d\Gamma^{\mathrm{id}}_{a'',NVT}, \tag{35}$$

and the configurational contribution Q^{c}_{NVT}

$$Q^{\mathrm{c}}_{NVT} = \frac{1}{V^N} \int_{\Gamma^{\mathrm{c}}_{NVT}} e^{-\beta U^{\mathrm{c}}\left(\Gamma^{\mathrm{c}}_{NVT}\right)} \prod_a d\Gamma^{\mathrm{c}}_{a,NVT}. \tag{36}$$

The multiple integrals in the ideal contributions can be solved analytically. Only the simple analytical expression for $Q^{\mathrm{id}}_{a',NVT}$, cf. Equation (34), is given here exemplarily

$$Q^{\mathrm{id}}_{a',NVT} = \frac{V^{N_{a'}}}{N_{a'}! \cdot \Lambda_{a'}^{f^{\mathrm{tr}}_{a'} N_{a'}}}, \tag{37}$$

wherein $\Lambda_{a'}$ is the thermal de Broglie wavelength for component a'

$$\Lambda_{a'} = \frac{h}{\sqrt{2\pi m_{a'} k_{\mathrm{B}} T}}. \tag{38}$$

The somewhat cumbersome analytical solution of $Q^{\mathrm{id}}_{a'',NVT}$ is explained, for example, in [235, 410].

Thermophysical properties are related to the partition function. The average of the Helmholtz free energy F, which is the appropriate thermodynamic potential for the NVT-ensemble, depends on the partition function [3]

$$\langle F \rangle = -\frac{1}{\beta} \ln Q_{NVT}. \tag{39}$$

Moreover, with [388]

$$\left[\frac{\partial \langle F \rangle}{\partial T}\right]_{N,V} = -\langle S \rangle, \tag{40}$$

the macroscopic definition of the Helmholtz free energy

$$\langle F \rangle = \langle U \rangle - T \cdot \langle S \rangle \tag{41}$$

yields the following differential equation

$$\langle U \rangle = \langle F \rangle - T \cdot \frac{\partial \langle F \rangle}{\partial T}. \tag{42}$$

From Equations (39) and (42) the average internal energy of the NVT-ensemble is obtained as [235]

$$\langle U \rangle = - \left[\frac{\partial \ln Q_{NVT}}{\partial \beta} \right]_{N,V} . \tag{43}$$

Due to Equation (33), the average internal energy $\langle U \rangle$ can be decomposed into an ideal and a configurational contribution, cf. Equation (9),

$$\langle U \rangle = \langle U^{\mathrm{id}} \rangle + \langle U^{\mathrm{c}} \rangle . \tag{44}$$

From [388]

$$\left[\frac{\partial \langle F \rangle}{\partial V} \right]_{N,T} = - \langle p \rangle , \tag{45}$$

the average pressure of the NVT-ensemble is obtained as

$$\langle p \rangle = \frac{1}{\beta} \left[\frac{\partial \ln Q_{NVT}}{\partial V} \right]_{N,T} , \tag{46}$$

which yields the ideal and the configurational contributions to the average of the pressure, cf. Equation (10),

$$\langle p \rangle = \langle p^{\mathrm{id}} \rangle + \langle p^{\mathrm{c}} \rangle . \tag{47}$$

NpT-ensemble

For the m-component mixture considered here, the NpT-partition function is

$$Q_{NpT} = \frac{1}{\prod_{a=1}^{m} N_a ! \cdot h^{f_a N_a}} \cdot \frac{1}{V_0} \int_{V=0}^{\infty} \int_{\Gamma_{NpT}} e^{-\beta \left[\mathcal{H}(\Gamma_{NpT}) + pV \right]} \prod_{a=1}^{m} d\Gamma_{a,NpT} dV \tag{48}$$

$$= \prod_{a'} Q^{\mathrm{id}}_{a',NpT} \cdot \prod_{a''} Q^{\mathrm{id}}_{a'',NpT} \cdot Q^{\mathrm{c}}_{NpT} , \tag{49}$$

wherein V_0 is an arbitrarily chosen reference volume [3]. By means of the average volume $\langle V \rangle_{NpT}$, the ideal contributions in Equation (49) can be written as

$$Q^{\mathrm{id}}_{a',NpT} = \langle V \rangle^{N_{a'}}_{NpT} \cdot Q^{\mathrm{id}}_{a',NVT} , \tag{50}$$

$$Q^{\mathrm{id}}_{a'',NpT} = \langle V \rangle^{N_{a''}}_{NpT} \cdot Q^{\mathrm{id}}_{a'',NVT} , \tag{51}$$

so that the configurational contribution is

$$Q^{\mathrm{c}}_{NpT} = \frac{1}{\langle V \rangle^{N}_{NpT}} \cdot \frac{1}{V_0} \int_{V=0}^{\infty} \int_{\Gamma^{\mathrm{c}}_{NpT}} e^{-\beta \left(U^{\mathrm{c}}(\Gamma^{\mathrm{c}}_{NpT}) + pV \right)} \prod_{a=1}^{m} d\Gamma^{\mathrm{c}}_{a,NpT} dV . \tag{52}$$

In the configurational contribution, the outermost integration over the volume V prescribes the volume allowed for the phase space variable sets $\Gamma^{c}_{a,NpT}$.

μVT-ensemble

In the grand-canonical μVT-ensemble the chemical potentials $\mu_1, \ldots, \mu_m$, the volume V, and the temperature T are specified. Constant values of the chemical potentials are assured by fluctuating numbers of molecules in the constant volume. Due to this particle exchange, the μVT-partition function of the m-component mixture contains explicit sums running over the numbers of molecules of each component [235]

$$Q_{\mu VT} = \sum_{n_1=1}^{N_1} \ldots \sum_{n_m=1}^{N_m} e^{\beta\mu_1 N_1} \cdot \ldots \cdot e^{\beta\mu_m N_m} \cdot \frac{1}{n_1! \cdot \ldots \cdot n_m!} \cdot \frac{1}{h^{f_1 n_1 + \ldots + f_m n_m}} \int_{\Gamma_{\mu VT,n_1,\ldots,n_m}} e^{-\beta\mathcal{H}(\Gamma_{\mu VT,n_1,\ldots,n_m})} d\Gamma_{\mu VT,n_1,\ldots,n_m} \quad (53)$$

$$= \sum_{n_1=1}^{N_1} \ldots \sum_{n_m=1}^{N_m} \left[\prod_{a=1}^{m} e^{\beta\mu_a N_a} \right] \cdot Q_{(N=n_1+\ldots+n_m)VT}. \quad (54)$$

The notation for the phase space $\Gamma_{\mu VT,n_1,\ldots,n_m}$ indicates, that the number of phase space variables varies with the number of molecules. As shown in Equation (33) for the NVT-ensemble, it is also possible to decompose the canonical partition function $Q_{(N=n_1+\ldots+n_m)VT}$ in Equation (54) into ideal and configurational contributions.

In general, no analytical solutions exist for the configurational contributions to thermophysical properties, but they can be estimated from adequate numerical methods. As described in Chapter 2.3, molecular simulation is applied here to estimate these configurational contributions.

2.4.2 Derivation, Test Particle Insertion, Gradual Insertion

The Gibbs free energy G is related to the NpT-partition function of a m-component mixture by

$$G(p, T, N_1, \ldots, N_m) = -k_B T \ln Q_{NpT}, \quad (55)$$

with Q_{NpT} according to Equation (49). The chemical potential of component a is the partial derivative of the Gibbs free energy with respect to the number of molecules at constant pressure p, temperature T, and numbers of molecules N_b of the remaining components $b \neq a$

$$\mu_a(p, T, \boldsymbol{x}) = \left[\frac{\partial G}{\partial N_a} \right]_{p,T,N_{b\neq a}}. \quad (56)$$

The chemical potential μ_a is an intensive property, that is expressed in terms of pressure, temperature, and mole fractions $\boldsymbol{x}$. The differentiation can be approximated by the difference of the Gibbs free energies of a system containing $N_a + 1_a$ molecules of component a and a system containing N_a molecules of component a

$$\mu_a(p,T,\boldsymbol{x}) \approx \frac{G(p,T,N_1,...,N_a+1_a,...,N_m) - G(p,T,N_1,...,N_a,...,N_m)}{1_a} \tag{57}$$

$$= -k_\mathrm{B}T \ln \frac{Q_{NpT}(N_a+1_a)}{Q_{NpT}(N_a)}. \tag{58}$$

The derivation of the following contributions to the chemical potential are given in Appendix B. As defined in Chapter 2.4.1, a'- and a''-components are distinguished.

As shown in Appendix B, the chemical potential of a component a is composed of three contributions

$$\mu_a(p,T,\boldsymbol{x}) = \mu^{\mathrm{id}}_{pTa}(p,T) + \mu^{\mathrm{id}}_{Txa}(T,x_a) + \mu^{\mathrm{res}}_a(p,T,\boldsymbol{x}). \tag{59}$$

In Equation (59) the ideal contribution $\mu^{\mathrm{id}}_{pTa}(p,T)$ is for an a' component

$$\mu^{\mathrm{id}}_{pTa'}(p,T) = -k_\mathrm{B}T \ln \frac{\langle V\rangle_{NpT}}{N \cdot \Lambda^{f^{\mathrm{tr}}_{a'}}_{a'}}, \tag{60}$$

that writes also

$$\mu^{\mathrm{id}}_{pTa'}(p,T) = k_\mathrm{B}T \ln \left[\langle\rho\rangle_{NpT} \cdot \Lambda^{f^{\mathrm{tr}}_{a'}}_{a'}\right], \tag{61}$$

and for an a'' component

$$\mu^{\mathrm{id}}_{pTa''}(p,T) = -k_\mathrm{B}T \ln \left[\frac{\langle V\rangle_{NpT}}{N} \cdot \frac{1}{R_{a''}(T)}\right], \tag{62}$$

that writes also

$$\mu^{\mathrm{id}}_{pTa'}(p,T) = k_\mathrm{B}T \ln \left[\langle\rho\rangle_{NpT} \cdot R_{a''}(T)\right], \tag{63}$$

wherein the ideal term $R_{a''}(T)$ is according to Equation (270) in Appendix B. The composition dependent ideal contribution $\mu^{\mathrm{id}}_{Txa}(T,x_a)$ in Equation (59) is

$$\mu^{\mathrm{id}}_{Txa}(T,x_a) = k_\mathrm{B}T \ln x_a, \tag{64}$$

for an a' or an a'' component. The residual contribution $\mu^{\mathrm{res}}_a(p,T,\boldsymbol{x})$ in Equation (59) is for an a' component

$$\mu^{\mathrm{res}}_{a'}(p,T,\boldsymbol{x}) = -k_\mathrm{B}T \ln \left[\frac{\langle V \cdot \langle e^{-\beta\psi_{a'}}\rangle_r\rangle_{NpT}}{\langle V\rangle_{NpT}}\right], \tag{65}$$

and for an a'' component

$$\mu_{a''}^{\mathrm{res}}(p,T,\boldsymbol{x}) = -k_{\mathrm{B}}T\ln\left[\frac{\langle V\cdot\Omega\cdot\langle e^{-\beta\psi_{a''}}\rangle_{\omega,r}\rangle_{NpT}}{\langle V\rangle_{NpT}}\right], \tag{66}$$

wherein the total orientational integral Ω is according to Equation (272) in Appendix B.

Partial molar volume

The partial molar volume of the component a is the partial derivative of the chemical potential μ_a with respect to the pressure at given temperature and mole fractions

$$v_a = \left[\frac{\partial\mu_a}{\partial p}\right]_{T,x}. \tag{67}$$

With the chemical potential according to Equations (266) or (269) in Appendix B, Equation (67) yields for a' components, cf. [147],

$$v_{a'} = \frac{\langle V^2\cdot\langle e^{-\beta\psi_{a'}}\rangle_r\rangle_{NpT}}{\langle V\cdot\langle e^{-\beta\psi_{a'}}\rangle_r\rangle_{NpT}} - \langle V\rangle_{NpT}, \tag{68}$$

and for a'' components

$$v_{a''} = \frac{\langle V^2\cdot\langle e^{-\beta\psi_{a''}}\rangle_{\omega,r}\rangle_{NpT}}{\langle V\cdot\langle e^{-\beta\psi_{a''}}\rangle_{\omega,r}\rangle_{NpT}} - \langle V\rangle_{NpT}. \tag{69}$$

Test particle insertion, gradual insertion

Equations (65), (66), (68), and (69) clarify, that the key to obtaining the chemical potentials and the partial molar volumes during a NpT simulation is the adequate calculation of the average of the Boltzmann factor $\exp(-\beta\psi_a)$. This can be done by means of the test particle insertion method, that evaluates ψ_a by placing test particles of species a at randomly chosen positions (and orientations) within the fluid volume for each configuration obtained during the NpT simulation. In low to mid density phases, this method yields the desired properties with reasonable accuracy. It fails, however, in the case of dense liquid phases with strong molecular interactions, for example from polarities or partial charges. In such cases, the application of the gradual insertion method significantly improves the statistics for averages of the Boltzmann factor, and thus the accuracy of the chemical potential and partial molar volume.

The gradual insertion method is briefly described here, further details and required simulation parameters are discussed in [300, 420].

In the gradual insertion method the one-step insertion of test particles is replaced by a multiple-step insertion of fluctuating particles. The method is an expanded ensemble method that can be implemented in molecular dynamics and Monte Carlo simulations [241], as was done in the present work. Embedded into a NpT simulation of a m-component

mixture with $N = N_1 + ... + N_a + ... + N_m$ molecules, a particle of species a, selected at random, is defined as fluctuating particle, that evolves over a sequence of intermediate states f_i, with $i = 0...c$, where f_0 is a completely decoupled state, and f_c is a fully coupled state, whose properties are identical to those of real particles of the species a. That is, the simulation evolves, by means of the fluctuating particle, between a system of N molecules and an expanded system of $N_1 + ... + (N_a + 1_a) + ... + N_m$ molecules. For each intermediate state f_i of the fluctuating particle, a NpT-sub-ensemble, referred to as $[N + f_i]$ with weight w_i, is defined. This requires, in addition to the standard Monte Carlo moves in NpT simulations, cf. Chapter 2.3, trial transitions from a state f_i to a state f_j, that are accepted with the probability

$$\min\left(1, \frac{w_j \Pi(f_j \to f_i)}{w_i \Pi(f_i \to f_j)} e^{-\beta(\psi_j - \psi_i)}\right), \tag{70}$$

wherein $\Pi(f_j \to f_i)$ and $\Pi(f_i \to f_j)$ are a priori transition probabilities, and ψ_i and ψ_j are the interaction energies of the fluctuating particle in state f_i or f_j with all remaining particles. The Monte Carlo sequence of a NpT simulation with gradual insertion and preferential sampling in the vicinity of the fluctuating particle, as it was applied in the present work, is described in [420]. The average Boltzmann factor needed for the calculation of μ_a and v_a is

$$\langle e^{-\beta\psi_a} \rangle_{(\omega,)r} = \frac{w_0}{w_c} \frac{\text{Prob}[N_1 + ... + (N_a + 1_a) + ... + N_m]}{\text{Prob}[N_1 + ... + N_a + ... + N_m]}, \tag{71}$$

wherein Prob$[M]$ denotes the probability of observing the M particle system during the simulation.

2.5 Vapor-Liquid Equilibria

Coexisting liquid and vapor phases are in thermal, mechanical, and chemical equilibrium, i.e. temperature T, pressure p, and the chemical potentials μ_i for each component a are equal in both phases. With the closing conditions for the mole fractions in both phases the complete the set of equations, that are needed for phase equilibrium calculations of m-component mixtures, is

$$T' = T'', \tag{72}$$

$$p' = p'', \tag{73}$$

$$\mu'_a(p', T', \boldsymbol{x}') = \mu''_a(p'', T'', \boldsymbol{y}''), \qquad a = 1 \ldots m, \tag{74}$$

$$\sum_{a=1}^{m} x'_a = 1, \tag{75}$$

$$\sum_{a=1}^{m} y''_a = 1. \tag{76}$$

In Equations (72) to (76) the superscripts (′) for the liquid phase and (″) for the vapor phase indicate, that the property is meant at phase equilibrium conditions.

Various methods are available for the calculation of vapor-liquid equilibria of pure fluids and mixtures from molecular simulation. Among these, the Gibbs Ensemble Monte Carlo Method [313, 314] is the most widespread one. Further methods are the Gibbs-Duhem Integration [183, 184], that is based on the integration of the Clausius-Clapeyron equation, Thermodynamic Scaling Methods [176, 400], Pseudo-Ensemble Methods avoiding particle insertion [270], Histogram-Reweighting Methods [60, 174, 175, 315, 324], the bubble point pseudo ensemble simulation [398], Grand Canonical Monte Carlo methods [14, 15, 16], and the temperature-quench molecular dynamics method [126]. For simulations near the critical point Finite Size Scaling Methods were suggested [436, 437]. The reaction ensemble Monte Carlo method [367] was developed for the simulation of phase equilibria of chemically reactive systems. In the present work, the *NpT*+Test Particle Method, for which a multitude of implementations of the basic idea of series expansions of the chemical potential exist [191, 280, 281, 413, 415], was applied in the version of Vrabec [413] for the calculation of vapor-liquid equilibria of pure fluids. Vapor-liquid equilibria of mixtures were calculated with the Grand Equilibrium Method of Vrabec and Hasse [418]. Both methods were chosen due to favorable experience especially concerning accuracy. They are described in Chapters 2.5.1 and 2.5.2.

2.5.1 NpT+Test Particle Method

The *NpT*+Test Particle Method is described here for pure fluids only. In this case, the phase equilibrium conditions, cf. Equations (72) to (76), reduce to

$$T' = T'', \tag{77}$$

$$p' = p'', \tag{78}$$

$$\mu'(p_\sigma, T') = \mu''(p_\sigma, T''), \tag{79}$$

wherein $p_\sigma = p' = p''$ is the vapor pressure. For specified temperature $T = T' = T''$, the *NpT*+Test Particle Method yields the vapor pressure by solving Equation (79) with data from molecular simulations of the liquid and the vapor phase. The approximated expressions of the chemical potentials in the liquid and the vapor phase, that are needed for that purpose, are given in the following derivation.

According to Equation (59), the chemical potential $\mu(p,T)$ of a pure substance is composed of an ideal and a residual contribution

$$\mu(p,T) = \mu^{\mathrm{id}}_{pT}(p,T) + \mu^{\mathrm{res}}(p,T). \tag{80}$$

Moreover, based on liquid phase and vapor phase reference states indicated by the subscript "0", the chemical potentials in the liquid (superscript "l") and the vapor phase

(superscript "v") can be written as

$$\mu^{\mathrm{l}}(p,T) = \mu^{\mathrm{l}}(p_0^{\mathrm{l}},T) + \int_{p_0^{\mathrm{l}}}^{p} \left[\frac{\partial \mu^{\mathrm{l}}}{\partial p}\right]_{p_0^{\mathrm{l}},T} dp, \tag{81}$$

$$\mu^{\mathrm{v}}(p,T) = \mu^{\mathrm{v}}(p_0^{\mathrm{v}},T) + \int_{p_0^{\mathrm{v}}}^{p} \left[\frac{\partial \mu^{\mathrm{v}}}{\partial p}\right]_{p_0^{\mathrm{v}},T} dp, \tag{82}$$

wherein p_0^{l} and p_0^{v} are the pressures in the reference states.

Decomposing the chemical potential $\mu^{\mathrm{l}}(p_0^{\mathrm{l}},T)$ in Equation (81) and linearizing the pressure integral by the relation

$$\left[\frac{\partial \mu^{\mathrm{l}}}{\partial p}\right]_{p_0^{\mathrm{l}},T} = v_0^{\mathrm{l}} \approx \text{const.}, \tag{83}$$

which holds with good accuracy for liquid phases, yields the desired approximated expression for the chemical potential of the liquid phase

$$\mu^{\mathrm{l}}(p,T) = \mu_{pT}^{\mathrm{l,id}}(p_0^{\mathrm{l}},T) + \mu^{\mathrm{l,res}}(p_0^{\mathrm{l}},T) + v_0^{\mathrm{l}} \cdot (p - p_0^{\mathrm{l}}). \tag{84}$$

Due to the high compressibility of the vapor phase, another approach is chosen for deriving an approximated expression for the chemical potential of the vapor phase. The pressure influence on the chemical potential of the vapor phase is taken into account, as not only $\mu^{\mathrm{v}}(p_0^{\mathrm{v}},T)$ in Equation (82) is decomposed according to Equation (80), but also the integrand in the pressure integral in Equation (82), i.e.

$$\mu^{\mathrm{v}}(p,T) = \mu_{pT}^{\mathrm{v,id}}(p_0^{\mathrm{v}},T) + \mu^{\mathrm{v,res}}(p_0^{\mathrm{v}},T) + \int_{p_0^{\mathrm{v}}}^{p} \left[\frac{\partial \mu_{pT}^{\mathrm{v,id}}}{\partial p}\right]_{p_0^{\mathrm{v}},T} dp + \int_{p_0^{\mathrm{v}}}^{p} \left[\frac{\partial \mu^{\mathrm{v,res}}}{\partial p}\right]_{p_0^{\mathrm{v}},T} dp. \tag{85}$$

With the ideal gas law

$$v^{\mathrm{v,id}} = \frac{k_{\mathrm{B}}T}{p}, \tag{86}$$

the pressure derivative of the ideal contribution is

$$\frac{\partial \mu_{pT}^{\mathrm{v,id}}}{\partial p} = v^{\mathrm{v,id}} = \frac{k_{\mathrm{B}}T}{p} \tag{87}$$

and so the first integral in Equation (85) becomes

$$\int_{p_0^{\mathrm{v}}}^{p} \left[\frac{\partial \mu_{pT}^{\mathrm{v,id}}}{\partial p}\right]_{p_0^{\mathrm{v}},T} dp = k_{\mathrm{B}}T \ln \frac{p}{p_0^{\mathrm{v}}}. \tag{88}$$

The integrand in the second integral in Equation (85) is the configurational molar volume of the vapor phase, which is rewritten as difference of the molar volume v^{v} of the vapor phase and the ideal molar volume $v^{\mathrm{v,id}}$ of the vapor phase

$$\left[\frac{\partial \mu^{\mathrm{v,res}}}{\partial p}\right]_{p_0^{\mathrm{v}},T} = v^{\mathrm{v,c}} = v^{\mathrm{v}} - v^{\mathrm{v,id}} = v^{\mathrm{v}} - \frac{k_{\mathrm{B}}T}{p}, \tag{89}$$

wherein $v^{\mathrm{v,id}}$ is expressed in terms of pressure and temperature according to the ideal gas law. Then the second integral in Equation (85) is linearized in the vicinity of the pressure p_0^{v}, so that the approximated expression for the chemical potential of the vapor phase is

$$\mu^{\mathrm{v}}(p,T) = \mu_{pT}^{\mathrm{v,id}}(p_0^{\mathrm{v}},T) + \mu^{\mathrm{v,res}}(p_0^{\mathrm{v}},T) + k_{\mathrm{B}}T\ln\frac{p}{p_0^{\mathrm{v}}} + \left(v_0^{\mathrm{v}} - \frac{k_{\mathrm{B}}T}{p_0^{\mathrm{v}}}\right)\cdot(p-p_0^{\mathrm{v}}). \tag{90}$$

The phase equilibrium condition Equation (79) is fulfilled by equating the approximated expressions for the chemical potentials of the liquid and the vapor phase, cf. Equations (84) and (90), and yields a non-linear equation, that allows to calculate the vapor pressure p_σ for the specified temperature T

$$\begin{aligned}\mu_{pT}^{\mathrm{l,id}}(p_0^{\mathrm{l}},T) + \mu^{\mathrm{l,res}}(p_0^{\mathrm{l}},T) + v_0^{\mathrm{l}}\cdot(p_\sigma - p_0^{\mathrm{l}}) \;=\; & \mu_{pT}^{\mathrm{v,id}}(p_0^{\mathrm{v}},T) + \mu^{\mathrm{v,res}}(p_0^{\mathrm{v}},T) + k_{\mathrm{B}}T\ln\frac{p_\sigma}{p_0^{\mathrm{v}}} \\ & + \left(v_0^{\mathrm{v}} - \frac{k_{\mathrm{B}}T}{p_0^{\mathrm{v}}}\right)\cdot(p_\sigma - p_0^{\mathrm{v}}).\end{aligned} \tag{91}$$

For the practical evaluation of Equation (91) with results from molecular simulation, it is convenient to cancel the average volume $\langle V\rangle_{NpT}$ contained in the ideal and residual contributions of the chemical potential, cf. Equations (266) and (269) in Appendix B, i.e. to use temperature dependent ideal contributions

$$\mu_{Ta'}^{\mathrm{id}}(T) = -k_{\mathrm{B}}T\ln\frac{1}{\Lambda_{a'}^{f^{\mathrm{tr}}_{a'}}}, \tag{92}$$

or

$$\mu_{Ta''}^{\mathrm{id}}(T) = -k_{\mathrm{B}}T\ln R_{a''}(T), \tag{93}$$

and configurational contributions

$$\mu_{a'}^{\mathrm{c}}(p,T) = -k_{\mathrm{B}}T\ln\left[\frac{\langle V\cdot\langle e^{-\beta\psi_{a'}}\rangle_V\rangle_{NpT}}{N}\right], \tag{94}$$

or

$$\mu_{a''}^{\mathrm{c}}(p,T) = -k_{\mathrm{B}}T\ln\left[\frac{\langle V\cdot\Omega\cdot\langle e^{-\beta\psi_{a''}}\rangle_{\omega,V}\rangle_{NpT}}{N}\right], \tag{95}$$

instead. With these properties, the conveniently applicable form of Equation (91), as it was applied in the present work, is

$$\mu^{\mathrm{l,c}}(p_0^{\mathrm{l}},T) + v_0^{\mathrm{l}}\cdot(p_\sigma - p_0^{\mathrm{l}}) = \mu^{\mathrm{v,c}}(p_0^{\mathrm{v}},T) + k_{\mathrm{B}}T\ln\frac{p_\sigma}{p_0^{\mathrm{v}}} + \left(v_0^{\mathrm{v}} - \frac{k_{\mathrm{B}}T}{p_0^{\mathrm{v}}}\right)\cdot(p_\sigma - p_0^{\mathrm{v}}), \tag{96}$$

wherein the temperature dependent ideal parts of the chemical potential disappear, as they are equal in both phases.

In Equation (96) the properties $\mu^{l,c}\left(p_0^l, T\right)$, $\mu^{v,c}\left(p_0^v, T\right)$, v_0^l, and v_0^v are obtained from NpT-simulations of the liquid and the vapor phases at temperature T in both phases and reference pressures p_0^l and p_0^v, respectively. These reference pressures can be chosen arbitrarily, but should not be too far off the vapor pressure. It is convenient for performing molecular simulations, that p_0^v may differ from p_0^l.

Apart from the vapor pressure p_σ, saturated densities ρ', ρ'', and saturated enthalpies h', h'' are important properties of the vapor-liquid equilibrium. They can be obtained from first order Taylor series

$$\rho' \approx \rho^l\left(p_0^l, T\right) + \beta_T^l\left(p_0^l, T\right) \cdot \rho^l\left(p_0^l, T\right) \cdot \left(p_\sigma - p_0^l\right), \tag{97}$$

$$\rho'' \approx \rho^v\left(p_0^v, T\right) + \beta_T^v\left(p_0^v, T\right) \cdot \rho^v\left(p_0^v, T\right) \cdot \left(p_\sigma - p_0^v\right), \tag{98}$$

and

$$h' \approx h^l\left(p_0^l, T\right) + \left[\frac{\partial h^l}{\partial p}\right]_{p_0^l, T} \cdot \left(p_\sigma - p_0^l\right), \tag{99}$$

$$h'' \approx h^v\left(p_0^v, T\right) + \left[\frac{\partial h^v}{\partial p}\right]_{p_0^v, T} \cdot \left(p_\sigma - p_0^v\right). \tag{100}$$

Both the isothermal compressibilities, defined as

$$\beta_T = \frac{1}{\rho}\left[\frac{\partial \rho}{\partial p}\right]_T, \tag{101}$$

in Equations (97) and (98), and the partial derivatives of the enthalpies with respect to the pressure in Equations (99) and (100) can be determined during the NpT-simulations of the liquid and the vapor phases according to fluctuation formulae taken from [421]

$$\beta_T = \frac{1}{k_B T} \cdot \frac{1}{\langle V\rangle_{NpT}} \cdot \left(\langle V^2\rangle_{NpT} - \langle V\rangle_{NpT}^2\right), \tag{102}$$

$$\left[\frac{\partial h}{\partial p}\right]_{p,T} = \frac{1}{N}\left[-\frac{1}{k_B T} \cdot \left(\langle HV\rangle_{NpT} - \langle H\rangle_{NpT}\langle V\rangle_{NpT}\right) + \langle V\rangle_{NpT}\right]. \tag{103}$$

2.5.2 Grand Equilibrium Method

The Grand Equilibrium Method is a two-step simulation method, that yields the equilibrium pressure $p' = p''$ and the vapor phase composition $\boldsymbol{y}''$ in equilibrium for specified temperature $T = T' = T''$ and specified liquid phase composition $\boldsymbol{x}'$ in equilibrium. The phase equilibrium conditions, cf. Equations (72) to (76), are evaluated in two steps by means of molecular simulation. In the case of a binary mixture of components a and b, Equations (74) and (76) represent three equations for finding three properties p'', y_a'', and y_b''. They represent four equations for calculating four properties p'', y_a'', y_b'', and y_c'' in the case of a ternary mixture of components a, b, and c, and so on.

The two steps of the Grand Equilibrium Method are explained on the basis of the phase equilibrium conditions according to Equation (74).

In the first step, approximated pressure dependent expressions for the chemical potential of each component in the liquid phase are calculated from a NpT molecular dynamics or Monte Carlo simulation of the liquid phase at temperature T, composition $\boldsymbol{x}'$, and reference pressure p_0^{l}. In analogy to the approach described in Chapter 2.5.1 for the NpT + Test Particle Method, these approximated expressions stem from

$$\mu_a^{\mathrm{l}}\left(p, T, \boldsymbol{x}'\right) = \mu_a^{\mathrm{l}}\left(p_0^{\mathrm{l}}, T, \boldsymbol{x}'\right) + \int_{p_0^{\mathrm{l}}}^{p} \left[\frac{\partial \mu_a^{\mathrm{l}}}{\partial p}\right]_{T,\boldsymbol{x}'} dp, \tag{104}$$

wherein the pressure integral can be linearized by assuming constant partial molar volume of component a at reference pressure

$$\left[\frac{\partial \mu_a^{\mathrm{l}}}{\partial p}\right]_{T,\boldsymbol{x}'} = v_a^{\mathrm{l}} \approx v_{a,0}^{\mathrm{l}} \approx \text{const.}, \tag{105}$$

and the chemical potential $\mu_a^{\mathrm{l}}\left(p_0^{\mathrm{l}}, T, \boldsymbol{x}'\right)$ in Equation (104) can be expressed in terms of the temperature dependent ideal contribution $\mu_{Ta}^{\mathrm{l,id}}(T)$ and the configurational contribution $\mu_a^{\mathrm{l,c}}\left(p_0^{\mathrm{l}}, T, \boldsymbol{x}'\right)$, cf. Equations (92) to (95). Hence, the approximated pressure dependent expression for the chemical potential of component a in the liquid phase is

$$\mu_a^{\mathrm{l}}\left(p, T, \boldsymbol{x}'\right) = \mu_{Ta}^{\mathrm{l,id}}(T) + \mu_a^{\mathrm{l,c}}\left(p_0^{\mathrm{l}}, T, \boldsymbol{x}'\right) + v_{a,0}^{\mathrm{l}} \cdot \left(p - p_0^{\mathrm{l}}\right). \tag{106}$$

The properties $\mu_a^{\mathrm{l,c}}\left(p_0^{\mathrm{l}}, T, \boldsymbol{x}'\right)$ and $v_{a,0}^{\mathrm{l}}$ in Equation (106) are obtained from test particle insertion or gradual insertion, cf. Chapter 2.4.2, during the molecular simulation of the liquid phase.

In the second step, the vapor phase in equilibrium with the liquid phase is evaluated by a quasi grand canonical Monte Carlo simulation at temperature T and constant volume V^{v}. In this vapor phase simulation, according to the phase equilibrium conditions, cf. Equation (74), the approximated expressions for the chemical potentials of each component given by Equation (106) are prescribed, i.e.

$$\mu_a^{\mathrm{v}}\left(p^{\mathrm{v}}, T, \boldsymbol{y}''\right) \stackrel{!}{=} \mu_a^{\mathrm{l}}\left(p^{\mathrm{v}}, T, \boldsymbol{x}'\right), \tag{107}$$

wherein, according to Equation (73), the pressure of the vapor phase is used for the evaluation of the specified chemical potentials. As the pressure of the vapor phase fluctuates during the simulation, the specified chemical potentials fluctuate, too. Therefore, the vapor phase simulation is called quasi grand canonical instead of grand canonical – the latter expression would assume constant specified chemical potentials. Insertion and deletion of molecules during the vapor phase simulation allows to drive the chemical potential of each component in the vapor phase to the specified values, cf. Equation (107). By this process, the vapor phase simulation finds its way to the equilibrium composition $\boldsymbol{y}''$ and to the equilibrium pressure p''.

For the practical application of the Grand Equilibrium Method it is useful to know, that the volume V^{v}, or, in other words, the number N of molecules, and the initial composition $\boldsymbol{y}$ of the vapor phase can be chosen arbitrarily. However, insertion and deletion of molecules may lead to a significant change of the number of molecules in the volume V^{v}, that may end up in an almost empty simulation box or in a very large number of molecules to be handled during the simulation. The first case leads to bad statistics, the second one increases computation time. It is therefore advisable, to start the vapor phase simulation at a composition near the (expected) equilibrium composition, and to choose the volume according to a typical vapor phase density for a desired number of molecules, for example some 200 - 300.

For the insertion and deletion of molecules, the acceptance criteria of a grand canonical Monte Carlo simulation were used [114]. For insertion, a species a, a position in the simulation box, where the molecule is to be inserted, (and an orientation) are chosen at random. With μ_a^{l} being the specified chemical potential of species a in the vapor phase, the new molecule is accepted with the probability

$$\min\left(1, \frac{1}{I_a(T)} \cdot \frac{V^{\mathrm{v}}}{N_a + 1_a} \cdot \exp\left[\beta\left(\mu_a^{\mathrm{l}} - U_{N+1} + U_N\right)\right]\right), \tag{108}$$

wherein $I_a(T)$ is $\lambda_{a'}^{f_{\mathrm{tr}}}$ in the case of insertion of a a' molecule and $R_{a''}(T)$, cf. Equation (270) in Appendix B, in the case of insertion of a a'' molecule. U_{N+1} is the internal energy of the system with the trial molecule, U_N is the internal energy of the system before trial insertion. For deletion, a molecule is chosen at random among the N molecules. The deletion is accepted with the probability

$$\min\left(1, I_a(T) \cdot \frac{N_a}{V^{\mathrm{v}}} \cdot \exp\left[-\beta\left(\mu_a^{\mathrm{l}} + U_{N-1} - U_N\right)\right]\right). \tag{109}$$

Herein, U_{N-1} is the internal energy of the system after trial deletion, U_N is the internal energy of the system without deletion. For μVT-simulations, probabilities that allow one trial insertion and one trial deletion within one Monte Carlo loop are reasonable.

In the same way as by the NpT+Test Particle Method in Chapter 2.5.1, the saturated liquid density $\rho'\left(p'', T, \boldsymbol{x}'\right)$ and enthalpy $h'\left(p'', T, \boldsymbol{x}''\right)$ can be calculated, when the equilibrium pressure is determined. The saturated vapor density $\rho''\left(p'', T, \boldsymbol{y}''\right)$ and enthalpy $h''\left(p'', T, \boldsymbol{y}''\right)$ result from the vapor phase simulation.

3 Vapor-Liquid Equilibria of Model Classes

Vapor-liquid equilibria of the 2CLJQ/2CLJD model fluids were calculated systematically over a wide range of the model parameters by the means of molecular simulation. The focus was on the critical temperature, the critical density, the saturated liquid and vapor densities, and the vapor pressure. This simulation work was aimed at developing empirical correlations of these properties in terms of the model parameters. These correlations allow to interpolate between the discrete parameter values of the simulations and were the most important tool for fitting the model parameters to experimental vapor-liquid equilibria, cf. Chapter 4.

For the 2CLJQ/2CLJD model fluids equations of state are available, cf. [268, 339], that describe the reduced Helmholtz free energies F^*_{2CLJQ} and F^*_{2CLJD} in terms of additive contributions from the two-center Lennard-Jones interactions (F^*_{2CLJ}, Mecke et al. [268]) and from the quadrupolar and dipolar interactions (F^*_{Q} and F^*_{D}, Saager et al. [339]), cf. Equations (110) and (111),

$$F^*_{\mathrm{2CLJQ}} = F^*_{\mathrm{2CLJ}} + F^*_{\mathrm{Q}}, \tag{110}$$

$$F^*_{\mathrm{2CLJD}} = F^*_{\mathrm{2CLJ}} + F^*_{\mathrm{D}}. \tag{111}$$

They are often called hybrid equations of state. The range of validity of Equations (110) and (111) is indicated as $Q^{*2} \leq 4$, $\mu^{*2} \leq 12$, $L^* \leq 0.8$, cf. Chapter 3.1 for the definition of Q^{*2}, μ^{*2}, L^*. The terms F^*_{Q} and F^*_{D} from the literature are based on energetic simulation data of 2CLJQ and 2CLJD model fluids with different values for the polar momenta ($Q^{*2} \leq 4$, $\mu^{*2} \leq 12$) at one elongation $L^* = 0.505$, i.e. inaccuracies of vapor-liquid equilibria from these equations of state can be expected for model fluids with elongations other than $L^* = 0.505$.

3.1 Quadrupolar and Dipolar Model Fluids

The 2CLJQ pair potential is composed of two identical Lennard-Jones sites a distance L apart (2CLJ) and an elongated ideal point quadrupole of momentum Q placed in the geometric center of the molecule along its elongated axis. The interaction energy of two elongated ideal point quadrupoles is the large distance approximation of the interaction energy of two linearly arranged Coulomb charge quadruples. The pair potential function u_{2CLJQ}

$$u_{\mathrm{2CLJQ}}(\boldsymbol{r}_{ij}, \boldsymbol{e}_i, \boldsymbol{e}_j, L, Q) = u_{\mathrm{2CLJ}}(\boldsymbol{r}_{ij}, \boldsymbol{e}_i, \boldsymbol{e}_j, L) + u_{\mathrm{Q}}(\boldsymbol{r}_{ij}, \boldsymbol{e}_i, \boldsymbol{e}_j, Q), \tag{112}$$

contains the contribution of the Lennard-Jones interactions

$$u_{\mathrm{2CLJ}}(\boldsymbol{r}_{ij}, \boldsymbol{e}_i, \boldsymbol{e}_j, L) = \sum_{s=1}^{2}\sum_{k=1}^{2} 4\varepsilon \left[\left(\frac{\sigma}{r_{isjk}} \right)^{12} - \left(\frac{\sigma}{r_{isjk}} \right)^{6} \right], \tag{113}$$

and the contribution of the quadrupole-quadrupole interaction [132]

$$u_{\mathrm{Q}}(\boldsymbol{r}_{ij}, \boldsymbol{e}_i, \boldsymbol{e}_j, Q) = \frac{1}{4\pi\varepsilon_0} \cdot \frac{3}{4} \frac{Q^2}{|\boldsymbol{r}_{ij}|^5} \left[1 - 5\left(\cos^2\theta_i + \cos^2\theta_j\right) - 15\cos^2\theta_i \cos^2\theta_j + 2\left(\cos\gamma_{ij} - 5\cos\theta_i \cos\theta_j\right)^2\right], \quad (114)$$

cf. Appendices A.1 and A.2. Herein $\boldsymbol{r}_{ij}$ is the center-center distance vector of two molecules i and j, r_{isjk} is one of the four Lennard-Jones site-site distances; s counts the two Lennard-Jones sites of molecule i, k counts those of molecule j. The vectors $\boldsymbol{e}_i$ and $\boldsymbol{e}_j$ are the unit vectors directed along the elongated axis of the molecules i and j. These unit vectors represent the orientations of the two molecules. θ_i is the angle between the axis $\boldsymbol{e}_i$ and the center-center connection line $\boldsymbol{r}_{ij}$, i.e. $\cos\theta_i = \boldsymbol{e}_i \cdot \boldsymbol{r}_{ij} / |\boldsymbol{r}_{ij}|$. γ_{ij} is the angle between $\boldsymbol{e}_i$ and $\boldsymbol{e}_j$, i.e. $\cos\gamma_{ij} = \boldsymbol{e}_i \cdot \boldsymbol{e}_j$. The Lennard-Jones parameters σ and ε represent size and energy, respectively.

Replacing the axial point quadrupole by an axial ideal point dipole of momentum μ yields the 2CLJD pair potential. In Equation (112), u_{Q} is replaced by the contribution of the dipole-dipole interaction u_{D} [132]

$$u_{\mathrm{D}}(\boldsymbol{r}_{ij}, \boldsymbol{e}_i, \boldsymbol{e}_j, \mu) = \frac{1}{4\pi\varepsilon_0} \cdot \frac{\mu^2}{|\boldsymbol{r}_{ij}|^3} \left(\cos\gamma_{ij} - 3\cos\theta_i \cos\theta_j\right), \quad (115)$$

cf. Appendix A.3. Both the 2CLJQ and the 2CLJD model have four model parameters: σ, ε, L, and Q or μ. The Lennard-Jones parameters σ and ε are used for the reduction of the thermodynamic properties as well as the model parameters L, Q, and μ:

$$T^* = Tk_{\mathrm{B}}/\varepsilon, \quad (116)$$
$$p^* = p\sigma^3/\varepsilon, \quad (117)$$
$$\rho^* = \rho\sigma^3, \quad (118)$$
$$E^* = E/\varepsilon, \quad (119)$$
$$L^* = L/\sigma, \quad (120)$$
$$Q^* = Q/\sqrt{4\pi\varepsilon_0\varepsilon\sigma^5}, \quad (121)$$
$$\mu^* = \mu/\sqrt{4\pi\varepsilon_0\varepsilon\sigma^3}, \quad (122)$$

wherein E represents any energetic property such as the internal energy U, the enthalpy H, or the Helmholtz free energy F. Furthermore, $k_{\mathrm{B}} = 1.38066 \cdot 10^{23}$ J/K is the Boltzmann constant and $\varepsilon_0 = 8.85419 \cdot 10^{-12}$ C^2/(Nm^2) is the permittivity of the vacuum.

As reduced properties are used, the systematic investigation of the 2CLJQ and 2CLJD model fluids require parameter grids of only two parameters: L^* and Q^*, or L^* and μ^*. For convenience, Q^{*2} and μ^{*2} are used instead of Q^* and μ^*. In the case of the 2CLJQ model fluid, the parameter grid contained 30 parameter pairs with $L^* = 0, 0.2, 0.4, 0.505, 0.6, 0.8$ and $Q^{*2} = 0, 1, 2, 3, 4$. For the 2CLJD model fluids the L^* parameter range was extended

to $L^* = 1$, as large elongations L^* were expected for some real multipolar fluids. The values for μ^{*2} were 0, 3, 6, 9, and 12. All combinations of these values lead to a grid of 35 2CLJD fluids. Additionally, the fluids with $L^* = 0.0, 0.2$, $\mu^{*2} = 16$ and $L^* = 0.0$, $\mu^{*2} = 20$ were investigated, as very strong dipolar momenta are only expected for molecules with small elongation L^*. So, altogether 38 2CLJD model fluids were considered.

With $L^* = 0$, the 2CLJQ/2CLJD pair potentials comprise the spherical single Lennard-Jones based pair potentials 1CLJQ and 1CLJD. Due to superposition of the two Lennard-Jones sites, the reduced temperatures, reduced pressures, reduced enthalpies and reduced squared polar momenta are four times the corresponding reduced values of the 1CLJQ/1CLJD pair potentials.

Hereafter, the symbol P^{*2} represents the squared polar momenta Q^{*2} or μ^{*2}.

3.2 Vapor-Liquid Equilibria and Critical Point

For a new model fluid the temperature range in which vapor-liquid equilibria occur is not known a priori. Therefore, knowledge on the critical point is a prerequisite for the determination of vapor-liquid equilibria state points of a new model fluid. The above mentioned hybrid equations of state, cf. Equations (110) and (111), were used here in order to determine estimates $T^*_{c,est}(P^{*2}, L^*)$ for the critical temperatures $T^*_c(P^{*2}, L^*)$ of all 30 2CLJQ model fluids and of the 2CLJD model fluids with $L^* \leq 0.8$ and $\mu^{*2} \leq 12$. Estimates for the critical temperatures of the remaining eight 2CLJD model fluids, whose dipole momenta $\mu^{*2} \geq 16$ or elongations $L^* = 1.0$ are out of the range of validity of the 2CLJD equation of state, were obtained from simple extrapolations on the basis of the available estimated critical temperatures.

For each 2CLJQ and 2CLJD model fluid, vapor-liquid equilibrium data were calculated for ten temperatures $T^* = 0.55$, 0.60, 0.65, 0.70, 0.75, 0.80, 0.85, 0.90, 0.925, $0.95 \cdot T^*_{c,est}(P^{*2}, L^*)$ with the NpT+Test Particle Method as described in Chapter 2.5.1. Vapor pressures p^*_σ, saturated liquid and vapor densities ρ'^* and ρ''^*, and residual enthalpies in equilibrium $h^{*res}(T^*, \rho^*) = h^*(T^*, \rho^*) - h^{*id}(T^*)$ were evaluated. Liquid simulations were performed for all ten temperatures, whereas vapor simulations were only performed at temperatures above $0.80 \cdot T^*_{c,est}$, as below this temperature the second virial coefficient, cf. [3, 132], is sufficiently precise for vapor-liquid equilibrium calculations.

For the 2CLJQ model fluids, all simulations were based on molecular dynamics in the NpT ensemble, and the configurational part of the chemical potential in both the liquid and the vapor phases was obtained from the test particle insertion method, cf. Chapter 2.4. Most of the 2CLJD simulations were performed in complete analogy to the 2CLJQ simulations. However, at dense low-temperature liquid state points large uncertainties of the configurational part of the chemical potential are obtained from the test particle insertion method, which cause largely uncertain vapor pressures. This effect is particularly important when highly dipolar model fluids with large elongations are

studied. Due to these difficulties at low temperature state points, molecular simulations of vapor-liquid equilibria of dipolar model fluids are performed typically only down to about $0.70 \cdot T_c^*$. Below, special techniques are needed for obtaining more accurate results. In the present work, accurate description of the vapor pressure of dipolar model fluids at low temperatures was obatined from applying the gradual insertion method based on Monte Carlo simulations as described in Chapter 2.4 at $0.55 \cdot T_{c,est}^*$ of the 2CLJD model fluids with $L^* = 0 \ldots 1.0$, $\mu^{*2} = 0 \ldots 12$, except for $L^* = 0$, $\mu^{*2} = 12$. For the 2CLJD model fluids $L^* = 0$, $\mu^{*2} \geq 12$ and $L^* = 0.2$, $\mu^{*2} \geq 16$ the test particle insertion method was applied with an increased number of test particles and extended simulation run lengths at $0.55 \cdot T_{c,est}^*$. Uniformly, the molecular simulations of 2CLJQ and 2CLJD model fluids were performed with a large number of particles and large cut-off radii, cf. Appendices C.1 and C.2 for technical details.

3.2.1 Simulation Results

Extracts of the vapor-liquid equilibrium data of the 30 2CLJQ model fluids and of the 38 2CLJD model fluids obtained from molecular simulation are reported in Tables 1 and 2, respectively. For the sake of brevity not all state points for which simulations were carried out are included in Tables 1 and 2. Reported are the vapor pressure p_σ^*, the saturated liquid density ρ'^*, the saturated vapor density ρ''^*, the residual saturated liquid enthalpy h'^{res*}, and the residual saturated vapor enthalpy h''^{res*} for three temperatures $T^* = 0.55$, 0.80, $0.95 \cdot T_{c,est}^*$ (P^{*2}, L^*). The full data set is given in [378].

Figures 1 to 4 illustrate the strong influence of the elongation and the polar momenta on the temperature-density coexistence curves and the vapor pressure curves. Increasing the elongation raises the size of the molecules and thus lowers the saturated liquid density. This effect is accompanied by a decrease of the mean attractive interactions seen from the decrease of the critical temperature and the high vapor pressures. In contrast, stronger polar interactions yield higher saturated liquid densities, higher critical temperatures and lower vapor pressures.

When the chemical potential is obtained from test particle insertion, the NpT + Test Particle Method yields the vapor pressure with large uncertainty at low temperatures in the case of fluids with large elongations or strong polar momenta, cf. Figures 2 and 4. Figure 4 illustrates, at lowest temperatures, the considerable decrease of the uncertainty of the vapor pressure when the chemical potential is obtained from gradual insertion instead of test particle insertion in the liquid phase. In the present work, gradual insertion was not applied to 2CLJQ fluids, as this method was available to the author only after work on pure 2CLJQ fluids was finished.

The comparison of the vapor-liquid equilibrium data from present work to the above mentioned hybrid equations of state reveals systematic deviations, cf. bottom of Figures 1 and 2 for 2CLJQ model fluids, and bottom of Figures 3 and 4 for 2CLJD model fluids.

Table 1: Vapor-liquid equilibria of 30 2CLJQ model fluids. Extract from simulation results. The numbers in parentheses indicate the uncertainties of the last digits. † indicates that instead of a vapor phase simulation the second virial coefficient was used.

T^*	p^*_σ	ρ'^*	ρ''^*	h'^{res*}	h''^{res*}
$L^*=0,\ Q^{*2}=0$					
2.92600†	0.00852 (33)	0.82938 (25)	0.00299 (12)	-26.8247 (86)	-0.2197 (89)
4.25600	0.1469 (14)	0.66404 (55)	0.04347 (53)	-22.457 (15)	-2.459 (33)
5.05400	0.4120 (34)	0.4925 (31)	0.1475 (38)	-17.768 (77)	-6.98 (17)
$L^*=0,\ Q^{*2}=1$					
2.97000†	0.00796 (49)	0.84416 (22)	0.00275 (18)	-28.4469 (83)	-0.212 (14)
4.32000	0.1472 (13)	0.67461 (58)	0.04239 (62)	-23.448 (17)	-2.453 (43)
5.13000	0.4108 (34)	0.4994 (24)	0.1398 (56)	-18.453 (60)	-6.84 (26)
$L^*=0,\ Q^{*2}=2$					
3.09100†	0.0057 (11)	0.87669 (24)	0.00186 (36)	-32.4004 (97)	-0.165 (31)
4.49600	0.1417 (17)	0.69986 (61)	0.03877 (86)	-26.051 (19)	-2.490 (77)
5.33900	0.4199 (36)	0.5288 (22)	0.1375 (31)	-20.553 (59)	-7.27 (16)
$L^*=0,\ Q^{*2}=3$					
3.26700†	0.0046 (11)	0.91399 (29)	0.00144 (35)	-37.714 (14)	-0.155 (37)
4.75200	0.1352 (16)	0.73335 (52)	0.03653 (67)	-29.885 (19)	-2.745 (76)
5.64300	0.4213 (32)	0.5667 (17)	0.1220 (20)	-23.694 (53)	-7.09 (11)
$L^*=0,\ Q^{*2}=4$					
3.47600†	0.0036 (14)	0.95228 (25)	0.00106 (43)	-43.992 (13)	-0.144 (58)
5.05600	0.1202 (23)	0.77053 (46)	0.0260 (19)	-34.733 (19)	-2.04 (27)
6.00400	0.4186 (42)	0.6079 (15)	0.1082 (27)	-27.730 (54)	-7.09 (18)
$L^*=0.2,\ Q^{*2}=0$					
2.42000†	0.00576 (31)	0.73095 (24)	0.00244 (13)	-22.5710 (79)	-0.1737 (96)
3.52000	0.1092 (11)	0.58419 (52)	0.03850 (56)	-18.792 (14)	-2.024 (47)
4.18000	0.2990 (22)	0.4236 (23)	0.1279 (23)	-14.595 (52)	-5.769 (94)
$L^*=0.2,\ Q^{*2}=1$					
2.45850†	0.00514 (39)	0.74117 (23)	0.00214 (17)	-23.7142 (79)	-0.158 (12)
3.57600	0.1092 (12)	0.58928 (50)	0.03927 (80)	-19.412 (14)	-2.219 (69)
4.24650	0.3123 (23)	0.4320 (30)	0.1317 (26)	-15.102 (69)	-6.04 (13)
$L^*=0.2,\ Q^{*2}=2$					
2.55200†	0.00458 (49)	0.76427 (20)	0.00183 (20)	-26.5697 (78)	-0.151 (17)
3.71200	0.1062 (12)	0.60533 (59)	0.03580 (38)	-21.203 (17)	-2.147 (24)
4.40800	0.3213 (27)	0.4448 (22)	0.1298 (27)	-16.348 (56)	-6.21 (11)
$L^*=0.2,\ Q^{*2}=3$					
2.68950†	0.00300 (60)	0.79142 (26)	0.00113 (23)	-30.474 (11)	-0.110 (22)
3.91200	0.1081 (16)	0.62931 (54)	0.03498 (66)	-23.918 (18)	-2.353 (57)
4.64550	0.3234 (27)	0.4559 (26)	0.1147 (41)	-18.074 (70)	-6.11 (21)
$L^*=0.2,\ Q^{*2}=4$					
2.86000†	0.0044 (15)	0.81978 (22)	0.00158 (53)	-35.098 (11)	-0.187 (63)
4.16000	0.1061 (17)	0.65261 (48)	0.0281 (14)	-27.201 (18)	-1.94 (15)
4.94000	0.3428 (31)	0.4877 (20)	0.1137 (42)	-20.837 (61)	-6.60 (24)

Table 1: continued.

T^*	p_σ^*	ρ'^*	ρ''^*	$h'^{\mathrm{res}*}$	$h''^{\mathrm{res}*}$
$L^* = 0.4$, $Q^{*2} = 0$					
1.78750†	0.00325 (21)	0.59531 (20)	0.00187 (13)	-17.2882 (61)	-0.1312 (89)
2.60000	0.06524 (64)	0.47244 (58)	0.03277 (80)	-14.213 (14)	-1.708 (73)
3.08750	0.1892 (18)	0.3417 (26)	0.1231 (59)	-10.955 (54)	-5.08 (21)
$L^* = 0.4$, $Q^{*2} = 1$					
1.81500†	0.00267 (19)	0.60158 (20)	0.00150 (11)	-18.0097 (64)	-0.1077 (76)
2.64000	0.06547 (71)	0.47589 (47)	0.03121 (59)	-14.605 (12)	-1.626 (41)
3.13500	0.1910 (20)	0.3273 (46)	0.1163 (41)	-10.845 (96)	-4.90 (16)
$L^* = 0.4$, $Q^{*2} = 2$					
1.88100†	0.00226 (33)	0.61695 (19)	0.00122 (18)	-19.8956 (69)	-0.096 (14)
2.73600	0.06747 (71)	0.48583 (52)	0.03174 (31)	-15.731 (14)	-1.772 (22)
3.24900	0.2002 (20)	0.3332 (39)	0.1166 (39)	-11.498 (91)	-5.12 (16)
$L^* = 0.4$, $Q^{*2} = 3$					
1.97450†	0.00308 (45)	0.63581 (17)	0.00160 (24)	-22.5113 (73)	-0.144 (22)
2.87200	0.06607 (81)	0.49850 (43)	0.02904 (41)	-17.378 (13)	-1.759 (33)
3.41050	0.2118 (21)	0.3515 (25)	0.1200 (36)	-12.817 (63)	-5.69 (16)
$L^* = 0.4$, $Q^{*2} = 4$					
2.09000†	0.0023 (11)	0.65625 (20)	0.00112 (54)	-25.654 (10)	-0.118 (57)
3.04000	0.0670 (11)	0.51516 (44)	0.02688 (71)	-19.512 (15)	-1.773 (58)
3.61000	0.2246 (21)	0.3635 (20)	0.1184 (34)	-14.256 (51)	-6.07 (16)
$L^* = 0.505$, $Q^{*2} = 0$					
1.55650†	0.00275 (15)	0.54062 (17)	0.00182 (10)	-15.3895 (52)	-0.1289 (72)
2.26400	0.05086 (49)	0.42814 (44)	0.02815 (29)	-12.583 (11)	-1.385 (17)
2.68850	0.1487 (15)	0.2927 (50)	0.1093 (38)	-9.31 (10)	-4.42 (14)
$L^* = 0.505$, $Q^{*2} = 1$					
1.57850†	0.00219 (20)	0.54667 (17)	0.00142 (14)	-16.0333 (55)	-0.1021 (97)
2.29600	0.05150 (62)	0.43263 (51)	0.02783 (28)	-12.959 (13)	-1.381 (13)
2.72650	0.1525 (16)	0.2972 (64)	0.1123 (40)	-9.55 (12)	-4.59 (15)
$L^* = 0.505$, $Q^{*2} = 2$					
1.63350†	0.00197 (51)	0.56070 (18)	0.00123 (33)	-17.6851 (69)	-0.097 (26)
2.37600	0.05095 (61)	0.44022 (43)	0.02713 (70)	-13.902 (12)	-1.470 (50)
2.82150	0.1611 (19)	0.3072 (31)	0.1142 (42)	-10.273 (72)	-4.83 (15)
$L^* = 0.505$, $Q^{*2} = 3$					
1.71600†	0.00153 (37)	0.57667 (18)	0.00091 (22)	-19.9069 (70)	-0.081 (20)
2.49600	0.05254 (69)	0.45184 (47)	0.0277 (10)	-15.321 (14)	-1.686 (96)
2.96400	0.1684 (21)	0.3064 (36)	0.1138 (54)	-10.964 (90)	-5.17 (22)
$L^* = 0.505$, $Q^{*2} = 4$					
1.81500†	0.00089 (50)	0.59445 (18)	0.00049 (28)	-22.5908 (89)	-0.052 (30)
2.64000	0.05430 (87)	0.46561 (47)	0.02598 (77)	-17.109 (16)	-1.672 (69)
3.13500	0.1781 (19)	0.3220 (31)	0.1099 (37)	-12.274 (84)	-5.45 (18)
$L^* = 0.6$, $Q^{*2} = 0$					
1.40250†	0.00202 (15)	0.50020 (15)	0.00148 (12)	-14.0888 (46)	-0.1052 (82)
2.04000	0.04288 (48)	0.39339 (41)	0.02746 (70)	-11.408 (10)	-1.387 (55)
2.42250	0.1286 (13)	0.2643 (34)	0.1075 (33)	-8.299 (70)	-4.26 (13)

Table 1: continued.

T^*	p_σ^*	ρ'^*	ρ''^*	h'^{res*}	h''^{res*}
$L^* = 0.6$, $Q^{*2} = 1$					
1.41900†	0.00173 (16)	0.50637 (16)	0.00125 (11)	-14.7048 (52)	-0.0909 (83)
2.06400	0.04212 (47)	0.39815 (47)	0.02676 (68)	-11.785 (12)	-1.407 (55)
2.45100	0.1301 (14)	0.2800 (20)	0.1153 (58)	-8.804 (41)	-4.55 (18)
$L^* = 0.6$, $Q^{*2} = 2$					
1.46850†	0.00136 (23)	0.51998 (17)	0.00094 (16)	-16.2362 (63)	-0.075 (13)
2.13600	0.04282 (62)	0.40725 (46)	0.0307 (19)	-12.696 (13)	-1.89 (17)
2.53650	0.1311 (12)	0.2598 (65)	0.1016 (32)	-8.79 (14)	-4.32 (12)
$L^* = 0.6$, $Q^{*2} = 3$					
1.54000†	0.00144 (25)	0.53541 (17)	0.00095 (17)	-18.2738 (74)	-0.086 (15)
2.24000	0.04270 (57)	0.41820 (41)	0.02300 (33)	-13.986 (13)	-1.289 (25)
2.66000	0.1398 (15)	0.2792 (44)	0.1058 (48)	-9.87 (10)	-4.73 (19)
$L^* = 0.6$, $Q^{*2} = 4$					
1.62800†	0.00083 (32)	0.55127 (21)	0.00052 (20)	-20.655 (11)	-0.055 (22)
2.36800	0.04378 (81)	0.43014 (48)	0.02306 (70)	-15.565 (16)	-1.495 (68)
2.81200	0.1487 (16)	0.2959 (20)	0.1028 (31)	-11.108 (55)	-4.99 (14)
$L^* = 0.8$, $Q^{*2} = 0$					
1.17700†	0.00143 (15)	0.43844 (13)	0.00124 (14)	-12.2840 (39)	-0.090 (10)
1.71200	0.03152 (36)	0.34003 (50)	0.02282 (22)	-9.768 (12)	-1.090 (12)
2.03300	0.0972 (11)	0.2103 (44)	0.0969 (32)	-6.664 (91)	-3.71 (11)
$L^* = 0.8$, $Q^{*2} = 1$					
1.18800†	0.00120 (18)	0.44763 (13)	0.00103 (16)	-13.0246 (43)	-0.078 (12)
1.72800	0.02961 (36)	0.34908 (40)	0.02164 (26)	-10.278 (10)	-1.099 (12)
2.05200	0.0922 (10)	0.2460 (15)	0.0874 (24)	-7.628 (38)	-3.493 (83)
$L^* = 0.8$, $Q^{*2} = 2$					
1.22650†	0.00083 (20)	0.46255 (15)	0.00069 (17)	-14.5252 (60)	-0.058 (15)
1.78400	0.02859 (42)	0.36096 (43)	0.01992 (37)	-11.232 (12)	-1.109 (19)
2.11850	0.09230 (95)	0.2449 (25)	0.0813 (22)	-8.067 (56)	-3.461 (87)
$L^* = 0.8$, $Q^{*2} = 3$					
1.27600†	0.00053 (16)	0.47977 (14)	0.00042 (13)	-16.4793 (60)	-0.043 (13)
1.85600	0.02629 (53)	0.37721 (36)	0.0144 (11)	-12.622 (12)	-0.76 (11)
2.20400	0.0887 (10)	0.2694 (15)	0.0699 (34)	-9.309 (38)	-3.29 (17)
$L^* = 0.8$, $Q^{*2} = 4$					
1.34200†	0.00033 (26)	0.49548 (17)	0.00025 (19)	-18.6173 (83)	-0.030 (24)
1.95200	0.02440 (67)	0.39236 (38)	0.01619 (54)	-14.226 (13)	-1.157 (71)
2.31800	0.09208 (95)	0.2893 (14)	0.0684 (15)	-10.673 (36)	-3.521 (74)

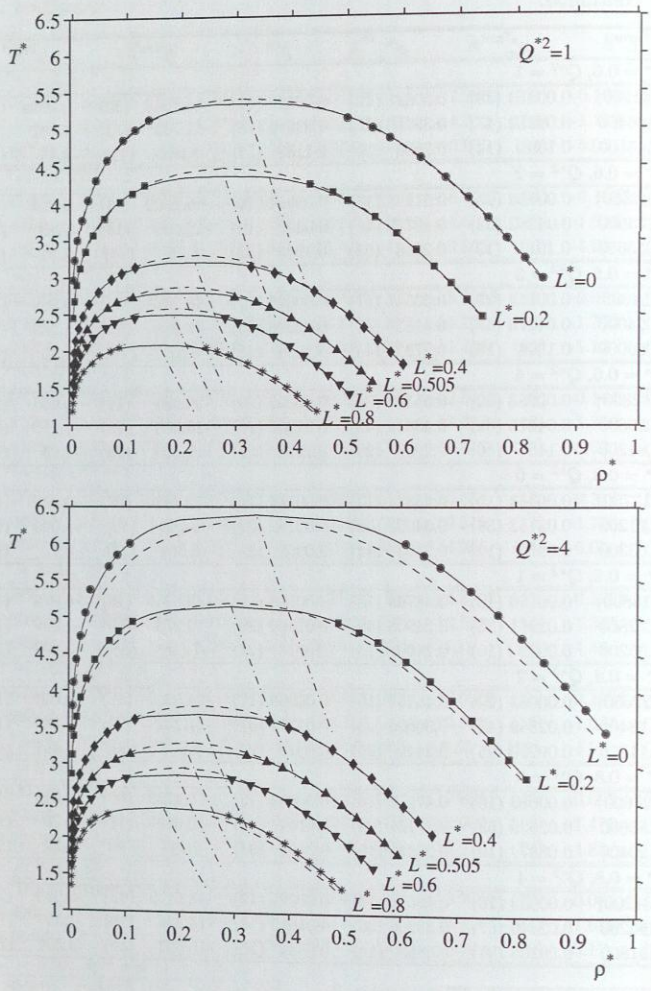

Figure 1: Temperature–density coexistence curves of 2CLJQ model fluids with $Q^{*2} = 1$ (top) and $Q^{*2} = 4$ (bottom). Symbols: simulation data. —— 2CLJQ correlation, cf. Chapter 3.2.2.2. – · – Rectilinear diameter from 2CLJQ correlation. – – – 2CLJQ equation of state [268, 339]. Error bars are, if not indicated, within symbol size.

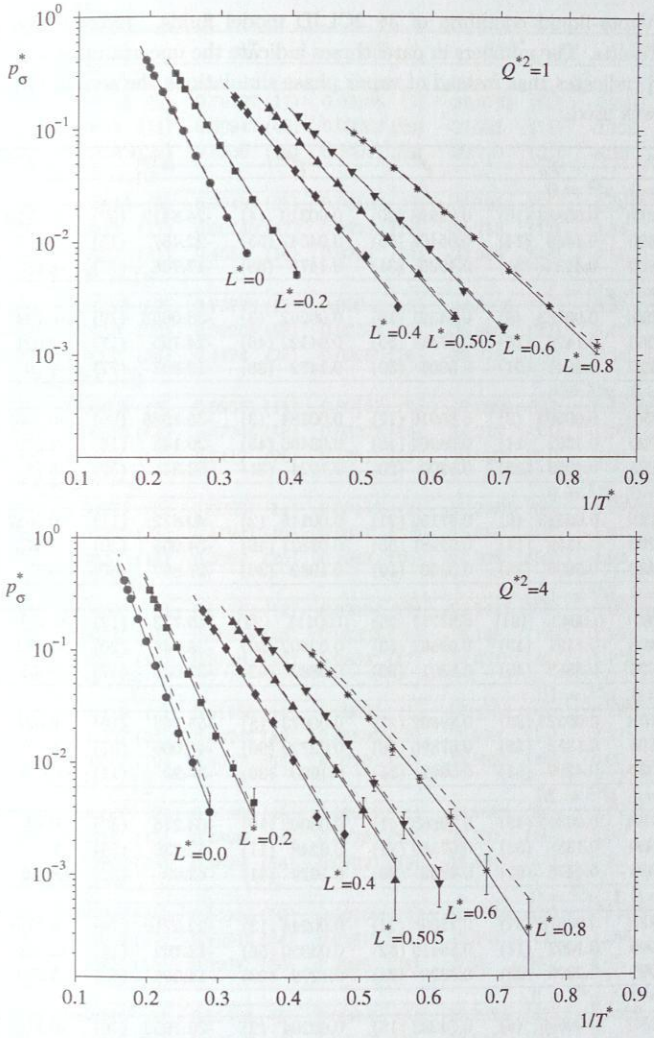

Figure 2: Vapor pressure curves of 2CLJQ model fluids with $Q^{*2} = 1$ (top) and $Q^{*2} = 4$ (bottom). Symbols: simulation data. —— 2CLJQ correlation, cf. Chapter 3.2.2.2. – – – 2CLJQ equation of state [268, 339]. Error bars are, if not indicated, within symbol size.

Table 2: Vapor-liquid equilibria of 38 2CLJD model fluids. Extract from simulation results. The numbers in parentheses indicate the uncertainties of the last digits. † indicates that instead of vapor phase simulations the second virial coefficient was used.

T^*	p^*_σ	ρ'^*	ρ''^*	h'^{res*}	h''^{res*}
$L^*=0,\ \mu^{*2}=0$					
2.92600†	0.00883 (10)	0.82998 (20)	0.00310 (4)	-26.8419 (57)	-0.2279 (27)
4.25600	0.1469 (14)	0.66404 (55)	0.04347 (53)	-22.457 (15)	-2.459 (33)
5.05400	0.4120 (34)	0.4925 (31)	0.1475 (38)	-17.768 (77)	-6.98 (17)
$L^*=0,\ \mu^{*2}=3$					
3.07290†	0.00783 (8)	0.84391 (19)	0.00262 (3)	-30.0653 (79)	-0.2347 (26)
4.46960	0.1476 (16)	0.67441 (56)	0.04122 (46)	-24.795 (17)	-2.621 (26)
5.30770	0.4245 (37)	0.5001 (30)	0.1472 (38)	-19.507 (77)	-7.70 (18)
$L^*=0,\ \mu^{*2}=6$					
3.33250†	0.00599 (8)	0.85910 (17)	0.00184 (3)	-35.1985 (96)	-0.2665 (37)
4.84720	0.1352 (14)	0.68964 (48)	0.03466 (45)	-29.143 (16)	-2.970 (43)
5.75065	0.4053 (35)	0.5200 (20)	0.1224 (31)	-23.346 (59)	-8.11 (20)
$L^*=0,\ \mu^{*2}=9$					
3.63830†	0.00513 (8)	0.87156 (21)	0.00145 (2)	-40.872 (11)	-0.3687 (60)
5.29200	0.1199 (17)	0.69981 (55)	0.02821 (48)	-34.055 (20)	-3.475 (63)
6.28430	0.3909 (35)	0.5362 (19)	0.1082 (30)	-27.867 (60)	-9.37 (22)
$L^*=0,\ \mu^{*2}=12$					
4.01780†	0.00435 (91)	0.87717 (26)	0.00111 (24)	-46.773 (12)	-0.483 (104)
5.84400	0.1191 (19)	0.69862 (53)	0.02602 (39)	-38.948 (20)	-4.482 (44)
6.93975	0.3852 (45)	0.5301 (20)	0.0889 (62)	-32.038 (67)	-10.51 (53)
$L^*=0,\ \mu^{*2}=16$					
4.53370†	0.00323 (35)	0.88692 (27)	0.00073 (8)	-55.163 (19)	-0.626 (70)
6.77600	0.1352 (28)	0.67890 (68)	0.02720 (96)	-45.066 (27)	-6.84 (29)
7.91330	0.4209 (54)	0.5062 (31)	0.1000 (26)	-37.29 (11)	-15.05 (35)
$L^*=0,\ \mu^{*2}=20$					
5.11670†	0.00305 (48)	0.89663 (41)	0.00062 (10)	-64.216 (33)	-0.94 (15)
7.60000	0.1335 (33)	0.67349 (71)	0.0248 (11)	-52.230 (28)	-9.14 (44)
8.93080	0.4475 (92)	0.4862 (89)	0.1029 (41)	-42.93 (32)	-19.56 (62)
$L^*=0.2,\ \mu^{*2}=0$					
2.42000†	0.00576 (31)	0.73095 (24)	0.00244 (13)	-22.5710 (79)	-0.1737 (96)
3.52000	0.1092 (11)	0.58419 (52)	0.03850 (56)	-18.792 (14)	-2.024 (47)
4.18000	0.2990 (22)	0.4236 (23)	0.1279 (23)	-14.595 (52)	-5.769 (94)
$L^*=0.2,\ \mu^{*2}=3$					
2.53720†	0.00506 (6)	0.74233 (15)	0.00204 (2)	-25.1959 (76)	-0.1784 (21)
3.69040	0.1080 (10)	0.59307 (52)	0.03727 (31)	-20.711 (15)	-2.292 (19)
4.38240	0.3046 (26)	0.4289 (35)	0.1265 (32)	-15.990 (86)	-6.34 (15)
$L^*=0.2,\ \mu^{*2}=6$					
2.74340†	0.00397 (5)	0.75312 (20)	0.00148 (2)	-29.2578 (80)	-0.2074 (26)
3.99040	0.0971 (10)	0.60338 (46)	0.03053 (47)	-24.126 (15)	-2.555 (45)
4.73860	0.2965 (27)	0.4490 (24)	0.1115 (30)	-19.121 (64)	-6.97 (18)

Table 2: continued.

T^*	p_σ^*	ρ'^*	ρ''^*	h'^{res*}	h''^{res*}
$L^* = 0.2,\ \mu^{*2} = 9$					
2.98490†	0.00315 (5)	0.76127 (17)	0.00108 (2)	-33.6769 (83)	-0.2596 (40)
4.34160	0.0845 (11)	0.60947 (45)	0.02362 (29)	-27.941 (15)	-2.726 (38)
5.15570	0.2825 (29)	0.4630 (18)	0.1001 (30)	-22.710 (53)	-8.23 (20)
$L^* = 0.2,\ \mu^{*2} = 12$					
3.28790†	0.00319 (5)	0.76489 (21)	0.00100 (2)	-38.165 (11)	-0.3912 (59)
4.78240	0.0830 (17)	0.60746 (47)	0.0229 (10)	-31.755 (17)	-3.84 (20)
5.67910	0.2921 (31)	0.4581 (16)	0.0966 (44)	-25.958 (48)	-9.82 (36)
$L^* = 0.2,\ \mu^{*2} = 16$					
3.71250†	0.00191 (57)	0.76778 (17)	0.00053 (16)	-44.4425 (75)	-0.37 (11)
5.44000	0.0913 (20)	0.59958 (58)	0.02294 (83)	-36.866 (22)	-5.47 (24)
6.41250	0.3067 (36)	0.4424 (22)	0.0966 (26)	-30.213 (73)	-12.92 (29)
$L^* = 0.4,\ \mu^{*2} = 0$					
1.78750†	0.00326 (3)	0.59571 (11)	0.00187 (2)	-17.2882 (60)	-0.1314 (14)
2.60000	0.06524 (64)	0.47244 (58)	0.03277 (80)	-14.213 (14)	-1.708 (73)
3.08750	0.1892 (18)	0.3417 (26)	0.1231 (59)	-10.955 (54)	-5.08 (21)
$L^* = 0.4,\ \mu^{*2} = 3$					
1.86835†	0.00271 (3)	0.60327 (11)	0.00149 (2)	-19.2066 (54)	-0.1316 (16)
2.71760	0.06292 (78)	0.47941 (49)	0.0317 (13)	-15.655 (13)	-1.97 (13)
3.22715	0.1830 (14)	0.3362 (25)	0.1048 (26)	-11.808 (58)	-4.92 (12)
$L^* = 0.4,\ \mu^{*2} = 6$					
2.01025†	0.00205 (3)	0.61042 (12)	0.00104 (1)	-22.1685 (55)	-0.1547 (20)
2.92400	0.05441 (67)	0.48638 (43)	0.02355 (39)	-18.139 (13)	-1.993 (34)
3.43968	0.1632 (15)	0.3710 (16)	0.0839 (17)	-14.631 (42)	-5.123 (89)
$L^* = 0.4,\ \mu^{*2} = 9$					
2.17415†	0.00156 (2)	0.61655 (14)	0.00073 (1)	-25.4563 (61)	-0.1937 (29)
3.16240	0.04737 (81)	0.49242 (42)	0.01895 (42)	-20.979 (14)	-2.271 (50)
3.75535	0.1605 (19)	0.3697 (16)	0.0770 (21)	-16.889 (46)	-6.02 (13)
$L^* = 0.4,\ \mu^{*2} = 12$					
2.38315†	0.00137 (2)	0.61865 (16)	0.00059 (1)	-28.7404 (84)	-0.2600 (35)
3.46640	0.0455 (15)	0.48990 (44)	0.0179 (32)	-23.731 (15)	-3.06 (69)
4.09920	0.1590 (28)	0.3699 (16)	0.0732 (33)	-19.401 (47)	-7.23 (24)
$L^* = 0.505,\ \mu^{*2} = 0$					
1.55650†	0.00237 (3)	0.54105 (10)	0.00156 (2)	-15.3899 (52)	-0.1103 (13)
2.26400	0.05086 (49)	0.42814 (44)	0.02815 (29)	-12.583 (11)	-1.385 (17)
2.68850	0.1487 (15)	0.2927 (50)	0.1093 (38)	-9.31 (10)	-4.42 (14)
$L^* = 0.505,\ \mu^{*2} = 3$					
1.58070†	0.00147 (2)	0.55324 (9)	0.00095 (1)	-17.2624 (51)	-0.0898 (12)
2.36500	0.04830 (58)	0.43338 (43)	0.02539 (69)	-13.835 (12)	-1.464 (53)
2.80820	0.1479 (18)	0.3121 (36)	0.1016 (33)	-10.593 (82)	-4.65 (15)
$L^* = 0.505,\ \mu^{*2} = 6$					
1.74520†	0.00148 (2)	0.55403 (11)	0.00087 (1)	-19.6812 (58)	-0.1371 (19)
2.53800	0.04245 (64)	0.44031 (36)	0.02117 (49)	-16.031 (11)	-1.758 (46)
3.01435	0.1365 (12)	0.3203 (32)	0.0849 (34)	-12.472 (75)	-4.99 (17)

Table 2: continued.

T^*	p_σ^*	ρ'^*	ρ''^*	h'^{res*}	h''^{res*}
$L^* = 0.505$, $\mu^{*2} = 9$					
1.88320†	0.00108 (2)	0.55953 (11)	0.00059 (1)	-22.5779 (61)	-0.1731 (27)
2.73900	0.03763 (74)	0.44532 (42)	0.0211 (23)	-18.511 (13)	-2.77 (41)
3.25280	0.1252 (14)	0.3321 (16)	0.0715 (16)	-14.842 (41)	-5.59 (11)
$L^* = 0.505$, $\mu^{*2} = 12$					
2.06030†	0.00096 (1)	0.56200 (13)	0.00048 (1)	-25.4946 (73)	-0.2481 (35)
2.99000	0.0352 (10)	0.44477 (41)	0.0159 (30)	-20.985 (13)	-2.73 (66)
3.56000	0.1256 (19)	0.3223 (19)	0.0702 (30)	-16.723 (56)	-6.79 (20)
$L^* = 0.6$, $\mu^{*2} = 0$					
1.40250†	0.00197 (2)	0.50039 (9)	0.00144 (2)	-14.0889 (46)	-0.1027 (11)
2.04000	0.04288 (48)	0.39339 (41)	0.02746 (70)	-11.408 (10)	-1.387 (55)
2.42250	0.1286 (13)	0.2643 (34)	0.1075 (33)	-8.299 (70)	-4.26 (13)
$L^* = 0.6$, $\mu^{*2} = 3$					
1.40800†	0.00106 (2)	0.51372 (8)	0.00076 (1)	-15.8529 (52)	-0.0751 (11)
2.12500	0.04056 (48)	0.39966 (40)	0.02425 (41)	-12.580 (11)	-1.407 (25)
2.45952	0.1047 (11)	0.3067 (13)	0.0706 (38)	-10.124 (29)	-3.35 (17)
$L^* = 0.6$, $\mu^{*2} = 6$					
1.56640†	0.00117 (2)	0.51251 (11)	0.00077 (1)	-18.0029 (61)	-0.1286 (18)
2.27840	0.03499 (59)	0.40589 (38)	0.01938 (59)	-14.577 (11)	-1.615 (54)
2.70560	0.1181 (14)	0.2987 (32)	0.0863 (27)	-11.399 (77)	-4.91 (14)
$L^* = 0.6$, $\mu^{*2} = 9$					
1.68800†	0.00082 (1)	0.51756 (11)	0.00050 (1)	-20.6624 (61)	-0.1637 (23)
2.45500	0.0276 (12)	0.40916 (39)	0.01464 (57)	-16.807 (12)	-1.888 (56)
2.88515	0.0979 (13)	0.3160 (11)	0.0629 (33)	-13.769 (27)	-4.94 (21)
$L^* = 0.6$, $\mu^{*2} = 12$					
1.84250†	0.00071 (1)	0.52036 (13)	0.00040 (1)	-23.3629 (78)	-0.2435 (31)
2.68000	0.0265 (15)	0.40876 (41)	0.0123 (13)	-19.059 (13)	-2.06 (26)
3.15552	0.0989 (18)	0.3071 (21)	0.0632 (37)	-15.509 (56)	-6.18 (26)
$L^* = 0.8$, $\mu^{*2} = 0$					
1.17700†	0.00135 (2)	0.43871 (9)	0.00118 (2)	-12.2841 (39)	-0.0855 (11)
1.71200	0.03152 (36)	0.34003 (50)	0.02282 (22)	-9.768 (12)	-1.090 (12)
2.03300	0.0972 (11)	0.2103 (44)	0.0969 (32)	-6.664 (91)	-3.71 (11)
$L^* = 0.8$, $\mu^{*2} = 3$					
1.17150†	0.00065 (1)	0.45198 (9)	0.00057 (1)	-13.8571 (45)	-0.05905 (90)
1.77200	0.02847 (34)	0.34700 (35)	0.02044 (37)	-10.8032 (93)	-1.193 (26)
2.10430	0.0925 (10)	0.2421 (96)	0.0952 (36)	-7.98 (20)	-4.09 (13)
$L^* = 0.8$, $\mu^{*2} = 6$					
1.30130†	0.00070 (1)	0.45104 (10)	0.00055 (1)	-15.7904 (55)	-0.1031 (15)
1.89280	0.02375 (53)	0.35393 (41)	0.01654 (77)	-12.575 (11)	-1.482 (86)
2.24770	0.0846 (10)	0.2567 (15)	0.0687 (26)	-9.692 (38)	-4.12 (19)
$L^* = 0.8$, $\mu^{*2} = 9$					
1.38160†	0.00043 (1)	0.45755 (10)	0.00032 (1)	-18.3431 (57)	-0.1412 (25)
2.02720	0.02041 (58)	0.36185 (34)	0.01305 (52)	-14.691 (10)	-1.707 (65)
2.40730	0.0725 (11)	0.2632 (21)	0.0517 (19)	-11.524 (51)	-4.07 (14)

Table 2: continued.

T^*	p_σ^*	ρ'^*	ρ''^*	h'^{res*}	h''^{res*}
$L^* = 0.8$, $\mu^{*2} = 12$					
1.52096†	0.00037 (1)	0.46033 (13)	0.00025 (1)	-20.8029 (69)	-0.2326 (40)
2.19840	0.01671 (78)	0.36363 (33)	0.0084 (11)	-16.796 (11)	-1.62 (23)
2.61060	0.0658 (12)	0.2648 (12)	0.0442 (44)	-13.318 (33)	-4.62 (36)
$L^* = 1.0$, $\mu^{*2} = 0$					
0.97900†	0.00050 (1)	0.41024 (7)	0.00052 (1)	-11.5972 (43)	-0.04220 (67)
1.50750	0.02504 (30)	0.30729 (43)	0.0184 (14)	-8.871 (11)	-0.931 (89)
1.69100	0.05413 (62)	0.2461 (13)	0.0436 (44)	-7.358 (29)	-1.93 (18)
$L^* = 1.0$, $\mu^{*2} = 3$					
1.02850†	0.00044 (1)	0.41346 (9)	0.00043 (1)	-12.8117 (48)	-0.04662 (66)
1.50750	0.01711 (27)	0.32581 (31)	0.01378 (28)	-10.1499 (90)	-0.848 (17)
1.77650	0.05688 (68)	0.25218 (96)	0.0495 (52)	-8.122 (23)	-2.39 (24)
$L^* = 1.0$, $\mu^{*2} = 6$					
1.08900†	0.00026 (1)	0.42225 (8)	0.00024 (1)	-15.0377 (51)	-0.0568 (11)
1.62000	0.01403 (48)	0.32977 (34)	0.01014 (65)	-11.761 (10)	-0.921 (74)
1.90000	0.05034 (73)	0.2575 (10)	0.0464 (16)	-9.533 (27)	-2.98 (10)
$L^* = 1.0$, $\mu^{*2} = 9$					
1.17700†	0.00018 (1)	0.42930 (9)	0.00015 (1)	-17.5873 (90)	-0.0976 (45)
1.71200	0.01020 (51)	0.34335 (28)	0.0103 (18)	-14.056 (10)	-2.24 (56)
2.03300	0.04132 (86)	0.26785 (87)	0.0294 (28)	-11.437 (24)	-2.77 (22)
$L^* = 1.0$, $\mu^{*2} = 12$					
1.30740†	0.00014 (1)	0.43197 (11)	0.00011 (1)	-20.166 (12)	-0.1711 (40)
1.90160	0.01033 (65)	0.34090 (33)	0.00665 (27)	-15.996 (12)	-1.484 (15)
2.28190	0.0501 (10)	0.2482 (23)	0.0471 (31)	-12.506 (62)	-5.09 (32)

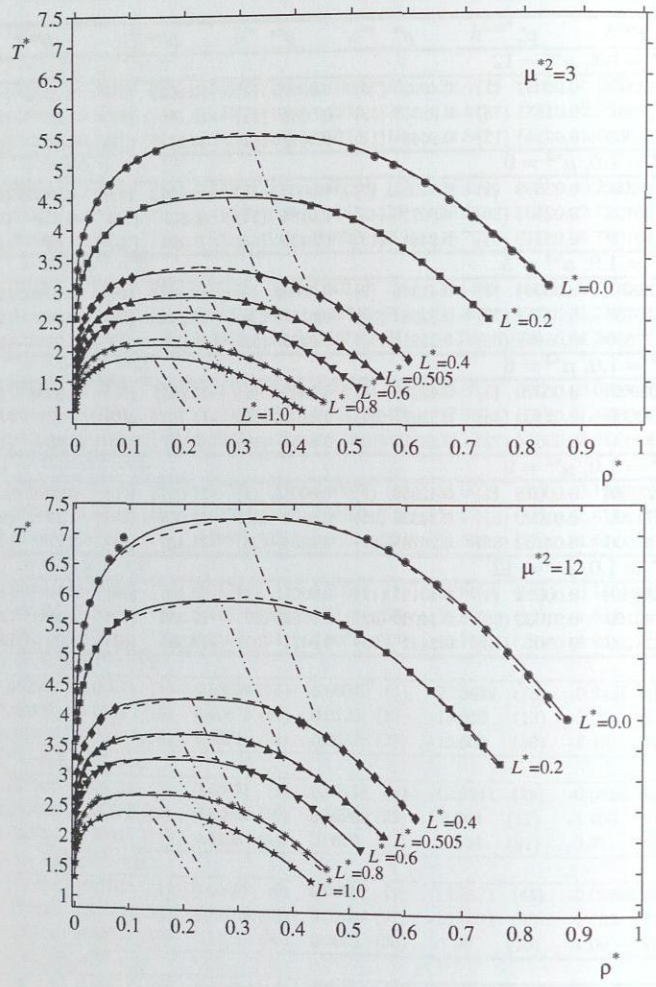

Figure 3: Temperature–density coexistence curves of 2CLJD model fluids with $\mu^{*2} = 3$ (top) and $\mu^{*2} = 12$ (bottom). Symbols: simulation data. —— 2CLJD correlation, cf. Chapter 3.2.2.2. – · – Rectilinear diameter from 2CLJD correlation. – – – 2CLJD equation of state [189, 268, 339], range of validity $L^* \leq 0.8$, cf. page 27. Error bars are, if not indicated, within symbol size.

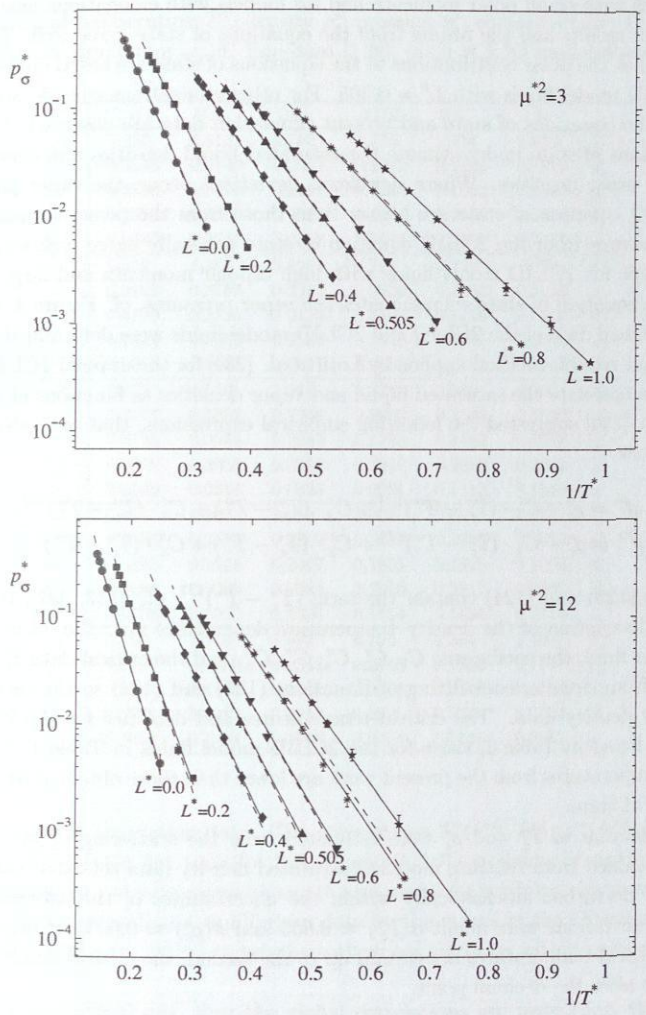

Figure 4: Vapor pressure curves of the 2CLJD model fluids with $\mu^{*2} = 3$ (top) and $\mu^{*2} = 12$ (bottom). Symbols: simulation data. —— 2CLJD correlation, cf. Chapter 3.2.2.2. – – – 2CLJD equation of state [189, 268, 339], range of validity $L^* \leq 0.8$, cf. page 27. Error bars are, if not indicated, within symbol size.

For models with small polar momenta and for models with elongations near $L^* = 0.505$, the present results and the results from the equations of state agree well. This is due to the fact, that the polar contributions to the equations of state are based on data of 2CLJQ and 2CLJD model fluids with $L^* = 0.505$. For other elongations considerable deviations between the equations of state and present simulation data are observed. In most cases the equations of state underestimate the saturated liquid densities and overestimate the saturated vapor densities. Where significant deviations occur, the vapor pressures from the 2CLJQ equation of state are higher than those from the present simulations. The vapor pressures from the 2CLJD equation of state generally agree well with simulation data, except for 2CLJD model fluids with high dipolar momenta and large elongations, where the equation of state overestimates the vapor pressures, cf. Figure 4, bottom.

The critical data of the 2CLJQ and 2CLJD model fluids were determined according to a simple but reliable method applied by Lotfi et al. [234] for the unpolar 1CLJ model fluid. In order to correlate the saturated liquid and vapor densities as functions of temperature, Lotfi et al. [234] suggested the following empirical expressions, that were also used in the present work

$$\rho'^* = \rho_c^* + C_1 \cdot (T_c^* - T^*)^{1/3} + C_2' \cdot (T_c^* - T^*) + C_3' \cdot (T_c^* - T^*)^{3/2}, \tag{123}$$

$$\rho''^* = \rho_c^* - C_1 \cdot (T_c^* - T^*)^{1/3} + C_2'' \cdot (T_c^* - T^*) + C_3'' \cdot (T_c^* - T^*)^{3/2}. \tag{124}$$

Equations (123) and (124) contain the term $(T_c^* - T^*)^{1/3}$, cf. [137, 337], that is known for good description of the density–temperature dependence near the critical point. For each model fluid, the coefficients C_1, C_2', C_3', C_2'', C_3'', and the critical data T_c^* and ρ_c^* were obtained from simultaneous fitting of Equations (123) and (124) to the saturated liquid and vapor density data. The critical temperatures and densities for the 2CLJQ model fluids are listed in Table 3, those for the 2CLJD model fluids in Table 4. In most cases critical temperatures from the present work are lower than those obtained from the hybrid equations of state.

Uncertainties of T_c^* and ρ_c^* were estimated from the scattering of the values of T_c^* and ρ_c^* obtained from refitting modified saturated density data sets that contained data that were perturbed stochastically within the uncertainties of the saturated densities. Standard deviations were about $\sigma(T_c^*) \approx 0.005$ and $\sigma(\rho_c^*) \approx 0.0005$. Consequently, the present critical temperatures are certain up to the second, the critical densities up to the third digit after the decimal point.

3.2.2 Global Correlation

In order to obtain vapor-liquid equilibrium data for any value of polarity, elongation or temperature, global correlation functions for the critical temperatures $T_c^*(P^{*2}, L^*)$, the critical densities $\rho_c^*(P^{*2}, L^*)$, the saturated liquid and vapor densities $\rho'^*(P^{*2}, L^*, T^*)$ and $\rho''^*(P^{*2}, L^*, T^*)$, and the vapor pressures $\ln p_\sigma^*(P^{*2}, L^*, T^*)$ were developed on the

Table 3: Critical temperature T_c^*, density ρ_c^*, pressure p_c^*, compressibility factor Z_c, and the acentric factor ω, cf. Equation (129), of 30 2CLJQ model fluids.

Q^{*2}	$L^*=0$	0.2	0.4	0.505	0.6	0.8	
0	5.236	4.313	3.163	2.735	2.454	2.049	T_c^*
	0.3143	0.2740	0.2251	0.2032	0.1850	0.1577	ρ_c^*
	0.4736	0.3670	0.2116	0.1616	0.1353	0.0995	p_c^*
	0.2878	0.3106	0.2972	0.2908	0.2980	0.3079	Z_c
	-0.0542	-0.0245	0.0308	0.0514	0.0589	0.0755	ω
1	5.312	4.388	3.195	2.771	2.499	2.097	T_c^*
	0.3169	0.2796	0.2259	0.2036	0.1863	0.1619	ρ_c^*
	0.4770	0.3795	0.2116	0.1646	0.1416	0.1047	p_c^*
	0.2834	0.3093	0.2932	0.2918	0.3041	0.3084	Z_c
	-0.0313	-0.0095	0.0486	0.0662	0.0701	0.0914	ω
2	5.575	4.554	3.316	2.875	2.580	2.160	T_c^*
	0.3197	0.2832	0.2256	0.2090	0.1888	0.1652	ρ_c^*
	0.5128	0.3944	0.2243	0.1753	0.1465	0.1028	p_c^*
	0.2877	0.3058	0.2998	0.2917	0.3008	0.2881	Z_c
	0.0125	0.0351	0.0825	0.0991	0.1113	0.1549	ω
3	5.968	4.807	3.489	3.007	2.695	2.266	T_c^*
	0.3303	0.2880	0.2309	0.2097	0.1940	0.1680	ρ_c^*
	0.5686	0.4166	0.2407	0.1835	0.1525	0.1069	p_c^*
	0.2884	0.3009	0.2988	0.2910	0.2917	0.2808	Z_c
	0.0605	0.0902	0.1305	0.1514	0.1656	0.2154	ω
4	6.398	5.143	3.692	3.195	2.866	2.408	T_c^*
	0.3395	0.2908	0.2358	0.2143	0.1960	0.1710	ρ_c^*
	0.5944	0.4460	0.2540	0.2003	0.1665	0.1134	p_c^*
	0.2736	0.2982	0.2918	0.2925	0.2964	0.2754	Z_c
	0.1067	0.1394	0.1900	0.2034	0.2145	0.2652	ω

basis of the present simulation data. The correlations $T_c^*(P^{*2}, L^*)$, $\rho'^*(P^{*2}, L^*, T^*)$, and $\ln p_\sigma^*(P^{*2}, L^*, T^*)$ are the key tools for 2CLJQ and 2CLJD modeling of real fluids.

The global vapor pressure correlations are also useful for verifying the thermodynamic consistency of the vapor-liquid equilibrium data by the means of the Clausius-Clapeyron equation. Moreover, the global correlations allow comparisons with results of other authors.

It should be pointed out, that the global correlations are mere tools that cast the present simulation results into a manageable mathematical context needed for a particular application. They are not designed to compete with equations of state, and it was not in the scope of the present work to develop new or improved equations of state for the 2CLJQ or 2CLJD model fluids.

Table 4: Critical temperature T_c^*, density ρ_c^*, pressure p_c^*, compressibility factor Z_c, and the acentric factor ω, cf. Equation (129), of 38 2CLJD model fluids.

μ^{*2}	$L^*=0$	0.2	0.4	0.505	0.6	0.8	1.0	
3	5.475	4.521	3.311	2.871	2.558	2.127	1.876	T_c^*
	0.3197	0.2808	0.2237	0.2028	0.1868	0.1611	0.1449	ρ_c^*
	0.5157	0.3619	0.2133	0.1711	0.1378	0.0932	0.0856	p_c^*
	0.2946	0.2851	0.2880	0.2939	0.2884	0.2720	0.3149	Z_c
	-0.0191	0.0055	0.0528	0.0720	0.0958	0.1475	0.1797	ω
6	5.990	4.917	3.591	3.100	2.774	2.316	2.010	T_c^*
	0.3169	0.2781	0.2202	0.2017	0.1839	0.1576	0.1428	ρ_c^*
	0.5179	0.3624	0.2105	0.1677	0.1342	0.0894	0.0824	p_c^*
	0.2728	0.2650	0.2662	0.2682	0.2631	0.2449	0.2871	Z_c
	0.0214	0.0471	0.0976	0.1179	0.1429	0.1987	0.2398	ω
9	6.585	5.382	3.909	3.377	3.040	2.520	2.178	T_c^*
	0.3124	0.2700	0.2164	0.1959	0.1790	0.1510	0.1382	ρ_c^*
	0.5098	0.3594	0.2078	0.1646	0.1304	0.0839	0.0765	p_c^*
	0.2478	0.2473	0.2457	0.2488	0.2396	0.2205	0.2542	Z_c
	0.0687	0.0938	0.1457	0.1669	0.1936	0.2565	0.3114	ω
12	7.289	5.945	4.282	3.676	3.273	2.713	2.370	T_c^*
	0.3033	0.2647	0.2122	0.1921	0.1765	0.1519	0.1376	ρ_c^*
	0.5067	0.3619	0.2095	0.1651	0.1291	0.0797	0.0716	p_c^*
	0.2292	0.2300	0.2306	0.2338	0.2235	0.1934	0.2196	Z_c
	0.1159	0.1396	0.1921	0.2145	0.2435	0.3163	0.3881	ω
16	8.249	6.654	–	–	–	–	–	T_c^*
	0.2961	0.2565	–	–	–	–	–	ρ_c^*
	0.5202	0.3795	–	–	–	–	–	p_c^*
	0.2130	0.2224	–	–	–	–	–	Z_c
	0.1732	0.1945	–	–	–	–	–	ω
20	9.164	–	–	–	–	–	–	T_c^*
	0.2884	–	–	–	–	–	–	ρ_c^*
	0.5567	–	–	–	–	–	–	p_c^*
	0.2106	–	–	–	–	–	–	Z_c
	0.2220	–	–	–	–	–	–	ω

3.2.2.1 Critical Properties

The correlation functions $T_c^*(P^{*2}, L^*)$ and $\rho_c^*(P^{*2}, L^*)$ are linear combinations of elementary functions. These elementary functions are a constant c, plus further functions $\psi_i(P^{*2})$ or $\xi_i(L^*)$ or $\chi_i(P^{*2}, L^*)$. Thus, the linear combination of elementary functions writes as

$$y(P^{*2}, L^*) = c + \sum_i \alpha_i \cdot \psi_i(P^{*2}) + \sum_j \beta_j \cdot \xi_j(L^*) + \sum_k \gamma_k \cdot \chi_k(P^{*2}, L^*), \qquad (125)$$

wherein $y(P^{*2}, L^*)$ represents the critical temperature or the critical density. In Equation (125), the number of the elementary functions $\psi_i(P^{*2})$ and $\xi_i(L^*)$ was restricted to

up to two and the number of the elementary functions $\chi_i(P^{*2}, L^*)$ was limited to four in the 2CLJQ case and to three in the 2CLJD case.

The elementary functions $\psi_i(P^{*2})$, $\xi_i(L^*)$, and $\chi_i(P^{*2}, L^*)$ were chosen empirically in order to obtain low relative deviations between correlation and simulation data. The same elementary function $\xi_i(L^*)$ were used for both the 2CLJQ and the 2CLJD case, whereas the elementary functions ψ_i and χ_i differed for the two cases.

The constant and the coefficients in Equation (125) were determined by a non-weighted least squares fit of the sets of critical data of all 30 2CLJQ or all 38 2CLJD model fluids. The elementary functions and the coefficients for the global correlations $T_c^*(Q^{*2}, L^*)$ and $\rho_c^*(Q^{*2}, L^*)$ are given in Table 35 in Appendix D. Table 36 in Appendix D contains the elementary functions and the coefficients for the global correlations $T_c^*(\mu^{*2}, L^*)$ and $\rho_c^*(\mu^{*2}, L^*)$. The quality of the correlations can be studied in Figures 5 and 6. Most relative deviations of T_c^* are within 1 %. The critical densities are represented with roughly the same quality.

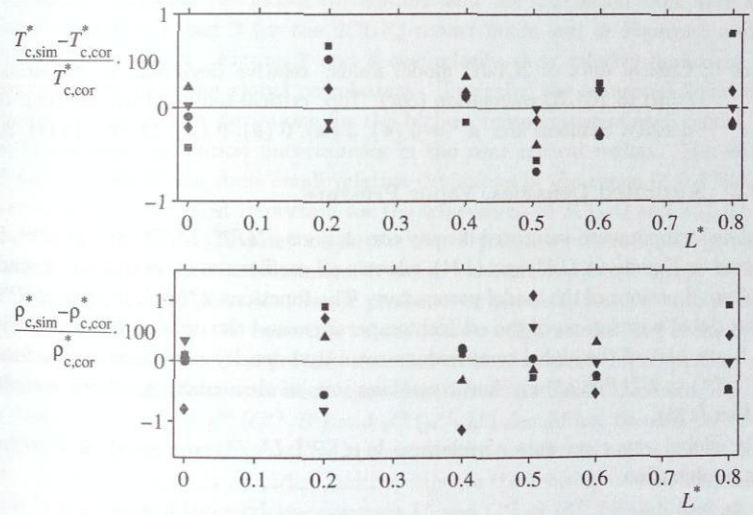

Figure 5: Critical data of 2CLJQ model fluids: relative deviation of simulation data (sim) to 2CLJQ correlation (cor). Top: critical temperature. Bottom: critical density. Symbols are: $Q^{*2} = 0$ (●), 1 (■), 2 (♦), 3 (▲), 4 (▼).

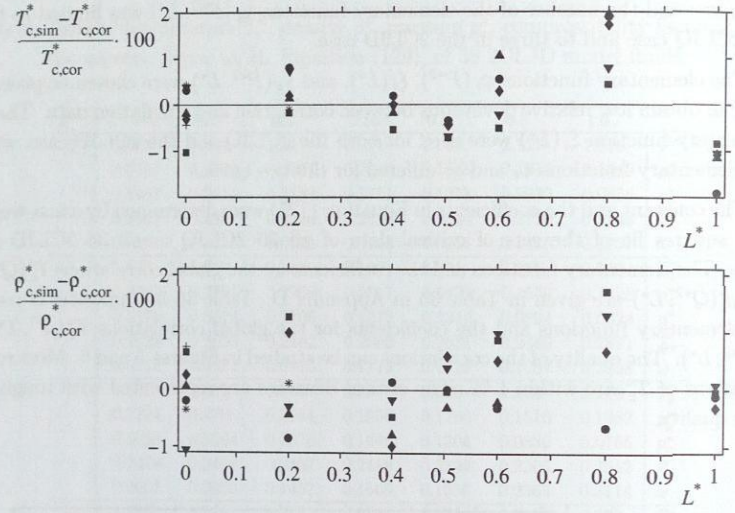

Figure 6: Critical data of 2CLJD model fluids: relative deviation of simulation data (sim) to 2CLJD correlation (cor). Top: critical temperature. Bottom: critical density. Symbols are: $\mu^{*2} = 0$ (●), 3 (■), 6 (♦), 9 (▲), 12 (▼), 16 (∗), 20 (+).

3.2.2.2 Saturated Densities, Vapor Pressure

The global temperature–saturated density correlations $\rho'^*(P^{*2}, L^*, T^*)$ and $\rho''^*(P^{*2}, L^*, T^*)$ are based on Equations (123) and (124), wherein all coefficients C_1 to C_3'' and, of course, T_c^* and ρ_c^* are functions of the model parameters. The functions $T_c^*(P^{*2}, L^*)$ and $\rho_c^*(P^{*2}, L^*)$, i.e. the global correlations of the critical temperature and the critical density, cf. Chapter 3.2.2.1, are part of the global temperature–saturated density correlations. The functions $C_1(P^{*2}, L^*)$ to $C_3''(P^{*2}, L^*)$ are linear combinations of elementary functions according to Equation (125).

The global vapor pressure correlations $\ln p_\sigma^*(P^{*2}, L^*, T^*)$ are based on a polynomial linear combination

$$\ln p_\sigma^*(T^*) = c_1 + \frac{c_2}{T^*} + \frac{c_3}{T^{*4}}, \tag{126}$$

that has been chosen due to its excellent performance in correlating vapor pressure data for each of the 2CLJQ and 2CLJD model fluids. It has already been used in previous works of Lotfi et al. [234] and Kriebel et al. [191]. In Equation (126) the coefficients c_1, c_2, and c_3 are functions of the model parameters, they are linear combinations of elementary functions according to Equation (125).

The elementary functions required for the coefficient functions $C_1(P^{*2}, L^*)$ to $C_3''(P^{*2}, L^*)$ and $c_1(P^{*2}, L^*)$ to $c_3(P^{*2}, L^*)$ were chosen empirically in order to obtain low relative deviations between correlation and simulation data.

Given the elementary functions, all coefficients required for the global temperature–saturated density correlations $\rho'^*(P^{*2}, L^*, T^*)$ and $\rho''^*(P^{*2}, L^*, T^*)$ and for the global vapor pressure correlations $\ln p_\sigma^*(P^{*2}, L^*, T^*)$ are determined by uncertainty-weighted least squares minimizations

$$\sum_i \left[\frac{1}{\delta\rho_i'^{*2}} \left[\rho'^* \left(P_i^{*2}, L_i^*, T_i^*\right) - \rho_{\mathrm{sim},i}'^*\right]^2 + \frac{1}{\delta\rho_i''^{*2}} \left[\rho''^* \left(P_i^{*2}, L_i^*, T_i^*\right) - \rho_{\mathrm{sim},i}''^*\right]^2 \right] \stackrel{!}{=} \min, \quad (127)$$

$$\sum_i \frac{1}{\left(\delta \ln p_{\sigma,i}\right)^2} \left[\ln p_\sigma \left(P_i^{*2}, L_i^*, T_i^*\right) - \ln p_{\sigma,\mathrm{sim},i}\right]^2 \stackrel{!}{=} \min, \quad (128)$$

wherein the sums run over the complete saturated density data sets or the complete vapor pressure data sets. The elementary functions and the coefficients for these global correlations are given in Appendix D in Table 35 for the 2CLJQ model fluids and in Table 36 for the 2CLJD model fluids.

Comparisons between the global correlations and the simulation data were already presented in Figures 1 and 2 for the 2CLJQ model fluids and in Figures 3 and 4 for the 2CLJD model fluids. Figures 7 and 8 exemplarily show relative deviations of the simulation results from the global correlations. Typically, the saturated liquid density correlation has the largest deviations for the highest temperature of each model, which is due to the large simulation uncertainties in the near critical region. The saturated liquid density correlations show small relative deviations in the range of 0.4 % for mid temperatures which are most important for the adjustment of 2CLJQ and 2CLJD model parameters to real fluids. In most cases, the vapor pressure correlations represent the simulation data within their uncertainties. It has to be mentioned, that, except for 2CLJD simulations with gradual insertion, vapor pressures at low temperature state points can be largely uncertain due to the uncertain values of the configurational part of the chemical potential obtained from the test particle insertion method in dense liquid phases.

Relative deviations of the saturated vapor densities are not illustrated here. The global vapor density correlations $\rho''^*(Q^{*2}, L^*)$ and $\rho''^*(\mu^{*2}, L^*)$ should not be used below about $0.60 \cdot T_c(P^{*2}, L^*)$. At low temperatures these two correlations are not useful as they do not, due to their completely empirical nature, capture the limiting case of the ideal gas, which is independent of the model parameters L^* and Q^{*2} or μ^{*2}. Nonetheless, as shown in Figures 1 and 3, these two global correlations describe the saturated vapor densities correctly for temperatures beyond $0.60 \cdot T_c(P^{*2}, L^*)$.

The acentric factor [319] can be calculated from the global vapor pressure correlations when it is slightly extrapolated to the critical point

$$\omega\left(P^{*2}, L^*\right) = -\log_{10} \frac{p^*\left(P^{*2}, L^*, 0.7 \cdot T_c^*\right)}{p_c^*\left(P^{*2}, L^*\right)} - 1. \quad (129)$$

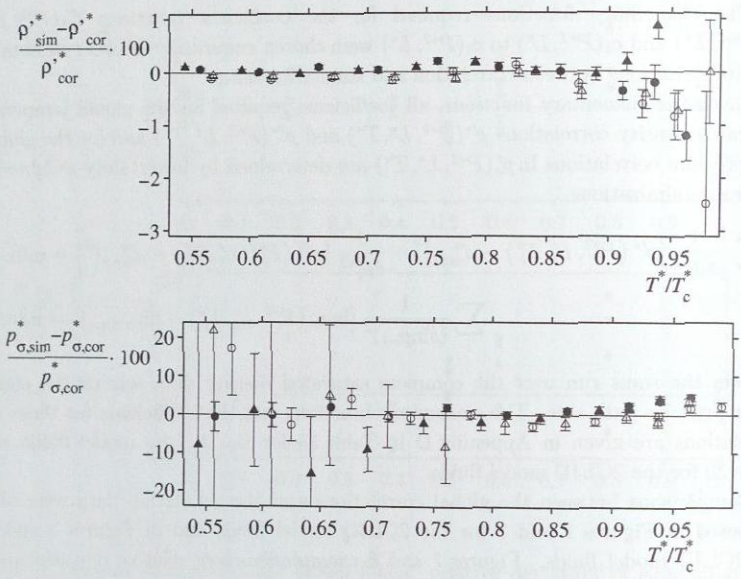

Figure 7: Vapor-liquid equilibria of 2CLJQ model fluids: relative deviation of simulation data (sim) to 2CLJQ correlations (cor). Top: saturated liquid density, full and empty symbols are for $L^* = 0$ and $L^* = 0.505$ respectively, with $Q^{*2} = 1$ (●, ○), 4 (▲, △). Bottom: vapor pressure, full and empty symbols are for $L^* = 0$ and $L^* = 0.8$ respectively, with $Q^{*2} = 0$ (●, ○), 4 (▲, △).

The critical pressures and the acentric factors for the 2CLJQ model fluids are given in Table 3, those for the 2CLJD model fluids in Table 4. As expected, the acentric factor increases with increasing polarity and elongation. Moreover, Tables 3 and 4 contain the critical compressibility factor

$$Z_c = p_c^* / (\rho_c^* \, T_c^*) \,. \tag{130}$$

3.2.3 Comparison to Results of Other Authors

Similar, but less comprehensive investigations of vapor-liquid equilibria of various of the model fluids discussed in Chapter 3.2.2 are available in literature, cf. Table 5. In that table, also systematic studies of vapor-liquid equilibria of other model fluids than those studied here are summarized. Furthermore, in those works, other simulation methods such as the Gibbs Ensemble Monte Carlo or Gibbs-Duhem Integration were applied. Among

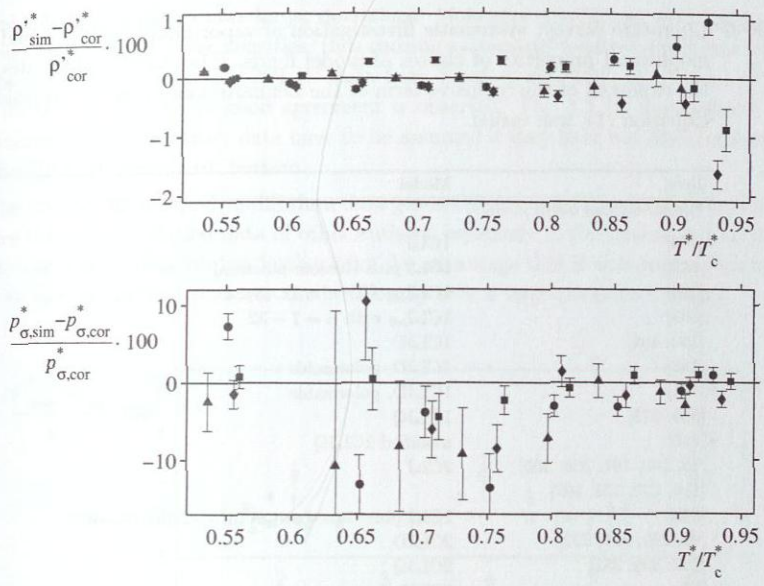

Figure 8: Vapor-liquid equilibria of 2CLJD model fluids: relative deviation of simulation data (sim) to 2CLJD correlation (cor). Top: saturated liquid density. Bottom: vapor pressure. Symbols are: ● 1CLJD with $\mu^{*2} = 9$, ■ 2CLJD with $\mu^{*2} = 6$ and $L^* = 0.4$, ♦ 2CLJD with $\mu^{*2} = 9$ and $L^* = 0.505$, ▲ 2CLJD with $\mu^{*2} = 6$ and $L^* = 1$.

these investigations, the work of Lísal et al. [221] on the vapor-liquid equilibria of twenty 2CLJD model fluids, with $\mu^{*2} = 0 \ldots 12$ and $L^* = 0.22 \ldots 0.67$, is the most extensive one. Lísal et al. [221] reported critical data and correlations for vapor pressures and saturated densities for each of the twenty 2CLJD model fluids. Apart from vapor-liquid equilibria, systematic investigations of second virial coefficients of 2CLJD fluids are available from Vega et al. [406], and of third virial coefficients of 2CLJQ fluids from MacDowell et al. [244].

In Figures 9 and 10, the results from the present work are compared with the simulation results of other authors for the 2CLJQ and 2CLJD model fluids. Data is taken from Lotfi et al. [234] for 1CLJ model fluids, from van Leeuwen et al. [405] for 1CLJD (Stockmayer) model fluids, from Stapleton et al. [373] and Smit et al. [365] for 1CLJQ model fluids, from Kriebel et al. [191] and Kronome et al. [197] for 2CLJ model fluids, from Dubey et al. [83] and Lísal et al. [220, 221, 222] for 2CLJD model fluids, and from Möller et al.

Table 5: Literature survey: systematic investigation of vapor-liquid equilibria and thermophysical properties of classes of model fluids. The index $n6$ indicates, that the exponent of the repulsive term of the Lennard-Jones potential function, cf. Equation (1), was varied.

Refs.	Model
Lennard-Jones based models	
[234]	1CLJ
[342]	1CLJ plus Keesom potential
[108]	1CLJ$_{n6}$ with $n = 12, 18, 24$
[309]	1CLJ$_{n6}$ with $n = 7 - 32$
[192, 402]	1CLJD
[193]	1CLJD, polarizable
[174]	1CLJD, polarizable
[365, 373]	1CLJQ
[310]	modified 1CLJQ
[18, 108, 191, 366, 405] [116, 120, 122, 197]	2CLJ
[343]	2CLJ plus three-body Axilrod-Teller potential
[83, 220, 221, 222]	2CLJD
[282, 339, 381]	2CLJQ
[82]	2CLJDQ
Other models	
[128, 408]	spherical square-well
[136]	spherical square-well plus point octupole
[387]	two-center square-well
[224]	two-center square-well, homo- and heteronuclear
[256]	square-well spherocylinders
[386, 440]	Buckingham exponential-6
[92]	modified Buckingham exponential-6
[123]	Kihara plus point quadrupole
[124]	Kihara plus point dipole
[428]	hard sphere reference potential plus augmented Sutherland potential plus point quadrupole

[282] for 2CLJQ model fluids.

Figures 9 and 10 show the relative deviations of the saturated liquid density and the vapor pressure between simulation data of these authors and the global 2CLJQ and 2CLJD correlations from the present work.

The saturated liquid densities of the other authors agree in almost all cases within the combined uncertainties of present global correlation and the simulation data. Data near to

critical points, of course, shows larger deviations. Molecular simulations with low particle numbers yield slightly lower densities, thus causing systematic negative deviations, as can be observed, for example, for 2CLJD data from Lísal et al. [220], cf. Figure 10, top. Also for the vapor pressure good agreement is observed. For 2CLJD model fluids large uncertainties of the literature data have to be assumed if they have not been indicated in the literature, cf. Figure 10, bottom.

The present vapor-liquid equilibrium data generally show much lower statistical uncertainties than the simulation data of other authors, especially in the case of 2CLJD model fluids. The present data set has furthermore the advantage that it was produced from the same simulation method that was used uniformly over a large parameter range.

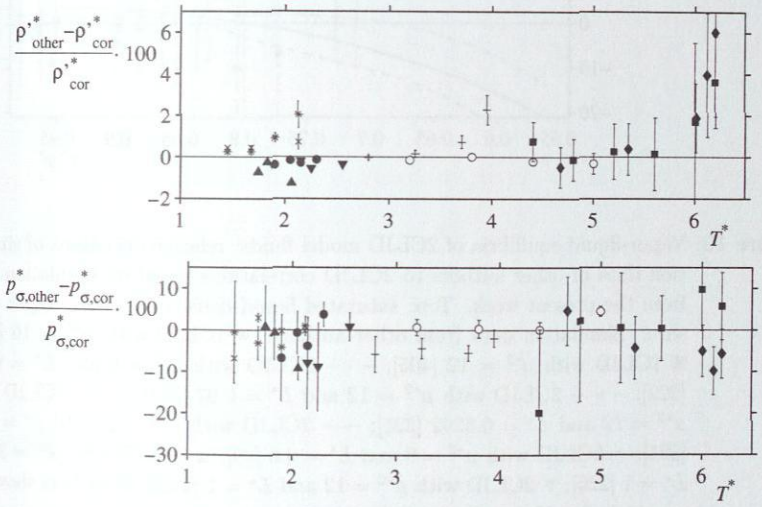

Figure 9: Vapor-liquid equilibria of 2CLJQ model fluids: relative deviation of simulation data of other authors to 2CLJQ correlations based on simulation data from the present work. Top: saturated liquid density. Bottom: vapor pressure. Simulation data from other authors: ○ 1CLJ [234]; + 2CLJ with $L^* = 0.22$, ∗ 2CLJ with $L^* = 0.67$ [191]; × 2CLJ with $L^* = 0.67$ [197]; ♦ 1CLJQ with $Q^{*2} = 4$ [373]; ■ 1CLJQ with $Q^{*2} = 4$ [365]; ● 2CLJQ with $Q^{*2} = 3.0255$ and $L^* = 0.65$, ▲ 2CLJQ with $Q^{*2} = 3.0255$ and $L^* = 0.779$, ▼ 2CLJQ with $Q^{*2} = 3.7$ and $L^* = 0.58$ [282]. Error bars show the uncertainties, if they are available.

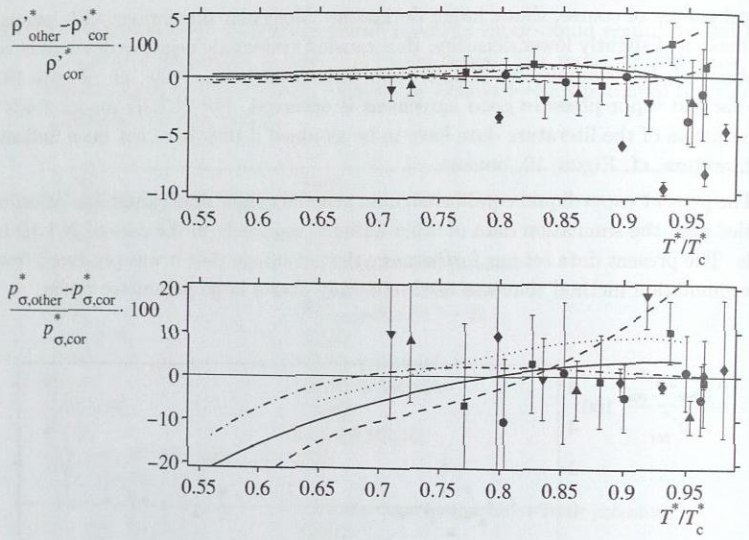

Figure 10: Vapor-liquid equilibria of 2CLJD model fluids: relative deviations of simulation data of other authors to 2CLJD correlations based on simulation data from the present work. Top: saturated liquid density. Bottom: vapor pressure. Simulation data from other authors: • 1CLJD with $\mu^{*2} = 16$ [405]; ■ 1CLJD with $\mu^{*2} = 12$ [405]; – · – 2CLJD with $\mu^{*2} = 6$ and $L^* = 0.505$ [222]; – – – 2CLJD with $\mu^{*2} = 12$ and $L^* = 0.67$ [221]; · · · · · 2CLJD with $\mu^{*2} = 12$ and $L^* = 0.3292$ [221]; —— 2CLJD with $\mu^{*2} = 12$ and $L^* = 0.22$ [221]; + 2CLJD with $\mu^{*2} = 9$ and $L^* = 0.6$ [83]; ▲ 2CLJD with $\mu^{*2} = 9$ and $L^* = 1$ [220]; ▼ 2CLJD with $\mu^{*2} = 12$ and $L^* = 1$ [220]. Error bars show the uncertainties, if they are available.

3.2.4 Thermodynamic Consistency Test

The thermodynamic consistency of the 2CLJQ and 2CLJD simulation data was tested with the Clausius-Clapeyron equation

$$\frac{\partial \ln p^*_\sigma}{\partial T^*} = \frac{\Delta h^*_v}{p^*_\sigma T^* (1/\rho''^* - 1/\rho'^*)}. \tag{131}$$

The left hand side of Equation (131) was evaluated with the global vapor pressure correlations, whereas the right hand side of Equation (131) was calculated from the present simulation data, the uncertainty was calculated by the error propagation law. The present

simulation data is thermodynamically consistent as the requirements of Equation (131) are fulfilled at almost all temperatures within the uncertainties of the right hand site of Equation (131).

4 Molecular Models of Classes of Real Fluids

The global correlations of the vapor-liquid equilibria of the 2CLJQ/2CLJD model fluids were used for the efficient development of sets of accurate state independent compatible 2CLJQ/2CLJD models of real low-molecular fluids. The values for the parameters of the molecular models are obtained from the adjustment of the vapor-liquid equilibria of the model fluids to vapor-liquid equilibrium data of real fluids.

The class of unpolar or quadrupolar real fluids comprises the 23 fluids listed in Table 8 and includes noble gases, halogens, nitrogen, oxygen, carbon dioxide, and various C_2-hydro- and -perhalocarbons. For all these fluids, molecular models of the 2CLJQ type were developed. Furthermore, two octupolar fluids, tetrafluoromethane and tetrachloromethane, as well as the hexadecapolar fluid sulfurhexafluoride were modeled with the 2CLJQ potential. For these three substances it is questionable whether the 2CLJQ potential is appropriate. They are therefore considered as "test cases" here.

The class of multipolar real fluids comprises 55 fluids, which include carbon monoxide and many halogenated methane, ethane, ethene, and ethyne derivatives, such as the alternative refrigerants R23, R134a or R152a, cf. Tables 10 and 9. Further C_2-halocarbons belong to this fluid class, but were not modeled here, as no reliable vapor-liquid equilibrium data were available. Depending on the importance of dipolarity or quadrupolarity, either 2CLJD or 2CLJQ modeling was chosen for these substances. This modeling approach and criteria for deciding between dipolar or quadrupolar modeling of multipolar fluids is discussed in Appendix E. Due to their importance for industrial applications, thermodynamic modeling of halocarbons is of particular interest.

Apart from molecular modeling, there is ongoing research on molecular based equations of state. For vapor-liquid equilibria of pure refrigerants and their mixtures obtained from equations of state, see [117] (SAFT-VR equation of state), [430] (BACKONE equation of state), and the series of papers [100, 101, 274] (PHSCT equation of state with parameters estimated from molecular simulation or quantum chemistry) for recent work.

All 2CLJQ/2CLJD models developed in the present work are optimized for simulations of vapor-liquid equilibria. Typical relative deviations of simulation results and experiment of the models for fluids with unpolar or quadrupolar molecules are $\pm 3\%$ for the vapor pressure, $\pm 0.5\%$ for the saturated liquid density, and $\pm 2\%$ for the enthalpy of vaporization. For fluids with multipolar molecules these relative deviations are typically $\pm 4\%$ for the vapor pressure, $\pm 0.5\%$ for the saturated liquid density, and $\pm 3\%$ for the enthalpy of vaporization. These deviations are distinctly lower than those observed for most molecular models available in the literature, often by a factor of 2 – 10. The present 2CLJQ/2CLJD models can straightforwardly be applied to the modeling of mixtures due to the complete compatibility of the models among each other.

In the following chapters, the modeling of low-molecular substances in literature is reviewed, an outline of the procedure applied in the present work to determine the

2CLJQ/2CLJD model parameters is given, and results of applications of the molecular models are presented and compared to experimental data and to results from models available in literature.

4.1 Literature Survey

Many of the fluids, for which new molecular models for engineering purposes are proposed in the present work, were previously investigated by other authors by means of molecular simulation on the basis of various molecular models. Tables 6 and 7 illustrates the situation, without claiming to give a complete picture. The literature models were optimized for different applications, such as the description of phenomena in the solid state, liquid state, thermophysical properties and structure, second virial coefficient in the gas phase, or, in some cases, for the description of vapor-liquid equilibria.

Tables 6 and 7 do not contain molecular models of further low-molecular hydrogen-bonding substances like ammonia (NH_3) [195, 327], or water (H_2O), which is subject of ongoing important modeling research. For recent overviews and insights concerning water, cf. [24, 34, 90, 129, 175, 223, 249, 301, 299, 332, 412]. For brevity, transferable force fields, like for example OPLS [162, 165, 166], AMBER [56, 61, 62, 429], CHARMM [30, 245], NERD [294, 295, 296, 298], TraPPE [254], TraPPE-UA [47, 255, 434], TraPPE-EH [48], OPPE [74], AUA [28, 397, 394], or COMPASS [384, 442] are omitted in Tables 6 and 7. These force fields comprehend models of the hydrocarbons and of many other substances modeled in the present work. Further works on models of fluids with larger molecules like *n*-alkanes [91, 364], cyclic alkanes [93, 302], or benzene [93] are just mentioned here to illustrate the extent of molecular modeling and simulation.

Two main approaches for developing molecular models for low-molecular substances can be distilled from literature, cf. Tables 6 and 7:

(i) All-atom multicenter modeling, typically with partial charges derived from ab-initio data, in some cases with internal degrees of freedom. Examples are molecular models of halocarbons [19, 20, 21, 44, 66, 80, 95, 99, 140, 149, 151, 159, 277, 312, 326, 347, 382], or a model of carbon dioxide [143]. The importance of electrostatic contributions in the molecular model is generally accepted today, so multicenter modeling without electrostatic contributions, cf. some models for tetrafluoromethane (CF_4), tetrachloromethane (CCl_4), or sulfur hexafluoride (SF_6) in Tables 6 and 7, is no longer state of the art. Except for some cases, cf. for example the model of the refrigerant R41 [382], models of the all-atom plus partial charge type were not developed for the description of vapor-liquid equilibria.

(ii) United-atom modeling, preferably with point dipoles or point quadrupoles, in some cases with partial charges. This model type, typically based on Lennard-Jones potential functions, features a lower number of model parameters and is therefore broadly used. Many models of this type are available in literature for the fluids considered in the present work. In some cases optimized for the description of vapor-liquid equilibria, 2CLJ or

Table 6: Literature survey: molecular models of low-molecular substances, sorted by substances.

Substance	Models and references
Neon (Ne)	1CLJ [111, 150, 279, 278, 314, 390, 426], nonc.appr.th. [265], ab-in. [206]
Argon (Ar)	1CLJ [98, 111, 116, 150, 263, 314, 362, 415, 427], modif. 1CLJ [9], 2-body+3-body [252, 345], nonc.appr.th. [265], ab-in. [206], exp-6 type [98], various others [98]
Krypton (Kr)	1CLJ [17, 98, 150, 263, 314, 413], 2-body+3-body [252], nonc.appr.th. [265], exp-6 type [98], various others [98]
Xenon (Xe)	1CLJ [17, 18, 150, 263, 314, 413], 2-body+3-body [252], nonc.appr.th. [265]
Methane (CH_4)	1CLJ [18, 108, 150, 164, 185, 254, 263, 415], nonc.appr.th. [75], ab initio [20], SSR-MPA [237]
Fluorine (F_2)	1CLJ [150], 2CLJ [108, 161, 363]
Chlorine (Cl_2)	1CLJ [150], 2CLJ [18, 161, 363, 441], 2CLJQ [286, 381], nonc.appr.th. [75], various others [116, 219, 333, 334, 432]
Bromine (Br_2)	1CLJ [150], 2CLJ [18, 161, 363], various others [2]
Iodine (I_2)	1CLJ [150]
Nitrogen (N_2)	1CLJ [17, 150, 263], 1CLJQ [10], 2CLJ [8, 51, 108, 116, 161, 284, 331], 2CLJQ [52, 247, 284], multic. LJ no chrg. [150], nonc.appr.th. [75], ab-in. [11, 153], Kihara based [201]
Oxygen (O_2)	1CLJ [17, 150, 263], 2CLJ [18, 161], nonc.appr.th. [75], Kihara based [201]
Carbon dioxide (CO_2)	1CLJ [150], 2CLJ [108, 285, 363, 385], $2CLJ_{96}$ [127, 285], 2CLJQ [247, 282, 285], $2CLJQ_{96}$ [285], 2CLJ chrg. [143], multic. 2CLJ no chrg. [150], ab-in. [13, 20], SSR-MPA [236]
Carbon disulfide (CS_2)	2CLJ [18], multic. LJ no chrg. [194, 391], ab-in. [21]
Ethane (C_2H_6)	1CLJ [17, 185], 2CLJ [18, 108, 164, 254, 439], multic. LJ no chrg. [150], exp-6 type [91]
Ethene (C_2H_4)	2CLJ [18], multic. LJ no chrg. [150]
Ethyne (C_2H_2)	exp-6 type [106, 118]
Perfluoroethane (C_2F_6)	2CLJ [185], Kihara based [201]
Perfluoroethene (C_2F_4)	Kihara based [201]
Sulfur hexafluoride (SF_6)	1CLJ [150], multic. LJ no chrg. [238]
Tetrafluoromethane (CF_4)	1CLJ [17, 150, 185], multic. LJ no chrg. [306], multic. LJ_{246} no chrg. [238], multic. LJ chrg.,int.flx. [326]
Tetrachloromethane (CCl_4)	1CLJ [17, 150, 185], $1CLJ_{246}$ [108], multic. LJ no chrg. [262, 292, 375], multic. LJ_{246} no chrg. [238], multic. LJ chrg.,polariz. [44], ab-in. [186], various others [368]
Propylene (CH_2=CH–CH_3)	multic. LJ no chrg. [150],
Carbon monoxide (CO)	1CLJ [17, 150, 263], 1CLJD [10, 402], 1CLJDQ [10], 2CLJ [18, 161], multic. LJ no chrg. [150]
R12 (CF_2Cl_2)	multic. (modif.) LJ chrg. [140, 149, 277]
R22 (CHF_2Cl)	1CLJD [120], 2CLJDα [189], multic. (modif.) LJ chrg. [277], ab initio [347]
R23 (CHF_3)	1CLJD [120, 402], 2CLJ chrg. [370], multic. (modif.) LJ chrg. [312], multic. LJ chrg.,polariz. [151], multic. LJ chrg.,int.flx. [326], ab-in. [20], multic. HB14-7 chrg.,int.flx. [229]
R32 (CH_2F_2)	1CLJD [120, 402], multic. (modif.) LJ chrg. [149, 159, 312], multic. LJ chrg.,int.flx. [326], multic. LJ_{96} chrg.,int.flx. [99], multic. HB14-7 chrg.,int.flx. [229], Kihara based [201]
R41 (CH_3F)	1CLJD [150, 402], multic. (modif.) LJ chrg. [312], ab initio [20, 382], Kihara based [201]

Table 6: continued.

Substance	Models and references
R125 (CF_3–CHF_2)	1CLJD [120], multic. LJ_{96} chrg.,int.flx. [99]
R134 (CHF_2–CHF_2)	multic. LJ_{96} chrg.,int.flx. [99], multic. HB14-7 chrg.,int.flx. [229]
R134a (CF_3–CH_2F)	1CLJ [185], 1CLJD [120], 2CLJ [185], 2CLJD [221, 222], 2CLJDα [185], multic. LJ_{96} chrg.,int.flx. [99], multic. HB14-7 chrg.,int.flx. [230]
R142b (CF_2Cl–CH_3)	1CLJ [185], 1CLJD [120], 2CLJ [185], 2CLJD [222], 2CLJDα [185]
R143 (CHF_2–CH_2F)	multic. LJ_{96} chrg.,int.flx. [99], multic. HB14-7 chrg.,int.flx. [230]
R143a (CF_3–CH_3)	1CLJ [185], 1CLJD [120, 402], 2CLJ [185], 2CLJD [222], 2CLJDα [185], multic. LJ_{96} chrg.,int.flx. [99], multic. HB14-7 chrg.,int.flx. [230]
R152 (CH_2F–CH_2F)	multic. HB14-7 chrg.,int.flx. [230]
R152a (CHF_2–CH_3)	1CLJ [185], 1CLJD [120, 402], 2CLJ [185], 2CLJD [189, 222, 407], 2CLJDα [185, 407], multic. LJ_{96} chrg.,int.flx. [99]
R161 (CH_2F–CH_3)	1CLJD [402], multic. LJ_{96} chrg.,int.flx. [99]
CH_3Cl	1CLJ [185], 1CLJD [150, 402], ab-in. [20], Kihara based [201]
CH_2Cl_2	1CLJ [185], multic. LJ chrg.,polariz. [66], ab-in. [20]
CHF_2Cl	1CLJ [185]
$CHCl_3$	1CLJD [150, 402], ab-in. [19]
$CHFCl_2$	1CLJD [150]
CH_2Br–CH_3	1CLJD [402]
$CHCl_2$–CH_3	1CLJD [402]
CHF=CH_2	Kihara based [201]
CF_2=CH_2	Kihara based [201]
Methanol (CH_3–OH)	1CLJD [402], a2CLJ chrg. [404] (cf. therein Table 1), exp-6 type [323]

The short-cut notations for the models used in this Table are: "1CLJ"/"2CLJ"/"a2CLJ"/"multic. LJ" are models based on one/two/two asymmetric/more than two Lennard-Jones interaction sites, the indices "96" or "246" indicate, that in the repulsive term of the Lennard-Jones potential function the exponents 9 or 24 instead of 12 are used, "modif." means modified, "D"/"Q" means with point dipole/point quadrupole, "α" means with inclined dipole "D", "2-body + 3-body" are potential functions for pair and three-body interactions, "multic." means multicenter, "chrg." means point charge, "polariz." means that polarizability was modeled explicitly, "int.flx." means with intramolecular degrees of freedom like bond bending or torsion, "nonc.approx.th." means nonconformal approximation theory, "ab-in." means, that the model was parametrized by means of ab-initio data, "SSR-MPA" means site-site repulsion multipole approximation, "Kihara based" means Kihara potential plus eventually a point dipole and/or point quadrupole, "exp-6 type" means potential function based on the Buckingham exponential-6 potential, "HB14-7" means Halgren's Buf 14-7 potential, "various others" are models other than those classified in this Table.

Table 7: Literature survey: molecular models of low-molecular substances, sorted by model types.

Models	Substances and references
1CLJ	Ne [111, 150, 278, 279, 314, 390, 426], Ar [98, 111, 116, 150, 263, 314, 362, 415, 427], Kr [17, 98, 150, 263, 314, 413], Xe [17, 18, 150, 263, 314, 413], CH_4 [18, 108, 150, 164, 185, 254, 263, 415], N_2 [17, 150, 263], O_2 [17, 150, 263], F_2 [150], Cl_2 [150], Br_2 [150], I_2 [150], CO_2 [150], C_2H_6 [17, 185], SF_6 [150], CF_4 [17, 150, 185], CCl_4 [17, 150, 185], CO [17, 150, 263], R134a [185], R142b [185], R143a [185], R152a [185], CH_3Cl [185], CH_2Cl_2 [185], CHF_2Cl [185]
modif. 1CLJ	Ar [9]
$1CLJ_{246}$	CCl_4 [108]
1CLJQ	N_2 [10]
1CLJD	CO [10, 402], R22 [120], R23 [120, 402], R32 [120, 402], R41 [150, 402], R125 [120], R134a [120], R142b [120], R143a [120, 402], R152a [120, 402], R161 [402], CH_3Cl [150, 402], $CHCl_3$ [150, 402], $CHFCl_2$ [150], CH_2Br–CH_3 [402] , $CHCl_2$–CH_3 [402], CH_3–OH [402]
1CLJDQ	CO [10]
2-body + 3-body	Ar [252, 345], Kr [252], Xe [252]
2CLJ	N_2 [8, 51, 108, 116, 161, 284, 331], O_2 [18, 161], F_2 [108, 161, 363], Cl_2 [18, 161, 363, 441], Br_2 [18, 161, 363], CO_2 [108, 285, 363, 385], CS_2 [18], C_2H_6 [18, 108, 164, 254, 439], C_2H_4 [18], CF_3CF_3 [185], CO [18, 161], R134a [185], R142b [185], R143a [185], R152a [185]
$2CLJ_{96}$	CO_2 [127, 285]
2CLJQ	N_2 [52, 247, 284], Cl_2 [286, 381], CO_2 [247, 285, 282]
$2CLJQ_{96}$	CO_2 [285]
2CLJD	R134a [221, 222], R142b [222], R143a [222], R152a [189, 222, 407]
2CLJDα	R22 [189], R134a [185], R142b [185], R143a [185], R152a [185, 407]
2CLJ chrg.	CO_2 [143], R23 [370]
a2CLJ chrg.	CH_3–OH [402]
multic. LJ no chrg.	N_2 [150], CO_2 [150], CS_2 [194, 391], C_2H_6 [150], C_2H_4 [150], Propylene [150], CF_4 [306], CCl_4 [262, 292, 375], CO [150]
multic. LJ_{246} no chrg.	SF_6 [238], CF_4 [238], CCl_4 [238]
multic. (modif.) LJ chrg.	R12 [140, 149, 277], R22 [277], R23 [312], R32 [149, 159, 312], R41 [312]
multic. LJ chrg.,polariz.	CCl_4 [44], R23 [151], CH_2Cl_2 [66]
multic. LJ chrg.,int.flx.	CF_4 [326], R23 [326], R32 [326]
multic. LJ_{96} chrg.,int.flx.	R32 [99], R125 [99], R134 [99], R134a [99], R143 [99], R143a [99], R152a [99], R161 [99]
nonc.appr.th.	Ne [265], Ar [265], Kr [265], Xe [265], CH_4 [75], N_2 [75], O_2 [75], Cl_2 [75]
ab-in.	CH_4 [20], N_2 [11, 153], CO_2 [13, 20], CS_2 [21], CCl_4 [186], R22 [347], R23 [20], R41 [20, 382], CH_3Cl [20], CH_2Cl_2 [20], $CHCl_3$ [19]
SSR-MPA	CH_4 [237], CO_2 [236]
Kihara based	N_2 [201], O_2 [201], CF_3CF_3 [201], CF_2CF_2 [201], R32 [201], R41 [201], R152a [201], CH_3Cl [201], $CHF{=}CH_2$ [201], $CF_2{=}CH_2$ [201]
exp-6 type	Ar [98], Kr [98], C_2H_6 [91], C_2H_2 [106, 118], CF_3CF_3 [201], CF_2CF_2 [201], CH_3–OH [323]
multic. HB14-7 chrg.,int.flx.	R23 [229], R32 [229], R134 [230], R134a [230], R143 [230], R143a [230], R152 [230]
various others	Ar [98], Kr [98], Cl_2 [116, 219, 333, 334, 432], Br_2 [2], CCl_4 [368]

The short-cut notations for the models used in this Table are described in Table 6.

2CLJQ models for nitrogen, oxygen, carbon monoxide, carbon dioxide, carbon disulfide, halogens, or ethane were developed, for example [18, 108, 116, 161, 286, 363]. Sets of Stockmayer models for calculations of vapor-liquid equilibria of carbon monoxide and halocarbons are available [120, 402]. 2CLJD models for the description of vapor-liquid equilibria of refrigerants were suggested [189, 221, 222]. Further 2CLJD-based models of refrigerants [185] were developed for the description of the second virial coefficient. Another 2CLJ-based model with partial charges was optimized for the description of vapor-liquid equilibria of R41 [370]. Dipolar and dipolar-quadrupolar Kihara models for the calculation of vapor-liquid equilibria of halocarbons were developed [201]. Note, that for carbon monoxide no 2CLJQ or 2CLJD models were published previously.

This literature survey underlines, that Lennard-Jones type potential functions are broadly used to model low-molecular substances. The subsequent comparison of the present molecular models to models from literature reveals, that the parametrization method of the present work is rewarding, as it explores the inherent optimization potential of the 2CLJQ/2CLJD models more thoroughly and more efficiently than in any previous work on these model types.

4.2 Parametrization Procedure

Several data points on the vapor-liquid coexistence curves between about 0.55 $T_{c,exp}$ up to about 0.95 $T_{c,exp}$ were used in the model parameter fitting procedure. With the global correlations the underlying non-linear optimization equations yielding the 2CLJQ or 2CLJD model parameters were

$$\left(T_c^*\left(P^{*2}, L^*\right) \cdot \varepsilon/k_B - T_{c,exp}\right)/T_{c,exp} \stackrel{!}{=} \min, \tag{132}$$

$$\sum_i \left[\left(p_\sigma^*\left(P^{*2}, L^*, T_i \cdot k_B/\varepsilon\right) \cdot \varepsilon/\sigma^3 - p_{\sigma,exp}(T_i)\right)/p_{\sigma,exp}(T_i)\right] \stackrel{!}{=} \min, \tag{133}$$

$$\sum_i \left[\left(\rho'^*\left(P^{*2}, L^*, T_i \cdot k_B/\varepsilon\right)/\sigma^3 - \rho'_{exp}(T_i)\right)/\rho'_{exp}(T_i)\right] \stackrel{!}{=} \min, \tag{134}$$

wherein P^{*2} symbolizes μ^{*2} or Q^{*2} in the case of 2CLJD or 2CLJQ modeling, respectively, and i counts the state points used for the optimization. Experimental critical temperatures $T_{c,exp}$ in Equation (132) were taken from Reid et al. [329] for unpolar or quadrupolar fluids and for propylene, and from the REFPROP data base [328] or from Daubert et al. [67] for the remaining multipolar fluids. The experimental data $p_{\sigma,exp}(T_i)$ and $\rho'_{exp}(T_i)$ in Equations (133) and (134) was taken from correlations of experimental data of vapor pressures and saturated liquid densities available in the references given in Table 37 in Appendix F. With respect to the statistical uncertainties of the molecular simulations these correlations of experimental data were assumed to be exact.

Tables 8, 9, and 10 report the 2CLJQ and 2CLJD parameters resulting from this optimization. Note that vapor-liquid equilibria of Stockmayer fluids (1CLJD) can be

calculated from the global 2CLJD correlations when the elongation L is zero and the Lennard-Jones energy parameter ε is divided by four. The determination of the signs of the parameter Q, cf. Tables 8 and 9, is described in Appendix G. Signs of Q are omitted, if they can not be determined with the method described there. In the case of the test fluids, no effort was made to determine the signs of the unphysical parameter Q. As described in Chapter 6.3.1, propylene was used as an example for determining the sign of Q empirically.

For the quantification of the performance of the present molecular models, mean relative deviations of the saturated liquid density

$$\overline{\delta\rho'} = \left[\frac{1}{n}\sum_{i=1}^{n}\left[\left(\rho'^{*}(P^{*}, L^{*}, T_i \cdot k_B/\varepsilon)/\sigma^3 - \rho'_{exp}(T_i)\right)/\rho'_{exp}(T_i)\right]^2\right]^{1/2}, \tag{135}$$

and mean relative deviations of the vapor pressure

$$\overline{\delta p_\sigma} = \left[\frac{1}{n}\sum_{i=1}^{n}\left[\left(p_\sigma^{*}(P^{*}, L^{*}, T_i \cdot k_B/\varepsilon)\cdot\varepsilon/\sigma^3 - p_{\sigma,exp}(T_i)\right)/p_{\sigma,exp}(T_i)\right]^2\right]^{1/2}, \tag{136}$$

are given in Tables 8, 9 and 10. They are calculated by the means of the global correlations for the saturated liquid densities and the vapor pressures of the 2CLJD and 2CLJQ model fluids for $n \approx 20$ temperatures T_i from about $0.60 \cdot T_{c,exp}$ to about $0.95 \cdot T_{c,exp}$.

For clarity, the CAS Registry Numbers of the fluids modeled in the present are given Table 38 in Appendix H.

Table 8: Parameters of the 2CLJQ potential model for unpolar or quadrupolar molecules. Mean relative deviation between simulation data and experimental data for saturated liquid density and vapor pressure of the pure fluids.

Fluid	σ Å	ε/k_B K	L Å	Q DÅ	$\overline{\delta\rho'}$ %	$\overline{\delta p_\sigma}$ %
Neon (Ne)	2.8010	33.921	–	0	0.60	2.47
Argon (Ar)	3.3952	116.79	–	0	0.89	2.13
Krypton(Kr)	3.6274	162.58	–	0	0.87	2.06
Xenon(Xe)	3.9011	227.55	–	0	1.39	1.72
Methane (CH_4)	3.7281	148.55	–	0	1.01	2.71
Fluorine (F_2)	2.8258	52.147	1.4129	+0.8920	0.30	1.92
Chlorine (Cl_2)	3.4016	160.86	1.9819	+4.2356	0.02	2.88
Bromine (Br_2)	3.5546	236.76	2.1777	+4.8954	0.02	1.53
Iodine (I_2)	3.7200	371.47	2.6784	+5.6556	1.12	2.13
Nitrogen (N_2)	3.3211	34.897	1.0464	−1.4397	0.22	1.10
Oxygen (O_2)	3.1062	43.183	0.9699	−0.8081	0.26	1.42

Table 8: continued.

Fluid	σ Å	ε/k_B K	L Å	Q DÅ	$\overline{\delta\rho'}$ %	$\overline{\delta p_\sigma}$ %
Carbon dioxide (CO_2)	2.9847	133.22	2.4176	−3.7938	0.20	1.49
Carbon disulfide (CS_2)	3.6140	257.68	2.6809	+3.8997	0.10	1.41
Ethane (C_2H_6)	3.4896	136.99	2.3762	−0.8277	0.36	2.11
Ethene (C_2H_4)	3.7607	76.950	1.2695	+4.3310	0.26	1.71
Ethyne (C_2H_2)	3.5742	79.890	1.2998	+5.0730	0.55	2.29
Perfluoroethane (C_2F_6)	4.1282	110.19	2.7246	−8.4943	0.44	3.72
Perfluoroethene (C_2F_4)	3.8611	106.32	2.2394	−7.0332	0.41	4.78
Perchloroethene (C_2Cl_4)	4.6758	211.11	2.6520	−16.143	0.58	2.46
Propadiene (CH_2=C=CH_2)	3.6367	170.52	2.4958	+5.1637	0.49	6.93
Test cases:						
Sulfur hexafluoride (SF_6)	3.9615	118.98	2.6375	8.0066	0.22	1.86
Tetrafluoromethane (CF_4)	3.8812	59.235	1.3901	5.1763	0.30	0.52
Tetrachloromethane (CCl_4)	4.8471	142.14	1.6946	14.346	0.49	1.16

Table 9: Parameters of the 2CLJQ potential model for multipolar molecules. Mean relative deviation between simulation data and experimental data for saturated liquid density and vapor pressure of the pure fluids.

Fluid	σ Å	ε/k_B K	L Å	Q DÅ	$\overline{\delta\rho'}$ %	$\overline{\delta p_\sigma}$ %
Carbon monoxide (CO)	3.3344	36.713	1.1110	−1.9170	0.18	1.91
R113 ($CFCl_2$–CF_2Cl)	4.5207	217.08	3.6166	12.984	0.27	2.46
R114 (CF_2Cl–CF_2Cl)	4.3772	183.26	3.5018	11.456	0.45	3.66
R115 (CF_2Cl–CF_3)	4.1891	155.77	3.3513	9.2246	0.34	5.03
R134 (CHF_2–CHF_2)	3.7848	170.46	3.0278	7.8745	0.24	3.31
CH_2Br_2	3.8683	274.97	3.0946	9.2682	0.10	2.42
CH_2Br–CH_2Br	4.1699	302.33	3.3359	10.903	0.47	2.61
CF_2Br–CF_2Br	4.5193	218.40	3.6154	12.822	0.29	2.68
CCl_2=CHCl	4.4120	201.03	2.6357	13.624	0.52	4.32
Propylene (CH_2=CH–CH_3)	3.8169	150.78	2.5014	5.9387	0.30	2.38
Propyne (CH≡C–CH_3)	3.5460	186.43	2.8368	−5.7548	0.45	2.06

Table 10: Parameters of the 2CLJD potential model for multipolar molecules. Mean relative deviation between simulation data and experimental data for saturated liquid density and vapor pressure of the pure fluids.

Fluid	σ Å	ε/k_B K	L Å	μ D	$\overline{\delta\rho'}$ %	$\overline{\delta p_\sigma}$ %
Carbon monoxide (CO)	3.3009	36.897	1.1405	0.7378	0.38	0.29
R11 ($CFCl_3$)	4.0213	224.15	3.3377	2.7009	0.31	2.95
R12 (CF_2Cl_2)	3.8286	185.66	3.2700	2.3219	0.51	1.62
R13 (CF_3Cl)	3.6184	145.95	3.0738	1.8261	0.55	1.66
R13B1 (CF_3Br)	3.6817	170.32	3.3573	2.0478	0.65	0.14
R22 (CHF_2Cl)	3.4682	177.43	3.1203	2.2667	0.54	2.99
R23 (CHF_3)	3.2643	123.56	2.5670	2.1607	0.55	6.13
R32 (CH_2F_2)	3.8971	155.97	–	2.4745	0.72	6.43
R41 (CH_3F)	3.0382	137.64	2.4530	1.8850	0.17	1.46
R123 ($CHCl_2$–CF_3)	4.0530	221.75	4.0530	3.7002	0.76	4.24
R124 ($CHFCl$–CF_3)	3.8852	192.25	3.8852	3.2190	0.77	5.42
R125 (CF_3–CHF_2)	3.6861	162.77	3.6861	2.8245	0.83	6.31
R134a (CF_3–CH_2F)	3.6138	175.12	3.6138	3.0214	0.73	6.45
R141b ($CFCl_2$–CH_3)	4.0209	231.43	3.6015	3.1484	0.36	2.98
R142b (CF_2Cl–CH_3)	3.8404	193.68	3.4675	2.9610	0.68	3.17
R143a (CF_3–CH_3)	3.5960	165.04	3.5395	2.7470	0.51	1.48
R152a (CHF_2–CH_3)	3.5168	182.01	3.3125	2.7354	0.32	3.48
R161 (CH_2F–CH_3)	3.3968	176.84	3.1006	2.4110	1.61	0.35
CH_3Cl	3.3409	186.57	2.5725	2.0217	0.22	1.09
CH_3Br	3.4557	213.81	2.6146	1.8536	0.15	2.54
CH_3I	3.6367	232.86	2.7083	2.4983	0.14	1.11
CH_2Cl_2	4.5106	269.44	–	3.3733	0.30	7.84
CH_2Br_2	4.7376	351.03	–	3.7104	0.26	10.7
CH_2I_2	5.0481	387.14	–	4.8971	0.29	1.44
CH_2ClBr	3.5838	274.49	3.5662	3.1998	1.13	0.47
$CHCl_3$	3.8153	265.29	3.7798	3.3920	0.29	1.31
$CHBr_3$	4.0575	357.41	3.9423	3.5204	0.35	0.98
$CHFCl_2$	3.6522	220.69	3.4396	2.7852	0.76	0.66
CF_2Br_2	4.1317	198.08	2.7356	2.5137	0.47	6.69
CF_2ClBr	3.8560	212.23	3.5957	2.6786	0.65	0.17
CCl_3Br	4.1366	305.34	3.9869	3.6313	1.03	0.26
$CHCl_2$–CH_3	3.8579	255.24	3.8135	3.5236	0.69	0.86
$CHCl_2$–CH_2Cl	4.0768	286.36	4.0095	4.2974	0.18	5.26
CCl_3–CH_3	4.2224	253.75	3.4898	3.5019	0.11	3.69
CCl_3–CH_2Cl	4.3282	292.86	4.1261	4.7919	0.52	2.82
CH_2Br–CH_3	3.6769	255.75	3.6769	2.9425	0.72	1.42
$CHBr_2$–CH_3	4.0234	341.29	4.0234	2.2097	0.31	6.22
CCl_3–CH_2F	4.1262	259.97	3.8469	4.3049	0.14	0.42
$CHClBr$–CF_3	4.6727	151.78	2.0700	3.7380	*0.37*	*0.11*
CCl_3–CF_2Cl	4.3651	258.25	4.2542	4.7132	0.33	0.33

Table 10: continued.

Fluid	σ Å	ε/k_B K	L Å	μ D	$\overline{\delta\rho'}$ %	$\overline{\delta p_\sigma}$ %
$CHF{=}CH_2$	3.3552	155.74	2.7513	1.6565	0.37	1.55
$CF_2{=}CH_2$	3.7848	71.963	1.4863	2.3643	0.49	0.41
$CHCl{=}CH_2$	3.6875	181.16	2.5049	2.1078	0.19	1.46
$CHCl{=}CF_2$	3.6501	193.24	3.4497	2.7449	0.61	0.42
$CFCl{=}CF_2$	3.7438	181.71	3.5521	2.8408	0.03	2.27
$CFBr{=}CF_2$	3.8290	218.12	3.5874	2.5273	0.68	0.18

4.3 Results for Thermodynamic Properties

The new 2CLJQ/2CLJD models were validated by applying them for molecular simulations of vapor-liquid equilibria with the NpT+Test Particle Method, cf. Chapter 2.5.1. For 2CLJD fluids, at the lowest temperatures the configurational part of the chemical potential needed for the NpT+Test Particle Method was obtained from the gradual insertion method of about 15000 Monte Carlo loops, otherwise the configurational part of the chemical potential was obtained from the test particle insertion method, cf. Chapter 2.4. Further technical details of the simulations were identical with those given in Appendices C.1 and C.2.

The vapor-liquid equilibrium data obtained from these simulations are compared in the following to experimental data of the modeled fluids. Furthermore, molecular models of other authors are compared to the present molecular models. For that purpose, the empirical correlations of the vapor pressure and the saturated densities developed in the present work were applied for 2CLJQ/2CLJD models from literature, or published vapor-liquid equilibrium data are used for more complex models. It was not in the scope of the present work to perform simulations with more complex molecular models for the purpose of comparison.

In order to demonstrate the performance of the new molecular models to predict thermophysical properties in homogeneous fluids states, molecular simulations of various homogeneous fluid state points were performed in the NpT ensemble. Technical details of these simulations without calculation of the chemical potential were identical to those given in Appendices C.1 and C.2.

Data from the present work shown in Figures 11 to 29 is available in [378].

4.3.1 Unpolar or Quadrupolar Fluids

Figures 11 to 14 and Figures 15 to 18 show saturated densities and vapor pressures from the present molecular models of unpolar or quadrupolar fluids in comparison to experi-

mental data and to data from models from other authors. Many of those models from the literature are of the 2CLJ type – also the OPLS model of ethane [164]. The parameters of those 2CLJ models and the mean relative deviations of the saturated liquid density and the vapor pressure, cf. Equations (135) and (136), are listed in Table 11. Vapor-liquid equilibrium data of more complex models of ethane (TraPPE-EH force field [48]), carbon dioxide (two-center plus point charges model [143]), carbon disulfide (multicenter model [194]), chlorine (anisotropic interaction potential [219]), sulfur hexafluoride (multicenter model [238]), tetrafluoromethane (multicenter models [238, 326]), and tetrachloromethane (multicenter models [108, 238]) was taken from literature and is shown in Figures 13, 14, 15, 17, and 18. The models from [18, 48, 108, 116, 143, 238, 282, 326] were optimized for the description of vapor-liquid equilibria.

Table 11: Parameters of 2CLJ and 2CLJQ models of quadrupolar fluids from literature. Mean relative deviation between model data and experimental data for saturated liquid density and vapor pressure.

Fluid	Ref.	Model	σ Å	ε/k_B K	L Å	Q DÅ	$\overline{\delta\rho'}$ %	$\overline{\delta p_\sigma}$ %
F_2	[363]	2CLJ	2.825	52.8	1.4266	0	0.70	1.49
F_2	[108]	2CLJ	2.8317	53.472	1.4300	0	0.66	7.61
Cl_2	[363]	2CLJ	3.332	178.3	2.0992	0	1.13	1.27
Cl_2	[286]	2CLJQ	3.374	164.3	2.01	3.60	0.87	9.66
Br_2	[18]	2CLJ	3.2843	345.47	3.2186	0	7.29	82.2
N_2	[116]	2CLJ	3.310	37.3	1.0890	0	1.94	14.1
N_2	[284]	2CLJQ (X1)	3.318	36.4	1.098	0	1.15	5.31
N_2	[108]	2CLJ	3.3078	36.673	1.0890	0	0.83	5.28
O_2	[18]	2CLJ	3.2104	38.003	0.7063	0	1.45	2.35
CO_2	[282]	2CLJQ	3.0354	125.317	2.1217	3.6727	0.75	4.21
CO_2	[108]	2CLJ	2.9376	161.83	2.3295	0	6.25	24.4
CS_2	[18]	2CLJ	3.7509	232.26	2.2130	0	3.07	15.1
C_2H_6	[18]	2CLJ	3.5120	139.81	2.3530	0	2.06	16.0
C_2H_6	[164]	2CLJ (OPLS)	3.775	104.22	1.53	0	4.67	20.5
C_2H_4	[18]	2CLJ	3.3268	137.73	2.4618	0	2.80	18.7

For almost all fluids, the relative deviations of the saturated liquid densities from simulations to experimental data $|\delta\rho'| = \left|(\rho'_{\text{sim}} - \rho'_{\text{exp}})/\rho'_{\text{exp}})\right|$ obtained from the present molecular models are clearly below 1 %. This can also be seen from the values of the mean relative deviations $\overline{\delta\rho'}$ given in Table 8. For temperatures around $0.7 \cdot T_c$ the relative deviations of the vapor pressures $|\delta p_\sigma| = |(p_\sigma - p_{\sigma,\text{exp}})/p_{\sigma,\text{exps}})|$ are about $\pm 3\%$ or less (for example ethane, fluorine, chlorine, bromine, iodine). For temperatures above about $0.85 \cdot T_c$ and below about $0.65 \cdot T_c$ relative deviations of the vapor pressures increase to

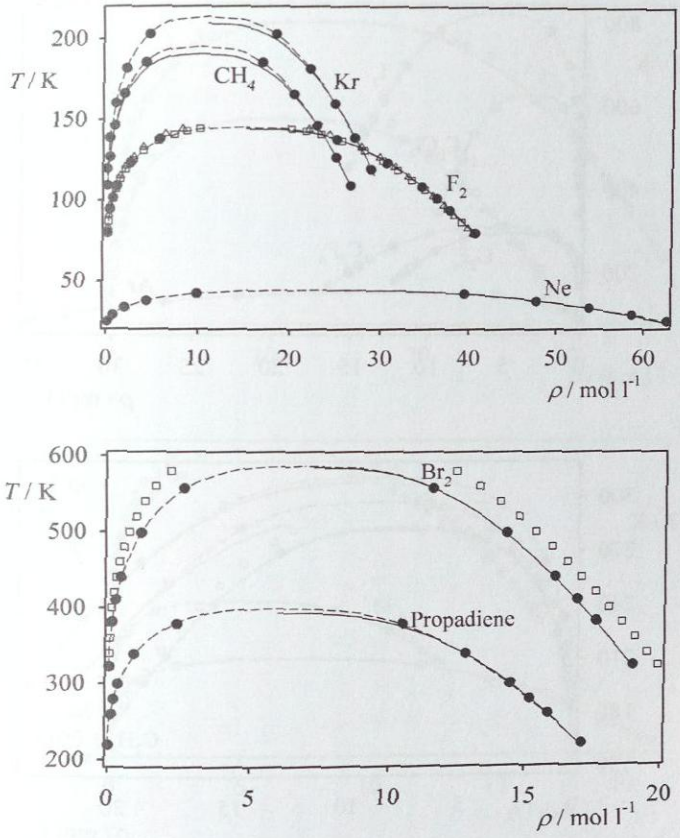

Figure 11: Comparison of experimental data of saturated densities to different models: —— experiment (cf. Table 37), – – – global correlation, cf. *Chapter* 3.2.2.2. • Simulation results from present models; error bars are, if not indicated, within symbol size. Results from models from the literature (cf. Table 11), top: □ F_2 [363], △ F_2 [108], bottom: □ Br_2 [18].

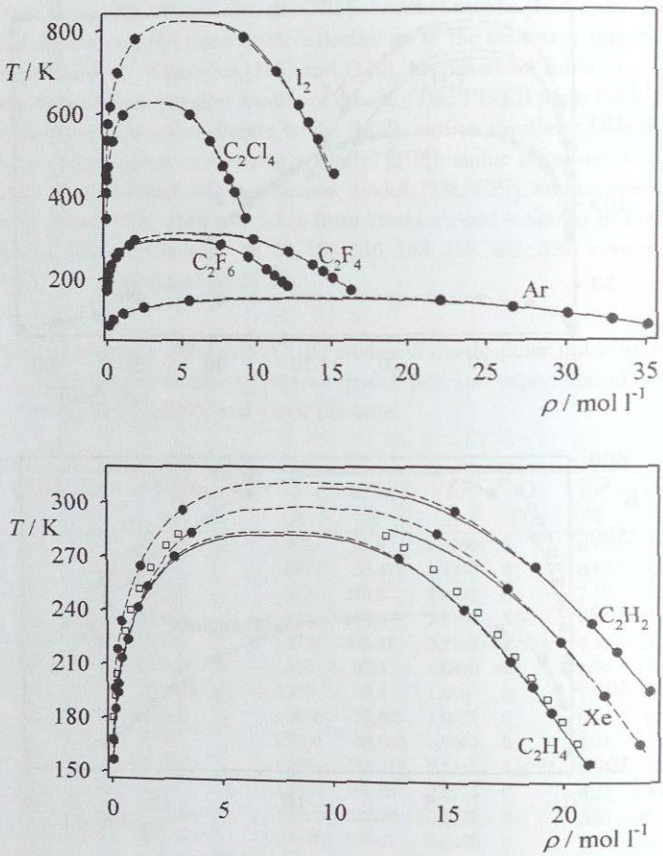

Figure 12: Comparison of experimental data of saturated densities to different models: —— experiment (cf. Table 37), – – – global correlation, cf. Chapter 3.2.2.2. • Simulation results from present models; error bars are, if not indicated, within symbol size. Bottom: □ results from a model of C_2H_4 from the literature [18] (cf. Table 11).

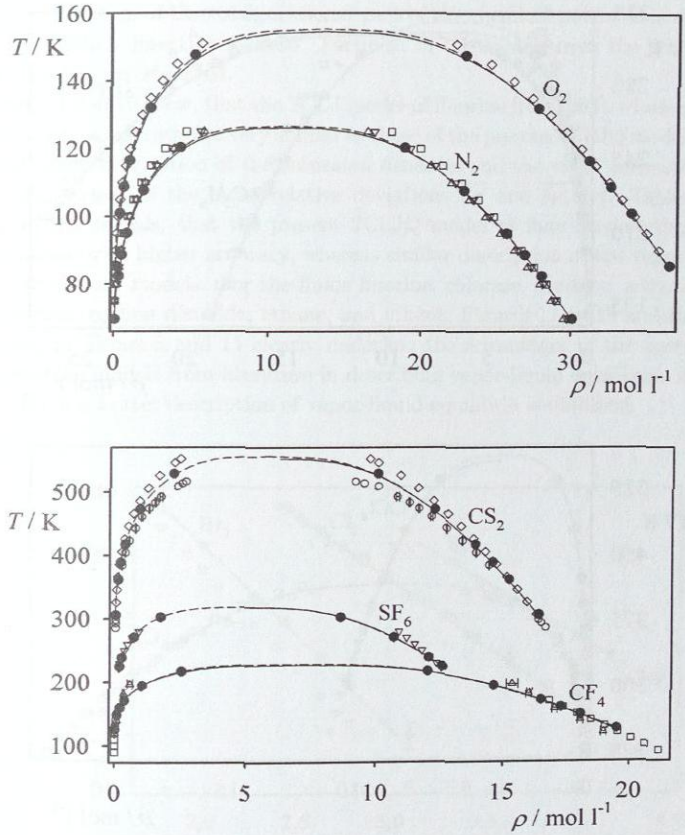

Figure 13: Comparison of experimental data of saturated densities to different models: —— experiment (cf. Table 37), – – – global correlation, cf. Chapter 3.2.2.2. • Simulation results from present models; error bars are, if not indicated, within symbol size. Results from models from the literature (cf. Table 11), top: ◇ O_2 [18], □ N_2 [116], △ N_2 [284], ▽ N_2 [108], bottom: ◇ CS_2 [18], ○ CS_2 [194], ▽ SF_6 [238], □ CF_4 [238], △ CF_4 [326]; error bars are indicated, if data is given in the literature.

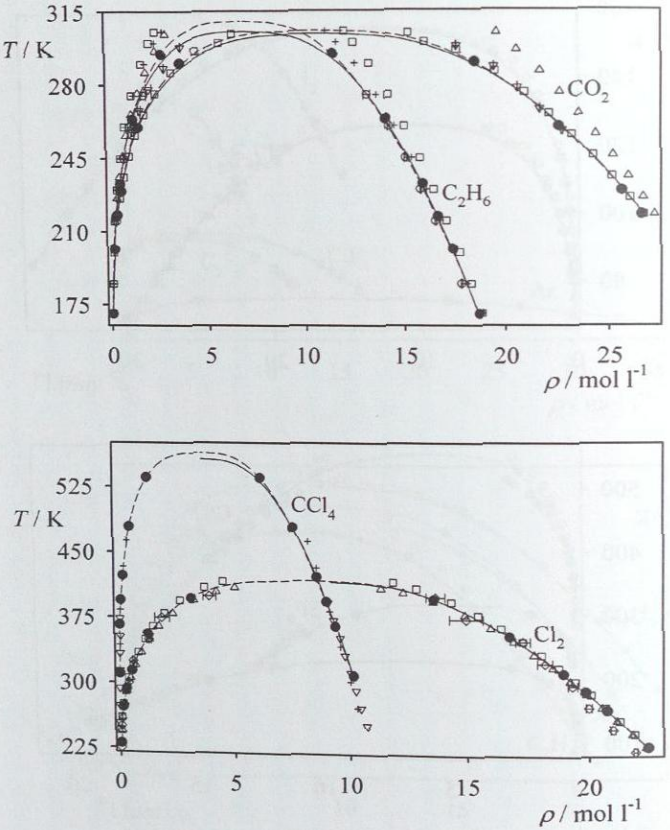

Figure 14: Comparison of experimental data of saturated densities to different models: —— experiment (cf. Table 37), – – – global correlation, cf. Chapter 3.2.2.2. • Simulation results from present models; error bars are, if not indicated, within symbol size. Results from models from the literature (cf. Table 11), top: □ CO_2 [282], △ CO_2 [108], ▽ CO_2 [143], ○ C_2H_6 [48], + C_2H_6 [18], □ C_2H_6 [164], bottom: + CCl_4 [108], ▽ CCl_4 [238], □ Cl_2 [363], △ Cl_2 [286], ◇ Cl_2 [219]; error bars are indicated, if data is given in the literature.

about ±5%. This is due to the increasing influence of critical effects and to the relatively uncertain calculation of the configurational part of the chemical potential in dense phases by the test particle insertion method. For most of the models from the literature much larger deviations are observed.

Figures 11 and 16 show, that the 2CLJ model of fluorine from [363], whose size, energy, and elongation parameters are very similar to those of the present 2CLJQ model of fluorine, yields very good description of the saturated densities and the vapor pressure. However, a direct comparison of the mean relative deviations $\overline{\delta\rho'}$ and $\overline{\delta p_\sigma}$ (cf. Tables 8 and 11) of both models reveals, that the present 2CLJQ model of fluorine describes saturated liquid densities with higher accuracy, whereas similar description of the vapor pressure is obtained from both models. For the fluids fluorine, chlorine, bromine, nitrogen, oxygen, carbon dioxide, carbon disulfide, ethane, and ethene, Figures 11 to 18 and the values of $\overline{\delta\rho'}$ and $\overline{\delta p_\sigma}$ in Tables 8 and 11 clearly underline the advantages of the present 2CLJQ models over the models from literature in describing vapor-liquid equilibria. Also for the test case fluids a better description of vapor-liquid equilibria is obtained.

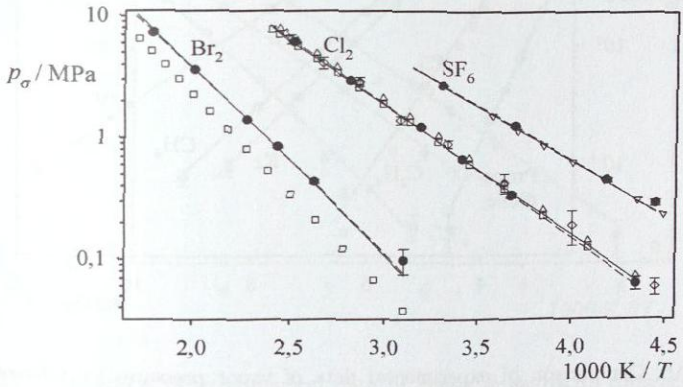

Figure 15: Comparison of experimental data of vapor pressures to different models: —— experiment (cf. Table 37), – – – global correlation, cf. Chapter 3.2.2.2. • Simulation results from present models; error bars are, if not indicated, within symbol size. Results from models from the literature (cf. Table 11): □ Br_2 [18], □ Cl_2 [363], △ Cl_2 [286], ◇ Cl_2 [219], ▽ SF_6 [238]; error bars are indicated, if data is given in the literature.

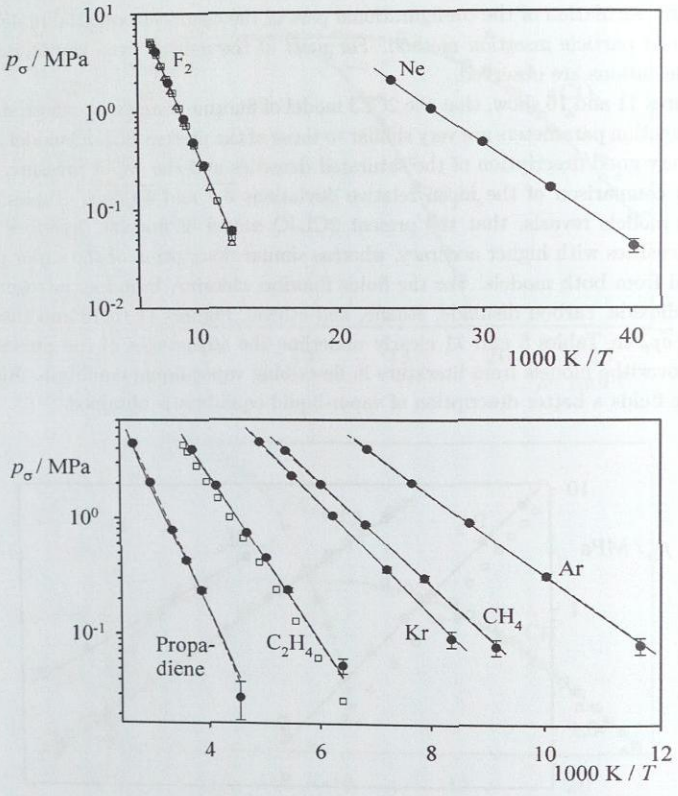

Figure 16: Comparison of experimental data of vapor pressures to different models: —— experiment (cf. Table 37), – – – global correlation, cf. Chapter 3.2.2.2. • Simulation results from present models; error bars are, if not indicated, within symbol size. Results from models from the literature (cf. Table 11), top: □ F_2 [363], △ F_2 [108], bottom: □ C_2H_4 [18].

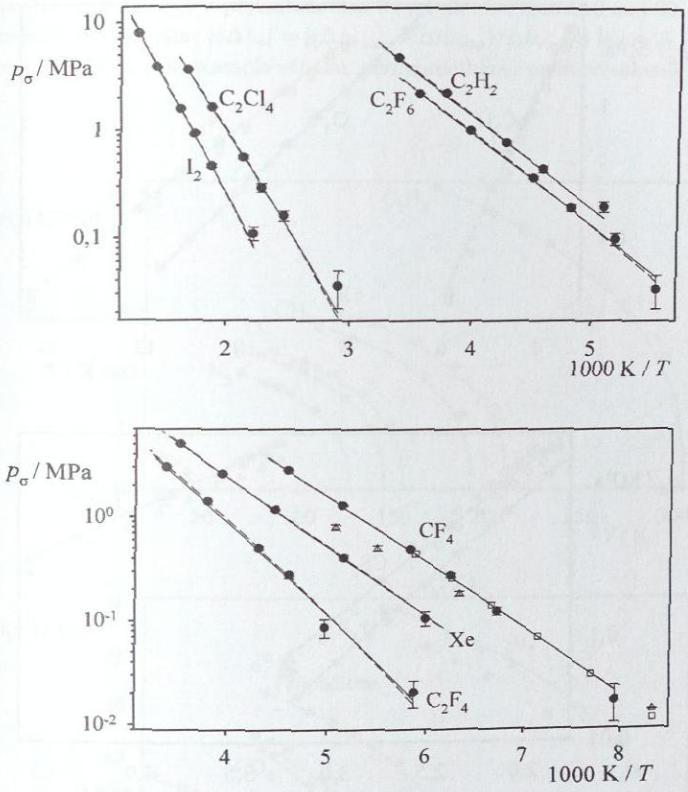

Figure 17: Comparison of experimental data of vapor pressures to different models: —— experiment (cf. Table 37), – – – *global correlation*, cf. Chapter 3.2.2.2. • Simulation results from present models; error bars are, if not indicated, within symbol size. Results from models from the literature (cf. Table 11), *bottom:* □ CF_4 [238], △ CF_4 [326]; error bars are indicated, if data is given in the literature.

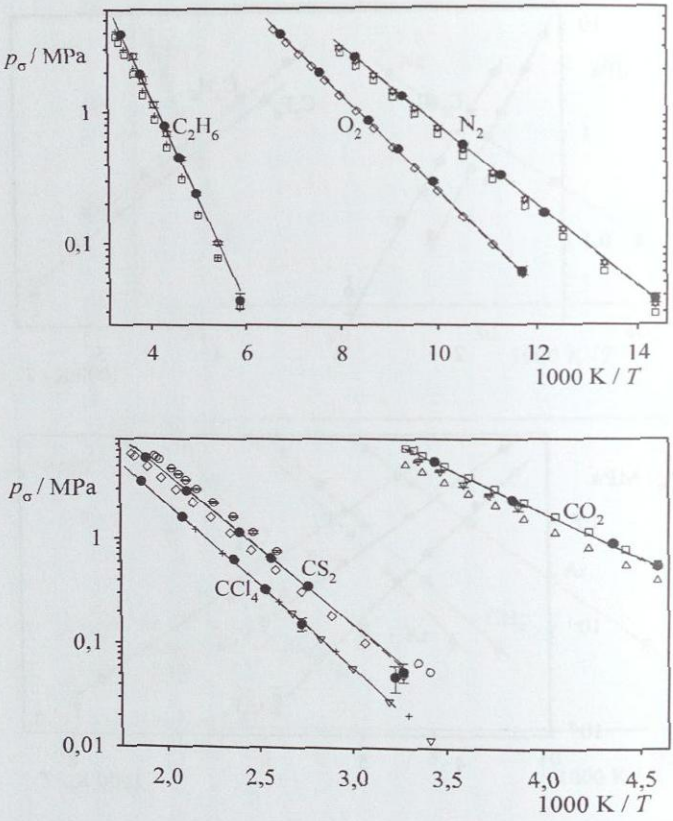

Figure 18: Comparison of experimental data of vapor pressures to different models: —— experiment (cf. Table 37), – – – global correlation, cf. Chapter 3.2.2.2. • Simulation results from present models; error bars are, if not indicated, within symbol size. Results from models from the literature (cf. Table 11), top: □ N_2 [116], △ N_2 [284], ▽ N_2 [108], ◇ O_2 [18], ○ C_2H_6 [48], + C_2H_6 [18], □ C_2H_6 [164], bottom: □ CO_2 [282], △ CO_2 [108], ▽ CO_2 [143], ◇ CS_2 [18], ○ CS_2 [194], + CCl_4 [108], ▽ CCl_4 [238]; error bars are indicated, if data is given in the literature.

As can be expected from the thermodynamic consistency, most of the present molecular models predict enthalpies of vaporization also very well, cf. Figures 19 and 20. Typically, they have relative deviations $|\delta\Delta h_v| = |(\Delta h_{v,sim} - \Delta h_{v,exp})/\Delta h_{v,exp})|$ below 3 %, in many cases even below 1 % (for example ethane, perfluoroethane, perfluoroethene, iodine, or oxygen).

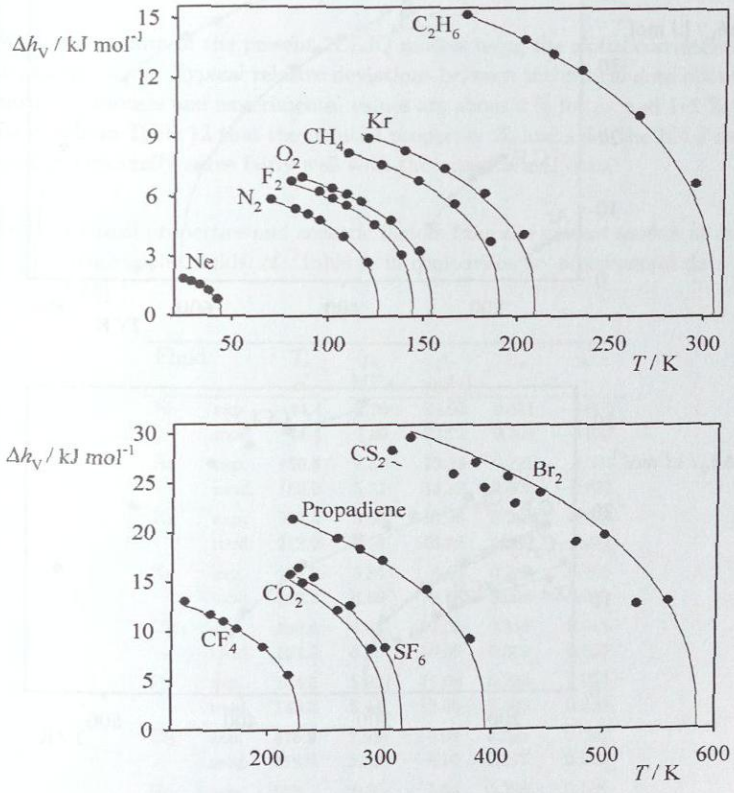

Figure 19: Comparison of experimental data of enthalpies of vaporization to present models: —— experiment (cf. Table 37), • simulation results from present models. Error bars of simulation results are, if not indicated, within symbol size.

Deviations increase for state points close to the critical point, as the critical temperature given by the molecular models is in most cases slightly higher than the experimental value. For carbon disulfide and tetrachloromethane experimental data for the enthalpies of vaporization are only available in a small temperature range.

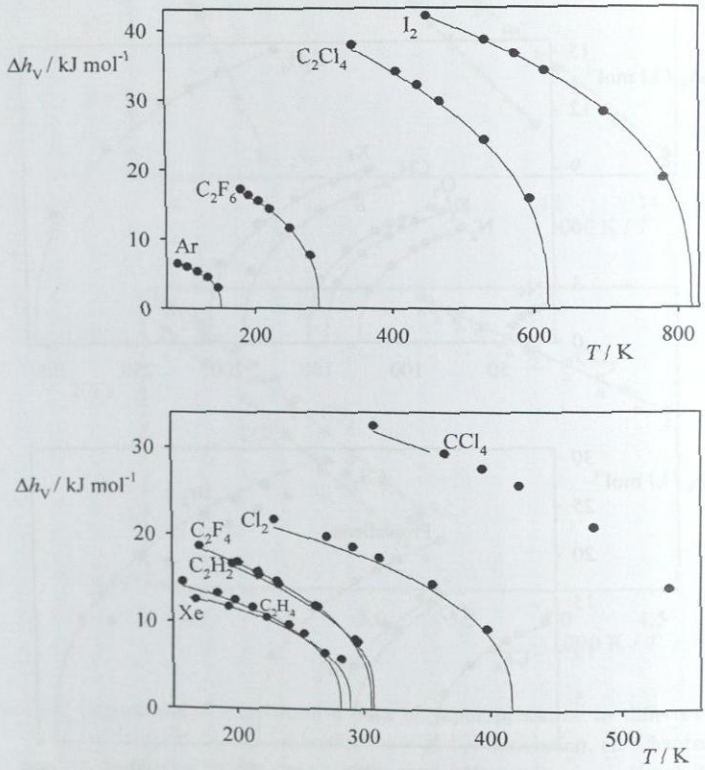

Figure 20: Comparison of experimental data of enthalpies of vaporization to present models: —— experiment (cf. Table 37), • simulation results from present models. Error bars of simulation results are, if not indicated, within symbol size.

In Table 12 experimental data of the critical temperature T_c, critical pressure p_c, critical density ρ_c, and critical compressibility

$$Z_c = \frac{p_c}{\rho_c R T_c}, \tag{137}$$

as well as the acentric factor

$$\omega = -\log_{10}\left[\frac{p_\sigma(0.7T_c)}{p_c}\right] - 1, \tag{138}$$

are compared to data of the present 2CLJQ models using the global correlations for the 2CLJQ model fluids. Typical relative deviations between the critical data obtained from the molecular models and experimental values are about 4 % for p_c, and 1–2 % for ρ_c. It can be seen from Table 12 that the reduced properties Z_c and ω for the 1CLJ models are all equal and generally agree fairly well with the experimental data.

Table 12: Critical properties and acentric factors from the present models of unpolar or quadrupolar fluids, cf. Table 8, in comparison to experimental data [329], or [359] †.

Fluid		T_c K	p_c MPa	ρ_c mol/l	Z_c	ω
Ne	exp.	44.4	2.76	24.04	0.311	−0.029
	mod.	44.4	2.69	23.72	0.306	−0.032
Ar	exp.	150.8	4.87	13.35	0.291	0.001
	mod.	153.0	5.21	13.32	0.306	−0.032
Kr	exp.	209.4	5.50	10.96	0.288	0.005
	mod.	213.0	5.94	10.92	0.306	−0.032
Xe	exp.	289.7	5.84	8.45	0.287	0.008
	mod.	298.1	6.69	8.78	0.306	−0.032
CH_4	exp.	190.4	4.60	10.08	0.288	0.011
	mod.	194.6	5.00	10.06	0.306	−0.032
F_2	exp.	144.3	5.22	15.08	0.288	0.054
	mod.	145.2	5.44	15.05	0.300	0.050
Cl_2	exp.	416.9	7.98	8.08	0.285	0.090
	mod.	418.6	8.39	8.10	0.297	0.100
Br_2	exp.	588	10.3	7.86	0.268	0.108
	mod.	587	10.0	6.86	0.298	0.086
I_2	exp.	819	11.73†	6.45	n.a.	n.a.
	mod.	820	11.12	5.44	0.300	0.087
N_2	exp.	126.2	3.39	11.14	0.290	0.039
	mod.	126.7	3.46	11.13	0.295	0.034

Table 12: continued.

Fluid		T_c K	p_c MPa	ρ_c mol/l	Z_c	ω
O_2	exp.	154.6	5.04	13.62	0.288	0.025
	mod.	155.4	5.18	13.58	0.295	0.018
CO_2	exp.	304.1	7.38	10.65	0.274	0.239
	mod.	305.6	7.49	10.55	0.279	0.232
CS_2	exp.	552	7.90	6.25	0.276	0.109
	mod.	556	8.13	5.83	0.302	0.083
C_2H_6	exp.	305.4	4.88	6.74	0.285	0.099
	mod.	310.2	5.27	6.74	0.303	0.065
C_2H_4	exp.	282.4	5.04	7.67	0.280	0.089
	mod.	284.0	5.29	7.62	0.294	0.091
C_2H_2	exp.	308.3	6.14	8.87	0.270	0.190
	mod.	311.4	6.67	8.88	0.290	0.186
C_2F_6	exp.	293.0	3.06	4.50	0.279	n.a.
	mod.	296.0	3.15	4.41	0.290	0.227
C_2F_4	exp.	306.5	3.94	5.81	0.267	0.223
	mod.	309.5	4.36	5.75	0.295	0.210
C_2Cl_4	exp.	620.2	4.76	3.45	0.250	n.a.
	mod.	626.2	5.02	3.27	0.294	0.212
Propadiene	exp.	393	5.47	6.17	0.271	0.313
	mod.	399	5.94	6.08	0.295	0.121
Test cases:						
SF_6	exp.	318.7	3.76	5.03	0.282	0.286
	mod.	318.7	3.82	4.97	0.290	0.231
CF_4	exp.	227.6	3.74	7.16	0.276	0.177
	mod.	228.9	3.85	6.94	0.291	0.169
CCl_4	exp.	556.4	4.56	3.62	0.272	0.193
	mod.	563.6	4.91	3.61	0.290	0.179

Apart from simulations of vapor-liquid equilibria, the molecular models were used at various homogeneous fluid state points. In Table 13 results of these simulations for the fluids perfluoroethane, ethene, nitrogen, and oxygen are compared to experimental data of density ρ and residual enthalpy defined as

$$h^{\mathrm{res}}(T,p) = h(T,p) - h^{\mathrm{id}}(T). \tag{139}$$

Also data points far from the vapor-liquid equilibrium region are included in this comparison. In most cases densities from the simulation agree very well with the experimental data. Residual enthalpies are also reasonably predicted. Relative deviations $|\delta h^{\mathrm{res}}| = \left|(h^{\mathrm{res}}_{\mathrm{sim}} - h^{\mathrm{res}}_{\mathrm{exp}})/h^{\mathrm{res}}_{\mathrm{exp}})\right|$ are typically about 3%.

Table 13: Results from NpT simulations with present 2CLJQ models of quadrupolar fluids, cf. Table 8, at various homogeneous fluid state points and comparison to experimental data [328]. Numbers in parenthesis are uncertainties of the last digits.

Fluid	T K	p MPa		ρ mol/l	h^{res} J/mol
C_2F_6	222	0.1	exp.	0.056	-214
			sim.	0.057 (1)	-205 (3)
	222	7	exp.	11.046	-14849
			sim.	11.008 (3)	-14787 (8)
	222	20	exp.	11.489	-14339
			sim.	11.487 (5)	-14303 (8)
	423	2.845	exp.	0.882	-1215
			sim.	0.876 (2)	-1196 (8)
	423	7.393	exp.	2.52	-3316
			sim.	2.520 (5)	-3169 (11)
	423	49.551	exp.	8.5	-6653
			sim.	8.543 (5)	-6339 (9)
C_2H_4	213	0.3	exp.	0.178	-260
			sim.	0.177 (1)	-220 (10)
	213	10	exp.	18.410	-11978
			sim.	18.385 (8)	-12151 (58)
	213	20	exp.	18.914	-11748
			sim.	18.889 (7)	-11942 (5)
	450	5.311	exp.	1.524	-1136
			sim.	1.511 (2)	-1010 (6)
	450	13.95	exp.	4.354	-2908
			sim.	4.260 (7)	-2642 (9)
	450	171.51	exp.	17.6	-2651
			sim.	17.379 (5)	-2410 (6)
N_2	95	0.2	exp.	0.266	-103
			sim.	0.2647 (9)	-96 (2)
	95	7	exp.	26.60	-5045
			sim.	26.64 (1)	-5055 (3)
	95	20	exp.	27.99	-4816
			sim.	27.99 (1)	-4827 (2)
	280	5.198	exp.	2.260	-355
			sim.	2.255 (2)	-343 (3)
	280	14.930	exp.	6.360	-882
			sim.	6.317 (5)	-846 (3)
	280	114.92	exp.	22.26	-138
			sim.	22.08 (1)	-109 (3)

Table 13: continued.

Fluid	T	p		ρ		h^{res}	
	K	MPa		mol/l		J/mol	
CO_2	260	1.2	exp.	0.618		-749	
			sim.	0.612	(3)	-648	(8)
	260	10	exp.	23.52		-13558	
			sim.	23.30	(2)	-13809	(13)
	260	20	exp.	24.31		-13544	
			sim.	24.04	(2)	-13809	(11)
	550	99.98	exp.	16.08		-4623	
			sim.	15.44	(1)	-4464	(11)
	600	10.3	exp.	2.110		-954	
			sim.	2.088	(4)	-887	(10)
	600	29.74	exp.	6.029		-2420	
			sim.	5.846	(6)	-2221	(9)

Figures 11 to 20 as well as Tables 12 and 13 demonstrate, that the present 2CLJQ models allow accurate simulation of vapor-liquid equilibria of the pure fluids with symmetric unpolar or quadrupolar molecules modeled here and that these molecular models have good predictive power (cf. Table 13) for thermophysical properties in homogeneous fluid states far away from the vapor-liquid equilibrium states. Similar results were found recently for the prediction of thermophysical properties of supercritical carbon dioxide [59] by the means of a 2CLJQ model of carbon dioxide available in literature [282].

Figure 21 shows a comparison of results for the second virial coefficient B of carbon dioxide obtained from the present 2CLJQ model and from a model based on ab initio calculations on MP2 level of theory [13] to experiment. The ab initio model [13] is in very good agreement with experimental data. Also the present 2CLJQ model of carbon dioxide, which was obtained from thermodynamic data alone, compares favorably to the experiments. This encouraging finding is an important hint that in future work results from quantum mechanical calculations may conveniently be used for the parametrization of effective molecular models, that quantitatively describe macroscopic thermodynamics.

4.3.2 Multipolar Fluids

For a representative sample of multipolar fluids, Figures 22 and 23 compare the saturated densities and Figures 24 to 26 the vapor pressures from the present molecular models to experimental data and to data from molecular models from other authors. Many of the models from the literature are 2CLJ, 2CLJD and Stockmayer models. The parameters of those models and the mean relative deviations of the saturated liquid density and the vapor pressure, cf. Equations (135) and (136), are given in Table 14. This comparison compri-

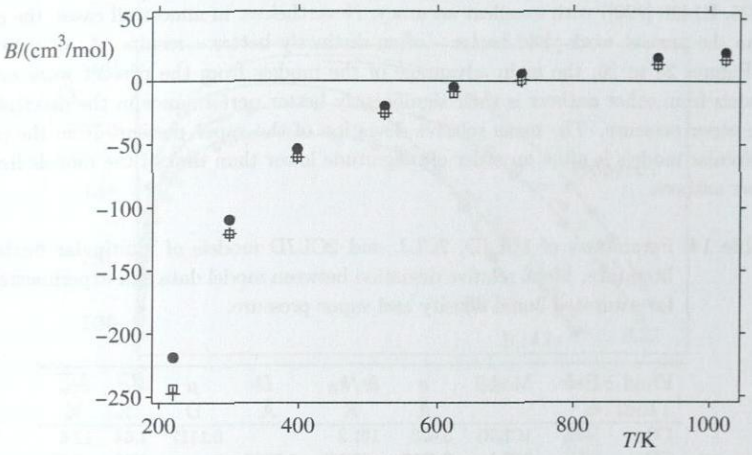

Figure 21: Second virial coefficient of carbon dioxide. + Experiment, data taken from [13], • present 2CLJQ model, □ model based on ab initio calculations [13].

ses also vapor-liquid equilibrium data from a 2CLJD-like model of R23 [370], which is composed of two Lennard-Jones centers plus two point charges. Except for one 2CLJD model of R152a [407], which has been developed for the investigation of the second virial coefficient, all models from the literature shown in Figures 22 to 26 were parametrized for the calculation of vapor-liquid equilibria.

For almost all multipolar fluids shown in this comparison, the relative deviations of the saturated liquid densities from simulation to experimental data $|\delta\rho'| = \left|(\rho'_{\text{sim}} - \rho'_{\text{exp}})/\rho'_{\text{exp}})\right|$ obtained from the present molecular models are clearly below 1%. This can also be seen from the values of the mean relative deviations $\overline{\delta\rho'}$ given in Tables 9 and 10. For temperatures around $0.7 \cdot T_c$ the relative deviations of the vapor pressures from simulation to experiment $|\delta p_\sigma| = |(p_{\sigma,\text{sim}} - p_{\sigma,\text{exp}})/p_{\sigma,\text{exp}})|$ are typically less than 4%. As illustrated in Figures 24 to 26, somewhat higher relative deviations of the vapor pressure are observed for some fluids, for example R23 or R32, for temperatures below about $0.65 \cdot T_c$. The use of both dipolar and quadrupolar models might improve the description of vapor pressures at low temperatures. However, the mean relative deviations of the vapor pressure $\overline{p_\sigma}$ are still generally below 3%, in some cases even below 1%. This shows that for many fluids the 2CLJD and 2CLJQ modeling yields an excellent description of the saturated liquid densities and the vapor pressures.

Figures 22 and 23 and Table 14 show, that the models from the literature describe the saturated densities with fair, but in some cases (cf. Stockmayer models of R23, R32,

R125, R142b [120]) with excellent accuracy. Nevertheless, in almost all cases, the models from the present work yield better – often distinctly better – results. As demonstrated in Figures 24 to 26, the main advantage of the models from the present work over the models from other authors is their significantly better performance in the description of the vapor pressure. The mean relative deviation of the vapor pressure from the present molecular models is often an order of magnitude lower than that of the models from the other authors.

Table 14: Parameters of 1CLJD, 2CLJ, and 2CLJD models of multipolar fluids from literature. Mean relative deviation between model data and experimental data for saturated liquid density and vapor pressure.

Fluid	Refs.	Model	σ Å	ε/k_B K	L Å	μ D	$\overline{\delta\rho'}$ %	$\overline{\delta p_\sigma}$ %
CO	[402]	1CLJD	3.623	101.2	–	0.1117	1.64	22.6
CO	[18]	2CLJ	3.2717	42.282	1.2760	0	1.30	6.48
R22	[189]	2CLJD	3.483	155.73	2.8247	2.6320	2.84	9.44
R23	[120]	1CLJD	4.034	146.2	–	2.2884	0.77	9.41
R23	[402]	1CLJD	4.007	199.6	–	1.6205	1.04	81.4
R32	[120]	1CLJD	3.900	163.1	–	2.4248	0.59	8.17
R32	[402]	1CLJD	3.881	213.0	–	1.9601	0.63	65.3
R125	[120]	1CLJD	4.727	166.7	–	3.0855	0.67	13.2
R134a	[222]	2CLJD	3.819	140.4	2.5587	2.7491	1.11	41.6
R142b	[120]	1CLJD	4.848	216.2	–	3.3675	0.59	9.49
R142b	[222]	2CLJD	3.996	153.9	2.6773	3.0807	1.02	14.3
R143a	[120]	1CLJD	4.559	169.2	–	2.9607	2.04	8.62
R143a	[402]	1CLJD	4.535	221.2	–	2.2801	2.64	68.4
R143a	[222]	2CLJD	3.793	129.8	2.5413	2.6164	1.33	26.6
R152a	[189]	2CLJD	3.661	131.29	2.5190	3.1397	1.11	3.94
R152a	[222]	2CLJD	3.678	145.0	2.4643	2.6405	1.03	31.8
R152a	[407]	2CLJD	3.845	119.0	1.9417	2.7334	1.87	19.6

Satisfactory results for the important refrigerant R32 can only be expected from more elaborate modeling than the simplistic 1CLJD approach chosen here. Such more complex molecular models of R32 are available in literature [149, 326], which, however, lack in accuracy in the description of vapor-liquid equilibria. Data from these models are therefore not shown here. The same is true for a molecular model of R23 also available in [326].

For the refrigerants modeled in the present work, Figures 27 to 29 compare the enthalpies of vaporization from the present molecular models to experimental data. As expected, most of the molecular models predict the enthalpies of vaporization very well. Typically, the relative deviations $|\delta\Delta h_v| = |(\Delta h_{v,sim} - \Delta h_{v,exp})/\Delta h_{v,exp})|$ of the enthalpies of vaporization are below 3%, in some cases even below 1% (for example CO, R142b, R152a).

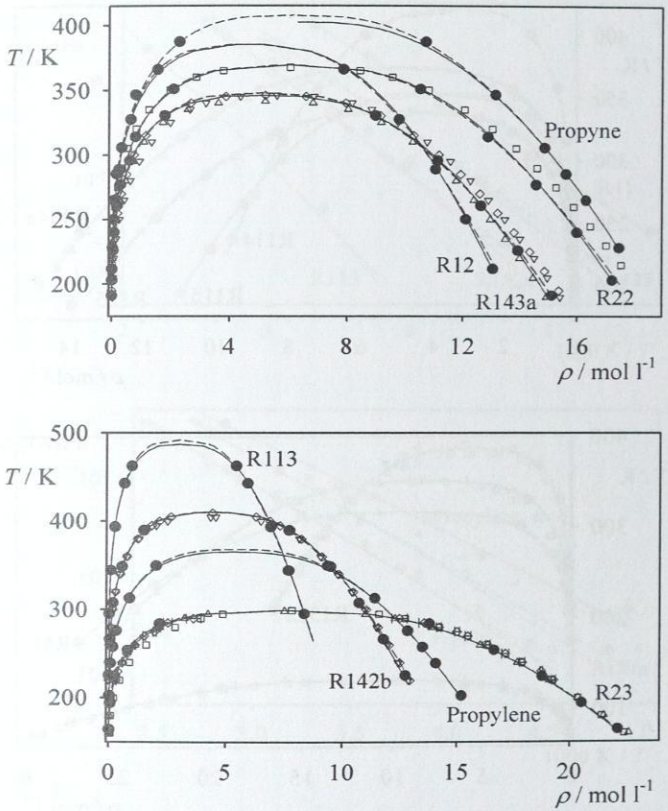

Figure 22: Comparison of experimental data of saturated densities to different models: —— experiment (cf. Table 37), – – – global correlation, cf. Chapter 3.2.2.2. • Simulation results from present models; error bars are, if not indicated, within symbol size. Results from models from the literature (cf. Table 14), top: ▽ R143a [402], ◇ R143a [120], △ R143a [222], □ R22 [189], bottom: □ R23 [402], △ R23 [120], ◇ R142b [120], ▽ R142b [222]; error bars are indicated, if data is given in the literature.

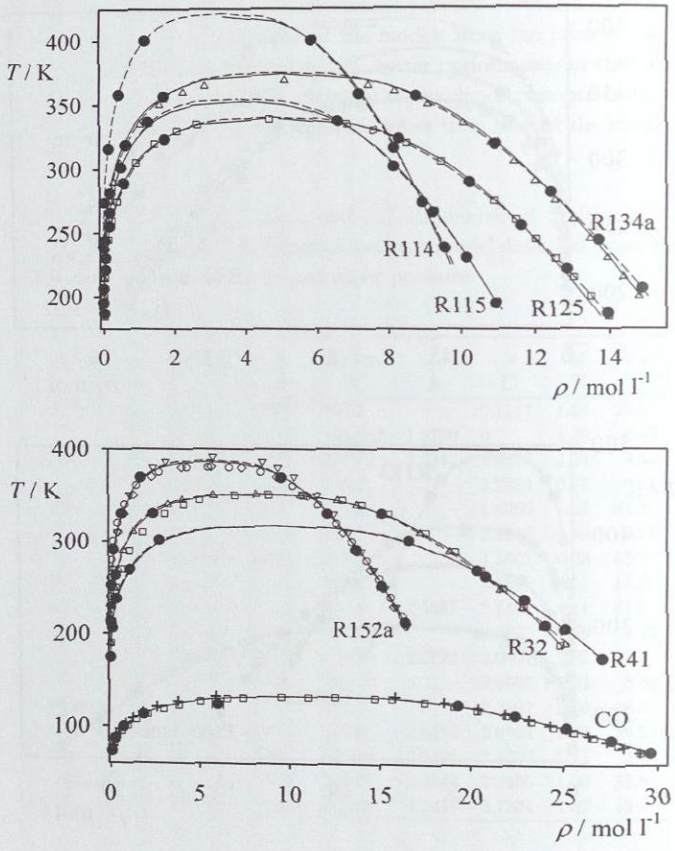

Figure 23: Comparison of experimental data of saturated densities to different models: —— experiment (cf. Table 37), – – – global correlation, cf. Chapter 3.2.2.2. • Simulation results from present models; error bars are, if not indicated, within symbol size. Results from models from the literature (cf. Table 14), top: □ R125 [120], △ R134a [222], bottom: + CO [18], □ CO [402], □ R32 [402], △ R32 [120], ▽ R152a [407], ◇ R152a [222], ○ R152a [189].

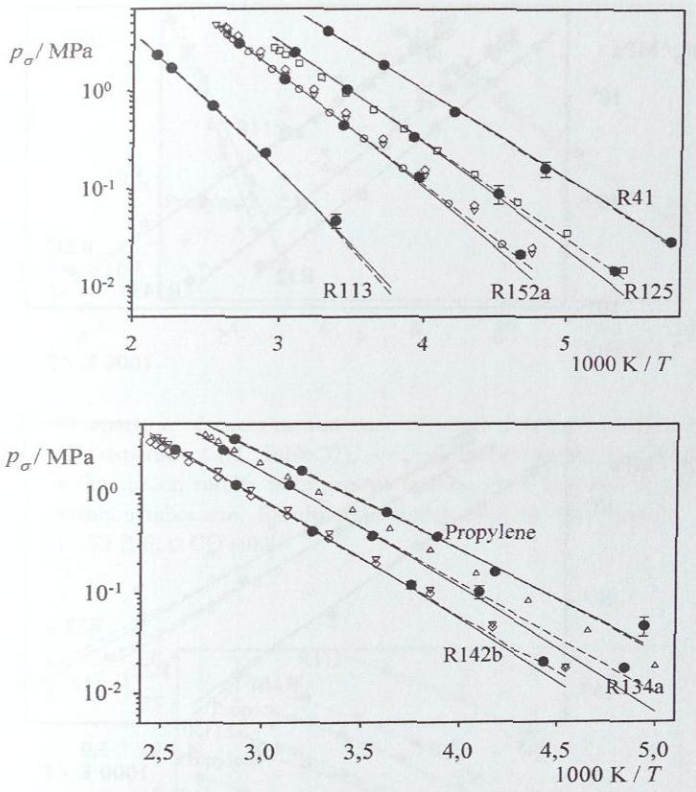

Figure 24: Comparison of experimental data of vapor pressures to different models: —— experiment (cf. Table 37), – – – global correlation, cf. Chapter 3.2.2.2. • Simulation results from present models; error bars are, if not indicated, within symbol size. Results from models from the literature (cf. Table 14), top: □ R125 [120], ▽ R152a [407], ◇ R152a [222], ○ R152a [189], bottom: △ R134a [222], ▽ R142b [222], ◇ R142b [120].

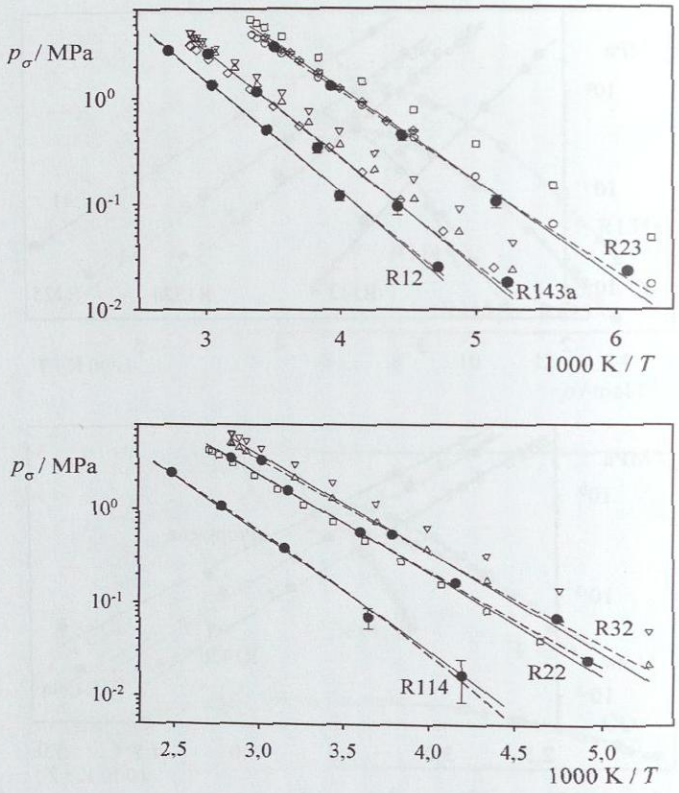

Figure 25: Comparison of experimental data of vapor pressures to different models: —— experiment (cf. Table 37), – – – global correlation, cf. Chapter 3.2.2.2. • Simulation results from present models; error bars are, if not indicated, within symbol size. Results from models from the literature (cf. Table 14), top: □ R23 [402], ○ R23 [120], ▽ R143a [402], ◇ R143a [120], △ R143a [222], bottom: □ R22 [189], ▽ R32 [402], △ R32 [120]; error bars are indicated, if data is given in the literature.

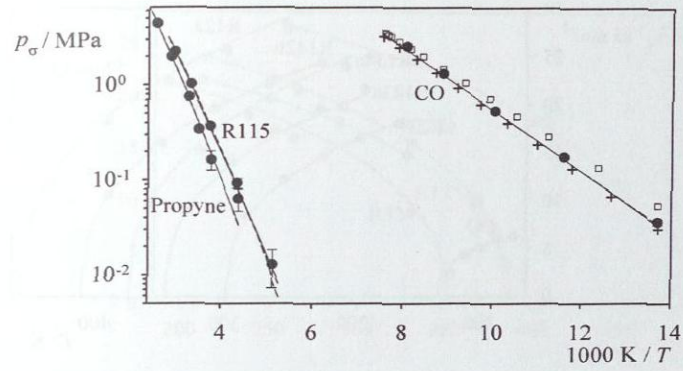

Figure 26: Comparison of experimental data of vapor pressures to different models: —— experiment (cf. Table 37), – – – global correlation, cf. Chapter 3.2.2.2. • Simulation results from present models; error bars are, if not indicated, within symbol size. Results from models from the literature (cf. Table 14): + CO [18], □ CO [402].

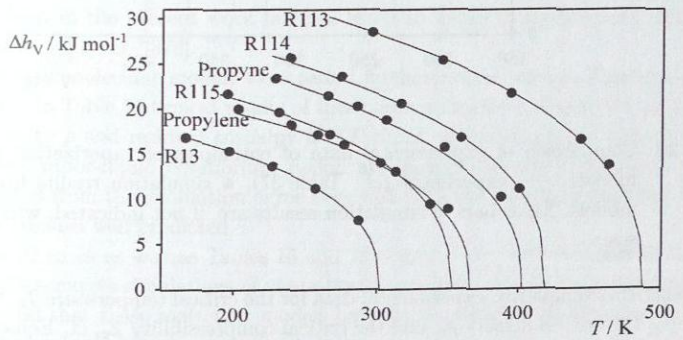

Figure 27: Comparison of experimental data of enthalpies of vaporization to present models: —— experiment (cf. Table 37), • simulation results from present models. Error bars of simulation results are, if not indicated, within symbol size.

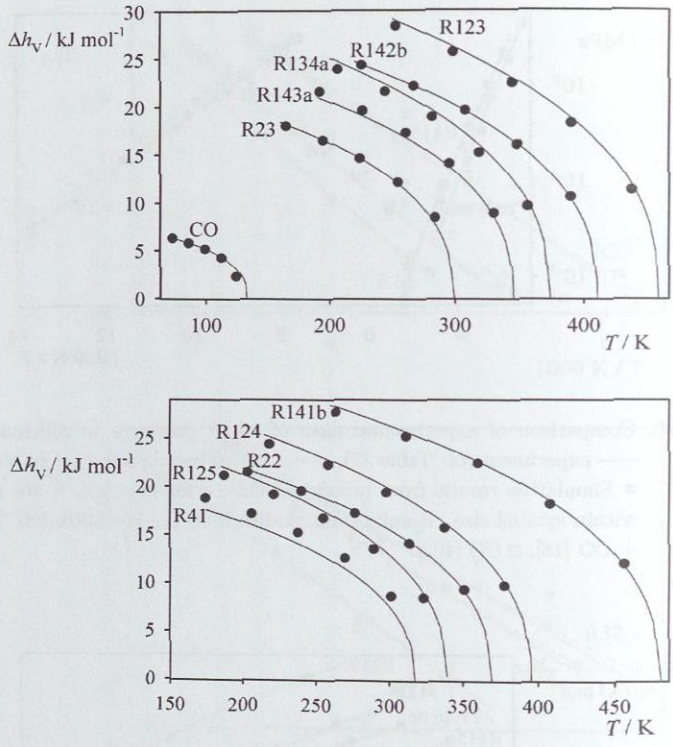

Figure 28: Comparison of experimental data of enthalpies of vaporization to present models: —— experiment (cf. Table 37), • simulation results from present models. Error bars of simulation results are, if not indicated, within symbol size.

In Table 15, exemplarily, experimental data for the critical temperature T_c, the critical pressure p_c, the critical density ρ_c, and the critical compressibility Z_c, cf. Equation (137), are compared to the results from the present molecular models using results of global correlations. Typical relative deviations between the critical data obtained from the molecular models and experimental data are about 3% for p_c, and 1–2% for ρ_c. Larger relative deviations for the critical pressure p_c occur for fluids that were modeled with the Stockmayer potential, for example R32, or those that are not well described with the 2CLJD/2CLJQ models, for example R23. The 2CLJD models from the present work describe the critical

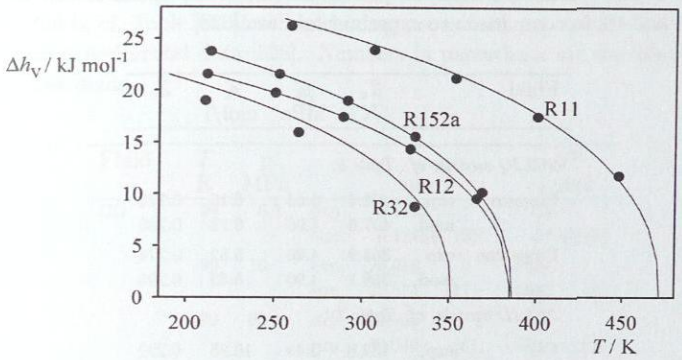

Figure 29: Comparison of experimental data of enthalpies of vaporization to present models: —— experiment (cf. Table 37), • simulation results from present models. Error bars of simulation results are, if not indicated, within symbol size.

temperature T_c with excellent accuracy, for example R22, R142b, R23, and R32. In the case of the 2CLJQ models, the relative deviations between the critical temperature from the model and the experimental data are typically about 1%. The remaining multipolar fluids modeled in the present work but not listed in Table 15 describe the critical data with similar quality, cf. [378].

The present molecular models were tested furthermore at various homogeneous fluid state points. In Table 16 typical results of these simulations are compared to experimental data of density ρ and residual enthalpy $h^{res}(T,p)$, cf. Equation (139). Also data points far from the vapor-liquid equilibrium region are included in the comparison. In most cases densities from the simulation agree very well with the experimental data. Residual enthalpies are also well predicted.

Figures 22 to 29 as well as Tables 15 and 16 demonstrate, that the present molecular models allow accurate simulations of vapor-liquid equilibria of pure fluids with multipolar molecules and that these molecular models have good predictive power also for thermophysical properties in homogeneous fluid states.

Table 15: Critical properties from the present models of multipolar fluids, cf. Tables 9 and 10, in comparison to experimental data [328].

Fluid		T_c K	p_c MPa	ρ_c mol/l	Z_c
2CLJQ models, cf. Table 9:					
Propyne	exp.	402.4	5.63	6.10	0.275
	mod.	407.6	5.96	6.18	0.285
Propylene	exp.	364.9	4.60	5.52	0.274
	mod.	368.1	4.90	5.43	0.295
2CLJD models, cf. Table 10:					
CO	exp.	132.8	3.49	10.85	0.292
	mod.	132.8	3.41	10.96	0.282
R22	exp.	369.3	4.99	6.06	0.268
	mod.	369.3	4.87	5.95	0.267
R23	exp.	299.1	4.84	7.50	0.259
	mod.	299.1	4.31	7.45	0.232
R32	exp.	351.3	5.78	8.15	0.243
	mod.	351.3	4.98	8.09	0.211
R113	exp.	487.2	3.39	2.99	0.280
	mod.	492.1	3.50	3.03	0.282
R114	exp.	418.8	3.26	3.39	0.276
	mod.	421.4	3.30	3.36	0.281
R115	exp.	353.1	3.12	3.97	0.268
	mod.	354.9	3.17	3.82	0.281
R125	exp.	339.2	3.62	4.78	0.269
	mod.	340.4	3.60	4.72	0.270
R134a	exp.	374.2	4.06	5.02	0.260
	mod.	375.3	4.02	4.98	0.259
R142b	exp.	410.3	4.07	4.44	0.269
	mod.	410.3	3.85	4.36	0.259
R143a	exp.	345.9	3.76	5.13	0.255
	mod.	347.8	3.88	5.11	0.263
R152a	exp.	386.4	4.52	5.57	0.252
	mod.	388.3	4.55	5.56	0.254

Table 16: Results from NpT simulations with the present 2CLJD models of multipolar fluids, cf. Table 10, at various homogeneous fluid state points and comparison to experimental data [328]. Numbers in parenthesis are uncertainties of the last digits.

Fluid	T K	p MPa		ρ mol/l		h^{res} J/mol	
CO	99	0.1	exp.	0.1242		-52	
			sim.	0.12464	(0)	-57.4	(13)
	99	10	exp.	26.616		-5404	
			sim.	26.571	(11)	-5382	(2)
	99	60	exp.	29.990		-4331	
			sim.	30.049	(6)	-4338	(2)
	400	1	exp.	0.2999		-35	
			sim.	0.30006	(0)	-37.5	(16)
	400	10	exp.	2.9020		-294	
			sim.	2.8962	(14)	-269.2	(20)
	400	60	exp.	12.844		-361	
			sim.	12.678	(6)	-292	(4)
R13	226	0.1	exp.	0.0544		-144	
(CF_3Cl)			sim.	0.05502	(0)	-168.4	(51)
	226	10	exp.	13.677		-14152	
			sim.	13.636	(6)	-14094	(7)
	226	30	exp.	14.337		-13457	
			sim.	14.375	(6)	-13427	(7)
	403	1	exp.	0.3086		-405	
			sim.	0.3098	(4)	-436.6	(40)
	403	10	exp.	4.1312		-4606	
			sim.	4.092	(10)	-4549	(15)
	403	30	exp.	9.1263		-7636	
			sim.	9.034	(11)	-7637	(13)
R41	238	0.1	exp.	0.0516		-154	
(CH_3F)			sim.	0.05210	(0)	-159.2	(51)
	238	10	exp.	23.587		-15180	
			sim.	23.426	(11)	-15951	(8)
	238	50	exp.	25.370		-14436	
			sim.	24.975	(8)	-15248	(7)
	490	1	exp.	0.2488		-256	
			sim.	0.2498	(18)	-262.3	(31)
	490	10	exp.	2.8018		-2513	
			sim.	2.7505	(30)	-2129	(8)
	490	50	exp.	13.381		-7281	
			sim.	12.521	(14)	-6738	(12)

Table 16: continued.

Fluid	T K	p MPa		ρ mol/l		h^{res} J/mol	
R143a	258	0.1	exp.	0.0480		-233	
(CH_3–CF_3)			sim.	0.04856	(0)	-272.6	(55)
	258	10	exp.	13.199		-17657	
			sim.	13.199	(7)	-18094	(10)
	258	60	exp.	14.471		-15740	
			sim.	14.565	(5)	-16294	(8)
	610	1	exp.	0.1990		-286	
			sim.	0.20030	(0)	-352.4	(60)
	610	10	exp.	2.1060		-2694	
			sim.	2.0977	(29)	-2666	(11)
	610	60	exp.	8.4521		-6108	
			sim.	8.1768	(64)	-6098	(13)
R152a	289	0.1	exp.	0.0426		-211	
(CH_3–CHF_2)			sim.	0.04313	(0)	-243.5	(71)
	289	10	exp.	14.370		-19994	
			sim.	14.269	(7)	-20018	(8)
	289	50	exp.	15.463		-18689	
			sim.	15.380	(5)	-18757	(9)
	495	1	exp.	0.2513		-549	
			sim.	0.2535	(4)	-605.5	(64)
	495	10	exp.	3.5545		-6109	
			sim.	3.534	(11)	-5968	(23)
	495	50	exp.	10.843		-11673	
			sim.	10.611	(9)	-11511	(15)

4.4 Discussion of the Model Parameters

The parameters of the 2CLJQ/2CLJD models developed in the present work were adjusted to vapor-liquid equilibrium data only. No direct information on polar momenta or molecular geometry was included. It is therefore interesting to compare the results for the parameters Q, μ, and L to experimental data of quadrupole and dipole momenta and atom-atom distances. It is ovious that no exact matches can be expected from such a comparison. For example real polar momenta of molecules are state dependent, whereas in the present work effective state independent polar momenta are used, which were determined from vapor-liquid equilibrium data and, hence, reflect mainly liquid phase properties.

Table 17 shows that for the diatomic fluids fluorine, chlorine, bromine, iodine, oxygen, and nitrogen and for carbon dioxide, carbon disulfide, ethyne, and propadiene the param-

Table 17: Comparison of the model parameter Q to experimental data for the quadrupole momentum Q_{exp}. For C_2H_4 values of $|Q_{\text{exp}}|$ are obtained through $Q^2_{\text{exp}} = 2/3\left(Q^2_{\text{xx,exp}} + Q^2_{\text{yy,exp}} + Q^2_{\text{zz,exp}}\right)$ [94] with $Q_{\text{xx,exp}}$, $Q_{\text{yy,exp}}$, $Q_{\text{zz,exp}}$ from [132].

Fluid	$\|Q\|$ DÅ	$\|Q_{\text{exp}}\|$ DÅ	Refs.
F_2	0.89	0.45–1.5	[132]
Cl_2	4.24	3.23–5.5	[132]
Br_2	4.90	4.78	[132]
I_2	5.66	5.61	[132]
N_2	1.44	1.39–1.6, 0.8–2.05	[132, 431]
O_2	0.81	0.4, 0.32–1.90	[132, 431]
CO_2	3.79	1.64–4.87, 2.5–5.9	[132, 431]
CS_2	3.90	1.8–6.8	[132]
C_2H_6	0.83	0.41–3.2, 0.3–0.75	[132, 431]
C_2H_4	4.33	3.05–3.90, 1.3–4.0	[132, 431]
C_2H_2	5.07	3.0–8.4	[132]
Propadiene	5.16	4.17–7.3	[132]

eter Q is within the range of experimental quadrupole momenta. In the case of ethene, the parameter Q is only about 8 % higher than the largest value of the experimental quadrupole momentum.

For the diatomic fluids fluorine, chlorine, bromine, iodine, and nitrogen the parameter L agrees within 5 % to the experimental atom-atom distances, cf. Table 18. The parameter L of further quadrupolar molecules may conveniently be compared to their real geometries, cf. Table 18. For this purpose, average atom-atom distances are considered. For example, the distance of the sulfur atoms in carbon disulfide is about $2 \cdot 1.56$ Å $= 3.12$ Å [204], cf. top of Figure 30. The parameter $L = 2.6809$ Å of carbon disulfide has to be smaller than the sulfur-sulfur distance, as each of the Lennard-Jones sites in the 2CLJQ model has to account for one sulfur atom but also for "half" a carbon atom. In the case of ethyne, the carbon-carbon-distance of 1.36 Å [204] is close to its parameter $L = 1.30$ Å. For the planar geometric halogenated ethene derivatives similar considerations are possible. For example, by basic geometric calculations (cf. bottom of Figure 30) the average elongation of perfluoroethene can be estimated to $|\text{C}{=}\text{C}| + |\text{C}{-}\text{F}| \cdot \cos(\angle\text{FCF}/2) = 1.31$ Å $+ 1.31$ Å$\cdot\cos(114°/2) = 2.02$ Å [204] which compares fairly well to its parameter $L = 2.2394$ Å. In these considerations, carbon-hydrogen distances are not regarded, but carbon-halogen distances are taken into account, as the influence of bonded hydrogen atoms on the position of Lennard-Jones sites can be neglected, whereas the influence of bonded halogen atoms is important.

For ethane an acceptable description of the vapor-liquid equilibria could only be ob-

Table 18: Comparison of the model parameter L to experimental data of bond geometry.

Fluid	L Å	Bond geometry	Refs.
F_2	1.413	F–F: 1.435	[204]
Cl_2	1.982	Cl–Cl: 2.00	[204]
Br_2	2.178	Br–Br: 2.28	[204]
I_2	2.678	J–J: 2.66	[204]
N_2	1.046	N≡N: 1.0975	[389]
O_2	0.970	O–O: 1.208	[389]
CO_2	2.418	C=O: 1.15	[204]
CS_2	2.681	C=S: 1.56	[204]
C_2H_6	2.376	C–C: 1.55, C–H: 1.09	[204]
C_2H_4	1.269	C=C: 1.33, C–H: 1.06	[204]
C_2H_2	1.300	C≡C: 1.205, C–H: 1.06	[204]
C_2F_6	2.725	C–C: 1.57, C–F: 1.36, bond angle FCF: 108°	[204]
C_2F_4	2.239	C=C: 1.31, C–F: 1.31, bond angle FCF: 114°	[204]
C_2Cl_4	2.652	C=C: 1.38, C–Cl: 1.71, bond angle ClCCl: 116°	[204]

tained, when high numbers for either the parameter Q or the parameter L were accepted. The 2CLJQ potential model used in this work has no internal degrees of freedom. The unphysical values for these two parameters are needed in order to compensate for the energy stored in conformation changes of the methyl groups in real ethane molecules, that substantially influence the thermodynamics of fluid ethane. In the present work, a high value for the parameter L was accepted, thus arbitrarily representing mechanical energy of internal conformation changes by mechanical energy of external rotation of the molecule. The present parameter $L = 2.3762$ Å of ethane is considerably larger than the experimental carbon-carbon distance of 1.53–1.55 Å [204], which was used in the OPLS [164], TraPPE [254], and TraPPE-EH [48] force field parameters for ethane. The parameter Q of the present 2CLJQ model of ethane is in agreement with the experimental quadrupole momentum within the experimental uncertainty, cf. Table 17.

When average atom-atom distances are considered as described above, also the elongation $L = 2.7246$ Å of the perfluoroethane molecule with intramolecular rotation is oversized.

In analogy to the 2CLJQ modeling of ethane and perfluoroethane, large parameters L, i.e. reduced elongation L^* typically higher than 0.9, were accepted for the modeling of halogenated ethane derivatives among the fluids with multipolar molecules in order to compensate for neglecting the intramolecular rotation.

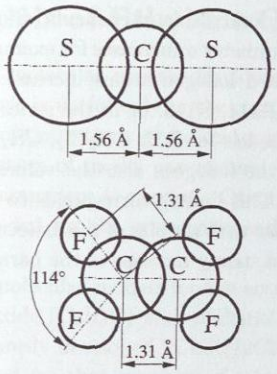

Figure 30: Bond lengths and molecular geometry for carbon disulfide and perfluoroethene, *cf.* Table 18.

In general, the parameters μ of the present 2CLJD models for fluids with multipolar molecules are larger than the corresponding experimental gas phase dipole momenta μ_{exp}. This may be explained by the fact, that the parameter μ must account for polarization effects in the liquid phase, where dipole momenta are usually higher, and that the dipole often has to compensate for higher polarities that were not modeled explicitly. In some cases, fair to good agreement between μ and μ_{exp} can be observed, for example for R41 (μ=1.89 D, μ_{exp}=1.98 D [328]), R143a (μ=2.75 D, μ_{exp}=2.34 D [328]), R152a (μ=2.74 D, μ_{exp}=2.26 D [328]), CH_3Cl (μ=2.02 D, μ_{exp}=1.8 D [321]), CH_3Br (μ=1.85 D, μ_{exp}=1.81 [67]), and $CHF{=}CH_2$ (μ=1.66 D, μ_{exp}=1.43 D [67]).

The modeling of carbon monoxide with a two-center Lennard-Jones based model is reasonable. Carbon monoxide is slightly dipolar, $\mu_{exp} \approx 0.1$ D, and has a quite strong quadrupole momentum $Q_{exp} \approx 2$ DÅ [132]. In Table 10 a 2CLJD model is given for carbon monoxide. It gives slightly better results than the also very accurate 2CLJQ model given in Table 9, whose parameter Q is close to Q_{exp}. As expected, the parameter μ of the 2CLJD model is higher than μ_{exp}. However, in both cases, the model parameter L is very close to the C-O bond length of 1.128 Å, cf. [64].

In the following, a brief discussion of the physical interpretation of the size parameters σ and the energy parameters ε is given.

Generally, for larger groups of bonded atoms in molecules larger numbers for σ can be expected, as is seen by a comparison of the size parameters σ of ethene, perfluoroethene, and perfluoroethane, cf. Table 8. In the case of the noble gases neon, argon, krypton, and xenon or the halogens fluorine, chlorine, bromine, and iodine the values for σ increase with the molecular mass. This finding corresponds to the increase of van der Waals' radii

from top to bottom in the periodic table of elements. Similar rules apply to asymmetric multipolar molecules. The parameter σ increases for example in the following series, where the size and number of bonded halogen atoms increase: R152a, R143a, R134a, R125, R142b, R141b, R123, R115, R114, R113, or in the series R41, CH_3Cl, CH_3Br, CH_3I, or in the series of Stockmayer models for R32, CH_2Cl_2, CH_2Br_2, CH_2I_2, cf. Table 10.

For the noble gases and the halogens also the values for ε increase with increasing molecular mass, cf. Table 8. This finding corresponds to the empirical rule, that van der Waals dispersion forces increase with the size of the molecule. Also in the above mentioned series of Stockmayer models a steady increase of the parameter ε is observed.

5 Molecular Models of Ethylene Oxide and Methanol

The approach for optimizing molecular models developed in the previous chapters and used for 2CLJQ/2CLJD models is useful only in the case of one or two adjustable model parameters. Such grid based optimizations of molecular models become computationally too expensive for higher numbers of model parameters. For most real fluids, however, a higher number of model parameters is needed. Other routes than that proposed in the previous chapters are needed for the systematic and efficient optimization of such molecular models.

In this chapter, effective molecular models for the accurate description of the vapor-liquid equilibria of ethylene oxide (C_2H_4O) and methanol (CH_3OH) are developed, that are compatible with the previously developed 2CLJQ/2CLJD models. A fast converging optimization method is applied for that purpose, cf. Appendix I. Ethylene oxide and methanol were ideal candidates for continuing the work on molecular modeling of low-molecular real fluids. Both are important basis chemicals. From the modeling point of view, they are examples for more complex real fluids, that need tailored molecular models, whose parametrization yet still allows the transfer of knowledge gained in the 2CLJQ/2CLJD modeling approach.

In the case of ethylene oxide, a rigid, effective, non-polarizable molecular model consisting of three Lennard-Jones sites plus a central point dipole is constructed. Using molecular structure data and results from the previous modeling of classes of real fluids, the number of model parameters which have to be optimized is reduced to three.

The model of methanol is an asymmetric, rigid, effective, non-polarizable two-center Lennard-Jones model with partial charges, that, as described in Chapter 2.1, account for polarities and hydrogen bonding. The methanol model developed here can be considered as an optimized version of the model proposed in [404]. Similar to ethylene oxide, also for methanol three model parameters were subject to optimization.

Results for the new models are presented in Chapters 5.1 and 5.2.

5.1 Ethylene Oxide

The ethylene oxide molecule consists of two CH_2-groups, bound to each other directly and via an oxygen atom. This bonding situation allows only little intramolecular torsion, therefore a rigid molecular model is adequate. Applying the united-atom modeling approach, each CH_2-group and the oxygen atom were modeled by a Lennard-Jones interaction site, cf. Figure 31. This basic structure leads to six model parameters l_1, l_2, σ_{CH_2}, ε_{CH_2}, σ_O, and ε_O. The interaction of the Lennard-Jones sites is described in Appendix A.1.

Several alternatives are possible for modeling the multipolarity of the molecule, caused by the polarity of the C–O-bonds, among those are: several partial charges; a point dipole along the axis a (*cf.* Figure 31) plus a point quadrupole parallel to the axis b, both located in the center of mass; a single point dipole along axis a, located in the center of

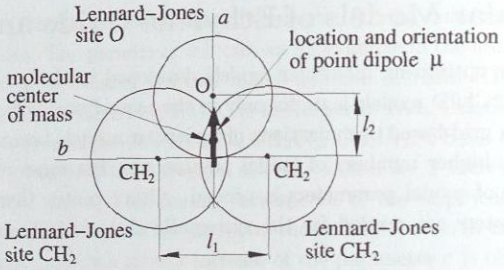

Figure 31: Structure of the molecular model of ethylene oxide.

mass; a single point quadrupole along axis b, located in the center of mass. Due to the neutrality of the molecule, point charges would involve a single parameter, if they were placed on the locations of the Lennard-Jones sites, and they would model the multipolarity in detail. However, the use of partial charges is considered here more appropriate for hydrogen bonding substances, cf. the modeling of methanol in Chapter 5.2. Moreover, the calculation of the configurational part of the chemical potential for models with partial charges requires high efforts, that should be avoided whenever possible. The results from the 2CLJQ/2CLJD-modeling indicate, that a single point dipole located in the center of mass should be sufficient for modeling the multipolarity, and was therefore chosen here, cf. Appendix A.3 for the interaction between point dipoles. The model then has seven parameters l_1, l_2, σ_{CH_2}, ε_{CH_2}, σ_O, ε_O, and the dipole momentum μ.

For a reasonable optimization, the number of adjustable model parameters had to be reduced. Experimental data on the molecular structure [204] was adopted to specify the geometry parameters $l_1 = 1.56$ Å and $l_2 = 1.22$ Å. This direct use of the geometric data is motivated by the results for the 2CLJQ models discussed in Chapter 4.4. The Lennard-Jones parameters for the CH_2-groups, σ_{CH_2} and ε_{CH_2}, were optimized, whereas those for the oxygen atom, σ_O and ε_O, were coupled to them by constant factors f_σ and f_ε

$$\sigma_O = f_\sigma \cdot \sigma_{CH_2}, \tag{140}$$

$$\varepsilon_O = f_\varepsilon \cdot \varepsilon_{CH_2}, \tag{141}$$

that were set equal to the proportions of the Lennard-Jones size and energy parameters resulting from the 2CLJQ-modeling of ethylene ($CH_2 = CH_2$) and oxygen (O_2), cf. Table 8,

$$f_\sigma = \frac{\sigma_{O_2}}{\sigma_{\text{Ethylene}}}, \tag{142}$$

$$f_\varepsilon = \frac{\varepsilon_{O_2}}{\varepsilon_{\text{Ethylene}}}. \tag{143}$$

The dipole momentum μ was subject to optimization, as, according to the 2CLJD-modeling, model dipole momenta are essentially higher than dipole momenta measured in the gas phase (1.89 D for ethylene oxide [204]).

Correlations of experimental data of the saturated liquid density [67] and the vapor pressure [329] were used for the optimization of σ_{CH_2}, ε_{CH_2}, and μ. The vapor-liquid equilibria were calculated with the NpT+Test Particle Method described in Chapter 2.5.1, based on molecular dynamics simulations and the test particle insertion method, cf. Chapter 2.4. All molecular simulations were performed with 864 particles and cut-off radii of 18.8 Å. After each time step, 1,728 test particles were inserted in the liquid phase, and 864 test particles were inserted in the vapor phase. The fluids were equilibrated over 5,000 time steps, and sampling was done over 150,000 time steps, the time steps was 4.696 fs.

The critical data of ethylene oxide are $T_{c,exp} = 469.15$ K, $p_{c,exp} = 7.194$ MPa, $\rho_{c,exp} = 7.128$ mol/l [67]. For the optimization, vapor-liquid equilibria were calculated for temperatures from 290 K up to 440 K, i.e. between about 60% and about 95% of $T_{c,exp}$.

Vapor-liquid equilibria of the optimized model ($\sigma_{CH_2} = 3.5673$ Å, $\sigma_O = 2.9464$ Å, $\varepsilon_{CH_2}/k_B = 86.3938$ K, $\varepsilon_O/k_B = 48.4823$ K, $\mu = 2.5703$ D) are shown in Table 19 and Figure 32. The optimized model describes the vapor pressure p_σ and the saturated liquid density ρ' with mean relative deviations according to Equations (135) and (136) of $\overline{\delta p_\sigma} = 6.5$ %

Table 19: Comparison of experimental data [67] of vapor pressure, saturated liquid density, and enthalpy of vaporization to results from the optimized molecular model of ethylene oxide. No experimental data is available for saturated vapor densities. The numbers in parentheses indicate the uncertainties of the last digits.

T K	$p_{\sigma,sim}$ MPa	$p_{\sigma,exp}$ MPa	ρ'_{sim} mol/l	ρ'_{exp} mol/l	ρ''_{sim} mol/l	$\Delta h_{v,sim}$ kJ/mol	$\Delta h_{v,exp}$ kJ/mol
290	0.130 (13)	0.130	19.8523 (50)	19.842	0.0573 (38)	24.778 (54)	25.37
302.5	0.223 (13)	0.203	19.4401 (50)	19.435	0.109 (14)	23.852 (55)	24.69
315	0.286 (21)	0.335	19.0200 (60)	19.015	0.118 (11)	23.823 (59)	23.98
327.5	0.479 (22)	0.443	18.5912 (66)	18.614	0.200 (11)	22.823 (71)	23.23
340	0.647 (19)	0.625	18.1189 (78)	18.125	0.2633 (94)	22.221 (73)	22.43
352.5	0.820 (25)	0.880	17.6606 (88)	17.593	0.325 (12)	21.555 (78)	21.59
365	1.146 (31)	1.153	17.1729 (92)	17.153	0.458 (16)	20.552 (82)	20.69
377.5	1.409 (39)	1.516	16.609 (10)	16.627	0.551 (21)	19.741 (87)	19.71
390	1.958 (29)	1.957	16.088 (13)	16.065	0.796 (17)	18.472 (96)	18.65
402.5	2.393 (46)	2.533	15.469 (14)	15.459	0.968 (29)	17.469 (97)	17.48
415	3.045 (34)	3.223	14.789 (16)	14.793	1.283 (25)	16.01 (12)	16.17
427.5	*3.743 (41)*	*3.783*	*14.040 (19)*	*14.043*	*1.635 (37)*	*14.51 (34)*	*14.65*
440	4.718 (38)	4.697	13.216 (23)	13.162	2.249 (39)	12.5 (16)	12.81

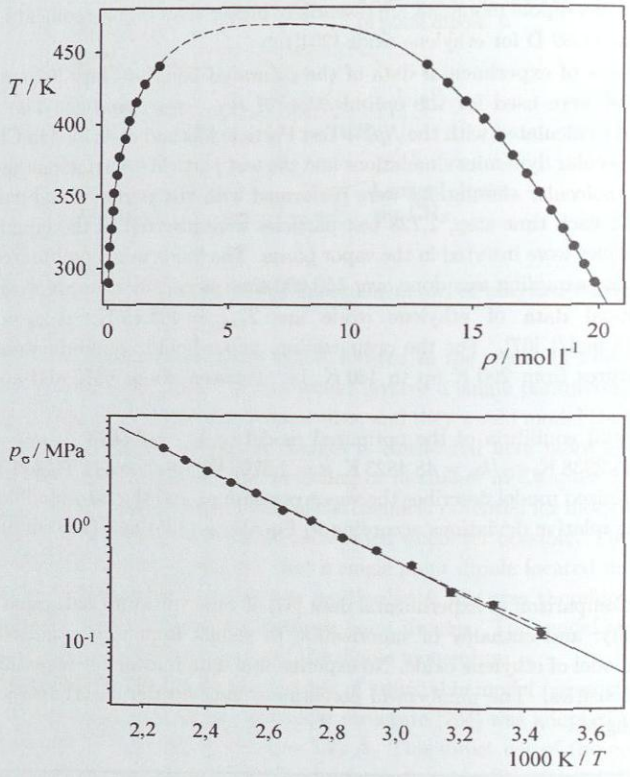

Figure 32: Comparison of experimental data of saturated densities (top) and vapor pressure (bottom) to simulation results for ethylene oxide. —— Experiment [67]. ● Simulation with optimized molecular model. – – – Correlations of simulation results. Error bars of simulation results are, if not indicated, within symbol size.

and $\overline{\delta\rho'} = 0.17$ %. The somewhat high mean relative deviation of the vapor pressure is due to the scattering of the simulated vapor pressure data. Nonetheless, the vapor pressure is described with good accuracy, as shows the smoothening correlation of the vapor pressure data in Figure 32. The description of the saturated liquid density is excellent. Moreover, the critical temperature $T_c = 468.43$ K, critical density $\rho_c = 7.241$ mol/l, and critical pressure $p_c = 7.170$ MPa of the optimized model are very close to the experimental

critical data. Also the enthalpies of vaporization, cf. Table 19, are described within 3%.

5.2 Methanol

The methanol molecule consists of a CH_3-group bound to an OH-group. It is multipolar and hydrogen bonding.

In the works of Walser et al. [424] and van Leeuwen and Smit [404] overviews on molecular models of methanol are given, and new three-site united-atom models with point charges are presented. In the present work, the model of methanol developed by van Leeuwen and Smit [404] for the description of vapor-liquid equilibria, here referred to as model M_0, is used as initial model for optimization.

The effective, rigid, united-atom model M_0 consists of two different Lennard-Jones sites that model the methylene group CH_3, with the parameters $\sigma_{CH_3} = 3.740$ Å and $\varepsilon_{CH_3}/k_B = 105.2$ K, and the oxygen atom, with the parameters $\sigma_O = 3.030$ Å and $\varepsilon_O/k_B = 86.5$ K, cf. Figure 33. Two point charges, $q_{CH_3} = 0.265\,e$ and $q_O = -0.7\,e$, are located directly on the Lennard-Jones sites, another one, $q_H = 0.435\,e$, that models the H-atom, is located acentrically. For intramolecular bond lengths and bond angles van Leeuwen adopted the experimental gas phase values $l_{CH_3-O} = 1.4246$ Å, $l_{O-H} = 0.9451$ Å, and $\alpha_{CH_3-O-H} = 108.53°$.

The interactions between Lennard-Jones sites are described in Appendix A.1, and the expressions for the interactions between sets of point charges are given in Appendix A.4.

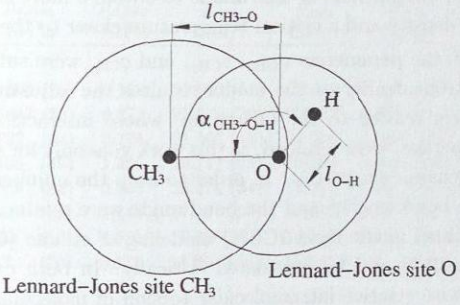

Figure 33: Structure of the molecular model of methanol.

Van Leeuwen and Smit [404] calculated vapor-liquid equilibria of the model M_0 by the means of the Gibbs Ensemble Monte Carlo simulation technique with 216 molecules, handling the long-range corrections of the partial charges with Ewald summation [114]. The results of van Leeuwen and Smit, cf. Figure 34, though subject to large scattering, show a good agreement with the vapor-liquid equilibrium data for methanol.

For a clearer view on the performance of the model $\boldsymbol{M}_0$, vapor-liquid equilibria with very small statistical uncertainties were calculated in the present work by the means of the NpT+Test Particle Method based on accurate data of the configurational part of the chemical potential in the liquid phase from the gradual insertion method. The configurational part of the chemical potential in the vapor phase was calculated with the test particle insertion method. Technical details of these simulations are given in Appendix C.3.

The present results for model $\boldsymbol{M}_0$ are given in Table 20 and are shown in Figure 34. Compared to the results of van Leeuwen [403], the present statistical uncertainties of the vapor pressure and the saturated liquid density are about an order of magnitude lower. Therefore, the vapor-liquid equilibrium data from the present work allow a reevaluation of the performance of model $\boldsymbol{M}_0$. The model $\boldsymbol{M}_0$ yields already a good description of the vapor-liquid equilibria of methanol. The mean relative deviation of the vapor pressure according to Equation (136) is $\overline{\delta p_\sigma} = 7$ %. However, for temperatures above 370 K the saturated liquid densities are somewhat too low, therefore the mean relative deviation of the saturated liquid density according to Equation (135) is $\overline{\delta \rho'} = 2.6$ %. Consequently, the critical temperature $T_{\mathrm{c,sim}} = 509.8$ K of model $\boldsymbol{M}_0$ obtained from correlation of present saturated density data with Equations (123) and (124), is lower than the experimental value $T_{\mathrm{c,exp}} = 512.6$ K [321].

The very low statistical uncertainties of the vapor-liquid equilibria obtained in the present work allow the fine tuning of the parameters of the model $\boldsymbol{M}_0$ by the means of the method described in Appendix I. The aim is to obtain a more accurate description of the saturated liquid density and a critical temperature closer to the experimental value.

For that purpose, the parameters $\sigma_{\mathrm{CH_3}}$, $\varepsilon_{\mathrm{CH_3}}$, and $q_{\mathrm{CH_3}}$ were subject to optimization. Note, that the electroneutrality of the model requires the adjustment of q_{O}, if $q_{\mathrm{CH_3}}$ is modified. Parameters related to the OH-group, whose interactions strongly influence thermodynamic properties, were retained, as this work goes only for small and controllable changes of thermodynamic properties. In order to keep the number of adjustable model parameters low, the bond lengths and the bond angle were retained. Note, that in light of the experience gained in the rigid 2CLJQ modeling of ethane ($\mathrm{CH_3-CH_3}$), retaining the C–O bond length should be considered critically. In both cases, a rigid model is used for molecules with relative intramolecular torsion of molecular groups. In the case of the ethane molecule, the C–C bond allows relative intramolecular torsion of the two $\mathrm{CH_3}$-groups. Consequently, for obtaining good accuracy of vapor-liquid equilibria, the elongation of the rigid 2CLJQ model of ethane had to be essentially larger than the real C–C bond length. In analogy, the C–O bond of the methanol molecule allows relative intramolecular torsion of the $\mathrm{CH_3}$- and the OH-group. Hence, this analogy would justify to choose the distance of the two Lennard-Jones sites in the rigid methanol model larger than the real C–O bond length.

The optimization yielded the model $\boldsymbol{M}_{\mathrm{opt}}$ ($\sigma_{\mathrm{CH_3}} = 3.7527$ Å, $\varepsilon_{\mathrm{CH_3}}/k_{\mathrm{B}} = 117.81$ K,

$q_{CH_3} = 0.25174e$), cf. Table 20 for the vapor-liquid equilibrium data. As can be seen in Table 20 and in Figure 34, the model M_{opt} describes the saturated liquid densities with better accuracy ($\overline{\delta\rho'} = 0.56$ %) than model M_0. Hence, the critical temperature of model M_{opt} ($T_c = 511.6$ K) is closer to the experimental value. The reduction of the mean relative deviation in the representation of the liquid density of about a factor of four was, however, only possible at the expense of a slight increase of the mean relative deviation in the representation of the vepor pressure by about 20% ($\overline{p_\sigma} = 9.9$ %). The slightly larger deviation of the vapor pressure of model M_{opt} from experiment is still tolerable. A better description of the vapor pressure without loosing quality in the description of the saturated liquid densities could not be obtained. Due to the analogy discussed above, subjecting also the C−O bond length to optimization might be a good starting point for achieving a more accurate representation of the vapor pressure. It was, however, not in the scope of the present work to handle another parameter for that purpose. Therefore, model M_{opt} was accepted as model of methanol that describes saturated liquid densities with very good accuracy.

Table 20: Comparison of experimental data [78] of vapor pressure and saturated liquid density to results from the molecular models M_0 and M_{opt} of methanol. No experimental data is available for the saturated vapor densities. The numbers in parentheses indicate the uncertainties of the last digits.

T	$p_{\sigma,sim}$	$p_{\sigma,exp}$	ρ'_{sim}	ρ'_{exp}	ρ''_{sim}	ρ''_{exp}
K	MPa	MPa	mol/l	mol/l	mol/l	mol/l
M_0						
350	0.1575 (23)	0.162	22.902 (17)	22.995	0.056 (1)	0.060
375	0.3647 (70)	0.375	21.970 (20)	22.152	0.134 (2)	0.134
400	0.792 (24)	0.774	21.007 (18)	21.206	0.296 (11)	0.273
425	1.466 (49)	1.456	19.747 (29)	20.106	0.547 (43)	0.524
450	2.555 (84)	2.543	18.274 (34)	18.765	0.85 (12)	0.963
465	3.32 (15)	3.446	17.137 (51)	17.782	0.95 (30)	1.357
480	5.20 (13)	4.571	16.006 (80)	16.575	2.39 (16)	1.913
490	6.17 (70)	5.473	14.89 (46)	15.544	5.7 (37)	2.512
M_{opt}						
325	0.0504 (19)	0.060	23.761 (23)	23.773	0.0197 (11)	0.023
365	0.2315 (37)	0.272	22.463 (19)	22.499	0.0839 (14)	0.098
405	0.833 (34)	0.884	20.910 (25)	21.000	0.306 (17)	0.312
445	2.128 (56)	2.287	18.946 (37)	19.059	0.786 (25)	0.856
475	3.97 (13)	4.169	16.823 (78)	17.011	1.71 (12)	1.699
490	5.47 (31)	5.473	15.60 (14)	15.544	2.73 (32)	2.512

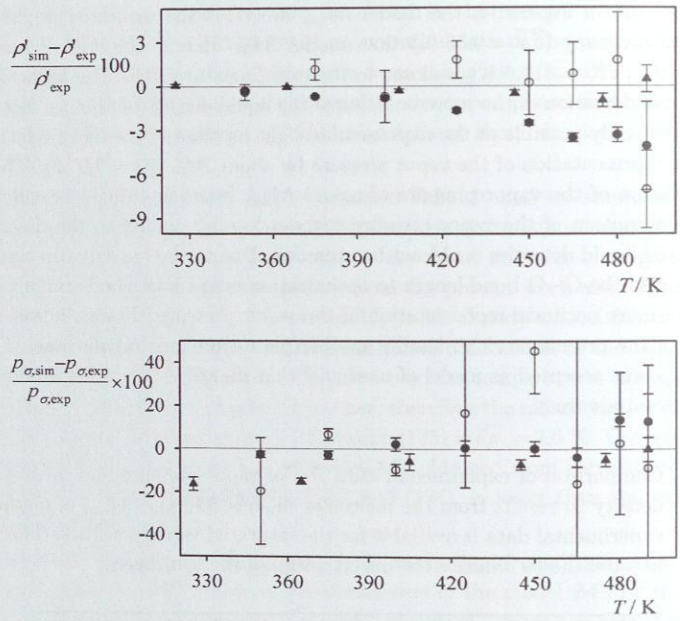

Figure 34: Vapor-liquid equilibria of methanol: relative deviation of simulation data (sim) to experiment [78] (exp). Top: saturated liquid density. Bottom: vapor pressure. Symbols for simulation data: ○ data from [403] with model M_0, • this work with model M_0, ▲ this work with model M_{opt}. Error bars of simulation results are, if not indicated, within symbol size.

In Table 21, densities of methanol in the homogeneous liquid phase obtained from the models M_0 and M_{opt} are compared to experimental data [78]. It can be seen, that the model M_{opt} describes the liquid densities with slightly better accuracy than the model M_0. The simulation data results from NpT Monte Carlo simulations with 864 molecules, cut-off radius 17.5 Å, 50,000 Monte Carlo loops for equilibration, 200,000 Monte Carlo loops for data production.

Table 21: Comparison of experimental data of densities in the homogeneous liquid phase [78] to results from the molecular models $\boldsymbol{M}_0$ and $\boldsymbol{M}_{\text{opt}}$ of methanol. The numbers in parentheses indicate the uncertainties of the last digits.

T	p	ρ		
K	MPa	mol/l		
		exp.	$\boldsymbol{M}_{\text{opt}}$	$\boldsymbol{M}_0$
190	0.1	27.787	27.858 (7)	27.947 (11)
210	0.1	27.164	27.258 (11)	27.387 (9)
247.15	0.1	26.038	26.134 (12)	26.182 (10)
285	0.1	24.925	24.964 (14)	24.988 (12)

6 Molecular Models of Mixtures

The application of molecular simulation to the description of vapor-liquid equilibria of real fluid mixtures requires compatible molecular models of the pure components. Obviously, the set of molecular models of pure real fluids developed in the present work is an excellent basis for the development of molecular models of a large number of real mixtures. Molecular models of 45 unlike interactions in real mixtures were developed in the present work. In this context, the literature survey in Table 22, that lists publications on thermophysical properties of real fluid mixtures from molecular simulation, shows, that the present work is the broadest one on molecular simulation applied to real fluid mixtures. The present work demonstrates, that molecular simulation is a powerful predictive tool for the description of thermophysical properties of real fluid mixtures.

Without considering real fluids, thermophysical properties of hypothetical binary and ternary mixtures of Lennard-Jones fluids were investigated in pioneering work [360, 361]. Such fluids are still commonly used to validate or apply new simulation methods [15, 23, 38, 39, 40, 142, 202, 203, 231, 324, 421]. Further authors investigated properties of mixtures of polar fluids [121, 342], or of polar and unpolar fluids [308], or focus on effects of three-body interactions or effects in ternary mixtures [341, 344]. Moreover, some authors studied such fluids to investigate mixing rules [49, 271, 396, 411], or vapor-liquid interfaces [267]. Simulation data for binary mixtures of 2CLJ and 2CLJQ fluids were used for the development of an equation of state [288].

Table 22 is related to molecular modeling of real mixtures. It shows, that most work was done on mixtures of a relatively narrow set of fluids – typically noble gases, methane, oxygen, nitrogen, carbon dioxide, n- and branched alkanes, methanol, and water. In many cases, the application of molecular simulation to real mixtures was aimed at the validation or comparison of molecular simulation methods, cf. [198, 218, 226, 398, 399, 446]. Other authors focused on the extension of molecular simulation methods to complex mixtures, cf. [26, 89], or applied molecular simulation to improve the understanding of particular mixtures, for example carbon dioxide + alkane/perfluoralkane [65]. Further works answered to the need of more accurate molecular models [47, 48, 73, 91, 295, 297, 323, 325, 331, 416, 434], or validated the predictive performance of existing molecular models, cf. [41, 42, 70, 71, 196, 246, 412]. A systematic study of phase equilibria from molecular simulation is available for alkanes [76].

Many of the results published in these works are in good agreement with experimental data, cf. for example [41, 42, 76, 198, 226, 218, 295, 325, 331, 416, 446], however, often large systematic deviations to experimental data, particularly of the liquid phase composition in calculations of vapor-liquid equilibria, are observed [47, 65, 70, 73, 76, 325]. Two causes for such deviations are discussed in literature:

(i) The inaccuracy of pure fluid models. Accurate and physically meaningful models of pure fluids are a prerequisite for obtaining quantitative results for mixtures.

Table 22: Literature survey: thermophysical properties of mixtures from molecular simulation.

Ref.	Systems
Mixtures containing noble gases	
[398]	Ar + Kr: bubble points (LJ, LB)
[265]	Ne + Ar, Ne + Kr, Ne + Xe, Ar + Kr, Ar + Xe, Kr + Xe: virial coefficients (nonc. approx. th.)
[440]	Ne + Xe, He + Ne, He + Ar, He + Xe: VLE (exp-6, LB)
[260]	binary mixtures of Ar, Kr, CH_4, N_2, O_2, CO: thermodynamic properties (LJ, LB)
[261]	binary mixtures of Ar, Kr, CH_4, N_2, O_2, CO: excess properties (LJ, LB)
[415], [416], [417]	mixtures of Ar, CH_4, C_2H_6, CO_2: VLE (LJ, LB with adjusted binary interaction parameters)
Mixtures of methane, ethane, carbon dioxide, nitrogen, ethene, propane, propylene, hydrogen, deuterium, oxygen, fluorine, chlorine, or bromine	
[446]	CH_4 + C_2H_6: VLE (LJ, LB)
[107]	CO_2 + C_2H_6: qualitative description of azeotropic behavior (LJ, adjusted unlike interaction parameters)
[217]	CO_2 + C_2H_6: excess properties (LJ, LB)
[41]	binary and ternary mixtures of N_2, CH_4, C_2H_6, CO_2: VLE (LJ, LB)
[198]	N_2 + C_2H_6: VLE (LJ, LB with adjusted binary interaction parameter)
[218]	CO_2 + C_2H_6, CH_4 + C_2H_6, CH_4 + CO_2, CH_4 + C_2H_6 + CO_2: VLE (LJ, LB with adjusted binary interaction parameters)
[325]	N_2 + CO_2, N_2 + CO_2 + propane: VLE (LJ, LB)
[42]	binary mixtures of CH_4, C_2H_6, C_2H_4, propylene: VLE, application of published models from present work [422] (LJ, LB)
[75]	binary mixtures of H_2, D_2, N_2, O_2, F_2, Cl_2: virial coefficients (nonc. approx. th.)
[225]	Br_2 + Cl_2 + BrCl: chemical and phase equilibria (LJ, LB)
Mixtures of refrigerants	
[119]	R22 + R142b, R22 + R152a: VLE (LJ, LB)
Mixtures containing n-alkanes, perfluoroalkanes, branched alkanes, benzene, cyclohexane	
[71]	CH_4 + *n*-pentane, CH_4 + *n*-dodecane: VLE (LJ, LB)
[399]	CH_4 + *n*-pentane, CH_4 + propane + *n*-pentane: bubble points (LJ, LB)
[397]	CO_2 + *n*-decane: VLE (LJ, LB)
[323]	CH_4 + *n*-pentane, CO_2 + C_2H_6/propane/*n*-pentane: VLE (exp-6, LB and Kong)
[48]	C_2H_6 + *n*-heptane: VLE (LJ, LB)

Table 22: continued

Ref.	Systems
[253]	C_2H_6 + *n*-heptane, *n*-octane + *n*-dodecane: VLE (LJ, LB)
[331]	N_2 + butane: VLE (LJ, LB)
[65]	CO_2 + alkane/perfluoroalkane: VLE (LJ, LB)
[91]	binary mixtures of *n*-alkanes: VLE (LJ and exp-6, LB)
[297]	binary mixtures of *n*-alkanes: VLE (LJ, LB)
[295]	binary mixtures of branched alkanes: VLE (LJ, LB)
[434]	C_2H_4 + *n*-heptane, benzene + *n*-pentane: VLE (LJ, LB)
[76]	CH_4 + *n*-pentane, CH_4 + cyclohexane, CH_4 + benzene: VLE (LJ, LB and OPLS)
[246]	CH_4 + *n*-pentane, CH_4 + *n*-dodecane: VLE (LJ, LB)
	Mixtures containing methanol, ethanol, water, or H_2S
[130]	CH_3OH + C_2H_6: VLLE (LJ, LB)
[383]	CH_3OH + acetonitrile: VLE (ab-in.)
[47]	CH_3OH + *n*-hexane, ethanol + *n*-hexane: VLE (LJ, LB)
[226]	binary mixtures of CH_3OH, isobutene, *n*-butane, MTBE: VLE (LJ, OPLS)
[227]	CH_3OH + isobutene + MTBE: reaction and phase equilibria (LJ, OPLS)
[228]	binary mixtures of CH_3OH, ethanol, H_2O, CO_2, C_2H_6: VLE (LJ, LB and OPLS)
[196]	CH_3OH + H_2O + CO_2: VLE (LJ, LB and OPLS)
[323]	CH_3OH, H_2O + C_2H_6 + CO_2, CH_3OH + *n*-hexane: VLE (exp-6, LB and Kong)
[412]	H_2O + CO_2: VLE (LJ, LB and OPLS)
[89]	H_2O + CH_4, H_2O + C_2H_6: phase equilibria (LJ and exp-6, LB)
[26]	*n*-alkanes in water, water in *n*-hexane: Henry's law constants (exp-6, LB and Kong)
[73]	H_2S + *n*-pentane: VLE (LJ, LB)
[70]	H_2S + propane/*n*-pentane/*n*-decane, H_2S + CO_2: VLE (LJ, LB)
	Further multicomponent mixtures
[303]	natural gas (multicomponent mixtures): volumetric properties (LJ, LB)

The short-cut notations used in this Table are: "LJ" Lennard-Jones based models, "exp-6" Buckingham exponential-6 based models, "nonc. approx. th." nonconformal approximation theory, "ab-in." model based on ab-initio data, "LB" Lorentz-Berthelot combining rules, "OPLS" OPLS combining rules, "Kong" Kong combining rules, "VL(L)E" vapor-liquid(-liquid) equilibria, "MTBE" methyl tert-butyl ether.

(ii) The inadequacy of combining rules, cf. Chapter 6.1. The predictive qualities of different combining rules and their modification by the introduction of binary interaction parameters are controversially discussed in literature [65, 72, 323, 371], but no particular combining rules are presently generally accepted or generally ruled out, though Table 22 underlines, that the Lorentz-Berthelot combining rules are preferred by most authors.

Starting from the pure component models, the unlike Lennard-Jones interactions are modeled in the present work on the basis of the Lorentz-Berthelot combining rules, which are known to give good results in many cases [41, 42, 325]. Predictions of vapor-liquid equilibria from pure component data alone are studied, as well as the adjustment of one parameter in the energetic term of these combining rules to binary data. For that adjustment, a simple and efficient procedure is proposed. An alternative approach followed by some authors, for example [325], is to determine parameters of *pure* fluids by including *binary* data in the model development. This route allows to avoid the introduction of binary parameters for certain classes of mixtures, for example alkanes, but is not generally applicable.

Throughout this chapter, results from molecular simulation are compared to results from the Peng-Robinson equation of state [316]. In some cases, also results from the PC-SAFT equation of state [133] and the BACKONE equation of state [287, 430] are shown.

6.1 Unlike Interactions

On the basis of compatible molecular models of pure fluids, molecular modeling of binary mixtures of components a and b reduces to modeling the unlike interactions between unlike molecules. The electrostatic interactions between quadrupoles, dipoles, or point charges are physically defined, cf. Appendices A.2 to A.6, and, therefore, do not require any particular modeling. For the description of unlike Lennard-Jones interactions, the unlike Lennard-Jones interaction parameters σ_{ab} and ε_{ab} have to be determined from the parameters of the pure fluid models by the means of combining rules, like the Lorentz-Berthelot rules [12, 232, 250], the OPLS rules [164], the Kong rules [187], the Waldman-Hagler rules [423], or the Fender-Halsey rules [98]. As shown in Table 22, the Lorentz-Berthelot combining rules are generally preferred, and are used here as basis for the determination of σ_{ab} and ε_{ab}

$$\sigma_{ab} = (\sigma_a + \sigma_b)/2, \tag{144}$$

$$\varepsilon_{ab} = \sqrt{\varepsilon_a \cdot \varepsilon_b}. \tag{145}$$

Despite the simplicity of the effective molecular models developed in the present work, predictions based on Equations (144) and (145) are already in reasonable agreement with experimental data in many cases, as shown in the following chapters. The agreement with experimental data can be improved by introducing binary interaction parameters η and ξ

into Equations (144) and (145)

$$\sigma_{ab} = \eta \cdot (\sigma_a + \sigma_b)/2, \tag{146}$$

$$\varepsilon_{ab} = \xi \cdot \sqrt{\varepsilon_a \cdot \varepsilon_b}, \tag{147}$$

as was shown by Fischer et al. [109], and Vrabec and Fischer [415, 416] for the mixtures argon + methane, methane + carbon dioxide, methane + ethane, and ethane + carbon dioxide. These authors proposed to adjust ξ and η to molar excess enthalpies and molar excess volumes. In all cases they found that the value of η was very close to unity. Accordingly, Kronome et al. [198], published vapor-liquid equilibria of the mixture nitrogen + ethane obtained from molecular simulation with $\eta = 1$ and with $\xi = 0.9841$ adjusted to experimental vapor-liquid equilibrium data.

Consequently, it was considered reasonable in the present work to assume throughout

$$\eta = 1. \tag{148}$$

For each unlike Lennard-Jones interaction the value of ξ was obtained from fitting the equilibrium pressure of the model mixture to the experimental equilibrium pressure of a single state point. This approach was chosen based on results from a case study, in which for several isotherms and mixtures at given liquid phase compositions x, the sensitivities of the equilibrium pressure p and of the vapor phase composition y to variations of ξ around unity were investigated. It was found in all cases that the equilibrium pressure decreases almost linearly with increasing ξ, whereas the vapor phase composition shows only little sensitivity to variations of ξ. This behavior was exploited to determine the value of ξ. For this purpose, at a selected experimental vapor-liquid equilibrium state point $(p, T, x, y)_{\text{exp}}$ for each binary mixture, the vapor pressures for three different values of ξ close to unity were calculated. A linear fit $p(\xi) = a \cdot \xi + b$ was sufficient to describe these three data points with good accuracy. The value of ξ was then obtained from equating that fit to the experimental value of the equilibrium pressure p_{exp}. Criteria for choosing the experimental state points for the adjustment of ξ were: preferably equimolar liquid mixture and medium temperature.

Altogether, models for 45 unlike Lennard-Jones interactions in fluid mixtures were developed. The experimental data chosen for the adjustment of ξ and the resulting value of ξ are given in Table 23 for fluid mixtures of unpolar or quadrupolar components and in Tables 24 for fluid mixtures containing multipolar components. Data for mixtures containing the multipolar component propylene is discussed separately in Chapter 6.3.1. The work on mixtures containing multipolar components is focussed on cases that are interesting for industrial applications, like mixtures containing carbon monoxide or refrigerants. Mixtures, for which no or poor experimental data was available, were not considered in the present work. It is important to note, that the modeling of unlike interactions in mixtures containing tetrafluoromethane or tetrachloromethane, that were unphysically modeled as

Table 23: Binary interaction parameter ξ for mixtures of unpolar or quadrupolar components. Experimental data point (exp) used for the adjustment of ξ and result for that data point from simulation (sim) with adjusted ξ.

Mixture (1+2)	ξ	T K	$x_{1,\mathrm{exp}}$ mol/mol	p_{exp} MPa	p_{sim} MPa	$y_{1,\mathrm{exp}}$ mol/mol	$y_{1,\mathrm{sim}}$ mol/mol	Ref.
Ne + Ar	0.854	110.78	0.145	12.2	12.1	0.828	0.836	[379]
Ne + N_2	0.945	82.70	0.122	4.05	3.90	0.923	0.916	[33]
Ne + O_2	0.921	110.39	0.159	14.0	14.2	0.848	0.855	[380]
Ne + CO_2	1.124	273.15	0.038	8.84	8.84	0.445	0.466	[350]
Ar + Kr	0.989	88.06	0.647	0.083	0.075	0.978	0.995	[351]
Ar + CH_4	0.964	123.05	0.448	0.811	0.833	0.808	0.793	[355]
Ar + N_2	1.008	84.50	0.521	0.150	0.144	0.280	0.287	[212]
Ar + O_2	0.988	104.95	0.500	0.440	0.436	0.546	0.549	[57]
Ar + CO_2	0.999	253.15	0.095	6.14	5.96	0.548	0.572	[168]
Kr + Xe	0.989	200.64	0.463	2.07	2.11	0.787	0.813	[36]
Kr + CH_4	1.005	115.77	0.532	0.107	0.108	0.375	0.367	[37]
Kr + O_2	0.979	109.80	0.500	0.297	0.293	0.076	0.084	[97]
CH_4 + CO_2	0.962	230.00	0.318	5.57	5.61	0.764	0.769	[68]
CH_4 + C_2H_6	0.997	172.04	0.504	1.24	1.16	0.966	0.985	[433]
CH_4 + C_2H_4	1.022	160.00	0.476	0.851	0.853	0.954	0.955	[273]
N_2 + CH_4	0.958	140.00	0.301	2.19	2.24	0.685	0.702	[170]
N_2 + O_2	1.007	105.00	0.500	0.743	0.734	0.702	0.707	[81]
N_2 + CO_2	1.041	270.00	0.132	9.29	9.19	0.417	0.457	[369]
N_2 + C_2H_6	0.974	260.00	0.165	7.11	6.96	0.558	0.590	[131]
N_2 + C_2H_4	0.962	200.00	0.274	8.18	7.72	0.816	0.845	[131]
O_2 + CO_2	0.979	253.15	0.141	8.11	8.24	0.574	0.616	[113]
CO_2 + C_2H_6	0.954	263.15	0.425	2.90	2.95	0.514	0.517	[112]
CO_2 + CS_2	0.918	360.01	0.477	11.5	10.8	0.875	0.924	[330]
CO_2 + Cl_2	0.936	233.15	0.228	4.86	4.68	0.880	0.862	[173]
C_2H_4 + C_2H_6	1.037	208.40	0.556	0.497	0.490	0.684	0.700	[169]
C_2H_4 + C_2H_2	0.975	235.93	0.818	1.56	1.53	0.842	0.849	[152]
C_2H_6 + C_2H_2	0.968	277.59	0.859	3.20	3.11	0.789	0.785	[259]
C_2H_4 + CO_2	0.944	243.15	0.459	1.93	1.95	0.515	0.524	[275]
C_2F_6 + CO_2	0.867	227.60	0.511	0.911	0.923	0.344	0.341	[357]

2CLJQ test cases in Chapter 4, was not successful, cf. [378]. The point quadrupole fails in modeling the electrostatic interactions of these molecules.

Results for vapor-liquid equilibria, saturated densities and enthalpies of vaporization are shown in Chapter 6.2 for mixtures containing quadrupolar components, and in Chapter 6.3 for mixtures containing multipolar components. All vapor-liquid equilibria of mixtures were obtained from the Grand Equilibrium method as described in Chapter 2.5.2. Technical details of the simulations are given in Appendix C.4. The complete numerical simulation data set for all mixtures considered in the present work is available in [378].

It should be summarized, that the present modeling approach, that does not model explicitly molecular polarization, yielded very satisfactory description of experimental data

Table 24: Binary interaction parameter ξ for mixtures containing multipolar components. Experimental data point (exp) used for the adjustment of ξ and result for that data point from simulation (sim) with adjusted ξ. The 2CLJD model of carbon monoxide from Table 10 was used for mixtures containing carbon monoxide.

Mixture (1+2)	ξ	T K	$x_{1,\mathrm{exp}}$ mol/mol	p_{exp} MPa	p_{sim} MPa	$y_{1,\mathrm{exp}}$ mol/mol	$y_{1,\mathrm{sim}}$ mol/mol	Ref.
CH_4 + CO	1.003	123.4	0.64	0.988	0.969	0.2	0.204	[54]
CO + C_2H_6	1.017	223.15	0.138	4.137	4.104	0.789	0.796	[395]
CO + CO_2	1.080	243.14	0.139	7.706	7.516	0.666	0.675	[53]
N_2 + CO	1.007	83.82	0.445	0.167	0.174	0.56	0.544	[372]
R22 + CS_2	0.950	398.15	0.1669	2.79	2.676	0.6888	0.698	[336]
CO_2 + R22	1.006	273.15	0.4666	1.695	1.683	0.7963	0.788	[336]
CO_2 + R23	0.997	263.35	0.4172	2.292	2.290	0.4818	0.491	[336]
R143a + R134a	0.994	293.15	0.442	0.798	0.832	0.567	0.563	[214]
R125 + R143a	0.987	264.014	0.5026	0.466	0.500	0.5158	0.522	[291]
R125 + R134a	0.999	283.053	0.4928	0.659	0.662	0.65	0.638	[290]
R143a + R152a	1.023	293.15	0.437	0.804	0.713	0.639	0.585	[214]

of thermophysical properties over wide temperature ranges. This is particularly interesting in the case of mixtures containing strongly dipolar or polarizable components, like carbon disulfide + R22, cf. Chapter 6.3, or carbon dioxide + methanol, cf. Chapter 6.4. The modeling of molecular polarization is considered an important issue in literature, as illustrates the discussion on different modeling approaches for the mixture hydrogen sulfide + *n*-pentane [70, 73, 293]. In the work of Delhommelle et al. [70, 73], the explicit modeling of the molecular polarization is considered important for obtaining quantitative description of the vapor-liquid equilibria of that mixture from molecular simulation. Their results agree well with experimental data, if the pressure is not too high. In contrast, Nath [293] developed non-polarizable molecular models of these molecules and obtained better results from molecular simulation for higher pressures, but systematic deviations of the liquid phase composition occur. The present satisfactory results, that were obtained with simple, non-polarizable models, will contribute fruitfully to this discussion.

6.2 Binary Mixtures Containing Quadrupolar Components

Vapor-liquid equilibria, saturated liquid densities, and enthalpies of vaporization of binary mixtures of unpolar or quadrupolar components at different state points were calculated with the molecular models listed in Table 23. Five binary mixtures of the quadrupolar components nitrogen, oxygen, carbon dioxide, and ethane were studied in more detail, cf. Chapter 6.2.1, in order to demonstrate the performance of molecular simulation as

predictive and reliable tool for the calculation of thermophysical properties of fluid mixtures in comparison to results from equations of state. Results for further binary mixtures containing quadrupolar components are discussed in Chapter 6.2.2. The focus is on mixtures with non-spherical molecules, the excellent results for mixtures of simple spherical molecules, *like argon + krypton or neon + methane, are not shown, but are available in* [378].

6.2.1 Binary Mixtures of Nitrogen, Oxygen, Carbon Dioxide, and Ethane

The present simulation results for the binary mixtures nitrogen + oxygen, carbon dioxide + ethane, oxygen + carbon dioxide, nitrogen + carbon dioxide, and nitrogen + ethane are compared to simulation results from other authors, to experimental vapor-liquid equilibrium data, to results from the multiparameter equation of state from the program package DDMIX provided by the NIST [86, 88], and to results from the Peng-Robinson equation of state [316]. The acentric factor ω, the critical temperature T_c, and the critical pressure p_c of the pure fluids needed for calculations with the Peng-Robinson equation of state were taken from Reid et al. [321]. Additionally, results for vapor-liquid equilibria from the PC-SAFT [133] and the BACKONE equations of state [287, 430], that are based on theoretical principles accounting for molecular interactions, are discussed. The binary parameters k_{ij} of these three equations of state were adjusted to the same data that were used for the determination of the binary interaction parameter ξ of the molecular models, cf. Table 23. The values of the binary parameters k_{ij} are given in Table 25.

Table 25: Binary equation of state parameters k_{ij} for mixtures of nitrogen, oxygen, carbon dioxide, and ethane.

Mixture	Peng-Robinson	PC-SAFT	BACKONE
$N_2 + O_2$	−0.00978	−0.00160	−0.003
$CO_2 + C_2H_6$	0.13008	0.10289	0.0914
$O_2 + CO_2$	−0.04838	0.05929	−0.01
$N_2 + CO_2$	−0.01493	−0.01793	−0.04
$N_2 + C_2H_6$	0.05233	0.04313	−0.025

Two types of calculations were carried out for both the molecular simulation and the equations of state. One calculation was performed without using the adjusted binary parameter ξ or k_{ij}, i.e. a prediction of the properties of the mixture from pure component data alone, and the other using the binary parameters. *As the prediction from pure* component data alone is used only as reference, it was not carried out for all isotherms. The vapor-liquid equilibrium calculation was done at given temperature T and liquid phase composition x. Data on the vapor pressure p, vapor phase composition y, saturated

liquid density ρ', and enthalpy of vaporization Δh_V are reported.

6.2.1.1 Vapor-Liquid Equilibria

Nitrogen + Oxygen

Knowledge on vapor-liquid equilibria of this binary system is fundamental in various industrial applications such as air liquefaction and air separation. Figure 35 shows results from the present work for the equilibrium pressure and the vapor phase mole fraction for three isotherms. The results for the 105 K isotherm show that predictions from pure component data alone are already in very good agreement with the experimental data for that system, both for the molecular simulation and for the Peng-Robinson equation of state. Simulations with adjusted binary interaction parameter ξ excellently describe the experimental data. The Peng-Robinson equation of state also yields excellent results with or without adjusted binary parameter.

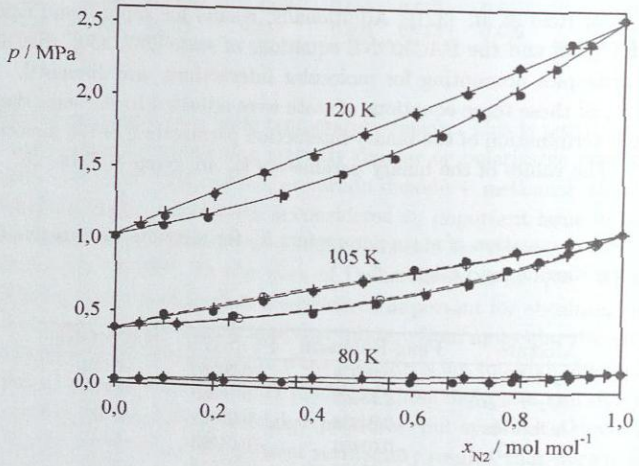

Figure 35: Vapor-liquid equilibria of the mixture N_2 + O_2. Simulation, this work: • (ξ adjusted), ○ ($\xi = 1$). Peng-Robinson equation of state: —— ($k_{ij} = -0.00978$), – – – ($k_{ij} = 0$). + Experiment [181].

Carbon Dioxide + Ethane

This mixture is important in the petrochemical industry. Due to its low boiling azeotrope, it has a more complex phase behavior than the system nitrogen + oxygen. For this system results for vapor-liquid equilibria from molecular simulation are available

from Liu and Beck [218] and from Potoff et al. [323]. Results from Gibbs Ensemble Monte Carlo simulations of Liu and Beck [218] and results from the present work are very similar. This could be expected as these authors used two-center Lennard-Jones type pure component models determined by Vrabec and Fischer [416] and Möller et al. [283] and Lorentz-Berthelot combining rules with two adjusted binary parameters η and ξ taken from [416]. Therefore, a direct comparison to results from Liu and Beck [218] is omitted here for brevity. Potoff et al. [323] performed grand canonical histogram-reweighting Monte Carlo simulations with computationally expensive exponential-6 type models with fixed partial charges and, in the case of ethane, intramolecular degrees of freedom [91]. The models used by Potoff et al. [323] were obtained from experimental pure substance vapor-liquid equilibrium data. Potoff et al. [323] performed simulations with the Lorentz-Berthelot and the Kong combining rules, without adjusting binary parameters.

In Figure 36 simulation results from the present work are compared to results from the Peng-Robinson equation of state and to simulation data from Potoff et al. [323] obtained with the Kong combining rules. Both Figures show, that even the purely predictive molecular simulations from the present work describe the azeotropic behavior. This is a clear advantage of molecular simulation over the Peng-Robinson equation of state, which predicts no azeotrope. The results of the sophisticated model of Potoff et al. [323] are in very good agreement with experimental data. A somewhat better accuracy is obtained using the model presented here with adjusted binary interaction parameter ξ.

Oxygen + Carbon Dioxide

Vapor-liquid equilibria of mixtures of oxygen and carbon dioxide are encountered in the petrochemical and food processing industries. Fluid phase equilibria in that system only exist at temperatures and pressures for which pure oxygen is supercritical, as the critical temperature of oxygen is lower than the triple temperature of carbon dioxide. No vapor-liquid equilibrium data from molecular simulation is available from other authors.

Results for phase diagrams of the mixture oxygen + carbon dioxide are shown in Figure 37. The prediction from molecular simulation without adjusting ξ is already in very good agreement with experimental data. In contrast, the prediction from the Peng-Robinson equation of state without using k_{ij} is poor for the bubble line. As long as the pressure is not too close to the critical pressure of the mixture, both methods with adjusted binary parameter are in fair agreement with experimental data. For this mixture, the average statistical uncertainties of the simulation data are quite large, they are about ± 0.35 MPa for the pressure and about ± 0.02 mol mol^{-1} for the vapor mole fraction. As shown in Figure 37, bottom, similar results were obtained for the 223.15 K and the 283.15 K isotherms.

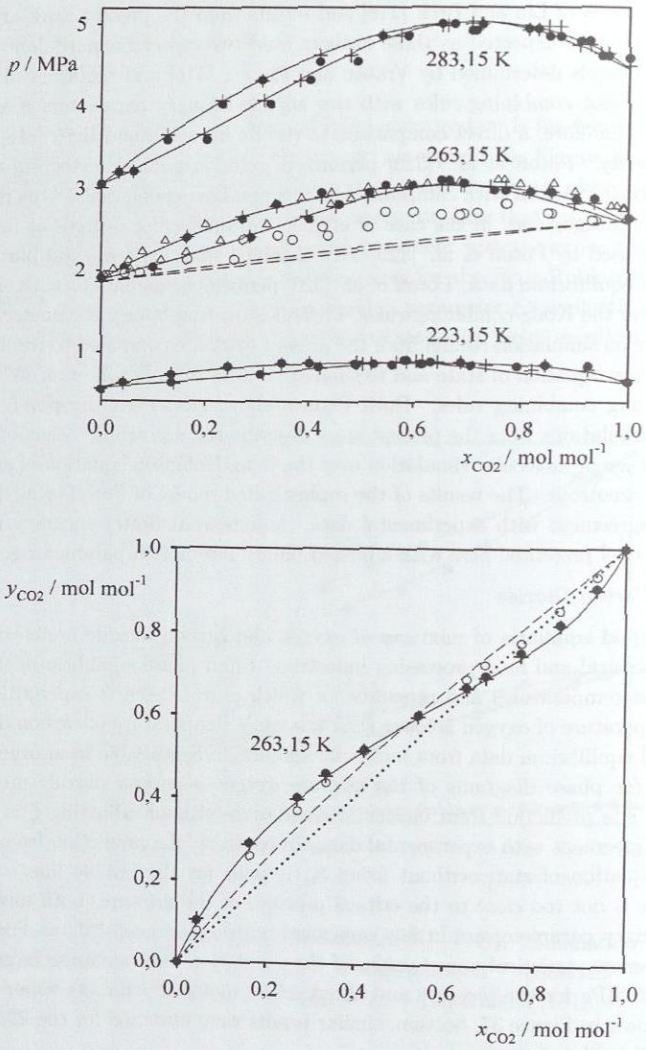

Figure 36: Vapor-liquid equilibria of the mixture CO_2 + C_2H_6. Simulation, this work: ● (ξ adjusted), ○ ($\xi = 1$). Simulation with Kong combining rules: △ [323]. Peng-Robinson equation of state: —— ($k_{ij} = 0.13008$), – – – ($k_{ij} = 0$). + Experiment [181].

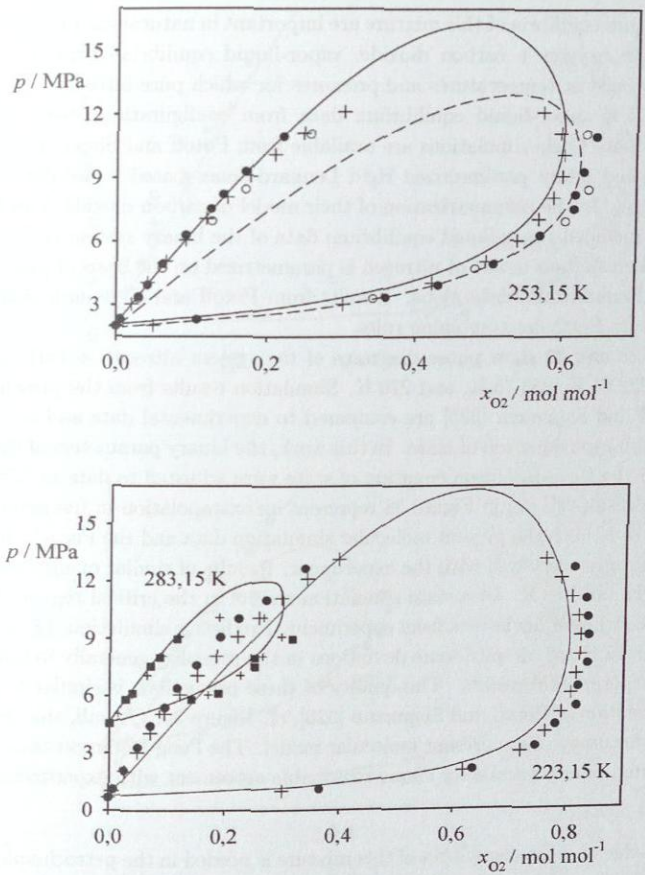

Figure 37: Vapor-liquid equilibria of the mixture O_2 + CO_2. Simulation, this work: ●, ■ (ξ adjusted), ○ ($\xi = 1$). Peng-Robinson equation of state: —— ($k_{ij} = -0.04838$), − − − ($k_{ij} = 0$) only shown for 253.15 K. + Experiment [113] (experimental data for the 283.15 K and the 223.15 K isotherms are distinguished by symbol size).

Nitrogen + Carbon Dioxide

Vapor-liquid equilibria of this mixture are important in natural gas processing. Similar to the system oxygen + carbon dioxide, vapor-liquid equilibria of nitrogen + carbon dioxide only exist at temperatures and pressures for which pure nitrogen is supercritical.

At 253.15 K vapor-liquid equilibrium data from configurational-bias histogram-reweighting Monte Carlo simulations are available from Potoff and Siepmann [325]. These authors applied newly parametrized rigid Lennard-Jones based molecular models with partial charges. In the parametrization of their model of carbon dioxide, Potoff and Siepmann [325] included vapor-liquid equilibrium data of the binary system carbon dioxide + propane, whereas their model of nitrogen is parametrized on the basis of pure component vapor-liquid equilibrium data alone. Results from Potoff and Siepmann [325] are based on the Lorentz-Berthelot combining rules.

Figures 38 and 39 show phase diagrams of the system nitrogen + carbon dioxide at 218.15 K, 232.85 K, 253.15 K, and 270 K. Simulation results from the present work and from Potoff and Siepmann [325] are compared to experimental data and to results from the Peng-Robinson equation of state. In this work, the binary parameters of the molecular models and the Peng-Robinson equation of state were adjusted to data at 270 K, so that the present results shown in Figure 38 represent an extrapolation in temperature.

At 218.15 K both the present molecular simulation data and the Peng-Robinson equation of state agree very well with the experiment. Results of similar quality were obtained for 232.15 K and 270 K. Uncertain simulation results in the critical region of the 270 K isotherm show larger deviations from experiment. Predictive simulations ($\xi = 1$) from this work at 218.15 K are, despite some deviations in the pressure, generally in fair agreement with the experimental results. The quality of these predictions is similar to the quality of the correlation of Potoff and Siepmann [325], cf. Figure 39. Overall, this demonstrates the higher accuracy of the present molecular model. The Peng-Robinson equation of state with adjusted binary parameter shows reasonable agreement with experimental data.

Nitrogen + Ethane

Knowledge on phase equilibria of this mixture is needed in the petrochemical industry. Similar to the systems discussed above, at temperatures and pressures where fluid phase equilibria exist in that mixture, pure nitrogen is always supercritical. At 200 K and 260 K vapor-liquid equilibria from the Extended NpT + Test Particle Method were published by Kronome et al. [198]. These authors applied unpolar 2CLJ models from Vrabec and Fischer [416] and Kriebel et al. [190], in which the unlike Lennard-Jones interactions were modeled with Lorentz-Berthelot combining rules with an adjusted binary interaction parameter ξ. This mixture model is very similar to the present model.

Figure 40 shows a comparison of simulation results from the present work and from Kronome et al. [198] to experimental data and to the Peng-Robinson equation of state. An excellent agreement between both molecular models and experiment is found. The re-

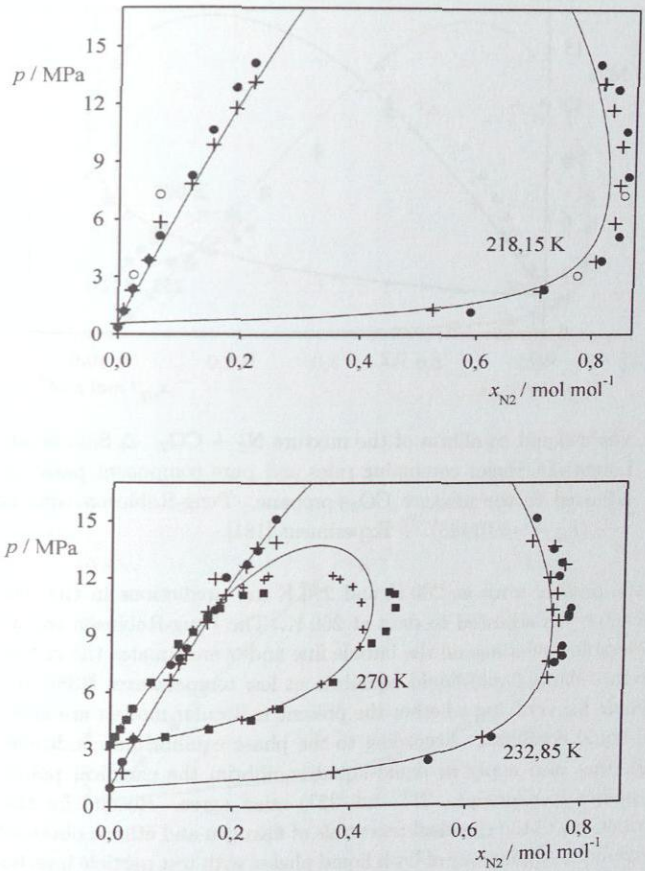

Figure 38: Vapor-liquid equilibria of the mixture N_2 + CO_2. Simulation, this work: ●, ■ (ξ adjusted), ○ ($\xi = 1$). Peng-Robinson equation of state: —— ($k_{ij} = -0.01493$). + Experiment [181] (experimental data for the 270 K and the 232.85 K isotherms are distinguished by symbol size).

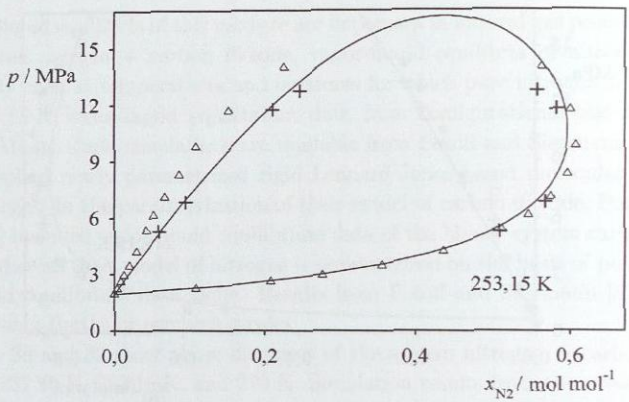

Figure 39: Vapor-liquid equilibria of the mixture N_2 + CO_2. △ Simulation [325] with Lorentz-Berthelot combining rules and pure component parameters of CO_2 adjusted to the mixture CO_2+propane. Peng-Robinson equation of state: —— ($k_{ij} = -0.01493$). + Experiment [181].

sults from the present work at 200 K and 290 K are predictions in the sense that the binary parameter was adjusted to data at 260 K. The Peng-Robinson equation of state shows considerable deviations on the bubble line and overestimates the critical region.

This mixture shows liquid-liquid equilibria at low temperatures [438]. It is therefore a good example for verifying whether the present molecular models are able to describe these liquid-liquid equilibria. According to the phase equilibrium conditions Equations (72) to (76), that also apply to liquid-liquid equilibria, the chemical potentials in the two liquid phases (superscripts "l1" and "l2") must agree. Results for the configurational contributions to the chemical potentials of nitrogen and ethane obtained from *NpT* molecular dynamics simulations of both liquid phases with test particle insertion are given in Table 26 (the simulations were performed with 500 molecules, 200,000 time steps for data production, and 3,000 test particles per species). The fair agreement of the chemical potentials in both phases shows that the present molecular models also comprehend liquid-liquid equilibria. It was not within the scope of the present work to investigate liquid-liquid equilibria in more detail.

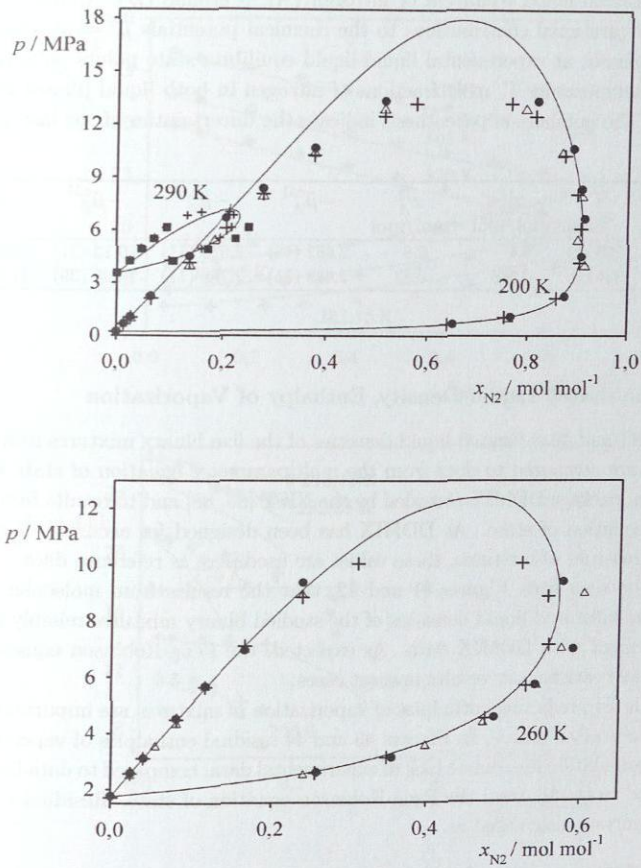

Figure 40: Vapor-liquid equilibria of the mixture N_2 + C_2H_6. ●, ■ Simulation with adjusted ξ, this work. △ Simulation [198] with Lorentz-Berthelot combining rules and adjusted ξ. Peng-Robinson equation of state: —— ($k_{ij} = 0.05233$). + Experiment [131] (experimental data for the 290 K and the 200 K isotherms are distinguished by symbol size).

Table 26: Liquid-liquid equilibria of nitrogen (A) + ethane (B). Comparison of configurational contributions to the chemical potentials $\tilde{\mu}^{c} = \mu^{c}/(k_{B}T)$ in both phases at experimental liquid-liquid equilibria state points [438] (pressure p, temperature T, mole fractions of nitrogen in both liquid phases x_A^{l1} and x_A^{l2}). The numbers in parenthesis indicate the uncertainties of the last digits.

p	T	x_A^{l1}	x_A^{l2}	$-\tilde{\mu}_A^{c,l1}$	$-\tilde{\mu}_A^{c,l2}$	$-\tilde{\mu}_B^{c,l1}$	$-\tilde{\mu}_B^{c,l2}$
MPa	K	mol/mol	mol/mol				
15	123.47	0.4	0.8	2.582 (48)	2.611 (11)	10.13 (21)	10.65 (6)
	116.80	0.336	0.87	2.688 (51)	2.788 (11)	10.05 (39)	11.50 (5)

6.2.1.2 Saturated Liquid Density, Enthalpy of Vaporization

In Figures 41 and 42 saturated liquid densities of the five binary mixtures from molecular simulation are compared to data from the multiparameter equation of state available in the program package DDMIX provided by the NIST [86, 88] and to results from the Peng-Robinson equation of state. As DDMIX has been designed for accurate descriptions of saturated densities of mixtures, these values are used here as reference data.

It can be seen from Figures 41 and 42, that the results from molecular simulation describe the saturated liquid densities of the studied binary mixtures reliably and in very good agreement with DDMIX data. As expected, the Peng-Robinson equation of state does not yield satisfactory results in most cases.

Methods for predicting enthalpies of vaporization of mixtures are important as experimental data is often scarce. In Figures 43 and 44 residual enthalpies of vaporization from molecular simulation are, due to lack of experimental data, compared to data from DDMIX [86, 88] and to results from the Peng-Robinson equation of state. Residual enthalpies of vaporization were calculated as

$$\Delta h_{V}^{res}(T,p,\boldsymbol{x},\boldsymbol{y}) = \left(h''(T,p,\boldsymbol{y}) - h^{id}(T,\boldsymbol{y})\right) - \left(h'(T,p,\boldsymbol{x}) - h^{id}(T,\boldsymbol{x})\right). \qquad (149)$$

The data from DDMIX are considered here as a reasonable estimate for values of the enthalpy of vaporization. In most cases results from molecular simulation are close to the data from DDMIX, whereas, in some cases the Peng-Robinson equation of state produces larger deviations from DDMIX data. Similar results found for the mixtures nitrogen + oxygen and oxygen + carbon dioxide are not shown here, they are available in [378].

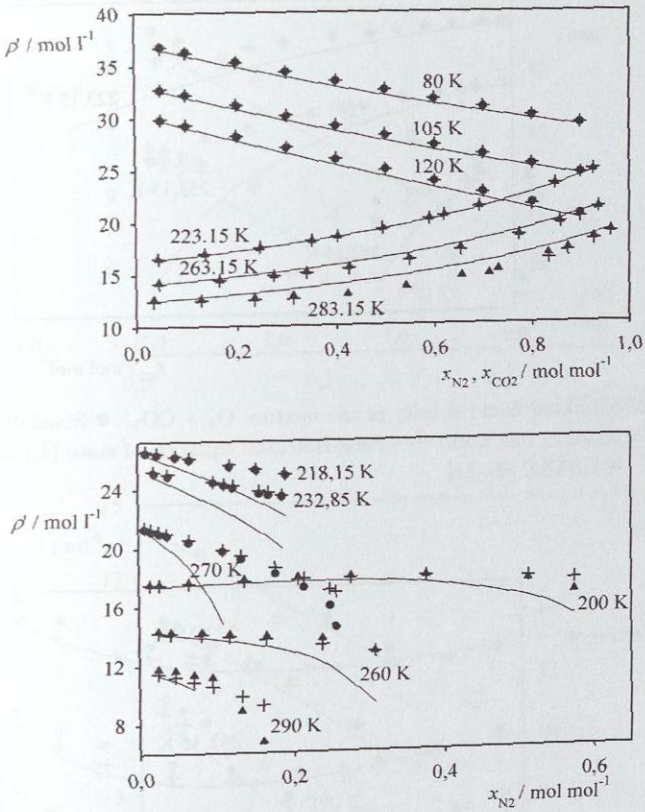

Figure 41: Top: Saturated liquid density of the mixtures N_2 + O_2 and CO_2 + C_2H_6. ● Simulation N_2 + O_2 with adjusted ξ, this work. ▲ Simulation CO_2 + C_2H_6 with adjusted ξ, this work. —— Peng-Robinson equation of state ($k_{ij} = -0.00978$ for N_2 + O_2, $k_{ij} = 0.13008$ for CO_2 + C_2H_6). + DDMIX [86, 88].
Bottom: Saturated liquid density of the mixtures N_2 + CO_2 and N_2 + C_2H_6. ● Simulation N_2 + CO_2 with adjusted ξ, this work. ▲ Simulation N_2 + C_2H_6 with adjusted ξ, this work. —— Peng-Robinson equation of state ($k_{ij} = -0.01493$ for N_2 + CO_2, $k_{ij} = 0.05233$ for N_2 + C_2H_6). + DDMIX [86, 88].

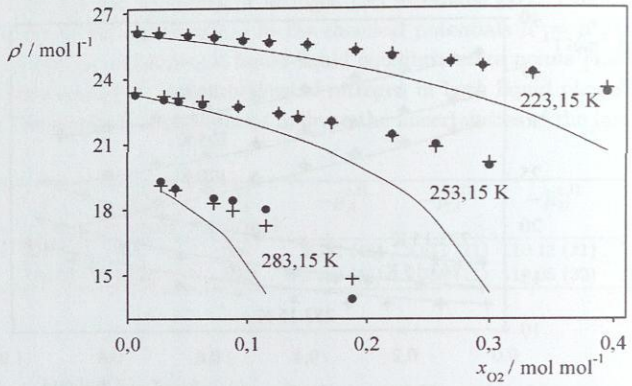

Figure 42: Saturated liquid density of the mixture O_2 + CO_2. ● Simulation with adjusted ξ, this work. —— Peng-Robinson equation of state ($k_{ij} = -0.04838$). + DDMIX [86, 88].

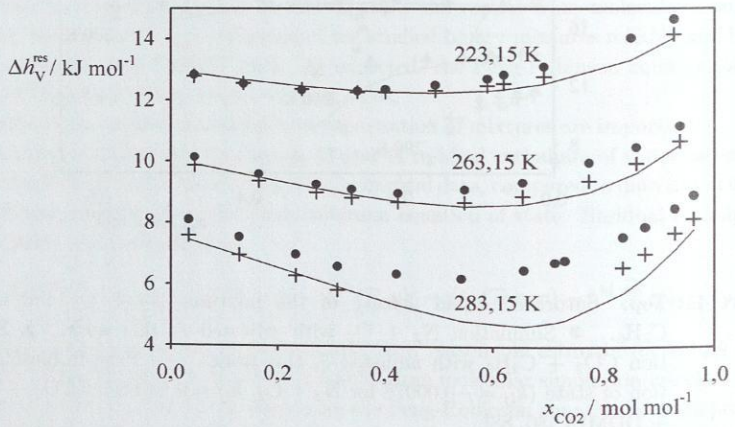

Figure 43: Enthalpy of vaporization of the mixture CO_2 + C_2H_6. ● Simulation with adjusted ξ, this work. —— Peng-Robinson equation of state ($k_{ij} = 0.13008$). + DDMIX [86, 88].

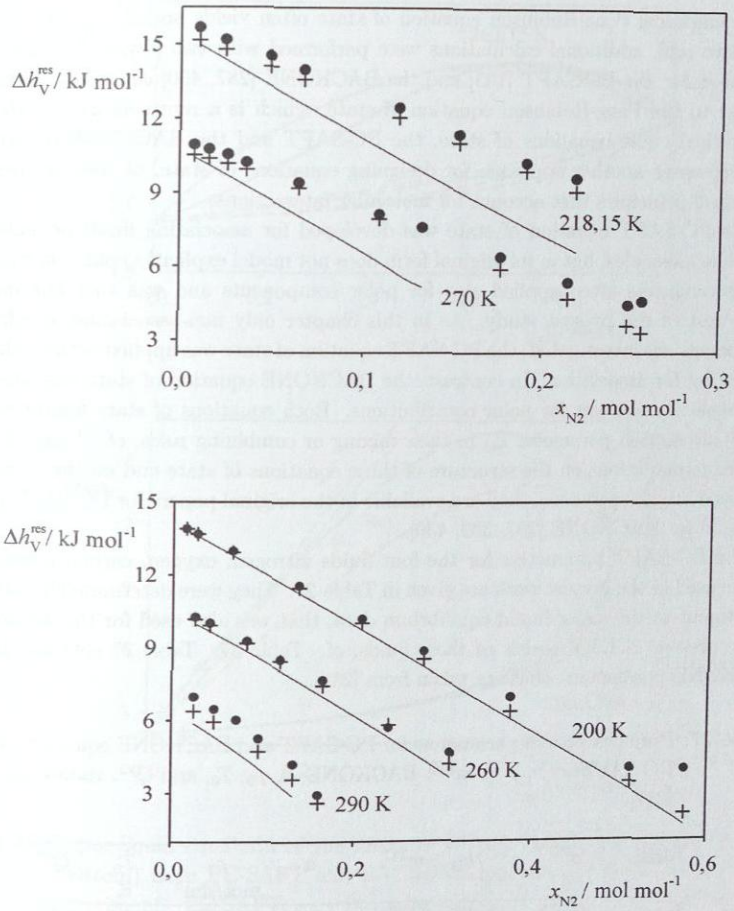

Figure 44: Top: Enthalpy of vaporization of the mixture N_2 + CO_2. ● Simulation with adjusted ξ, this work. —— Peng-Robinson equation of state ($k_{ij} = -0.01493$). + DDMIX [86, 88]. Results for 232.85 K are not shown here, they are available in [378].
Bottom: Enthalpy of vaporization of the mixture N_2 + C_2H_6. ● Simulation with adjusted ξ, this work. —— Peng-Robinson equation of state ($k_{ij} = 0.05233$). + DDMIX [86, 88].

6.2.1.3 Results from Physically Based Equations of State

As the empirical Peng-Robinson equation of state often yields no satisfactory results as predictive tool, additional calculations were performed with two physically based equations of state: the PC-SAFT [133] and the BACKONE [287, 430] equations of state. In contrast to the Peng-Robinson equation of state, which is a representative of the class of empirical cubic equations of state, the PC-SAFT and the BACKONE equations of state represent another approach for designing equations of state, as they are based on theoretical principles that account for molecular interactions.

The PC-SAFT equation of state was developed for associating fluids or fluids with chain-like molecules, but in its original form does not model explicitly polar contributions. It is nevertheless often applied also for polar components and was therefore included in the test of the present study. As in this chapter only non-associating, quadrupolar components are investigated, the PC-SAFT equation of state was applied without the term accounting for association. In contrast, the BACKONE equation of state contains terms that explicitly account for polar contributions. Both equations of state feature a single binary interaction parameter k_{ij} in their mixing or combining rules, cf. Table 25. More detailed explanations on the structure of these equations of state and on the parameters employed are skipped here, they are available in the original papers for PC-SAFT [45, 46, 133], and for BACKONE [287, 339, 430].

The PC-SAFT parameters for the four fluids nitrogen, oxygen, carbon dioxide, and ethane used in the present work are given in Table 27. They were determined here from an adjustment to the vapor-liquid equilibrium data, that was also used for the development of the present 2CLJQ models of these fluids, cf. Table 37. Table 27 contains also the BACKONE parameters, that are taken from [287].

Table 27: Pure component parameters for PC-SAFT and BACKONE equations of state. PC-SAFT: σ^{PC}, ε^{PC}, m^{PC}. BACKONE: α, ρ_0, T_0, and Q^{*2}, values taken from [287].

Fluid	σ^{PC} Å	ε^{PC}/k_B K	m^{PC}	α	ρ_0 mol/dm^3	T_0 K	Q^{*2}
N_2	3.2975	89.492	1.2365	1.0471	11.133	125.74	0.487
O_2	3.1711	113.98	1.1457	1.0244	13.629	154.58	0.0
CO_2	2.5731	152.85	2.5461	1.3919	10.549	291.28	2.181
C_2H_6	3.5186	191.15	1.6105	1.2127	6.800	305.32	0.0

In Figure 45, top, vapor-liquid equilibria of the binary mixture carbon dioxide + ethane from the PC-SAFT and from the BACKONE equations of state are compared to experimental data. It can be seen, that these equations of state show the same poor predictive qualities as the Peng-Robinson equation of state (cf. Figure 36), as they do not predict the

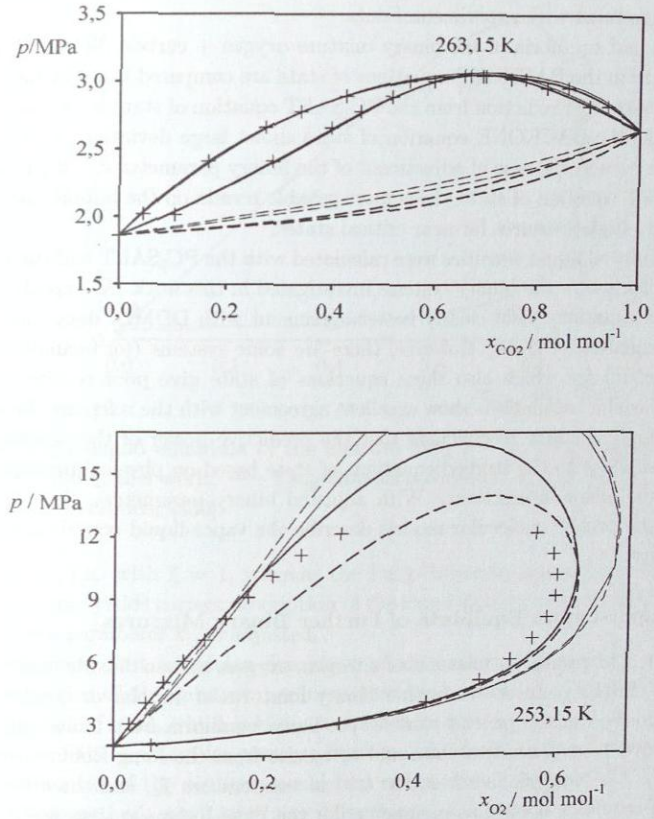

Figure 45: Vapor-liquid equilibria of the mixtures CO_2 + C_2H_6 (top) and O_2 + CO_2 (bottom) from PC-SAFT and *BACKONE equations of state* compared to experiment. PC-SAFT: —— (k_{ij} adjusted), – – – ($k_{ij} = 0$). BACKONE: —— (k_{ij} adjusted), – – – ($k_{ij} = 0$). + Experiment: CO_2 + C_2H_6 [181], O_2 + CO_2 [113].

azeotrope. In the case of adjusted binary parameter k_{ij}, both equations of state are in excellent agreement with experimental data.

Vapor-liquid equilibria of the binary mixture oxygen + carbon dioxide from the PC-SAFT and from the BACKONE equations of state are compared to experimental data in Figure 45, bottom. Prediction from the PC-SAFT equation of state is poor on the bubble line, whereas the BACKONE equation of state shows large deviations on the dew line, that remain even in the case of adjustment of the binary parameter k_{ij}. With adjusted k_{ij} the PC-SAFT equation of state yields more reliable results on the bubble line, but shows deviations to high pressures for near critical states.

Also saturated liquid densities were calculated with the PC-SAFT and the BACKONE equations of state for the binary systems investigated in this work. As expected, for many cases, these equations yield clearly better agreement with DDMIX data than the Peng-Robinson equation of state. However, there are some systems (for example nitrogen + carbon dioxide) for which also these equations of state give poor results whereas the present molecular simulations show excellent agreement with the reference data, cf. [378].

These findings allow to conclude that the predictive power of the present molecular models is superior to the studied equations of state based on physical principles that account for molecular interactions. With adjusted binary parameters, these equations of state and the present molecular models describe the vapor-liquid equilibria with comparable quality.

6.2.2 Vapor-Liquid Equilibria of Further Binary Mixtures

In Chapter 6.2.1 results for mixtures of nitrogen, oxygen, carbon dioxide, and ethane were presented. In this chapter, for further binary mixtures of unpolar or quadrupolar components modeled in the present work, vapor-liquid equilibria from molecular simulation are compared to experimental data and to results from the Peng-Robinson equation of state [316]. The acentric factor ω, the critical temperature T_c, and the critical pressure p_c of the pure fluids needed as parameters for the Peng-Robinson equation of state were taken from Reid et al. [321]. The binary parameter k_{ij} of the Peng-Robinson equation of state was adjusted to the same data used for the determination of the binary interaction parameters ξ of the molecular models, cf. Table 23.

In the case of the mixture carbon dioxide + carbon disulfide, cf. Figure 46, a considerable overestimation of the critical points is obtained from the Peng-Robinson equation of state. This overestimation is mainly due to the poor description of the bubble line by the Peng-Robinson equation of state. An essentially better description of the bubble line is obtained from molecular simulation. Analogous results were found for the mixtures nitrogen + ethane and oxygen + carbon dioxide, cf. Chapter 6.2.1.1, and for the mixture nitrogen + propylene, cf. Chapter 6.3.1.

In analogy to the mixture carbon dioxide + ethane, Figure 47 shows, that molecular simulation predicts correctly the azeotropic behavior of the mixture ethyne + ethane from

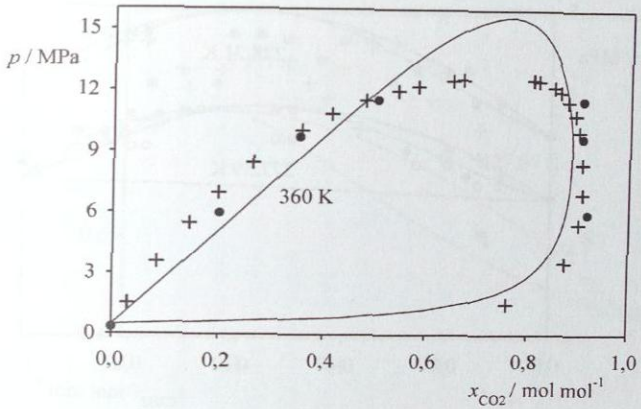

Figure 46: *Vapor-liquid equilibria of the mixture CO_2 + CS_2.* • *Simulation with adjusted ξ, this work.* —— Peng-Robinson equation of state ($k_{ij} = -0.00227$). + Experiment [330].

pure data alone, i.e. with $\xi = 1$, whereas the Peng-Robinson equation of state fails in prediction and only yields correct description of the vapor-liquid equilibria of this mixture when the binary parameter k_{ij} is adjusted.

Figure 48 shows, that molecular simulation yields a more reliable description of the azeotropic behavior of the mixture perfluoroethane + carbon dioxide than the Peng-Robinson equation of state, which is worse even when its binary parameter k_{ij} is adjusted. The scattering of the equilibrium pressure from molecular simulation is due to the uncertain determination of the configurational part of the chemical potential from the test particle insertion method, when large size differences of the molecules occur, as it is the case here.

Even stronger scattering of the equilibrium pressure and also of the vapor phase composition from molecular simulation was observed in the case of the mixture perfluoroethane + xenon. The simulation results are not shown here, the binary interaction parameter ξ could not be adjusted, cf. [378]. Compared to the mixture perfluoroethane + carbon dioxide, the size difference between perfluoroethane molecules and xenon atoms is even larger, which may have caused this behavior. For the mixtures perfluoroethane + carbon dioxide and perfluoroethane + xenon supposedly better results would be obtained if the gradual insertion method instead of the test particle insertion method was used for the calculation of the configurational part of the chemical potential and the partial molar volume needed for the Grand Equilibrium method. No simulations of this mixture were performed with the gradual insertion method, as this method was extended to simulations of mixtures on-

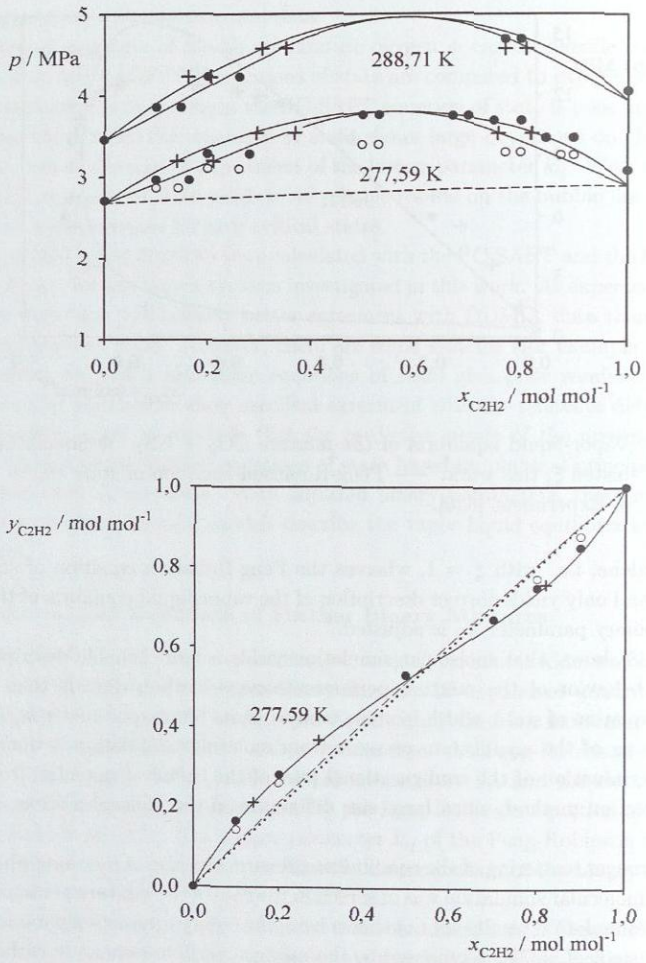

Figure 47: Vapor-liquid equilibria of the mixture C_2H_2 + C_2H_6. Simulation, this work: ● (ξ adjusted), ○ ($\xi = 1$). Peng-Robinson equation of state: —— ($k_{ij} = 0.15579$), − − − ($k_{ij} = 0$). + Experiment [259].

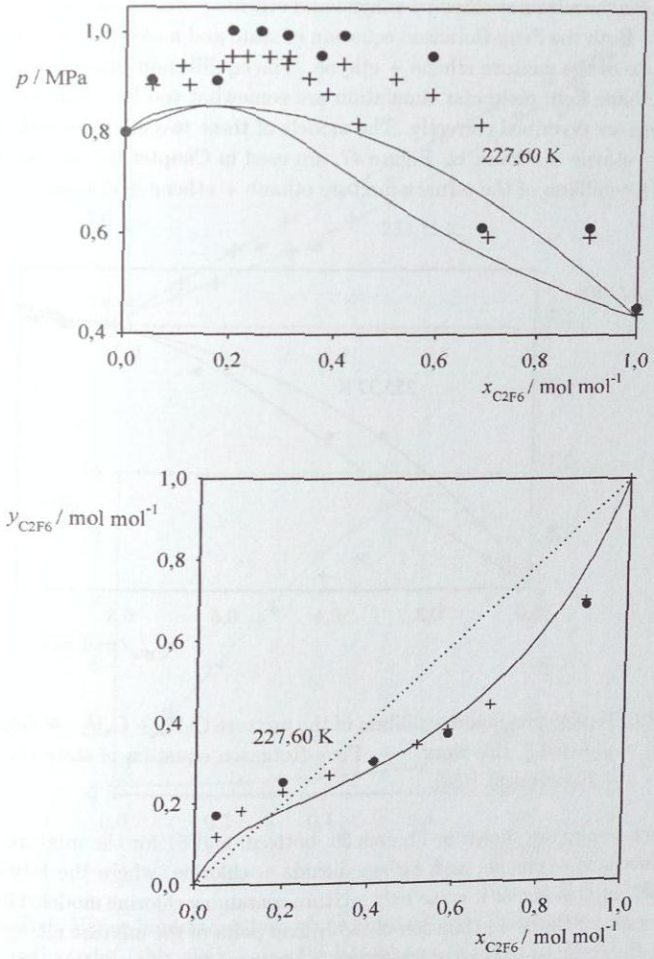

Figure 48: Vapor-liquid equilibria of the mixture C_2F_6 + CO_2. ● *Simulation* with adjusted ξ, this work. —— Peng-Robinson equation of state ($k_{ij} = 0.02800$). + Experiment [357].

ly in the final phase of the present work.

Results for the mixtures ethene + ethyne and ethene + ethane are shown in Figures 49 and 50, top. Both the Peng-Robinson equation of state and molecular simulation describe the azeotrope of the mixture ethene + ethyne. The equilibrium pressures of the mixture ethene + ethane from molecular simulation are somewhat too low, but the vapor phase compositions are described correctly. The models of these two mixtures and the model of the mixture ethyne + ethane, cf. Figure 47, are used in Chapter 6.5 for the prediction of vapor-liquid equilibria of the ternary mixture ethane + ethene + ethyne.

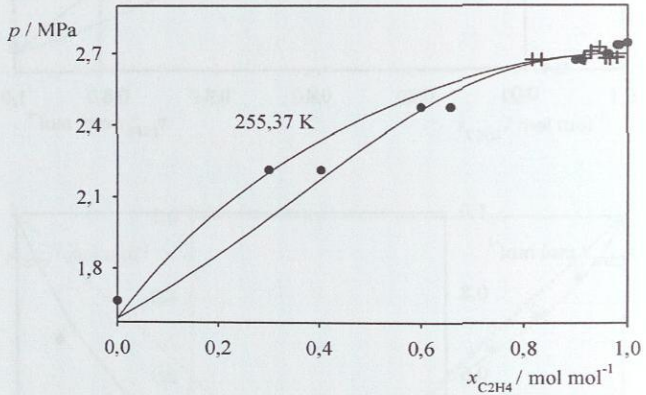

Figure 49: Top: Vapor-liquid equilibria of the mixture C_2H_4 + C_2H_2. ● Simulation with adjusted ξ, this work. —— Peng-Robinson equation of state ($k_{ij} = 0.06383$). + Experiment [152].

Further results are shown in Figures 50, bottom, and 51 for the mixtures nitrogen + ethene, methane + ethene, and carbon dioxide + chlorine, where the latter mixture is particularly interesting, as it is the only mixture containing chlorine modeled in the present work. Except for the overestimation of the critical point of the mixture nitrogen + ethene, the Peng-Robinson equation of state describes the vapor-liquid equilibria of these mixtures with good accuracy. Also results from molecular simulation agree well with experimental data within the simulation uncertainties.

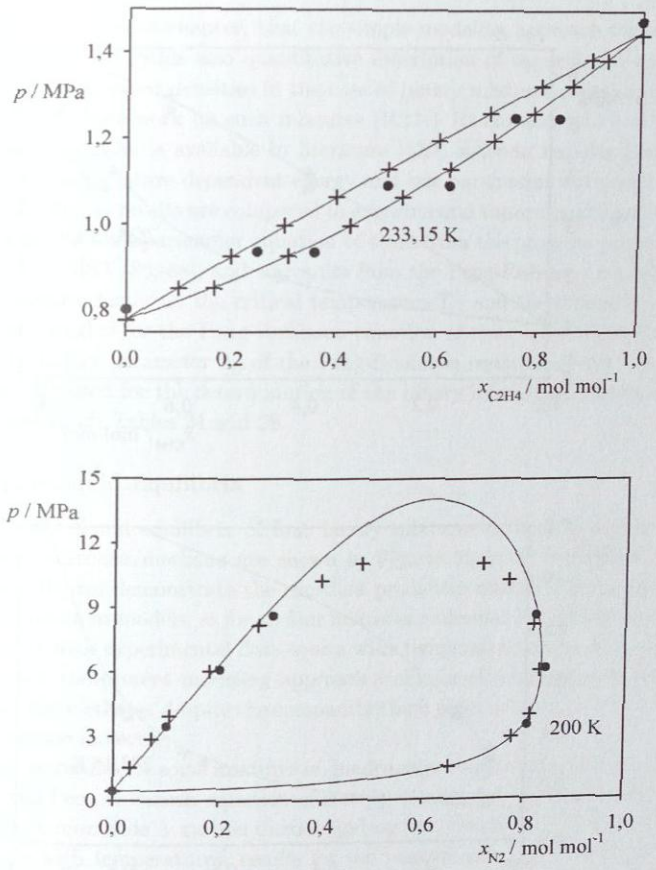

Figure 50: Top: Vapor-liquid equilibria of the mixture C_2H_4 + C_2H_6. ● Simulation with adjusted ξ, this work. —— Peng-Robinson equation of state ($k_{ij} = 0.012$). + Experiment [152].
Bottom: Vapor-liquid equilibria of the mixture N_2 + C_2H_4. ● Simulation with adjusted ξ, this work. —— Peng-Robinson equation of state ($k_{ij} = 0.0646$). + Experiment [131].

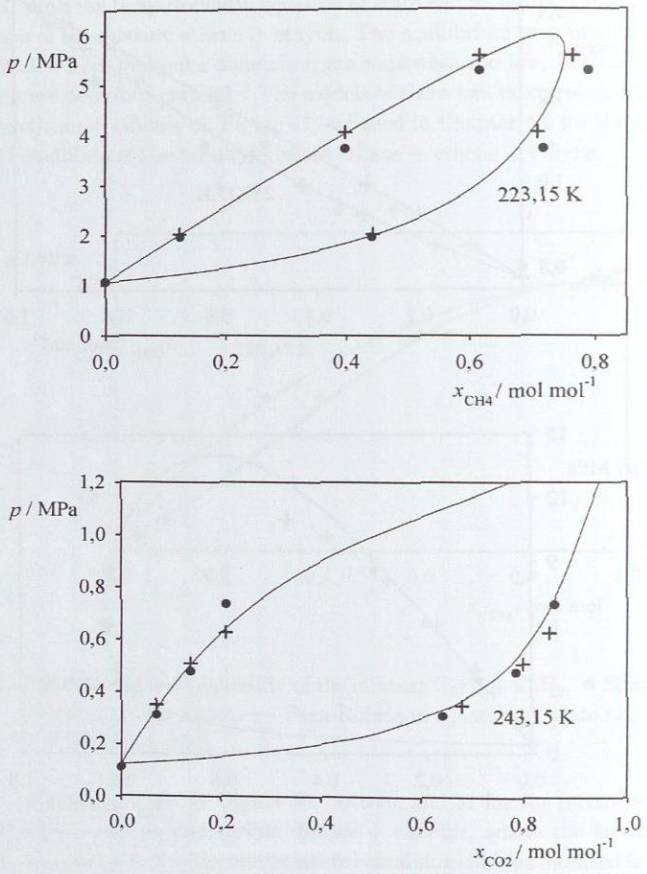

Figure 51: Top: Vapor-liquid equilibria of the mixture $CH_4 + C_2H_4$. ● Simulation with adjusted ξ, this work. —— Peng-Robinson equation of state ($k_{ij} = 0.0343$). + Experiment [346].
Bottom: Vapor-liquid equilibria of the mixture $CO_2 + Cl_2$. ● Simulation with adjusted ξ, this work. —— Peng-Robinson equation of state ($k_{ij} = 0.0932$). + Experiment [173].

6.3 Binary Mixtures Containing Multipolar Components

It is shown in the present chapter, that the simple modeling approach for mixtures described in Chapter 6.1 yields also quantitative description of vapor-liquid equilibria and saturated liquid and vapor densities in the case of binary mixtures containing multipolar components. Only one work on such mixtures (R22 + R142b and R22 + R152a) based on molecular simulation is available in literature [119], wherein unpolar Lennard-Jones potentials with temperature dependent energy and size parameters were used.

Present simulation results are compared to experimental vapor-liquid equilibrium data, to results from the multiparameter equation of state from the program package DDMIX provided by the NIST [86, 88], and to results from the Peng-Robinson equation of state [316]. The acentric factor ω, the critical temperature T_c, and the critical pressure p_c of the pure fluids needed for the Peng-Robinson equation of state were taken from Reid et al. [321]. The binary parameter k_{ij} of the Peng-Robinson equation of state was adjusted to the same data used for the determination of the binary interaction parameter ξ of the molecular models, cf. Tables 24 and 28.

6.3.1 Vapor-Liquid Equilibria

Results for vapor-liquid equilibria of four binary mixtures carbon monoxide + carbon dioxide/ethane/nitrogen/methane are shown in Figures 52 to 55 for wide temperature ranges. These figures demonstrate the excellent predictive qualities of the present state independent molecular models, as for all four mixtures molecular simulation data is in very good agreement with experimental data over a wide temperature range. It is particularly interesting, that the present modeling approach yields excellent results for the mixture carbon monoxide + ethane, despite the comparably high polarizability $\alpha \approx 4.4 \cdot 10^{-24}$ cm^3 [132] of the ethane molecule.

In analogy to results for some mixtures of quadrupolar components with an overcritical component, the Peng-Robinson equation of state overestimates the critical points of the mixtures carbon monoxide + carbon dioxide and carbon monoxide + ethane, cf. Figures 52 and 53. At high temperatures, results for the mixture nitrogen + carbon monoxide from the Peng-Robinson equation of state, become inaccurate, cf. Figure 54. In contrast, vapor-liquid equilibria of the mixture methane + carbon monoxide, cf. Figure 55, from the Peng-Robinson equation of state are in excellent agreement with experimental data. In all cases, molecular simulation yields reliable results on all isotherms also in the critical region.

Very satisfactory results are also obtained from molecular simulation for vapor-liquid equilibria of three mixtures containing the refrigerants R22 and R23: carbon dioxide + R22 and carbon dioxide + R23, cf. Figure 56, and carbon disulfide + R22, cf. Figure 57. Similar to the mixture carbon monoxide + ethane, the mixture carbon disulfide + R22 un-

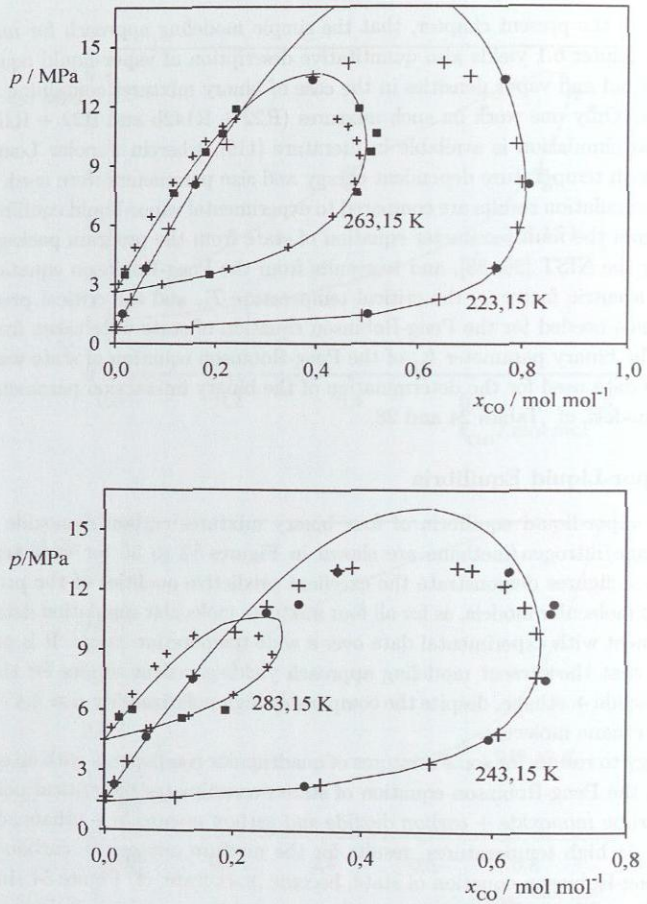

Figure 52: Vapor-liquid equilibria of the mixture CO + CO_2. ●, ■ Simulation with adjusted ξ, this work. —— Peng-Robinson equation of state ($k_{ij} = 0.03411$). + Experiment [53].

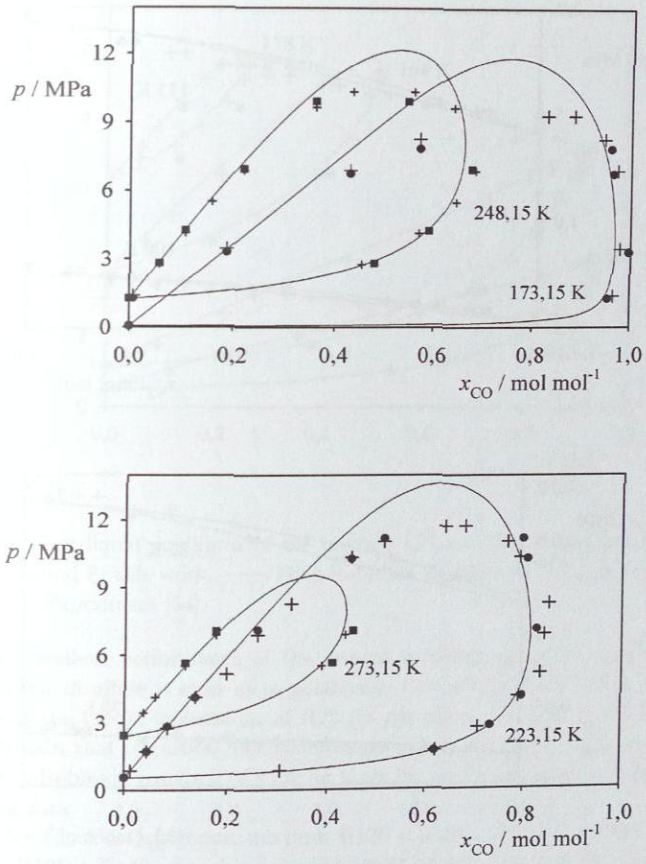

Figure 53: Vapor-liquid equilibria of the mixture CO + C_2H_6. ●, ■ Simulation with adjusted ξ, this work. —— Peng-Robinson equation of state ($k_{ij} = 0.01981$). + Experiment [395].

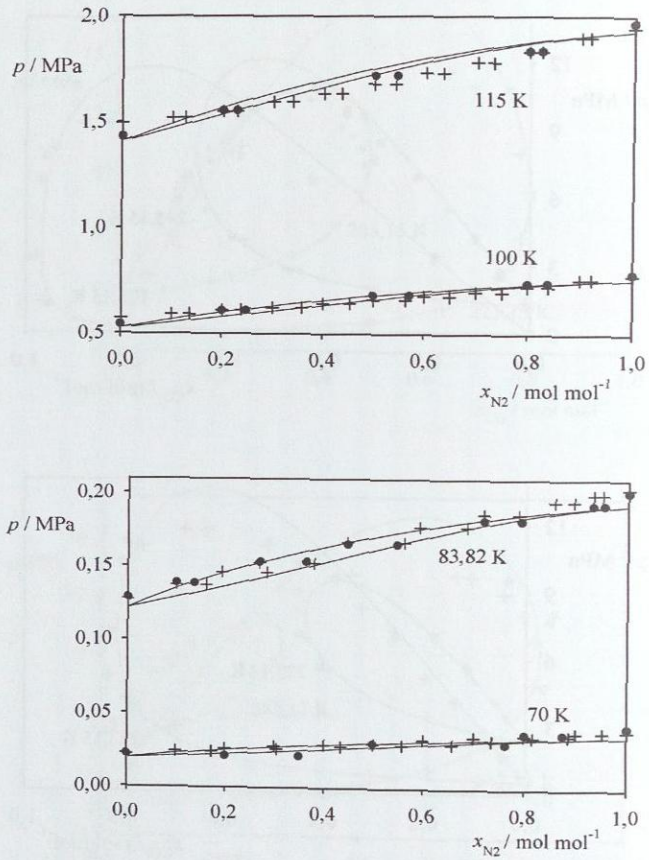

Figure 54: Vapor-liquid equilibria of the mixture $N_2 + CO$. ● *Simulation with adjusted* ξ, this work. —— Peng-Robinson equation of state ($k_{ij} = 0.02835$). + Experiment [372].

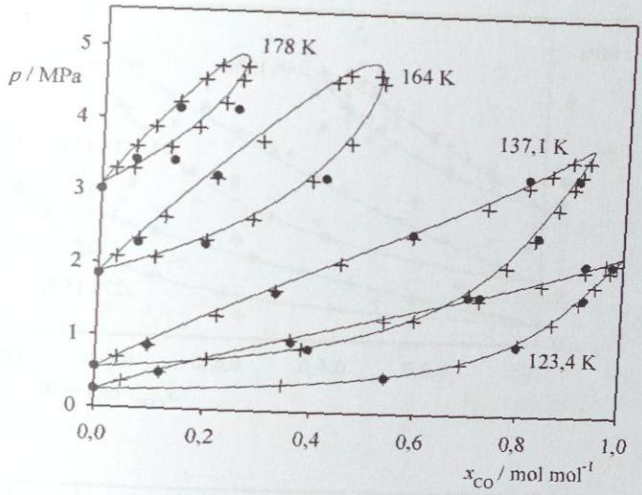

Figure 55: Vapor-liquid equilibria of the mixture CH_4 + CO. ● Simulation with adjusted ξ, this work. —— Peng-Robinson equation of state ($k_{ij} = 0.02550$). + Experiment [54].

derlines the excellent performance of the present modeling approach, as the unpolar molecule carbon disulfide is even more polarizable ($\alpha \approx 8 \cdot 10^{-24}$ cm^3) than the ethane molecule, and the dipole momentum of R22 (in gas phase $\mu \approx 1.46$ D [328]) is essentially higher than that of carbon monoxide (in gas phase $\mu \approx 0.1$ D [132]). Also results from the Peng-Robinson equation of state for these three mixtures agree excellently with experimental data.

Results for the four refrigerant mixtures R125 + R134a, R143a + R134a, R143a + R152a, and R125 + R143a are shown in Figures 58 to 60. The Peng-Robinson equation of state describes these vapor-liquid equilibria with excellent accuracy, except for high temperature isotherms of the azeotropic mixture R125 + R143a, where systematic deviations occur. Results from molecular simulation agree well with experimental data, the vapor phase compositions are described with excellent accuracy. The equilibrium pressures from molecular simulation scatter as the configurational parts of the chemical potentials were obtained with rather large uncertainties from test particle insertion. In the case of the mixture R125 + R134a, cf. Figure 58, systematic deviations occur at higher temperatures. The molecular models of the mixtures R125 + R134a, R125 + R143a, and R143a + R134a are used in Chapter 6.5 for the prediction of vapor-liquid equilibria of the ternary mixture R125 + R143a + R134a.

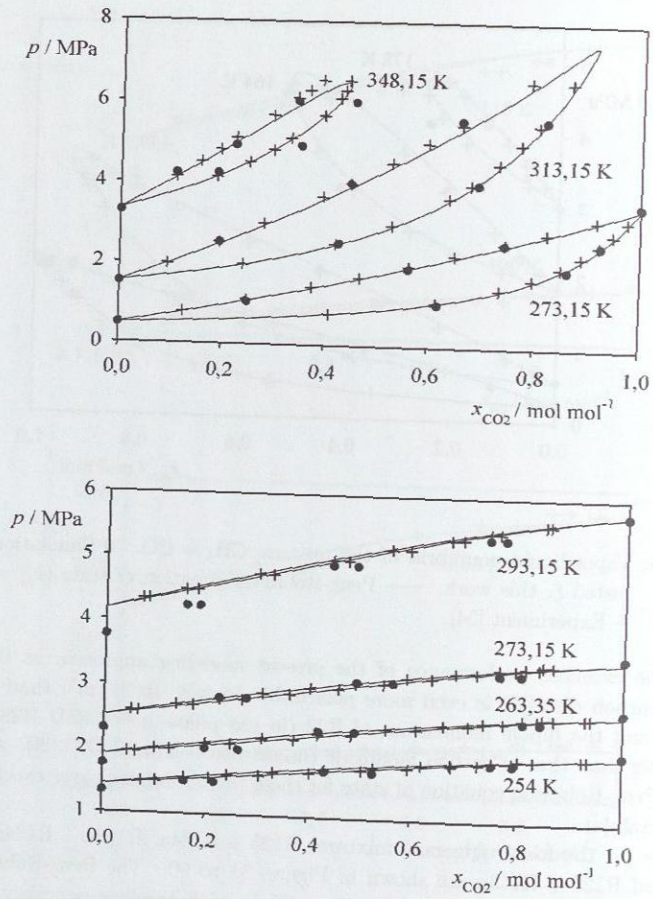

Figure 56: Top: Vapor-liquid equilibria of the mixture CO_2 + R22. ● Simulation with adjusted ξ, this work. —— Peng-Robinson equation of state ($k_{ij} = -0.00676$). + Experiment [336].
Bottom: Vapor-liquid equilibria of the mixture CO_2 + R23. ● Simulation with adjusted ξ, this work. —— Peng-Robinson equation of state ($k_{ij} = 0.01146$). + Experiment [336].

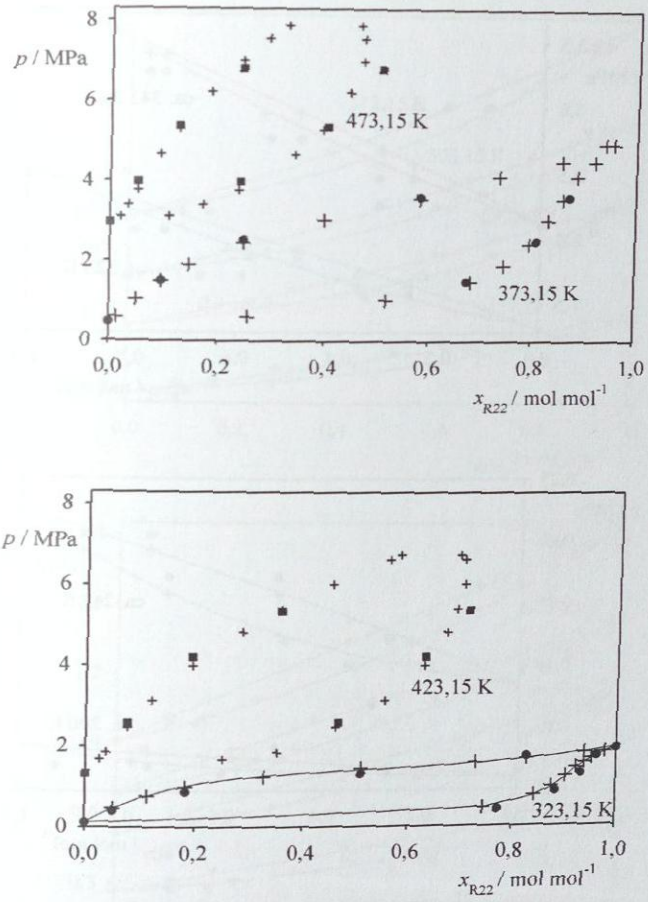

Figure 57: Vapor-liquid equilibria of the mixture CS_2 + R22. ●, ■ Simulation with adjusted ξ, this work. —— Peng-Robinson equation of state ($k_{ij} = 0.09$), no convergence was achieved at 373.15 K, 423.15 K, 473.15 K. + Experiment [336].

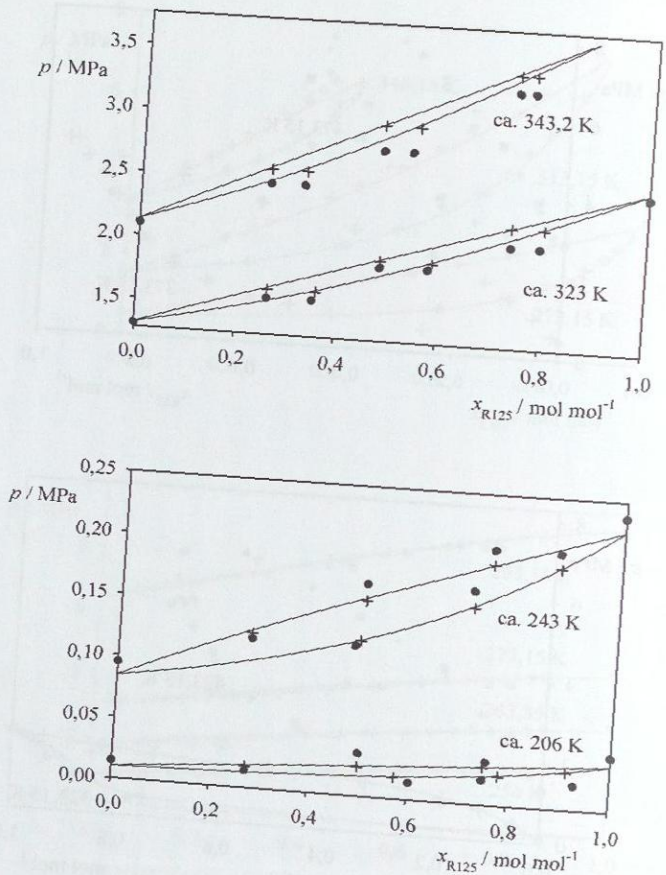

Figure 58: Vapor-liquid equilibria of the mixture R125 + R134a. ● Simulation with adjusted ξ, this work. —— Peng-Robinson equation of state ($k_{ij} = 0.0089$). + Experiment [290].

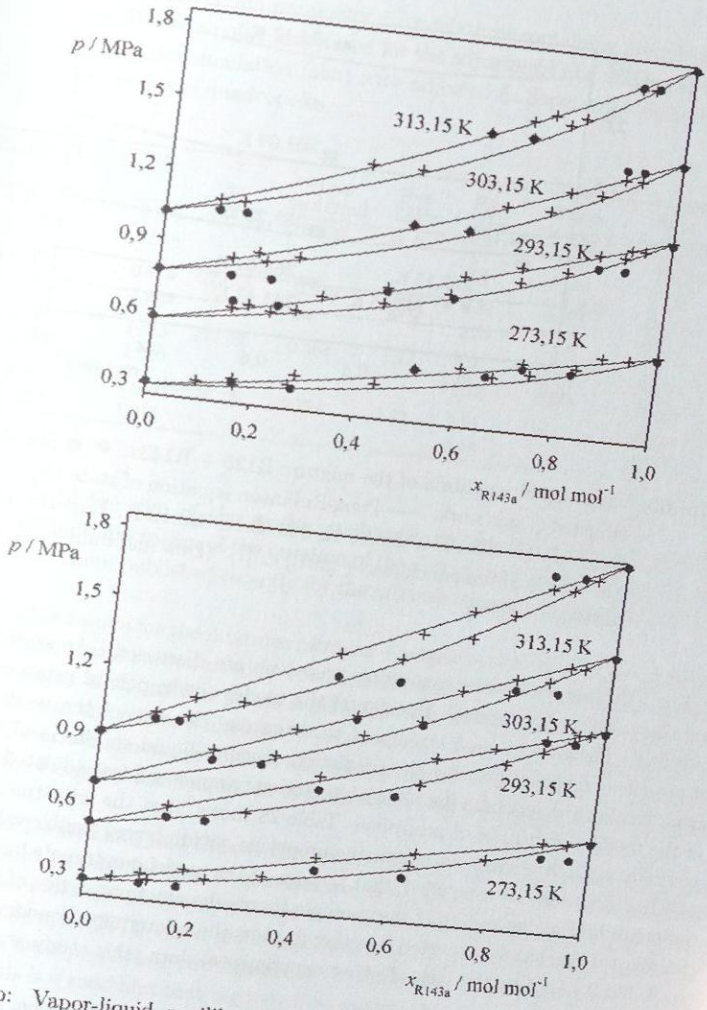

Figure 59: Top: Vapor-liquid equilibria of the mixture R143a + R134a. ● Simulation with adjusted ξ, this work. —— Peng-Robinson equation of state ($k_{ij} = -0.0125$). + Experiment [214].
Bottom: Vapor-liquid equilibria of the mixture R143a + R152a. ● Simulation with adjusted ξ, this work. —— Peng-Robinson equation of state ($k_{ij} = 0.00459$). + Experiment [214].

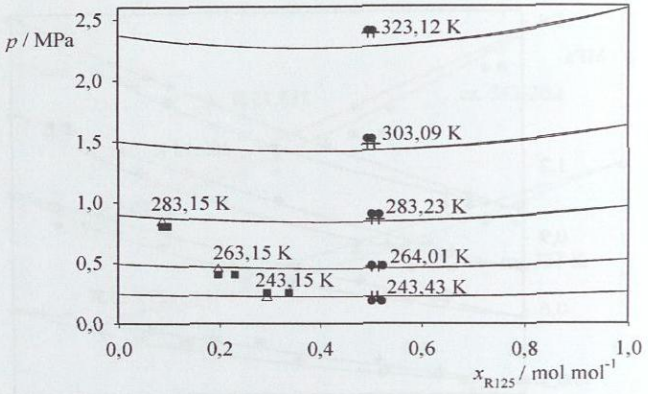

Figure 60: Vapor-liquid equilibria of the mixture R125 + R143a. ●, ■ Simulation with adjusted ξ, this work. —— Peng-Robinson equation of state ($k_{ij} = -0.04824$) at 243.15 K, 263.15 K, 283.15 K, 303.09 K, 323.12 K. Experimental data at the indicated temperatures: + [291], △ [7]. (Dew and bubble lines are hardly distinguishable.)

Finally, binary mixtures containing propylene are discussed. As stated in Table 9 and discussed in Appendix G, the sign of the model quadrupole of propylene is not yet specified. Therefore, it was attempted to determine the sign of the model quadrupole of propylene empirically using the prediction of vapor-liquid equilibria of mixtures as a criterion. For that purpose the binary interaction parameter ξ was adjusted for both signs of the model quadrupole of propylene. Table 28 shows, that the adjustment worked surprisingly well for all mixtures containing propylene, yielding very similar values of ξ. From this finding it may be concluded, that the sign of the model quadrupole has practically no influence on the description of macroscopic thermodynamic properties of these mixtures. Similar results may be expected for other fluids with undetermined quadrupole sign listed in Table 9. Due to the lack of other experimental data, this study was resctricted to propylene.

Results for the mixtures nitrogen + propylene, ethane + propylene, and carbon dioxide + propylene are shown in Figures 61 and 62. Results for the mixture ethylene + propylene are not shown here as only a narrow experimental data base is available in the literature. Figures 61 and 62 show, that molecular simulations with positive and negative model quadrupole momentum for propylene perform equally well, also for isotherms far away from the state point chosen for the adjustment of ξ. These results support the

Table 28: Binary interaction parameter ξ for mixtures containing propylene (P). Experimental data point (exp) used for the adjustment of ξ and result for that data point from simulation (sim) with adjusted ξ. Superscript signs indicate signs of the model quadrupoles.

Mixture (1+2)	ξ	T K	$x_{1,\mathrm{exp}}$ mol/mol	p_{exp} MPa	p_{sim} MPa	$y_{1,\mathrm{exp}}$ mol/mol	$y_{1,\mathrm{sim}}$ mol/mol	Ref.
$N_2 + P^-$	0.959	260.00	0.220	11.9	11.7	0.879	0.898	[131]
$N_2 + P^+$	0.958				12.4	0.879	0.879	
$CO_2 + P^-$	0.915	273.15	0.539	2.42	2.34	0.821	0.821	[289]
$CO_2 + P^+$	0.920				2.35	0.821	0.826	
$C_2H_6 + P^-$	1.015	277.59	0.568	1.72	1.77	0.775	0.785	[348]
$C_2H_6 + P^+$	1.019				1.72	0.775	0.785	
$C_2H_4 + P^-$	1.021	258.15	0.794	2.23	2.21	n.a.	0.952	[144]
$C_2H_4 + P^+$	1.018				2.18	n.a.	0.954	

negligible role of the sign of the model quadrupole on the description of vapor-liquid equilibria. Without discussion of the question of the sign of the model quadrupole, similar favorable results were published recently for the mixture ethane + propylene at 277.59 K [42].

Similar to the results for the mixtures nitrogen + ethane and oxygen + carbon dioxide, cf. Chapter 6.2.1.1, and carbon dioxide + carbon disulfide, cf. Chapter 6.2.2, a considerable overestimation of the critical points is obtained from the Peng-Robinson equation of state in the case of the mixture nitrogen + propylene, cf. Figure 61. In contrast, in the case of the mixtures ethane + propylene and carbon dioxide + propylene, cf. Figure 62, results from the Peng-Robinson equation of state are in very good agreement with experimental data.

It should be pointed out, that the excellent performance of the 2CLJQ model of propylene when applied to the modeling of mixtures was not presumed in view of the angular shape of the real molecule. However, it seems that this angular shape makes the molecule sufficiently compact for 2CLJ-based modeling. After all, this case teaches that molecular models of fluids must proof their performance in the application to fluid mixtures. If they work therein, this is a good hint that the pure fluid model is built on a reasonable physical basis.

6.3.2 Saturated Densities

For the mixtures carbon monoxide + carbon dioxide, carbon monoxide + ethane, and methane + carbon monoxide saturated liquid and vapor densities from molecular simula-

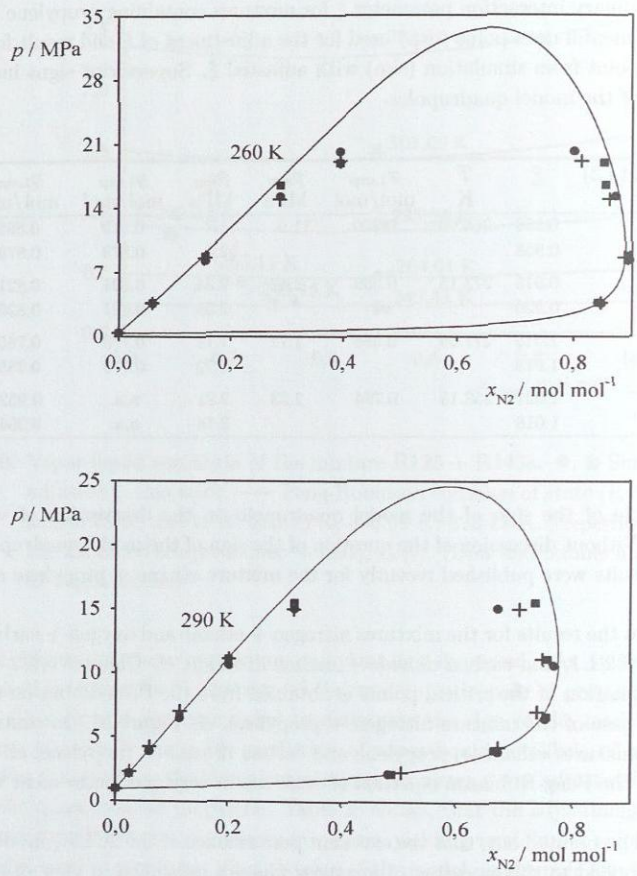

Figure 61: Vapor-liquid equilibria of the mixture N_2 + propylene. Simulation with adjusted ξ, this work: ● same quadrupole signs, ■ opposite quadrupole signs. —— Peng-Robinson equation of state ($k_{ij} = 0.08844$). + Experiment [131].

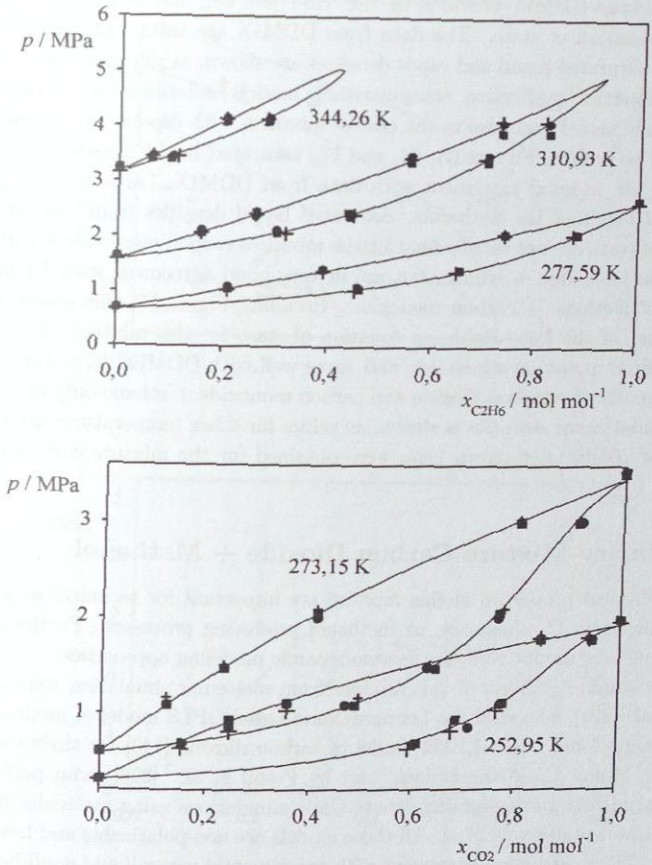

Figure 62: Top: Vapor-liquid equilibria of the mixture C_2H_6 + propylene. Simulation with adjusted ξ, this work: ● same quadrupole signs, ■ opposite quadrupole signs. —— Peng-Robinson equation of state (k_{ij} = 0.00701). + Experiment [348]. Bottom: Vapor-liquid equilibria of the mixture CO_2 + propylene. Simulation with adjusted ξ, this work: ● same quadrupole signs, ■ opposite quadrupole signs. —— Peng-Robinson equation of state (k_{ij} = 0.09493). + Experiment [289].

tion were compared to data from the multiparameter equation of state available in the program package DDMIX provided by the NIST [86, 88], and to results from the Peng-Robinson equation of state. The data from DDMIX are taken here as reference data. Results for saturated liquid and vapor densities are shown, as the quantitative description of these properties by effective, non-polarizable models underlines the predictive qualities of this simple model type also in the case of mixtures with dipolar components.

As can be seen in Figures 63, 64, and 65, saturated liquid densities from molecular simulation are in good agreement with data from DDMIX. Larger deviations occur in the critical region of the isotherms. Saturated liquid densities from the Peng-Robinson equation of state are not satisfactory for the mixtures carbon monoxide + carbon dioxide and carbon monoxide + ethane, but are in very good agreement with DDMIX data in the case of methane + carbon monoxide. Recalling Figure 55, this shows an excellent performance of the Peng-Robinson equation of state for this mixture. Saturated vapor densities from molecular simulation also agree well with DDMIX data. For the mixtures carbon monoxide + carbon dioxide and carbon monoxide + ethane only one isotherm for the saturated vapor densities is shown, as values for other temperatures are very similar.

Similar results, not shown here, were obtained for the mixture carbon monoxide + nitrogen.

6.4 Binary Mixture Carbon Dioxide + Methanol

Thermophysical properties of this mixture are important for technical applications like coal gasification, C_1 chemistry, or methanol producing processes. Furthermore, it is a demanding mixture for verifying thermodynamic modeling approaches.

Vapor-liquid equilibria of this mixture from molecular simulation were published by Lísal et al. [228], who used the Lennard-Jones based OPLS model of methanol [163] and the Lennard-Jones based EPM2 model of carbon dioxide [143] for their reaction Gibbs ensemble Monte Carlo simulations, and by Potoff et al. [323], who performed grand canonical histogram-reweighting Monte Carlo simulations using molecular models based on the exponential-6 potential. All those models are non-polarizable and have fixed point charges. They yield good agreement with experimental vapor-liquid equilibrium data.

In the present work, the non-polarizable model $\boldsymbol{M}_{\text{opt}}$ of methanol, cf. Chapter 5.2, and the simple, non-polarizable 2CLJQ model of carbon dioxide, cf. Table 8, were used for the calculation of vapor-liquid equilibria of this mixture. To the knowledge of the author the interaction of point charges and point quadrupoles was not yet investigated by molecular simulation methods. The vapor-liquid equilibria were obtained from the Grand Equilibrium method based on the gradual insertion method, cf. Appendix C.5 for technical details. These simulations are an important consistent extension of the modeling and simulation approach discussed in the previous chapters to mixtures containing associating components. The application of the gradual insertion method yielded the configurational

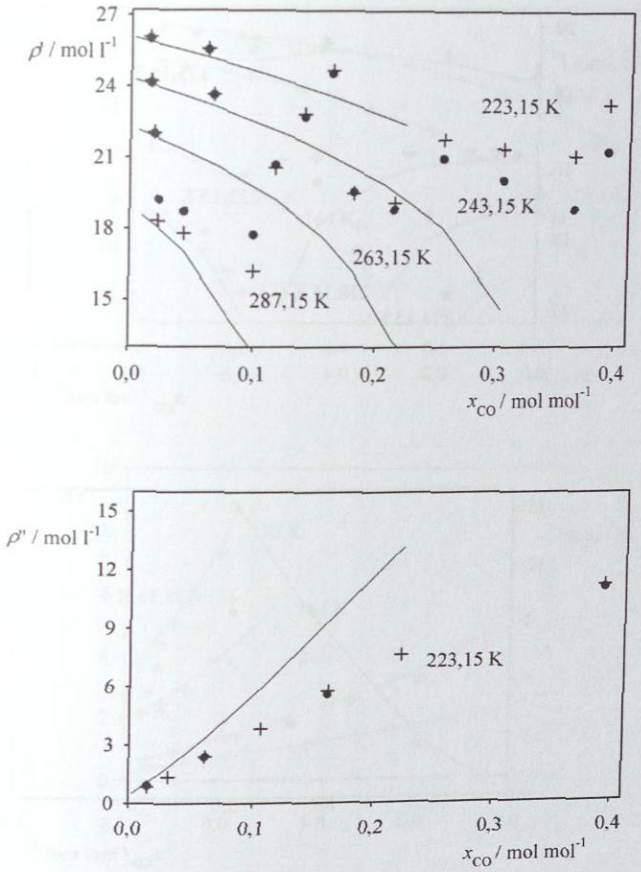

Figure 63: Saturated liquid density (top) and saturated vapor density (bottom) of the mixture $CO + CO_2$. ● *Simulation with adjusted* ξ, this work. —— Peng-Robinson equation of state ($k_{ij} = 0.03411$). + DDMIX [86, 88].

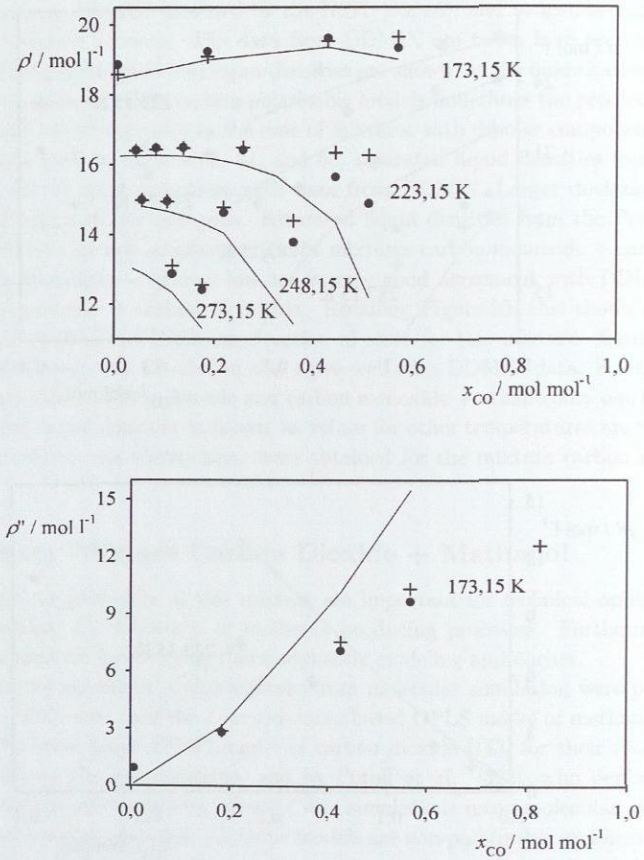

Figure 64: Saturated liquid density (top) and saturated vapor density (bottom) of the mixture CO + C_2H_6. ● Simulation with adjusted ξ, this work. —— Peng-Robinson equation of state ($k_{ij} = 0.01981$). + DDMIX [86, 88].

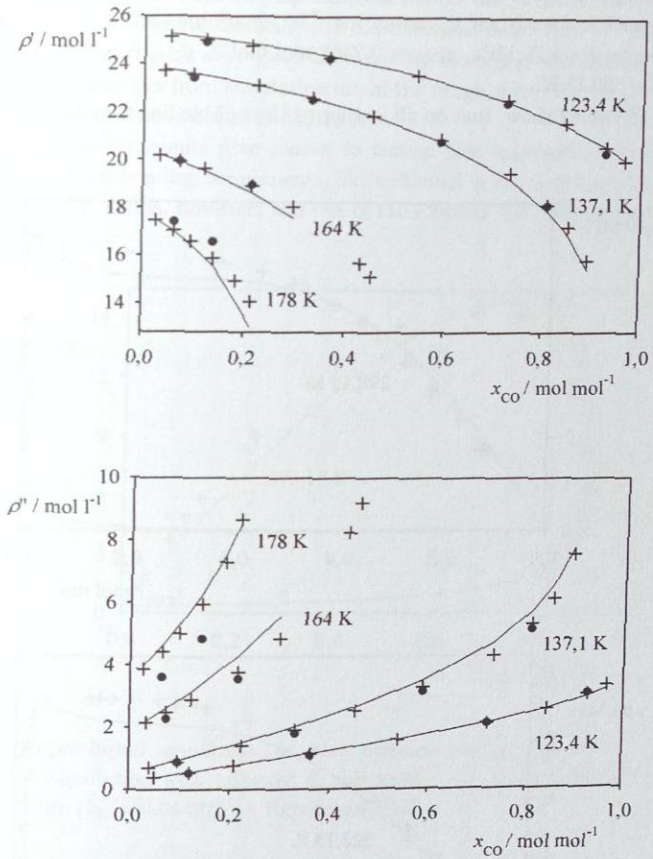

Figure 65: Saturated liquid density (top) and saturated vapor density (bottom) of the mixture CH_4 + CO. ● Simulation with adjusted ξ, this work. —— Peng-Robinson equation of state ($k_{ij} = 0.02550$). + DDMIX [86, 88].

part of the chemical potentials and the partial molar volumes of both components in the liquid phase with low statistical uncertainties. The binary interaction parameter $\xi = 1.124$ was adjusted to $p = 4.75$ MPa, $x_{CO_2} = 0.2368$ mol mol^{-1}, $y_{CO_2} \approx 0.98$ mol mol^{-1} on the isotherm $T = 323.15$ K.

Figures 66 and 67 show, that on all isotherms the bubble line from the Peng-Robinson

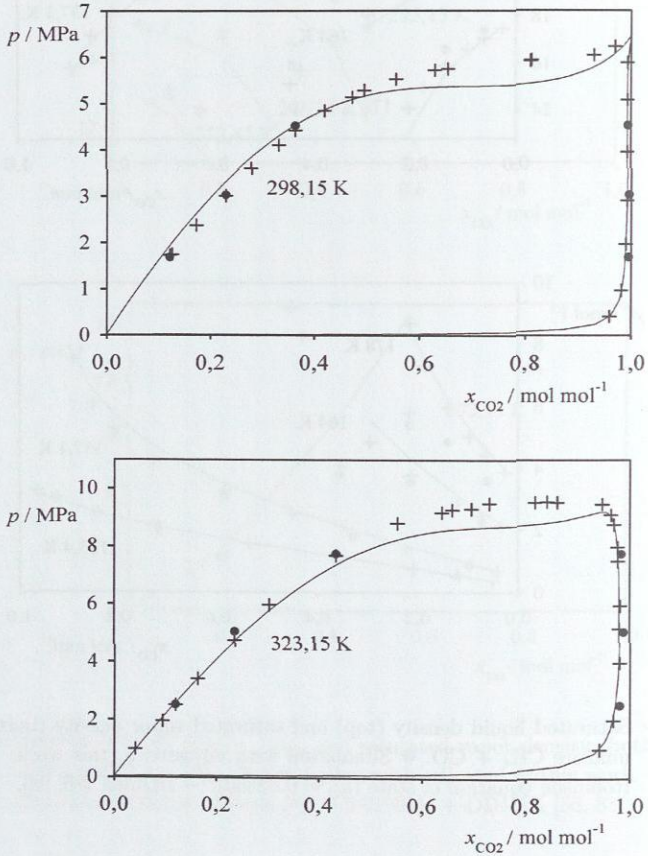

Figure 66: Vapor-liquid equilibria of the mixture carbon dioxide + methanol. ● Simulation with adjusted ξ, this work. —— Peng-Robinson equation of state ($k_{ij} = 0.04497$). + Experiment [31].

equation of state deviates from the experimental bubble line, whereas the present simulation results are in excellent agreement with experimental data. Also the saturated liquid densities are described with very good accuracy by molecular simulation, cf. Table 29. Saturated vapor densities from simulation are in the range of experimental values, though somewhat larger deviations occur at 323.15 K.

These encouraging results give reason to extend this approach to further mixtures containing hydrogen bonding components, like methanol + nitrogen/carbon monoxide, or methanol + water, which, however, was out of the scope of the present work.

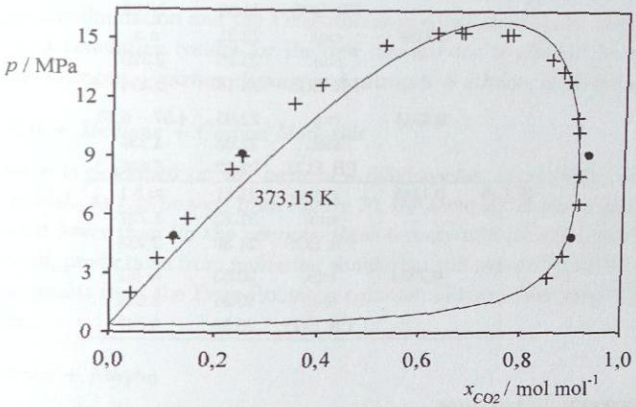

Figure 67: Vapor-liquid equilibria of the mixture carbon dioxide + methanol. ● Simulation with adjusted ξ, this work. —— Peng-Robinson equation of state ($k_{ij} = 0.04497$). + Experiment [31].

Table 29: Comparison of saturated densities of the mixture carbon dioxide + methanol from experiment [31] to results from molecular simulation and from the Peng-Robinson equation of state ($k_{ij} = 0.04497$).

T	x_{CO_2}		ρ'	ρ''
K	mol/mol		mol/l	mol/l
298.15	0.1214	exp.	24.36	n.a.
		sim.	24.36	0.738
		PR EOS	24.60	0.691

Table 29: continued.

T K	x_{CO_2} mol/mol		ρ' mol/l	ρ'' mol/l
298.15	0.2289	exp.	24.18	n.a.
		sim.	24.01	1.441
		PR EOS	24.32	1.300
	0.3642	exp.	23.60	n.a.
		sim.	23.62	2.424
		PR EOS	23.92	2.013
323.15	0.1197	exp.	23.54	n.a.
		sim.	23.51	1.025
		PR EOS	23.58	1.162
	0.2368	exp.	23.31	n.a.
		sim.	23.16	2.320
		PR EOS	23.18	2.494
	0.4344	exp.	22.05	4.57 – 6.83
		sim.	22.03	4.236
		PR EOS	22.32	5.435
373.15	0.1185	exp.	21.61	≈ 5.1
		sim.	21.72	1.737
		PR EOS	21.30	2.238
	0.2456	exp.	20.53	≈ 5.1
		sim.	20.91	3.524
		PR EOS	20.58	5.227

6.5 Ternary Mixtures

In the present work, pairwise additive interaction potentials are used for the modeling of molecular interactions, therefore ternary interaction parameters cannot be introduced. Hence, the molecular models developed on the basis of binary data can straightforwardly be applied without any alterations to predict vapor-liquid equilibria of ternary and multicomponent mixtures.

Vapor-liquid equilibria of five ternary systems containing unpolar, dipolar, or quadrupolar fluids were studied by the means of the Grand Equilibrium method: nitrogen + oxygen + carbon dioxide, nitrogen + carbon dioxide + ethane, ethane + ethene + ethyne, carbon monoxide + methane + carbon dioxide, R125 + R143a + R134a. Results from molecular simulation are compared to experimental data and to results from the Peng-Robinson equation of state.

Technical details of these simulations of ternary mixtures are given in Appendix C.4.

Nitrogen + Oxygen + Carbon Dioxide

Knowledge on vapor-liquid equilibria of this ternary mixture is needed in the food processing and brewing industry. In Figure 68, top, the mole fractions on the bubble

and on the dew lines are given at 232.85 K and 12.4 MPa. Predictions from molecular simulation are in excellent agreement with the experimental vapor-liquid equilibrium data. The Peng-Robinson equation of state yields good results for the dew line but shows clear deviations on the bubble line, which are due to shortcomings of the models for the binary systems. Similar results were obtained for 232.85 K and 5.17 MPa, cf. Figure 68, bottom, where vapor-liquid equilibria from simulation are compared to experimental data.

Nitrogen + Carbon Dioxide + Ethane

Results for the system nitrogen + carbon dioxide + ethane are shown in Figure 69. This system shows a strong curvature of the dew line which is predicted quantitatively both by molecular simulation and the Peng-Robinson equation of state. Slight deviations in the molecular simulation results for the dew line are due to similar deviations in the binary systems nitrogen + carbon dioxide and nitrogen + ethane, cf. Figures 38 and 40.

Carbon Dioxide + Methane + Carbon Monoxide

This mixture is described on the basis of a quadrupolar, an unpolar, and a dipolar 2CLJ-based model. As can be seen from Figure 70, the accuracy of the results on the dew line is somewhat lower than for the previous three ternary mixtures of quadrupolar components. Overall, predictions from molecular simulation still agree well with experimental data, whereas results from the Peng-Robinson equation of state show large deviations on the bubble line.

Ethane + Ethene + Ethyne

The present molecular models for the binary mixtures ethane + ethene, ethane + ethyne, and ethene + ethyne were used for the prediction of vapor-liquid equilibria of the ternary mixture ethane + ethene + ethyne, cf. Figure 71. The predictions from molecular simulation are in excellent agreement with experimental data, whereas phase equilibria from the Peng-Robinson equation of state show deviations.

R125 + R143a + R134a

Experimental data for this ternary refrigerant blend are available for two liquid compositions at various temperature and pressure states [180, 291]. The results from molecular simulation for this mixture of dipolar components are therefore listed in Tables 30 and 31, together with the experimental data. Over a wide temperature range the results from molecular simulation are in very good agreement with experimental data for both liquid compositions. Trustworthy results for other liquid phase compositions may be expected from this molecular model and can be interesting for engineering applications.

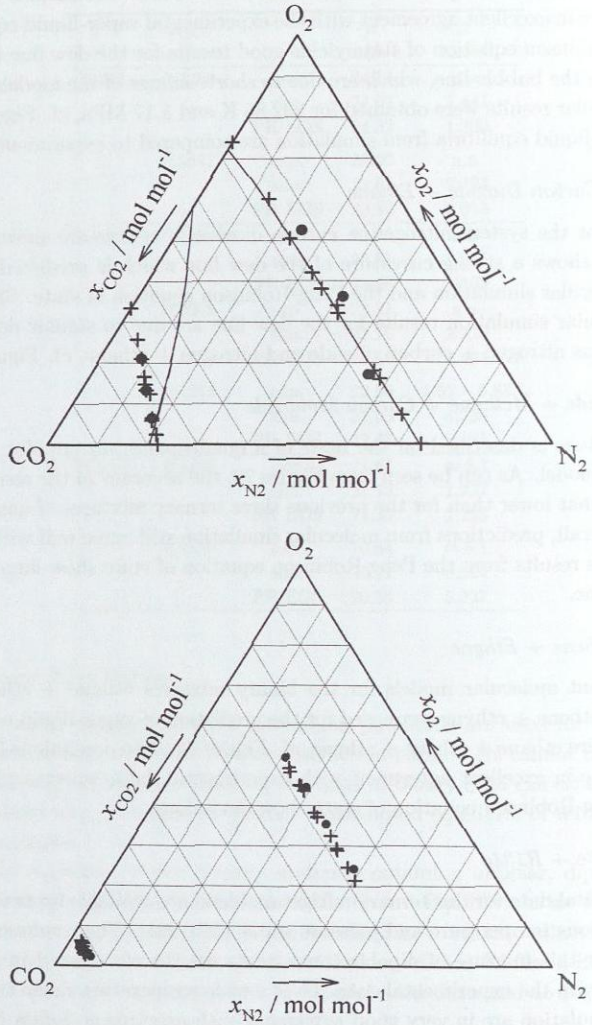

Figure 68: Vapor-liquid equilibria of the mixture N_2 + O_2 + CO_2 at $T = 232.85$ K, $p = 12.4$ MPa (top) and $T = 232.85$ K, $p = 5.17$ MPa (bottom). ● Simulation with ξ for binary subsystems adjusted, this work. —— Peng-Robinson equation of state with k_{ij} for binary subsystems adjusted. + Experiment [445].

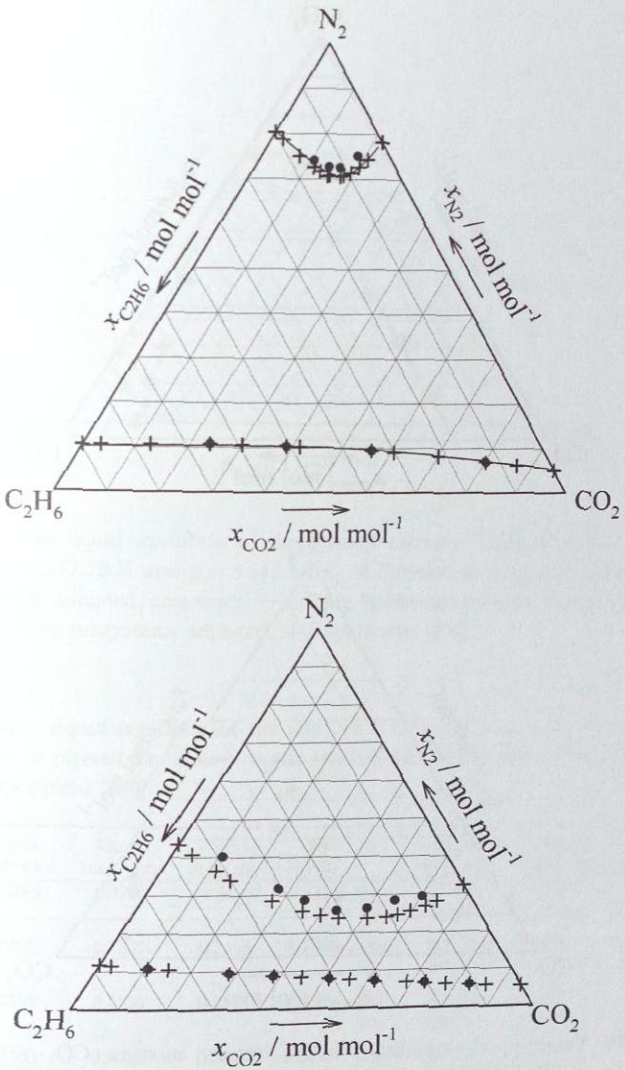

Figure 69: Vapor-liquid equilibria of the mixture N_2 + CO_2 + C_2H_6 at $T = 220$ K, $p = 4$ MPa (top), and $T = 270$ K, $p = 6$ MPa (bottom). ● *Simulation* with ξ for binary subsystems adjusted, this work. —— Peng-Robinson equation of state with k_{ij} for binary subsystems adjusted. + Experiment [29].

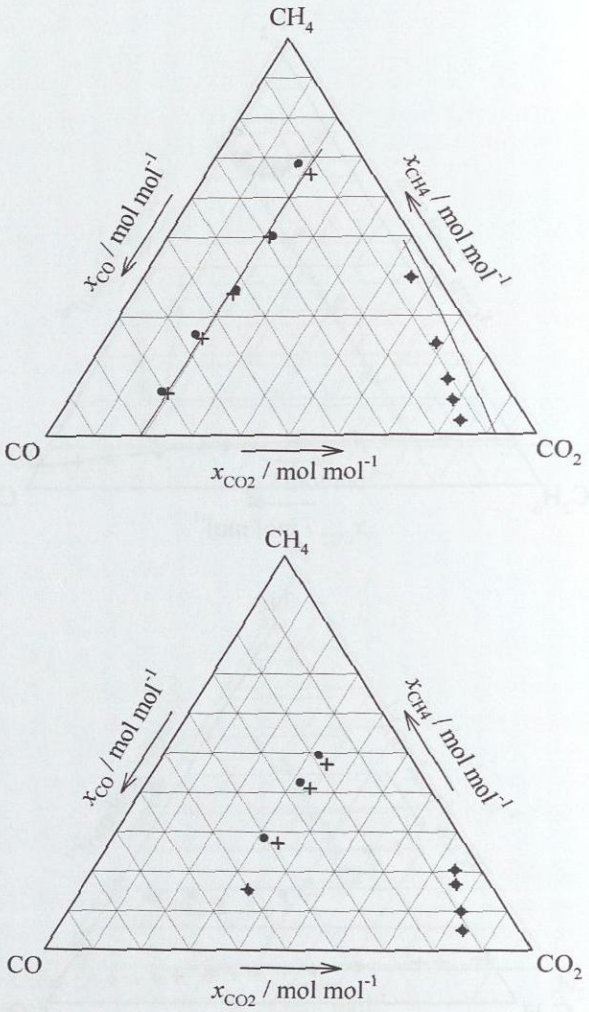

Figure 70: Vapor-liquid equilibria of the ternary mixture CO_2 + CH_4 + CO at $T = 223.15$ K and $p = 6.682$ MPa (top) and $T = 243.15$ K and $p = 6.899$ MPa (bottom). ● Simulation with ξ for binary subsystems adjusted, this work. —— Peng-Robinson equation of state with k_{ij} for binary subsystems adjusted. + Experiment [53].

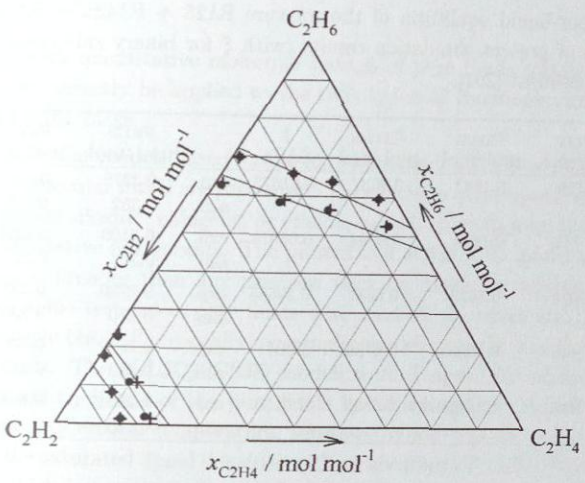

Figure 71: Vapor-liquid equilibria of the ternary mixture C_2H_6 + C_2H_4 + C_2H_2 at $T = 277.79$ K and $p = 3.547$ MPa. ● Simulation with ξ for binary subsystems adjusted, this work. —— Peng-Robinson equation of state with k_{ij} for binary subsystems adjusted. + Experiment [259].

Table 30: Vapor-liquid equilibria of the mixture R125 + R143a + R134a. Comparison of present simulation results (with ξ for binary subsystems adjusted) to experiment [180].

T K	x_{R125} mol/mol	x_{R143a} mol/mol	x_{R134a} mol/mol	p MPa		y_{R125} mol/mol	y_{R143a} mol/mol	y_{R134a} mol/mol
302.094	0.3299	0.3262	0.3439	1.1919	exp.	0.3909	0.3599	0.2492
					sim.	0.389	0.366	0.246
318.474	0.3235	0.3267	0.3498	1.7860	exp.	0.3777	0.3514	0.2709
					sim.	0.373	0.358	0.270
334.114	0.3197	0.3229	0.3574	2.5366	exp.	0.3602	0.3431	0.2967
					sim.	0.361	0.342	0.297
344.527	0.3163	0.3221	0.3616	3.1546	exp.	0.3474	0.3353	0.3173
					sim.	0.344	0.350	0.310

Table 31: Vapor-liquid equilibria of the mixture R125 + R143a + R134a. Comparison of present simulation results (with ξ for binary subsystems adjusted) to experiment [291].

T K	x_{R125} mol/mol	x_{R143a} mol/mol	x_{R134a} mol/mol	p MPa		y_{R125} mol/mol	y_{R143a} mol/mol	y_{R134a} mol/mol
204.557	0.1716	0.1647	0.6637	0.01675	exp.	0.3276	0.3109	0.3615
					sim.	0.352	0.235	0.413
223.286	0.1713	0.1643	0.6644	0.05019	exp.	0.3100	0.2826	0.4074
					sim.	0.314	0.252	0.434
263.988	0.1690	0.1623	0.6687	0.29685	exp.	0.2720	0.2381	0.4899
					sim.	0.270	0.236	0.494
303.158	0.1658	0.1603	0.6739	1.0041	exp.	0.2379	0.2087	0.5534
					sim.	0.233	0.217	0.550
343.288	0.1601	0.1569	0.6830	2.6110	exp.	0.2031	0.1842	0.6127
					sim.	0.193	0.186	0.622

7 Summary

In the present work quantitative molecular models of pure fluids and mixtures were developed, that can directly be applied to the calculation of thermophysical properties for chemical engineering tasks.

Effective molecular models based on the four-parameter 2CLJQ or 2CLJD model type for 78 real low-molecular fluids are presented. They include quadrupolar fluids, like nitrogen, oxygen, carbon dioxide, halogens, or ethane, as well as multipolar fluids, like carbon monoxide or alternative refrigerants. The present 2CLJQ/2CLJD modeling approach for real pure fluids is broader than any previous work on molecular modeling of pure fluids. Except for some test cases, only fluids were studied, for which the 2CLJQ/2CLJD model allows simple but still physically meaningful modeling of the molecular interactions of these real fluids. The 2CLJQ/2CLJD models were designed for accurate description of the vapor-liquid equilibria of the pure fluids by adjusting their model parameters to experimental data of critical temperature, saturated liquid density, and vapor pressure. They describe the saturated liquid densities with an accuracy of 0.5 % compared to experimental data, which is essentially better than results from conventional cubic equations of state. The vapor pressure is described with an accuracy of typically 3 %. Somewhat larger mean deviations of the vapor pressure occur in cases, for which the 2CLJQ/2CLJD modeling approach is too simplistic, for example for the refrigerant R32, or for other strongly asymmetric refrigerant molecules. For improvement, such fluids should rather be modeled individually and more elaborately. The models describe the enthalpy of vaporization with an accuracy typically better than 3 %, and they yield quantitative prediction of thermophysical properties also in the homogeneous fluid state far away from vapor-liquid equilibria. For the fluids studied here, the information on the thermophysical behavior of the pure fluid contained in vapor-liquid equilibrium data is sufficient for developing effective molecular models, which yield reliable predictive performance for the entire range of fluid states.

The rapid development of a large number of 2CLJQ/2CLJD models was possible, as in the present work a new method was applied, that is particularly well adapted to the parametrization of molecular models with a low number of adjustable model parameters. The vapor liquid equilibria of the 2CLJQ/2CLJD model fluids were comprehensively investigated with the NpT + Test Particle Method, and on the basis of this molecular simulation data empirical correlations of the critical temperature, the saturated liquid density and the vapor pressure of the 2CLJQ/2CLJD model fluids were developed. These correlations were used for the parametrization of the 2CLJQ/2CLJD models by fitting the model parameters to experimental data. This systematic modeling approach was more efficient than adjusting the 2CLJQ and 2CLJD model parameters for each real fluid individually. With this method, the final step in the development of quantitative molecular models was not more difficult than the adjustment of parameters of phenomenological

thermodynamic models.

The generalization of this optimization method to three or more adjustable model parameters is possible, but its efficiency becomes questionable for such cases. In this work, molecular models of ethylene oxide and methanol with three adjustable model parameters were optimized by another optimization method based on least squares minimization. Vapor-liquid equilibria of methanol, that were required for that optimization, were obtained from the NpT+Test Particle Method based on chemical potentials obtained from the gradual insertion method. This leads to results which are distinctly more accurate than those previously reported in literature.

The accuracy and the compatibility of the present molecular models with physically meaningful model parameters opens the route to applying them directly to the modeling of interactions of unlike molecules in real fluid mixtures. In the present work, 45 unlike interactions of unpolar, dipolar, or quadrupolar mixture components were uniformly modeled, which is the broadest systematic application of molecular simulation to the calculation of thermophysical properties of mixtures in literature. Modified Lorentz-Berthelot combining rules with an adjustable binary interaction parameter in the energetic term were used to describe the unlike Lennard-Jones interaction parameters. For enhanced quantitative description of vapor-liquid equilibria of mixtures, an efficient procedure was applied for the adjustment of the binary interaction parameter to a single experimental equilibrium pressure of the modeled mixture.

It was shown, that the present molecular models predict, without adjusted binary interaction parameter, vapor-liquid equilibria of mixtures more reliably than the Peng-Robinson equation of state. For instance, azeotropes were predicted by the molecular models, but not by the Peng-Robinson equation of state. With adjusted binary parameters, quantitative description of vapor-liquid equilibria of mixtures was obtained from the molecular models.

The present modeling approach with effective, non-polarizable molecular models held also for real mixtures of dipolar and strongly polarizable components.

The excellent performance of the present molecular models of unlike interactions was verified by the quantitative prediction of vapor-liquid equilibria of five ternary mixtures from molecular simulation.

The results of the present work show, that molecular modeling and simulation of real fluids and mixtures on the basis of relatively simple, but physically reasonable and carefully parametrized molecular models allows the quantitative prediction of thermophysical properties. These results underline, that molecular modeling and simulation methods offer a high potential for broader application. Future work should extend the present study to more complex fluids, in particular hydrogen bonding fluids, and larger molecules, for which the explicit modeling of internal degrees of freedom is indispensable. It should be verified, whether the present simple, effective, united-atom based modeling approach is still valid for those fluids. In the case of complex fluids, the NpT+Test Particle Method

based on gradual insertion is an excellent tool for the fine-tuning of model parameters. Quantum chemical calculations should help to specify the parameters of molecular models of complex fluids.

Many of the molecular models developed in the present work were already successfully applied to the quantitative prediction of further thermophysical properties, that are important for applications in process industry, like surface tensions and Henry's constants [414], or transport properties like diffusion coefficients [103, 104], viscosities, and thermal conductivities [105]. Also Joule-Thomson inversion curves are predicted quantitatively [419]. Usually, the description of these properties requires more than one classical model. This shows the excellent extrapolative quality of the present molecular models, and underlines, that "molecular simulation presents the advantage of providing a unified theoretical framework for the prediction of equilibrium and transport properties" [397].

Appendix A Forces, Torques, and Long-Range Corrections

Expressions for the intermolecular forces and torques, as well as expressions for the long-range corrections of the internal energy and the virial are given for m-component mixtures of multicenter Lennard-Jones fluids with linear point quadrupoles and point dipoles, cf. Appendices A.1, A.2, A.3 and A.5. In the case of model fluids with point charges, the expressions are given for a pure fluid or for a binary mixture only, cf. Appendices A.4 and A.6.

For the calculation of the configurational part of the chemical potential (and the partial molar volume), long-range corrections for the interaction energy ψ_{ia} of the inserted molecule i of component a with all other molecules

$$\psi_{ia} = \sum_{b=1}^{m} \sum_{j=1}^{N_b} u_{ij}^{ab}, \tag{150}$$

are given. Equation (150) contains contributions from Lennard-Jones and from electrostatic interactions.

All expressions are given for non-spherical molecules, i.e. a''-components as defined in Chapter 2.2. Orientational averaging disappears for spherical molecules.

A.1 Lennard-Jones Interaction

A.1.1 Forces and Torques

The Lennard-Jones interactions of two multicenter Lennard-Jones molecules i of type a and j of type b in a m-component mixture are considered. Each Lennard-Jones site s on molecule i interacts with each Lennard-Jones site k on molecule j, i.e. a total of $s \cdot k$ Lennard-Jones interactions between these molecules have to be evaluated. Let $\boldsymbol{r}_i$ and $\boldsymbol{r}_j$ be the position vectors of the centers of mass of these molecules, and $\Delta\boldsymbol{r}_{is}$ and $\Delta\boldsymbol{r}_{jk}$ the vectors pointing from the centers of mass to the site locations. Then $\boldsymbol{r}_{ij} = \boldsymbol{r}_i - \boldsymbol{r}_j$ is the center of mass distance vector, $\boldsymbol{r}_{is} = \boldsymbol{r}_i + \Delta\boldsymbol{r}_{is}$ and $\boldsymbol{r}_{jk} = \boldsymbol{r}_j + \Delta\boldsymbol{r}_{jk}$ are the position vectors of the sites, and $\boldsymbol{r}_{isjk} = \boldsymbol{r}_{is} - \boldsymbol{r}_{jk} = r_{isjk} \cdot \boldsymbol{e}_{isjk}$ is the site-site distance vector, wherein $r_{isjk} = |\boldsymbol{r}_{isjk}|$ and $\boldsymbol{e}_{isjk} = \boldsymbol{r}_{isjk}/r_{isjk}$. With these definitions, the force on the Lennard-Jones site s on molecule i due to the Lennard-Jones site k on molecule j is

$$\boldsymbol{F}_{isjk}^{\mathrm{LJ}ab} = -\frac{\partial u_{isjk}^{\mathrm{LJ}ab}(r_{isjk})}{\partial \boldsymbol{r}_{isjk}} = -\frac{\partial u_{isjk}^{\mathrm{LJ}ab}(r_{isjk})}{\partial r_{isjk}} \cdot \boldsymbol{e}_{isjk}, \tag{151}$$

that evaluates with the Lennard-Jones potential function

$$u_{isjk}^{\mathrm{LJ}ab}(\boldsymbol{r}_{isjk}) = 4\varepsilon_{isjk}^{ab}\left[\left(\frac{\sigma_{isjk}^{ab}}{r_{isjk}}\right)^{12} - \left(\frac{\sigma_{isjk}^{ab}}{r_{isjk}}\right)^{6}\right] \tag{152}$$

as

$$F_{isjk}^{\mathrm{LJ}ab} = \frac{24\varepsilon_{isjk}^{ab}}{r_{isjk}} \left[2\left(\frac{\sigma_{isjk}^{ab}}{r_{isjk}}\right)^{12} - \left(\frac{\sigma_{isjk}^{ab}}{r_{isjk}}\right)^{6} \right] \cdot \boldsymbol{e}_{isjk}. \tag{153}$$

This force causes a torque on molecule i with respect to its center of mass

$$\boldsymbol{\tau}_{isjk}^{\mathrm{LJ}ab} = \Delta\boldsymbol{r}_{is} \times \boldsymbol{F}_{isjk}^{\mathrm{LJ}ab}. \tag{154}$$

The force on site k on molecule j due to site s on molecule i is

$$\boldsymbol{F}_{jkis}^{\mathrm{LJ}ba} = -\boldsymbol{F}_{isjk}^{\mathrm{LJ}ab}, \tag{155}$$

and the torque on molecule j with respect to its center of mass is

$$\boldsymbol{\tau}_{jkis}^{\mathrm{LJ}ba} = \Delta\boldsymbol{r}_{js} \times \boldsymbol{F}_{jkis}^{\mathrm{LJ}ba} \neq \boldsymbol{\tau}_{isjk}^{\mathrm{LJ}ab}. \tag{156}$$

In isotropic, homogeneous media the long-range corrections of Lennard-Jones forces and torques are zero.

A.1.2 Internal Energy

The long-range correction for a fluid mixture of m rigid multicenter Lennard-Jones components is derived for the NVT-ensemble. The resulting long-range correction for the internal energy, cf. Equation (177), is also valid for the NpT-ensemble, when the density ρ is replaced by the NpT-average $\langle\rho\rangle_{NpT}$.

The contribution of the Lennard-Jones interactions to the configurational part of the internal energy is

$$\begin{aligned} U^{\mathrm{LJ}}(\Gamma_{NVT}^{\mathrm{c}}) &= \sum_{a=1}^{m} u^{\mathrm{LJ}aa}\left(\Gamma_{a,NVT}^{\mathrm{c}}\right) \\ &\quad + \sum_{a=1}^{m-1}\sum_{b=a+1}^{m} u^{\mathrm{LJ}ab}\left(\Gamma_{a,NVT}^{\mathrm{c}}\Gamma_{b,NVT}^{\mathrm{c}}\right) \qquad (157) \\ &= \sum_{a=1}^{m}\frac{1}{2}\sum_{i=1}^{N_a}\sum_{j\neq i}^{N_a}\sum_{s,k} u_{isjk}^{\mathrm{LJ}aa}\left(\gamma_{ia,NVT}^{\mathrm{c}}\gamma_{ja,NVT}^{\mathrm{c}}\right) \\ &\quad + \sum_{a=1}^{m-1}\sum_{b=a+1}^{m}\sum_{i=1}^{N_a}\sum_{j=1}^{N_b}\sum_{s,k} u_{isjk}^{\mathrm{LJ}ab}\left(\gamma_{ia,NVT}^{\mathrm{c}}\gamma_{jb,NVT}^{\mathrm{c}}\right), \qquad (158) \end{aligned}$$

wherein the sums on the indices s and k count the Lennard-Jones sites on molecules i and j, respectively. The phase space variable sets in Equations (157) and (158) are explained

in Chapter 2. In the NVT-ensemble, the average value of the configurational part of the internal energy per molecule is

$$\langle u^{\mathrm{LJ}}\rangle = \frac{1}{NQ^{\mathrm{c}}}\int_{\Gamma^{\mathrm{c}}} e^{-\beta U^{\mathrm{LJ}}(\Gamma^{\mathrm{c}})} U^{\mathrm{LJ}}(\Gamma^{\mathrm{c}}) \prod_{a=1}^{m} d\Gamma_a^{\mathrm{c}}, \tag{159}$$

wherein the index NVT is omitted and Q^{c} according to Equation (36). Separating like and unlike interactions, Equation (159) yields

$$\begin{aligned}\langle u^{\mathrm{LJ}}\rangle \;=\; & \frac{1}{N}\sum_{a=1}^{m}\frac{1}{Q^{\mathrm{c}}}\int_{\Gamma^{\mathrm{c}}} e^{-\beta U^{\mathrm{LJ}}(\Gamma^{\mathrm{c}})} U^{\mathrm{LJ}aa}(\Gamma_a^{\mathrm{c}})\, d\Gamma_a^{\mathrm{c}} \prod_{\bar{a}\neq a}^{m} d\Gamma_{\bar{a}}^{\mathrm{c}} \\ & + \frac{1}{N}\sum_{a=1}^{m-1}\sum_{b=a+1}^{m}\frac{1}{Q^{\mathrm{c}}}\int_{\Gamma^{\mathrm{c}}} e^{-\beta U^{\mathrm{LJ}}(\Gamma^{\mathrm{c}})} U^{\mathrm{LJ}ab}(\Gamma_a^{\mathrm{c}}\Gamma_b^{\mathrm{c}})\, d\Gamma_a^{\mathrm{c}} d\Gamma_b^{\mathrm{c}} \prod_{\bar{a}\neq a,b}^{m} d\Gamma_{\bar{a}}^{\mathrm{c}},\end{aligned} \tag{160}$$

or, applying Equation (158),

$$\begin{aligned}\langle u^{\mathrm{LJ}}\rangle = \; & \frac{1}{N}\sum_{a=1}^{m}\frac{1}{Q^{\mathrm{c}}}\int_{\Gamma^{\mathrm{c}}} e^{-\beta U^{\mathrm{LJ}}(\Gamma^{\mathrm{c}})}\left[\frac{1}{2}\sum_{i=1}^{N_a}\sum_{j\neq i}^{N_a}\sum_{s,k} u_{isjk}^{\mathrm{LJ}aa}\left(\gamma_{ia}^{\mathrm{c}}\gamma_{ja}^{\mathrm{c}}\right)\right] d\Gamma_a^{\mathrm{c}} \prod_{\bar{a}\neq a}^{m} d\Gamma_{\bar{a}}^{\mathrm{c}} \\ & + \frac{1}{N}\sum_{a=1}^{m-1}\sum_{b=a+1}^{m}\frac{1}{Q^{\mathrm{c}}}\int_{\Gamma^{\mathrm{c}}} e^{-\beta U^{\mathrm{LJ}}(\Gamma^{\mathrm{c}})}\left[\sum_{i=1}^{N_a}\sum_{j=1}^{N_b}\sum_{s,k} u_{isjk}^{\mathrm{LJ}ab}\left(\gamma_{ia}^{\mathrm{c}}\gamma_{jb}^{\mathrm{c}}\right)\right] d\Gamma_a^{\mathrm{c}} d\Gamma_b^{\mathrm{c}} \prod_{\bar{a}\neq a,b}^{m} d\Gamma_{\bar{a}}^{\mathrm{c}}.\end{aligned} \tag{161}$$

Interchanging in the terms of like and unlike interactions the double summation on particle numbers and the integration, and noting explicitly the integration on the phase space coordinates of particles i and j yields

$$\begin{aligned}\langle u^{\mathrm{LJ}}\rangle = \; & \frac{1}{N}\sum_{a=1}^{m}\frac{1}{2}\sum_{i=1}^{N_a}\sum_{j\neq i}^{N_a}\sum_{s,k}\frac{1}{Q^{\mathrm{c}}}\int_{\Gamma^{\mathrm{c}}} e^{-\beta U^{\mathrm{LJ}}(\Gamma^{\mathrm{c}})} u_{isjk}^{\mathrm{LJ}aa}\left(\gamma_{ia}^{\mathrm{c}}\gamma_{ja}^{\mathrm{c}}\right) \prod_{\bar{a}\neq a}^{m} d\Gamma_{\bar{a}}^{\mathrm{c}} d\Gamma_{a\setminus ij}^{\mathrm{c}} d\gamma_{ia}^{\mathrm{c}} d\gamma_{ja}^{\mathrm{c}} \\ & + \frac{1}{N}\sum_{a=1}^{m-1}\sum_{b=a+1}^{m}\sum_{i=1}^{N_a}\sum_{j=1}^{N_b}\sum_{s,k}\frac{1}{Q^{\mathrm{c}}}\int_{\Gamma^{\mathrm{c}}} e^{-\beta U^{\mathrm{LJ}}(\Gamma^{\mathrm{c}})} u_{isjk}^{\mathrm{LJ}ab}\left(\gamma_{ia}^{\mathrm{c}}\gamma_{jb}^{\mathrm{c}}\right) \prod_{\bar{a}\neq a,b}^{m} d\Gamma_{\bar{a}}^{\mathrm{c}} d\Gamma_{a\setminus i}^{\mathrm{c}} d\Gamma_{b\setminus j}^{\mathrm{c}} d\gamma_{ia}^{\mathrm{c}} d\gamma_{jb}^{\mathrm{c}}.\end{aligned} \tag{162}$$

Herein, the notation $\Gamma_{a\setminus ij}^{\mathrm{c}}$ symbolizes the omission of γ_{ia}^{c} and γ_{ja}^{c}. It is now obvious, that for any two fixed particle indices, the integrals in Equation (162) yield the same results and can therefore be replaced by $\frac{1}{2}N_a(N_a-1)\approx\frac{1}{2}N_a^2$ terms in the case of like interactions, or N_aN_b terms in the case of unlike interactions, wherein the integration only is on particles, say number 1 and 2 of each species a in the case of the like interactions, and number 1 of species a and b in the case of unlike interactions, i.e.

$$\begin{aligned}\langle u^{\mathrm{LJ}}\rangle = \; & \sum_{a=1}^{m}\frac{N_a^2}{2N}\sum_{s,k}\int u_{1s2k}^{\mathrm{LJ}aa}\left(\gamma_{1a}^{\mathrm{c}}\gamma_{2a}^{\mathrm{c}}\right)\left[\frac{1}{Q^{\mathrm{c}}}\int e^{-\beta U^{\mathrm{LJ}}(\Gamma^{\mathrm{c}})}\prod_{\bar{a}\neq a}^{m} d\Gamma_{\bar{a}}^{\mathrm{c}} d\Gamma_{a\setminus 12}^{\mathrm{c}}\right] d\gamma_{1a}^{\mathrm{c}} d\gamma_{2a}^{\mathrm{c}} \\ & + \sum_{a=1}^{m-1}\sum_{b=a+1}^{m}\frac{N_aN_b}{N}\sum_{s,k}\int u_{1s1k}^{\mathrm{LJ}ab}\left(\gamma_{1a}^{\mathrm{c}}\gamma_{1b}^{\mathrm{c}}\right)\left[\frac{1}{Q^{\mathrm{c}}}\int e^{-\beta U^{\mathrm{LJ}}(\Gamma^{\mathrm{c}})}\prod_{\bar{a}\neq a,b}^{m} d\Gamma_{\bar{a}}^{\mathrm{c}} d\Gamma_{a\setminus 1}^{\mathrm{c}} d\Gamma_{b\setminus 1}^{\mathrm{c}}\right] d\gamma_{1a}^{\mathrm{c}} d\gamma_{1b}^{\mathrm{c}}.\end{aligned} \tag{163}$$

The expressions in Equation (163) are already rearranged in order to identify conveniently the pair distribution functions for like and unlike pairs of molecules in terms of the configurational phase space variables

$$g^{aa}_{(2)}(\gamma^{c}_{1a},\gamma^{c}_{2a}) = V^2\Omega_{aa}\frac{1}{Q^c}\int e^{-\beta U^{LJ}(\Gamma^c)}\prod_{\bar{a}\neq a}^{m} d\Gamma^{c}_{\bar{a}} d\Gamma^{c}_{a\backslash 12}, \tag{164}$$

$$g^{ab}_{(2)}(\gamma^{c}_{1a},\gamma^{c}_{1b}) = V^2\Omega_{ab}\frac{1}{Q^c}\int e^{-\beta U^{LJ}(\Gamma^c)}\prod_{\bar{a}\neq a,b}^{m} d\Gamma^{c}_{\bar{a}} d\Gamma^{c}_{a\backslash 1} d\Gamma^{c}_{b\backslash 1}, \tag{165}$$

wherein Ω_{aa}, Ω_{ab} according to Equation (272). With Equations (164) and (165), Equation (163) becomes

$$\begin{aligned}\langle u^{LJ}\rangle = &\sum_{a=1}^{m}\frac{N_a^2}{2NV^2}\sum_{s,k}\frac{1}{\Omega_{aa}}\int u^{LJaa}_{1s2k}(\gamma^{c}_{1a},\gamma^{c}_{2a})\, g^{aa}_{(2)}(\gamma^{c}_{1a},\gamma^{c}_{2a})\, d\gamma^{c}_{1a} d\gamma^{c}_{2a}\\ &+\sum_{a=1}^{m-1}\sum_{b=a+1}^{m}\frac{N_a N_b}{NV^2}\sum_{s,k}\frac{1}{\Omega_{ab}}\int u^{LJab}_{1s1k}(\gamma^{c}_{1a},\gamma^{c}_{1b})\, g^{ab}_{(2)}(\gamma^{c}_{1a},\gamma^{c}_{1b})\, d\gamma^{c}_{1a} d\gamma^{c}_{1b}.\end{aligned} \tag{166}$$

As the fluide mixture is considered isotropic and homogeneous, the pair distribution functions depend only on pair distances and on relative pair orientations, noted here as γ^{c}_{12aa} for pairs of like molecules and γ^{c}_{11ab} for pairs of unlike molecules. Then Equation (166) is rewritten as

$$\begin{aligned}\langle u^{LJ}\rangle = &\sum_{a=1}^{m}\frac{N_a^2}{2NV^2}\sum_{s,k}\frac{1}{\Omega_{aa}}\int u^{LJaa}_{1s2k}(\gamma^{c}_{12aa})\, g^{aa}(\gamma^{c}_{12aa})\, d\gamma^{c}_{12aa} d\gamma^{c}_{1a}\\ &+\sum_{a=1}^{m-1}\sum_{b=a+1}^{m}\frac{N_a N_b}{NV^2}\sum_{s,k}\frac{1}{\Omega_{ab}}\int u^{LJab}_{1s1k}(\gamma^{c}_{11ab})\, g^{ab}(\gamma^{c}_{11ab})\, d\gamma^{c}_{11ab} d\gamma^{c}_{1a}.\end{aligned} \tag{167}$$

The integration on the configurational phase space variables $d\gamma^{c}_{1a}$ can be evaluated directly, i.e.

$$\begin{aligned}\langle u^{LJ}\rangle = &\sum_{a=1}^{m}\frac{N_a^2}{2NV}\sum_{s,k}\frac{1}{\bar{\Omega}_{aa}}\int u^{LJaa}_{1s2k}(\gamma^{c}_{12aa})\, g^{aa}(\gamma^{c}_{12aa})\, d\gamma^{c}_{12aa}\\ &+\sum_{a=1}^{m-1}\sum_{b=a+1}^{m}\frac{N_a N_b}{NV}\sum_{s,k}\frac{1}{\bar{\Omega}_{ab}}\int u^{LJab}_{1s1k}(\gamma^{c}_{11ab})\, g^{ab}(\gamma^{c}_{11ab})\, d\gamma^{c}_{11ab},\end{aligned} \tag{168}$$

wherein $\bar{\Omega}_{aa}$ is defined as

$$\bar{\Omega}_{aa} = \frac{\Omega_{aa}}{\int d\gamma^{c,rot}_{1a}}. \tag{169}$$

$\bar{\Omega}_{ab}$ is defined accordingly.

With mole fractions and particle density according to

$$\frac{N_a^2}{2NV} = \frac{1}{2}x_a^2\rho, \tag{170}$$

$$\frac{N_aN_b}{NV} = x_ax_b\rho, \tag{171}$$

and with separate integration over the relative pair distances and the relative pair orientations, i.e. $d\gamma_{12aa}^c = d\boldsymbol{\omega}_{12aa}d\boldsymbol{r}_{12aa}$ and $d\gamma_{11ab}^c = d\boldsymbol{\omega}_{11ab}d\boldsymbol{r}_{11ab}$, Equation (168) finally yields

$$\begin{aligned}\langle u^{\mathrm{LJ}}\rangle = \; & \rho\sum_{a=1}^{m}\frac{1}{2}x_a^2\sum_{s,k}\int_V\frac{1}{\bar{\Omega}_{aa}}\int_\Omega u_{1s2k}^{\mathrm{LJ}aa}(\boldsymbol{r}_{12aa}\boldsymbol{\omega}_{12aa})g^{aa}(\boldsymbol{r}_{12aa}\boldsymbol{\omega}_{12aa})d\boldsymbol{\omega}_{12aa}d\boldsymbol{r}_{12aa} \\ & +\rho\sum_{a=1}^{m-1}\sum_{b=a+1}^{m}x_ax_b\sum_{s,k}\int_V\frac{1}{\bar{\Omega}_{ab}}\int_\Omega u_{1s1k}^{\mathrm{LJ}ab}(\boldsymbol{r}_{11ab}\boldsymbol{\omega}_{11ab})g^{ab}(\boldsymbol{r}_{11ab}\boldsymbol{\omega}_{11ab})d\boldsymbol{\omega}_{11ab}d\boldsymbol{r}_{11ab}.\end{aligned} \tag{172}$$

Expressions for the long-range corrections of the Lennard-Jones contribution to the internal energy are deduced from Equation (172). For that purpose, the volume integrals are split up into integrals over a spherical volume of cut-off radius r_c and the remaining long-range integrals, that extend to infinity for a very large system supposed by the means of periodical boundary conditions in the molecular simulations. The expressions within the cut-off sphere are not considered here, as molecular simulations are performed to evaluate them. With the assumption, that the pair distribution functions are approximately unity beyond the cut-off sphere, the long-range correction for the Lennard-Jones contributions to the internal energy is

$$\begin{aligned}u^{\mathrm{LJ,LR}} = \; & \rho\sum_{a=1}^{m}\frac{1}{2}x_a^2\sum_{s,k}\int_{\boldsymbol{r}_c}^{\infty}\frac{1}{\bar{\Omega}_{aa}}\int_\Omega u_{1s2k}^{\mathrm{LJ}aa}(\boldsymbol{r}_{12aa}\boldsymbol{\omega}_{12aa})\,d\boldsymbol{\omega}_{12aa}d\boldsymbol{r}_{12aa} \\ & +\rho\sum_{a=1}^{m-1}\sum_{b=a+1}^{m}x_ax_b\sum_{s,k}\int_{\boldsymbol{r}_c}^{\infty}\frac{1}{\bar{\Omega}_{ab}}\int_\Omega u_{1s1k}^{\mathrm{LJ}ab}(\boldsymbol{r}_{11ab}\boldsymbol{\omega}_{11ab})\,d\boldsymbol{\omega}_{11ab}d\boldsymbol{r}_{11ab}.\end{aligned} \tag{173}$$

With the orientational averages of the Lennard-Jones potential functions

$$\langle u_{1s2k}^{\mathrm{LJ}aa}(\boldsymbol{r}_{12aa}\boldsymbol{\omega}_{12aa})\rangle_{\boldsymbol{\omega}_{12aa}} = \frac{1}{\bar{\Omega}_{aa}}\int_\Omega u_{1s2k}^{\mathrm{LJ}aa}(\boldsymbol{r}_{12aa}\boldsymbol{\omega}_{12aa})\,d\boldsymbol{\omega}_{12aa} \tag{174}$$

$$\langle u_{1s1k}^{\mathrm{LJ}ab}(\boldsymbol{r}_{11ab}\boldsymbol{\omega}_{11ab})\rangle_{\boldsymbol{\omega}_{11ab}} = \frac{1}{\bar{\Omega}_{ab}}\int_\Omega u_{1s1k}^{\mathrm{LJ}ab}(\boldsymbol{r}_{11ab}\boldsymbol{\omega}_{11ab})\,d\boldsymbol{\omega}_{11ab}, \tag{175}$$

and with the spherical integration written as unidimensional integration

$$\int_{\boldsymbol{r}_c}^{\infty}d\boldsymbol{r} = \int_{r_c}^{\infty}4\pi r^2dr, \tag{176}$$

Equation (173) becomes

$$u^{\mathrm{LJ,LR}} = \rho \sum_{a=1}^{m} \frac{1}{2} x_a^2 \sum_{s,k} 4\pi \int_{r_c}^{\infty} \langle u_{1s2k}^{\mathrm{LJaa}}(r_{12aa}\boldsymbol{\omega}_{12aa})\rangle_{\boldsymbol{\omega}_{12aa}} r_{12aa}^2 dr_{12aa}$$
$$+\rho \sum_{a=1}^{m-1} \sum_{b=a+1}^{m} x_a x_b \sum_{s,k} 4\pi \int_{r_c}^{\infty} \langle u_{1s1k}^{\mathrm{LJab}}(r_{11ab}\boldsymbol{\omega}_{11ab})\rangle_{\boldsymbol{\omega}_{11ab}} r_{11ab}^2 dr_{11ab}. \quad (177)$$

Lustig [239] has given analytical expressions for the evaluation of the orientational averages of the Lennard-Jones potential functions contained in Equation (177). Note, that in the case of rigid molecules all orientational averages contained in Equation (177) are decoupled. Summing up the analytical expressions from Lustig [239] is therefore correct [240]. Equation (177) also applies to the NpT-ensemble, when the density is replaced by its ensemble average $\langle\rho\rangle_{NpT}$.

A.1.3 Pressure

The average pressure for this mixture is

$$\langle p\rangle = \rho k_{\mathrm{B}}T - \frac{\rho}{3N} \sum_{a=1}^{m} \frac{1}{Q^{\mathrm{c}}} \int_{\Gamma^{\mathrm{c}}} e^{-\beta U^{\mathrm{LJ}}(\Gamma^{\mathrm{c}})} \left[\frac{1}{2} \sum_{i=1}^{N_a-1} \sum_{j\neq i}^{N_a} \boldsymbol{r}_{ijaa} \sum_{s,k} \frac{\partial u_{isjk}^{\mathrm{LJaa}}}{\partial \boldsymbol{r}_{ijaa}} \right] d\Gamma_a^{\mathrm{c}} \prod_{\bar{a}\neq a}^{m} d\Gamma_{\bar{a}}^{\mathrm{c}}$$
$$-\frac{\rho}{3N} \sum_{a=1}^{m-1} \sum_{b=a+1}^{m} \frac{1}{Q^{\mathrm{c}}} \int_{\Gamma^{\mathrm{c}}} e^{-\beta U^{\mathrm{LJ}}(\Gamma^{\mathrm{c}})} \left[\frac{1}{2} \sum_{i=1}^{N_a} \sum_{j=1}^{N_b} \boldsymbol{r}_{ijab} \sum_{s,k} \frac{\partial u_{isjk}^{\mathrm{LJab}}}{\partial \boldsymbol{r}_{ijab}} \right] d\Gamma_a^{\mathrm{c}} d\Gamma_b^{\mathrm{c}} \prod_{\bar{a}\neq a,b}^{m} d\Gamma_{\bar{a}}^{\mathrm{c}}. \quad (178)$$

After transformations analogous to those demonstrated for the internal energy, Equation (178) finally yields for the long-range corrections of the configurational part of the pressure

$$p^{\mathrm{LJ,LR}} = -\frac{1}{2}\cdot\frac{1}{3}\cdot\rho^2 \sum_{a=1}^{m} x_a^2 \sum_{s,k} 4\pi \int_{r_c}^{\infty} \langle r_{12aa} \frac{\partial u_{1s2k}^{\mathrm{LJaa}}}{\partial r_{12aa}} \rangle_{\boldsymbol{\omega}_{12aa}} r_{12aa}^2 dr_{12aa}$$
$$-\frac{1}{3}\cdot\rho^2 \sum_{a=1}^{m-1} \sum_{b=a+1}^{m} x_a x_b \sum_{s,k} 4\pi \int_{r_c}^{\infty} \langle r_{11ab} \frac{\partial u_{1s1k}^{\mathrm{LJab}}}{\partial r_{11ab}} \rangle_{\boldsymbol{\omega}_{11ab}} r_{11ab}^2 dr_{11ab}. \quad (179)$$

Note, that

$$\frac{\partial u_{1s2k}^{\mathrm{LJaa}}}{\partial \boldsymbol{r}_{12aa}} \equiv \frac{\partial u_{1s2k}^{\mathrm{LJaa}}}{\partial \boldsymbol{r}_{1s2kaa}}. \quad (180)$$

The same is true for the derivative of u_{11sk}^{LJab} in Equation (179). For the analytical evaluation of Equation (179) refer to the comment to Equation (177).

A.1.4 Chemical Potential

On the basis of the spherical cut-off concept, the Lennard-Jones contribution to the interaction energy ψ_{ia} of the inserted molecule i of species a with all other molecules in the mixture, cf. Equation (150), is

$$\psi_{ia}^{\mathrm{LJ}} = \sum_{b=1}^{m} \sum_{\substack{j=1 \\ r_{ij}<r_c}}^{N_b} \sum_{s} \sum_{k} u_{isjk}^{\mathrm{LJ}ab} + \psi_a^{\mathrm{LJ,LR}}. \tag{181}$$

The cut-off sphere of radius r_c is centered on the position of the inserted molecule. In Equation (181), the long-range correction is

$$\psi_a^{\mathrm{LJ,LR}} = \rho \sum_{b=1}^{m} x_b \sum_{s} \sum_{k} \int_{r_c}^{\infty} \langle u_{sk}^{\mathrm{LJ}ab} \rangle \omega_{ab} 4\pi r^2 dr. \tag{182}$$

A.2 Point Quadrupole Interaction

A m-component mixture of quadrupolar fluids is considered. Each molecule of each species has an elongated point quadrupole located in its center of mass. The pair interaction potential of the elongated point quadrupoles Q_i^a and Q_j^b located on molecule i of species a and molecule j of species b is, cf. Chapter 3.1,

$$u_{ij}^{QQab} = \frac{1}{4\pi\varepsilon_0}\frac{3}{4}\frac{Q_i^a Q_j^b}{|\boldsymbol{r}_{ij}|^5}\left[1-5\left(c_i^2+c_j^2\right)-15c_i^2c_j^2+2\left(c_{ij}-5c_ic_j\right)^2\right], \tag{183}$$

wherein $c_i = \cos\theta_i^a$, $c_j = \cos\theta_j^b$, and $c_{ij} = \cos\gamma_{ij}^{ab}$. The angles θ_i^a, θ_j^b, and γ_{ij}^{ab} indicate the relative angular orientation of the two point quadrupoles. If the fluid surrounding the cut-off sphere is assumed isotropic and homogeneous, equally weighted angular averaging is allowed and yields a zero contribution beyond the cut-off sphere. Therefore, quadrupolar contributions to forces, torques, internal energy, pressure, and the interaction energy ψ_{ia} need no long-range correction.

A.2.1 Forces and Torques

The force on Q_i^a due to Q_j^b is [3],

$$\begin{aligned} \boldsymbol{F}_{ij}^{QQab} &= -\frac{\partial u_{ij}^{QQab}}{\partial \boldsymbol{r}_{ij}} \\ &= -\boldsymbol{e}_{ij}\frac{\partial u_{ij}^{QQab}}{\partial r_{ij}} + \left(\boldsymbol{e}_{ij}c_i-\boldsymbol{e}_i\right)\frac{1}{r_{ij}}\frac{\partial u_{ij}^{QQab}}{\partial c_i} + \left(\boldsymbol{e}_{ij}c_j-\boldsymbol{e}_j\right)\frac{1}{r_{ij}}\frac{\partial u_{ij}^{QQab}}{\partial c_j}, \end{aligned} \tag{184}$$

wherein

$$\boldsymbol{e}_{ij} = \frac{\boldsymbol{r}_{ij}}{|\boldsymbol{r}_{ij}|}. \tag{185}$$

Equations (183) and (184) then yield

$$\begin{aligned} \boldsymbol{F}_{ij}^{QQab} &= \frac{5u_{ij}^{QQab}}{r_{ij}}\boldsymbol{e}_{ij} \\ &+ \left(\boldsymbol{e}_{ij}c_i-\boldsymbol{e}_i\right)\frac{1}{r_{ij}}\frac{1}{4\pi\varepsilon_0}\frac{3Q_i^aQ_j^b}{4r_{ij}^5}\left(-10c_i-30c_j^2c_i-20c_j\left(c_{ij}-5c_ic_j\right)\right) \\ &+ \left(\boldsymbol{e}_{ij}c_j-\boldsymbol{e}_j\right)\frac{1}{r_{ij}}\frac{1}{4\pi\varepsilon_0}\frac{3Q_i^aQ_j^b}{4r_{ij}^5}\left(-10c_j-30c_i^2c_j-20c_i\left(c_{ij}-5c_ic_j\right)\right). \end{aligned} \tag{186}$$

The force on Q_j^b due to Q_i^a is

$$\boldsymbol{F}_{ji}^{QQba} = -\boldsymbol{F}_{ij}^{QQab}. \tag{187}$$

The torque on Q_i^a due to Q_j^b is [3]

$$\begin{aligned}\boldsymbol{\tau}_{ij}^{QQab} &= -\boldsymbol{e}_i \times \frac{\partial u_{ij}^{QQab}}{\partial \boldsymbol{e}_i} \\ &= -\boldsymbol{e}_i \times \left[\boldsymbol{e}_{ij} \frac{\partial u_{ij}^{QQab}}{\partial c_i} + \boldsymbol{e}_j \frac{\partial u_{ij}^{QQab}}{\partial c_{ij}} \right] \\ &= -\boldsymbol{e}_i \times \frac{1}{4\pi\varepsilon_0} \frac{3Q_i^a Q_j^b}{4r_{ij}^5} \cdot \\ &\qquad \left[\left(-10c_i - 30c_j^2 c_i - 20c_j \left(c_{ij} - 5c_i c_j \right) \right) \boldsymbol{e}_{ij} + 4 \left(c_{ij} - 5c_i c_j \right) \boldsymbol{e}_j \right]. \end{aligned} \tag{188}$$

The torque on Q_j^b due to Q_i^a is

$$\begin{aligned}\boldsymbol{\tau}_{ji}^{QQba} &= -\boldsymbol{e}_j \times \frac{1}{4\pi\varepsilon_0} \frac{3Q_i^a Q_j^b}{4r_{ij}^5} \cdot \\ &\qquad \left[\left(-10c_j - 30c_i^2 c_j + 20c_i \left(c_{ij} - 5c_i c_j \right) \right) \boldsymbol{e}_{ij} + 4 \left(c_{ij} - 5c_i c_j \right) \boldsymbol{e}_i \right]. \end{aligned} \tag{189}$$

A.2.2 Internal Energy

The contribution of the quadrupolar interactions to the configurational part of the internal energy is

$$\langle U^{QQ} \rangle = \langle \frac{1}{2} \sum_{a=1}^{m} \sum_{b=1}^{m} \sum_{i=1}^{N_a} \sum_{\substack{j \neq i \\ r_{ij} < r_c}}^{N_b} u_{ij}^{QQab} \rangle, \tag{190}$$

wherein $j \neq i$ for the innermost sum indicates, that self interactions of the molecules do not occur, i.e. the undefined terms u_{ii}^{QQaa} are omitted. Note, that the compact notation of the multiple sums in Equation (190) differs from the extended notation used in Equation (158), where the sums on like and unlike species are deliberately separated with regard to obtaining explicitly the slightly different long-range corrections for like and unlike interactions of the Lennard-Jones part. That separation is not required here.

A.2.3 Pressure

Calculating the pair virial according to Equation (178) based on u_{ij}^{QQab} instead of $u_{isjk}^{\mathrm{LJ}ab}$, i.e.

$$w_{ij}^{QQab} = \boldsymbol{r}_{ij} \frac{\partial u_{ij}^{QQab}}{\partial \boldsymbol{r}_{ij}}, \tag{191}$$

yields

$$w_{ij}^{QQab} = -5u_{ij}^{QQab}. \tag{192}$$

This expression is a convenient way to evaluate rapidly the contribution of the quadrupolar interactions to the pressure.

A.2.4 Chemical Potential

The Lennard-Jones contributions to the interaction energy ψ_{ia}, cf. Equation (150), are given in Appendix A.1.4. The additive contribution to ψ_{ia} due to the interaction of point quadrupoles is

$$\psi_{ia}^{QQ} = \sum_{b=1}^{m} \sum_{\substack{j=1 \\ r_{ij}<r_c}}^{N_b} u_{ij}^{QQab}. \tag{193}$$

A.3 Point Dipole Interaction

A.3.1 Internal Energy

A m-component mixture of dipolar fluids is considered. Each molecule of each species has a point dipole located in its center of mass. The pair interaction potential of the point dipoles μ_i^a and μ_j^b located on molecule i of species a and molecule j of species b is, cf. Chapter 3.1,

$$u_{ij}^{\mu\mu ab} = \frac{1}{4\pi\epsilon_0} \frac{\mu_i^a \mu_j^b}{|\boldsymbol{r}_{ij}|^3} (c_{ij} - 3c_i c_j), \tag{194}$$

wherein $c_i = \cos\theta_i^a$, $c_j = \cos\theta_j^b$, and $c_{ij} = \cos\gamma_{ij}^{ab}$. The angles θ_i^a, θ_j^b, and γ_{ij}^{ab} indicate the relative angular orientation of the two point dipoles. As $u_{ij}^{\mu\mu ab}$ is no decay function, particular attention has to be paid to the long-range corrections of the dipolar interaction. Various approaches for calculating dipolar long-range corrections were suggested, among which the Ewald summation and the reaction field method are broadly used [114, 307]. The reaction field method [6, 340] is used consistently in the present work. It requires an essentially lower computational effort compared to the Ewald summation and it is convenient to implement.

The basic assumption of the reaction field method is, that the dipoles present in the cut-off sphere of radius r_c centered on a dipole $\boldsymbol{\mu}_i$ polarize the fluid outside the cut-off sphere, which is modeled as dielectric continuum with relative permittivity ε_s. This polarization gives raise to a homogeneous electric field, called the reaction field $\boldsymbol{E}_i^{\mathrm{RF}}$, in the cut-off sphere. With the short-cut notation

$$C = \frac{1}{4\pi\varepsilon_0} \frac{2(\varepsilon_s - 1)}{2\varepsilon_s + 1} \frac{1}{r_c^3}, \tag{195}$$

the reaction field $\boldsymbol{E}_i^{\mathrm{RF}}$ for a cut-off sphere centered on dipole $\boldsymbol{\mu}_i^a$ is

$$\boldsymbol{E}_i^{\mathrm{RF}} = C \sum_{b=1}^{m} \sum_{\substack{j=1 \\ r_{ij} < r_c}}^{N_b} \boldsymbol{\mu}_j^b, \tag{196}$$

wherein only the dipoles within the cut-off sphere are summed up. For sufficiently large systems, i.e. $N \geq 500$, the sensitivity of simulation results to the value of the relative permittivity ε_s is negligible, cf. [340]. Therefore, ε_s is often set to infinity in simulations of dipolar fluids [122, 160, 221, 228]. For reasons of consistency, the relative permittivity ε_s was uniformly set to infinity in the present work.

The interaction of the dipoles in the cut-off sphere with the reaction field $\boldsymbol{E}_i^{\mathrm{RF}}$ contributes to the torques exerted on the dipoles and to the dipolar interaction energies. The energetic contribution of the interaction of the dipole $\boldsymbol{\mu}_i^a$ with the reaction field $\boldsymbol{E}_i^{\mathrm{RF}}$ is

[3, 22]

$$u_i^{\mu\mathrm{RF}a} = -\frac{1}{2}\boldsymbol{\mu}_i^a \boldsymbol{E}_i^{\mathrm{RF}}. \tag{197}$$

Applying Equations (196) and (197), the contribution of the dipolar interactions including interactions with the reaction field to the configurational part of the internal energy is

$$\begin{aligned}
\langle U^{\mu\mu}\rangle &= \langle \frac{1}{2}\sum_{a=1}^{m}\sum_{b=1}^{m}\sum_{i=1}^{N_a}\sum_{\substack{j\neq i\\ r_{ij}<r_c}}^{N_b} u_{ij}^{\mu\mu ab} + \sum_{a=1}^{m}\sum_{i=1}^{N_a} u_i^{\mu\mathrm{RF}a}\rangle \\
&= \langle \frac{1}{2}\sum_{a=1}^{m}\sum_{b=1}^{m}\sum_{i=1}^{N_a}\sum_{\substack{j\neq i\\ r_{ij}<r_c}}^{N_b} u_{ij}^{\mu\mu ab} - \frac{C}{2}\sum_{a=1}^{m}\sum_{i=1}^{N_a}\boldsymbol{\mu}_i^a \sum_{b=1}^{m}\sum_{\substack{j=1\\ r_{ij}<r_c}}^{N_b}\boldsymbol{\mu}_j^b\rangle \\
&= \langle \frac{1}{2}\sum_{a=1}^{m}\sum_{b=1}^{m}\sum_{i=1}^{N_a}\sum_{\substack{j\neq i\\ r_{ij}<r_c}}^{N_b}\left(u_{ij}^{\mu\mu ab} - C\boldsymbol{\mu}_i^a\boldsymbol{\mu}_j^b\right)\rangle - \frac{C}{2}\sum_{a=1}^{m}\sum_{i=1}^{N_a}\boldsymbol{\mu}_i^a\boldsymbol{\mu}_i^a \\
&= \langle \frac{1}{2}\sum_{a=1}^{m}\sum_{b=1}^{m}\sum_{i=1}^{N_a}\sum_{\substack{j\neq i\\ r_{ij}<r_c}}^{N_b}\left(u_{ij}^{\mu\mu ab} - C\boldsymbol{\mu}_i^a\boldsymbol{\mu}_j^b\right)\rangle - \frac{C}{2}\sum_{a=1}^{m} N_a\left(\mu^a\right)^2.
\end{aligned} \tag{198}$$

The averaged term in Equation (198) can be written as hierarchical summation on particles that is conveniently evaluated in a molecular simulation code. Equation (198) shows, that the computational effort for the reaction field method is restricted to the additional pairwise evaluation of the simple term $-C\boldsymbol{\mu}_i^a\boldsymbol{\mu}_j^b$. The last term in Equation (198) is the dipolar self term, which is constant for a constant number of particles.

A.3.2 Forces and Torques

The reaction field $\boldsymbol{E}_i^{\mathrm{RF}}$ is a homogeneous electrical field, i.e. it is no function of position within the cut-off sphere. It therefore exerts no force on the dipoles, i.e.

$$\boldsymbol{F}_i^{\mu\mathrm{RF}a} = \boldsymbol{0}. \tag{199}$$

The force on $\boldsymbol{\mu}_i^a$ due to $\boldsymbol{\mu}_j^b$

$$\boldsymbol{F}_{ij}^{\mu\mu ab} = -\frac{\partial u_{ij}^{\mu\mu ab}}{\partial \boldsymbol{r}_{ij}} \tag{200}$$

is obtained from Equation (184), wherein u_{ij}^{QQab} is replaced by $u_{ij}^{\mu\mu ab}$

$$\boldsymbol{F}_{ij}^{\mu\mu ab} = \frac{1}{4\pi\varepsilon_0}\frac{3\mu_i^a\mu_j^b}{r_{ij}^4}\left[\left(c_{ij} - 5c_ic_j\right)\boldsymbol{e}_{ij} + c_j\boldsymbol{e}_i + c_i\boldsymbol{e}_j\right]. \tag{201}$$

The force on $\boldsymbol{\mu}_j^b$ due to $\boldsymbol{\mu}_i^a$ is

$$\boldsymbol{F}_{ji}^{\mu\mu ba} = -\boldsymbol{F}_{ij}^{\mu\mu ab}. \tag{202}$$

The torque on $\boldsymbol{\mu}_i^a$ due to $\boldsymbol{\mu}_j^b$

$$\boldsymbol{\tau}_{ij}^{\mu\mu ab} = -\boldsymbol{e}_i \times \frac{\partial u_{ij}^{\mu\mu ab}}{\partial \boldsymbol{e}_i} \tag{203}$$

is obtained from Equation (188), wherein u_{ij}^{QQab} is replaced by $u_{ij}^{\mu\mu ab}$

$$\boldsymbol{\tau}_{ij}^{\mu\mu ab} = -\frac{1}{4\pi\varepsilon_0}\frac{\mu_i^a \mu_j^b}{r_{ij}^3}\boldsymbol{e}_i \times [\boldsymbol{e}_j - 3c_j \boldsymbol{e}_{ij}], \tag{204}$$

and the torque on $\boldsymbol{\mu}_j^b$ due to $\boldsymbol{\mu}_i^a$ is

$$\boldsymbol{\tau}_{ji}^{\mu\mu ba} = -\frac{1}{4\pi\varepsilon_0}\frac{\mu_i^a \mu_j^b}{r_{ij}^3}\boldsymbol{e}_j \times [\boldsymbol{e}_i - 3c_i \boldsymbol{e}_{ij}]. \tag{205}$$

The additional torque for each $\boldsymbol{\mu}_i^a$ of each species a due to the reaction field $\boldsymbol{E}_i^{\mathrm{RF}}$ is [3]

$$\boldsymbol{\tau}_i^{\mu\mathrm{RF}a} = \boldsymbol{\mu}_i^a \times \boldsymbol{E}_i^{\mathrm{RF}}. \tag{206}$$

A.3.3 Pressure

In analogy to Equations (191) and (192), the pair virial for dipolar interactions is

$$\begin{aligned} w_{ij}^{\mu\mu ab} &= \boldsymbol{r}_{ij}\frac{\partial u^{\mu\mu ab}}{\partial \boldsymbol{r}_{ij}} \\ &= -3u_{ij}^{\mu\mu ab}. \end{aligned} \tag{207}$$

Note, that the reaction field does not contribute to the pair virial, when the pair virial is calculated by the means of the pair forces. In the present work, the pair virial of the dipolar interactions was calculated according to a suggestion of Saager et al. [340], who applied Equation (207) after adding the energetic contribution of the reaction field to $u_{ij}^{\mu\mu ab}$, cf. Equations (197) and (198). This allows reaction field contributions to the pressure.

A.3.4 Chemical Potential

The Lennard-Jones contributions to the interaction energy ψ_{ia}, cf. Equation (150), are given in Appendix A.1.4. The additive contributions to ψ_{ia} due to the interaction of point dipoles and the reaction field are

$$\psi_{ia}^{\mu\mathrm{RF}a} = \sum_{b=1}^{m}\sum_{\substack{j=1 \\ r_{ij}<r_c}}^{N_b}\left(u_{ij}^{\mu\mu ab} - \frac{C}{2}\boldsymbol{\mu}_i^a \boldsymbol{\mu}_j^b\right). \tag{208}$$

A.4 Set of Point Charges Interaction

A.4.1 Internal Energy

In a pure fluid of molecules bearing sets of point charges, the interactions between the point charges located on molecules i and j are considered. The notation scheme used for interactions of Lennard-Jones sites in Appendix A.1 is applied here analogously to sets of point charges. Each set of point charges is presumed to be electroneutral, i.e.

$$\sum_s q_s = 0. \tag{209}$$

According to Coulomb's law, the pair interaction potential of two point charges q_{is} and q_{jk} at distance r_{isjk} is

$$u^{qq}_{isjk} = \frac{1}{4\pi\varepsilon_0}\frac{q_{is}q_{jk}}{r_{isjk}}, \tag{210}$$

wherein $r_{isjk} = |\boldsymbol{r}_{isjk}|$. Consequently, the pair interaction potential of two sets of point charges on molecules i and j is

$$u^{qq}_{ij} = \frac{1}{4\pi\varepsilon_0}\sum_s\sum_k \frac{q_{is}q_{jk}}{r_{isjk}}. \tag{211}$$

As in the case of dipolar interactions, usual approaches to deal with the long-range correction of this non-decay interaction potential are the Ewald summation technique and the reaction field method [114, 307]. The application of the reaction field method to systems with point charges is generally accepted, cf. for example the works of Steinhauser [374] or van der Spoel et al. [401] on water. In the present work, the reaction field method is preferred for the reasons stated in Appendix A.3.

The application of the reaction field method to electroneutral sets of point charges allows a notation that is completely analogous to the one used for dipolar interactions. Consequently, the reaction field method is straightforwardly applicable to mixtures of fluids with dipoles and point charges, cf. Appendix A.6.

With the dipolar momenta of the electroneutral sets of point charges on a molecules i and j

$$\boldsymbol{\mu}^q_i = \sum_s q_{is}\boldsymbol{r}_{is} = \sum_s q_{is}\Delta\boldsymbol{r}_{is}, \tag{212}$$

$$\boldsymbol{\mu}^q_j = \sum_k q_{jk}\boldsymbol{r}_{jk} = \sum_k q_{jk}\Delta\boldsymbol{r}_{jk}, \tag{213}$$

the reaction field $\boldsymbol{E}^{\mathrm{RF}}_i$ for a cut-off sphere centered on the center of mass of molecule i is

$$\boldsymbol{E}^{\mathrm{RF}}_i = C\sum_{\substack{j=1\\ r_{ij}<r_c}}^{N}\boldsymbol{\mu}^q_j. \tag{214}$$

In analogy to Equation (197), the energetic contribution of the interaction of the dipolar momentum $\boldsymbol{\mu}_i^q$ of the set of point charges with the reaction field $\boldsymbol{E}_i^{\mathrm{RF}}$ is

$$u_i^{q\mathrm{RF}} = -\frac{1}{2}\boldsymbol{\mu}_i^q \boldsymbol{E}_i^{\mathrm{RF}}. \tag{215}$$

Then, in analogy to Equation (198), the contribution of the point charge interactions including interactions with the reaction field to the configurational part of the internal energy is

$$\langle U^{qq}\rangle = \langle \frac{1}{2}\sum_{i=1}^{N}\sum_{\substack{j\neq i \\ r_{ij}<r_c}}^{N}\left(u_{ij}^{qq} - C\boldsymbol{\mu}_i^q\boldsymbol{\mu}_j^q\right)\rangle - N\frac{C}{2}\left(\boldsymbol{\mu}^q\right)^2. \tag{216}$$

A.4.2 Forces and Torques

The force on point charge q_{is} due to point charge q_{jk} is

$$\begin{aligned} \boldsymbol{F}_{isjk}^{qq} &= -\frac{\partial u_{isjk}^{qq}}{\partial \boldsymbol{r}_{isjk}} \\ &= \frac{1}{4\pi\varepsilon_0}\frac{q_{is}q_{jk}}{r_{isjk}^2}\boldsymbol{e}_{isjk}, \end{aligned} \tag{217}$$

wherein

$$\boldsymbol{e}_{isjk} = \frac{\boldsymbol{r}_{isjk}}{|\boldsymbol{r}_{isjk}|}, \tag{218}$$

and the force on q_{is} due to a homogeneous electrical field $\boldsymbol{E}$ is

$$\boldsymbol{F}^{\mathrm{EF}} = q_{is}\boldsymbol{E}. \tag{219}$$

So the force on a point charge q_{is} as part of the set of point charges of molecule i due to the set of point charges on molecule j and due to the reaction field $\boldsymbol{E}_i^{\mathrm{RF}}$ according to Equation (214) is

$$\boldsymbol{F}_{is}^{qq\mathrm{RF}} = \sum_{\substack{j\neq i \\ r_{ij}<r_c}}\sum_{k}\frac{1}{4\pi\varepsilon_0}\frac{q_{is}q_{jk}}{r_{isjk}^2}\boldsymbol{e}_{isjk} + q_{is}\boldsymbol{E}_i^{\mathrm{RF}} \tag{220}$$

Summing up all forces $\boldsymbol{F}_{is}^{qq\mathrm{RF}}$ yields the force on the set of point charges on molecule i due to the set of point charges on molecule j

$$\begin{aligned} \boldsymbol{F}_i^{qq\mathrm{RF}} &= \sum_s \boldsymbol{F}_{is}^{qq\mathrm{RF}} \\ &= \sum_{\substack{j\neq i \\ r_{ij}<r_c}}\sum_s\sum_k \frac{1}{4\pi\varepsilon_0}\frac{q_{is}q_{jk}}{r_{isjk}^2}\boldsymbol{e}_{isjk}. \end{aligned} \tag{221}$$

Equation (221) shows, that the reaction field exerts no net force on the electroneutral set of point charges. However, the reaction field contributes to the torque on the set of point charges

$$\begin{aligned} \boldsymbol{\tau}_i^{qq\mathrm{RF}} &= \sum_s \Delta \boldsymbol{r}_{is} \times \boldsymbol{F}_{is}^{qq\mathrm{RF}} \\ &= \sum_{\substack{j \neq i \\ r_{ij} < r_c}} \sum_s \sum_k \frac{1}{4\pi\varepsilon_0} \frac{q_{is} q_{jk}}{r_{isjk}^2} \Delta \boldsymbol{r}_{is} \times \boldsymbol{e}_{isjk} + \boldsymbol{\mu}_i^q \times \boldsymbol{E}_i^{\mathrm{RF}}. \end{aligned} \tag{222}$$

Equations (221) and (222) show, that the action of the reaction field on sets of point charges is completely analogous to its action on dipoles, cf. Equations (199), (201) and (206).

A.4.3 Pressure

The pair virial for the interaction of two sets of point charges must be evaluated by the means of the pair forces between the charges, i.e.

$$\begin{aligned} w_{ij}^{qq} &= \boldsymbol{r}_{ij} \sum_s \sum_k \frac{\partial u_{isjk}^{qq}}{\partial \boldsymbol{r}_{isjk}} \\ &= \boldsymbol{r}_{ij} \sum_s \sum_k -\boldsymbol{F}_{isjk}^{qq}. \end{aligned} \tag{223}$$

As shown in Chapter A.4.2, the sum over all pair forces, as it is contained in Equation (223), makes disappear the influence of the reaction field on the pair virial w_{ij}^{qq}.

A.4.4 Chemical Potential

The Lennard-Jones contributions to the interaction energy ψ_i, cf. Equation (150), are given in Appendix A.1.4. The additive contributions to ψ_i due to the interaction of point charges and the reaction field are

$$\psi_i^{\mu\mathrm{RF}} = \sum_{\substack{j=1 \\ r_{ij} < r_c}}^{N} \left(u_{ij}^{qq} - \frac{C}{2} \mu_i^q \mu_j^q \right). \tag{224}$$

A.5 Point Dipole and Point Quadrupole Interaction

A.5.1 Internal energy

A m-component mixture of dipolar-quadrupolar fluids is considered. Each molecule of each species has a point dipole and an elongated point quadrupole located in its center of mass. The interactions between point dipoles and between point quadrupoles are described in Appendices A.2 and A.3. The pair interaction potential of the point dipole μ_i^a located on molecule i of species a and the point quadrupole Q_j^b located on molecule j of species b is [3, 132],

$$u_{ij}^{\mu Qab} = \frac{1}{4\pi\epsilon_0}\frac{3}{2}\frac{\mu_i^a Q_j^b}{r_{ij}^4}\left(c_i\left(5c_j^2-1\right)-2c_{ij}c_j\right), \tag{225}$$

and the pair interaction potential of the point quadrupole Q_i^a located on molecule i of species a and the point dipole μ_j^b located on molecule j of species b is [3, 132],

$$u_{ij}^{Q\mu ab} = -\frac{1}{4\pi\epsilon_0}\frac{3}{2}\frac{Q_i^a \mu_j^b}{r_{ij}^4}\left(c_j\left(5c_i^2-1\right)-2c_{ij}c_i\right), \tag{226}$$

wherein $c_i = \cos\theta_i^a$, $c_j = \cos\theta_j^b$, and $c_{ij} = \cos\gamma_{ij}^{ab}$. The angles θ_i^a, θ_j^b, and γ_{ij}^{ab} indicate the relative angular orientation of the point dipole and the point quadrupole considered.

Presuming, that the point quadrupoles do not influence the reaction field of the point dipoles, the reaction field $\boldsymbol{E}_i^{\mathrm{RF}}$ for a cut-off sphere centered on dipole $\boldsymbol{\mu}_i^a$ is given by Equation (196). The reaction field $\boldsymbol{E}_i^{\mathrm{RF}}$ acts on the point dipoles according to Equations (197) and (206), but, due to its homogeneity and due to the elongation and symmetry of the point quadrupoles, has got neither energetic nor force nor torque effects on the point quadrupoles.

Therefore, the total electrostatic energy that contributes to the configurational part of the internal energy is

$$\begin{aligned}
\langle U^{\mu Q}\rangle &= \langle\frac{1}{2}\sum_{a=1}^{m}\sum_{b=1}^{m}\sum_{i=1}^{N_a}\sum_{\substack{j\neq i\\ r_{ij}<r_c}}^{N_b}\left(u_{ij}^{QQab}+u_{ij}^{\mu\mu ab}+u_{ij}^{\mu Qab}+u_{ij}^{Q\mu ab}\right)+\sum_{a=1}^{m}\sum_{i=1}^{N_a}u_i^{\mu\mathrm{RF}a}\rangle \\
&= \langle\frac{1}{2}\sum_{a=1}^{m}\sum_{b=1}^{m}\sum_{i=1}^{N_a}\sum_{\substack{j\neq i\\ r_{ij}<r_c}}^{N_b}\left(u_{ij}^{QQab}+u_{ij}^{\mu\mu ab}+u_{ij}^{\mu Qab}+u_{ij}^{Q\mu ab}-C\boldsymbol{\mu}_i^a\boldsymbol{\mu}_j^b\right)\rangle \\
&\quad -\frac{C}{2}\sum_{a=1}^{m}N_a\left(\mu^a\right)^2,
\end{aligned} \tag{227}$$

wherein u_{ij}^{QQab} and $u_{ij}^{\mu\mu ab}$ are given by Equations (183) and (194).

A.5.2 Forces and Torques

The forces and torques between pairs of point dipoles and between pairs of point quadrupoles are given in Appendices A.2 and A.3. The force on μ_i^a due to Q_j^b is obtained from Equation (184), wherein u_{ij}^{QQab} is replaced by $u_{ij}^{\mu Qab}$

$$\begin{aligned} \boldsymbol{F}_{ij}^{\mu Qab} &= -\frac{\partial u_{ij}^{\mu Qab}}{\partial \boldsymbol{r}_{ij}} \\ &= \frac{1}{4\pi\varepsilon_0}\frac{3}{2}\frac{\mu_i^a Q_j^b}{r_{ij}^5}\cdot \\ &\quad \left[\left(5c_i\left(7c_j^2-1\right)-10c_{ij}c_j\right)\boldsymbol{e}_{ij}+\left(1-5c_j^2\right)\boldsymbol{e}_i+\left(2c_{ij}-10c_ic_j\right)\boldsymbol{e}_j\right], \end{aligned} \tag{228}$$

and the force on Q_i^a due to μ_j^b is

$$\begin{aligned} \boldsymbol{F}_{ij}^{Q\mu ab} &= -\frac{\partial u_{ij}^{Q\mu ab}}{\partial \boldsymbol{r}_{ij}} \\ &= \frac{1}{4\pi\varepsilon_0}\frac{3}{2}\frac{Q_i^a \mu_j^b}{r_{ij}^5}\cdot \\ &\quad \left[\left(5c_j\left(1-7c_i^2\right)+10c_{ij}c_i\right)\boldsymbol{e}_{ij}+\left(10c_ic_j-2c_{ij}\right)\boldsymbol{e}_i+\left(5c_i^2-1\right)\boldsymbol{e}_j\right]. \end{aligned} \tag{229}$$

The force on Q_j^b due to μ_i^a is

$$\boldsymbol{F}_{ji}^{Q\mu ba} = -\boldsymbol{F}_{ij}^{\mu Qab}, \tag{230}$$

and the force on μ_j^b due to Q_i^a is

$$\boldsymbol{F}_{ji}^{\mu Qba} = -\boldsymbol{F}_{ij}^{Q\mu ab}. \tag{231}$$

The torque on μ_i^a due to Q_j^b

$$\boldsymbol{\tau}_{ij}^{\mu Qab} = -\boldsymbol{e}_i \times \frac{\partial u^{\mu Qab}}{\partial \boldsymbol{e}_i} \tag{232}$$

is obtained from Equation (188), wherein u_{ij}^{QQab} is replaced by $u_{ij}^{\mu Qab}$

$$\boldsymbol{\tau}_{ij}^{\mu Qab} = \boldsymbol{e}_i \times \frac{1}{4\pi\varepsilon_0}\frac{3}{2}\frac{\mu_i^a Q_j^b}{r_{ij}^4}\left[-\left(5c_j^2-1\right)\boldsymbol{e}_{ij}+2c_j\boldsymbol{e}_j\right]. \tag{233}$$

The torque on Q_i^a due to μ_j^b is

$$\boldsymbol{\tau}_{ij}^{Q\mu ab} = \boldsymbol{e}_i \times \frac{1}{4\pi\varepsilon_0}\frac{3}{2}\frac{Q_i^a \mu_j^b}{r_{ij}^4}\left[-2\left(c_{ij}-5c_ic_j\right)\boldsymbol{e}_{ij}-2c_i\boldsymbol{e}_j\right], \tag{234}$$

the torque on Q_j^b due to μ_i^a is

$$\boldsymbol{\tau}_{ji}^{Q\mu ba} = \boldsymbol{e}_j \times \frac{1}{4\pi\varepsilon_0}\frac{3}{2}\frac{\mu_i^a Q_j^b}{r_{ij}^4}\left[\left(5c_j^2-1\right)\boldsymbol{e}_{ij}-2c_i\boldsymbol{e}_i\right], \tag{235}$$

and the torque on μ_j^b due to Q_i^a is

$$\boldsymbol{\tau}_{ji}^{\mu Qba} = \boldsymbol{e}_j \times \frac{1}{4\pi\varepsilon_0}\frac{3}{2}\frac{Q_i^a \mu_j^b}{r_{ij}^4}\left[2\left(c_{ij} - 5c_i c_j\right)\boldsymbol{e}_{ij} + 2c_j \boldsymbol{e}_i\right]. \tag{236}$$

Note, that there are no actions of the reaction field on forces and torques of the interaction of point dipole and point quadrupole.

A.5.3 Pressure

In analogy to Equations (191) and (192), the pair virial for the interaction of point dipole and point quadrupole is

$$\begin{aligned} w_{ij}^{\mu Qab} &= \boldsymbol{r}_{ij}\frac{\partial u^{\mu Qab}}{\partial \boldsymbol{r}_{ij}} \\ &= -4u_{ij}^{\mu Qab}, \end{aligned} \tag{237}$$

or

$$\begin{aligned} w_{ij}^{Q\mu ab} &= \boldsymbol{r}_{ij}\frac{\partial u^{Q\mu ab}}{\partial \boldsymbol{r}_{ij}} \\ &= -4u_{ij}^{Q\mu ab}. \end{aligned} \tag{238}$$

A.5.4 Chemical Potential

The Lennard-Jones contributions to the interaction energy ψ_{ia}, cf. Equation (150), are given in Appendix A.1.4. The additive contributions to ψ_{ia} due to the interaction of point quadrupoles, point dipoles, and the reaction field are given in Appendices A.2.4 and A.3.4. The additive contributions to ψ_{ia} due to the interactions of point dipole and point quadrupole are

$$\psi_{ia}^{\mu Q} = \sum_{b=1}^{m}\sum_{\substack{j=1 \\ r_{ij}<r_c}}^{N_b}\left(u_{ij}^{\mu Qab} + u_{ij}^{Q\mu ab}\right). \tag{239}$$

A.6 Interaction of a Set of Point Charges and Point Quadrupole or Point Dipole

A.6.1 Internal Energy

A binary fluid mixture of a component a bearing point charges and a dipolar-quadrupolar component b is considered. Each molecule of component b has a point dipole and a point quadrupole in its center of mass. The pair interactions between point quadrupoles, between point dipoles, between sets of point charges, and between point quadrupoles and point dipoles are described in Appendices A.2, A.3, A.4, and A.5. The interactions between a point dipole and a set of point charges are described for reasons of completeness, they were not required in the present work.

Presuming, that the point quadrupoles do not influence the reaction field of the point charges, both the dipolar momenta of the sets of point charges and the point dipoles contribute to the reaction field. Therefore, the reaction field $\boldsymbol{E}_{i_a}^{\mathrm{RF}a}$ for a cut-off sphere centered on the center of mass of a-molecule i_a is

$$\boldsymbol{E}_{i_a}^{\mathrm{RF}a} = C \sum_{\substack{j_a=1 \\ r_{i_a j_a} < r_c}}^{N_a} \boldsymbol{\mu}_{j_a}^{qa} + C \sum_{\substack{j_b=1 \\ r_{i_a j_b} < r_c}}^{N_b} \boldsymbol{\mu}_{j_b}^{b}. \tag{240}$$

The mathematical expression for the reaction field $\boldsymbol{E}_{j_b}^{\mathrm{RF}b}$ for a cut-off sphere centered on the point dipole $\boldsymbol{\mu}_{j_b}^{b}$ of b-molecule j_b is identical to the expression in Equation (240). According to Chapters A.3 and A.4, the reaction field acts on the point dipoles on molecules of species b and on the sets of point charges on molecules of species a. The reaction field does not act on the interactions of sets of point charges and point dipoles or point quadrupoles.

The pair interaction potential of the point charge $q_{i_a s}^{a}$ on a-molecule i_a and the point quadrupole $Q_{j_b}^{b}$ on b-molecule i_b at distance $\boldsymbol{r}_{i_a s j_b} = \boldsymbol{r}_{i_a s} - \boldsymbol{r}_{j_b}$ is [150, 233]

$$u_{i_a s j_b}^{qQab} = \frac{1}{4\pi\varepsilon_0} \frac{q_{i_a s}^{a} Q_{j_b}^{b}}{4 r_{i_a s j_b}^{3}} \left(3\cos^2\theta_{i_a s} - 1\right), \tag{241}$$

and the pair interaction potential of the point charge $q_{i_a s}^{a}$ on a-molecule i_a and the point dipole $\mu_{j_b}^{b}$ on b-molecule i_b at distance $\boldsymbol{r}_{i_a s j_b}$ is [150, 233],

$$u_{i_a s j_b}^{q\mu ab} = -\frac{1}{4\pi\varepsilon_0} \frac{q_{i_a s}^{a} \mu_{j_b}^{b}}{r_{i_a s j_b}^{2}} \cos\theta_{i_a s}, \tag{242}$$

wherein $r_{i_a s j_b} = |\boldsymbol{r}_{i_a s j_b}|$, and $\theta_{i_a s}$ is the angle between the distance unit vector $\boldsymbol{e}_{i_a s j_b} = \boldsymbol{r}_{i_a s j_b} / r_{i_a s j_b}$ and the orientation unit vector $\boldsymbol{e}_{j_b}$ of the point quadrupole or the point dipole, i.e.

$$\cos\theta_{i_a s} = \boldsymbol{e}_{j_b} \cdot \boldsymbol{e}_{i_a s j_b}. \tag{243}$$

Consequently, the pair interaction potential of the set of point charges on a-molecule i_a and the point quadrupole on b-molecule j_b is

$$u_{i_a j_b}^{qQab} = \frac{1}{4\pi\varepsilon_0} \sum_s \frac{q_{i_a s}^a Q_{j_b}^b}{4 r_{i_a s j_b}^3} \left(3\cos^2\theta_{i_a s} - 1\right), \tag{244}$$

and the pair interaction potential of the set of point charges on a-molecule i_a and the point dipole on b-molecule j_b is

$$u_{i_a j_b}^{q\mu ab} = -\frac{1}{4\pi\varepsilon_0} \sum_s \frac{q_{i_a s}^a \mu_{j_b}^b}{r_{i_a s j_b}^2} \cos\theta_{i_a s}. \tag{245}$$

Then the total electrostatic energy that contributes to the configurational part of the internal energy is

$$\begin{aligned}
\langle U^{\mu Qq} \rangle &= \frac{1}{2} \sum_{i_a=1}^{N_a} \sum_{\substack{j_a \neq i_a \\ r_{i_a j_a} < r_c}}^{N_a} \sum_{s,k} u_{i_a s j_a k}^{qqaa} + \frac{1}{2} \sum_{i_b=1}^{N_b} \sum_{\substack{j_b \neq i_b \\ r_{i_b j_b} < r_c}}^{N_b} \left(u_{i_b j_b}^{\mu\mu bb} + u_{i_b j_b}^{\mu Qbb} + u_{i_b j_b}^{Q\mu bb} + u_{i_b j_b}^{QQbb} \right) \\
&\quad + \sum_{i_a=1}^{N_a} \sum_{\substack{j_b=1 \\ r_{i_a j_b} < r_c}}^{N_b} \left(u_{i_a j_b}^{qQab} + u_{i_a j_b}^{q\mu ab} \right) - \sum_{i_a=1}^{N_a} \frac{1}{2} \boldsymbol{\mu}_{i_a}^{qa} \boldsymbol{E}_{i_a}^{\mathrm{RF}a} - \sum_{i_b=1}^{N_b} \frac{1}{2} \boldsymbol{\mu}_{i_b}^{b} \boldsymbol{E}_{i_b}^{\mathrm{RF}b} \\
&= \frac{1}{2} \sum_{i_a=1}^{N_a} \sum_{\substack{j_a \neq i_a \\ r_{i_a j_a} < r_c}}^{N_a} \left(\sum_{s,k} u_{i_a s j_a k}^{qqaa} - C \boldsymbol{\mu}_{i_a}^{qa} \boldsymbol{\mu}_{j_a}^{qa} \right) \\
&\quad + \frac{1}{2} \sum_{i_b=1}^{N_b} \sum_{\substack{j_b \neq i_b \\ r_{i_b j_b} < r_c}}^{N_b} \left(u_{i_b j_b}^{\mu\mu bb} + u_{i_b j_b}^{\mu Qbb} + u_{i_b j_b}^{Q\mu bb} + u_{i_b j_b}^{QQbb} - C \boldsymbol{\mu}_{i_b}^{b} \boldsymbol{\mu}_{j_b}^{b} \right) \\
&\quad + \sum_{i_a=1}^{N_a} \sum_{\substack{j_b=1 \\ r_{i_a j_b} < r_c}}^{N_b} \left(u_{i_a j_b}^{qQab} + u_{i_a j_b}^{q\mu ab} - C \boldsymbol{\mu}_{i_a}^{qa} \boldsymbol{\mu}_{j_b}^{b} \right) - \frac{C}{2} \left(N_s \left(\mu^{qa}\right)^2 + N_b \left(\mu^{b}\right)^2 \right).
\end{aligned} \tag{246}$$

A.6.2 Forces and Torques

The forces and torques between pairs of point quadrupoles, between pairs of point dipoles, between two sets of point charges, and between a point quadrupole and a point dipole are given in Appendices A.2, A.3, A.4, and A.5.

The force on $q_{i_a s}^a$ due to $Q_{j_b}^b$ is [305]

$$\begin{aligned}
\boldsymbol{F}_{i_a s j_b}^{qQab} &= -\frac{\partial u_{i_a s j_b}^{qQab}}{\partial \boldsymbol{r}_{j_b i_a s}} = \frac{\partial u_{i_a s j_b}^{qQab}}{\partial \boldsymbol{r}_{i_a s j_b}} \\
&= \frac{1}{4\pi\varepsilon_0} \frac{3 q_{i_a s}^a Q_{j_b}^b}{4 r_{i_a s j_b}^4} \left[2\cos\theta_{i_a s} \cdot \boldsymbol{e}_{j_b} + \left(1 - 5\cos^2\theta_{i_a s}\right) \boldsymbol{e}_{i_a s j_b} \right],
\end{aligned} \tag{247}$$

and the force on $q^a_{i_a s}$ due to $\mu^b_{j_b}$ is

$$\begin{aligned} \boldsymbol{F}^{q\mu ab}_{i_a s j_b} &= -\frac{\partial u^{q\mu ab}}{\partial \boldsymbol{r}_{j_b i_a s}} = \frac{\partial u^{q\mu ab}}{\partial \boldsymbol{r}_{i_a s j_b}} \\ &= -\frac{1}{4\pi\varepsilon_0}\frac{q^a_{i_a s}\mu^b_{j_b}}{r^3_{i_a s j_b}}\left(\boldsymbol{e}_{j_b} - 3\cos\theta_{i_a s}\cdot\boldsymbol{e}_{i_a s j_b}\right). \end{aligned} \tag{248}$$

The force on $Q^b_{j_b}$ due to $q^a_{i_a s}$ is

$$\boldsymbol{F}^{Qqba}_{j_b i_a s} = -\boldsymbol{F}^{qQab}_{i_a s j_b}, \tag{249}$$

and the force on $\mu^b_{j_b}$ due to $q^a_{i_a s}$ is

$$\boldsymbol{F}^{\mu qba}_{j_b i_a s} = -\boldsymbol{F}^{q\mu ab}_{i_a s j_b}. \tag{250}$$

The torque on the point dipole $\mu^b_{j_b}$ due to the spherically symmetric electrostatic field of the point charge $q^a_{i_a s}$ is

$$\boldsymbol{\tau}^{\mu qba}_{j_b i_a s} = -\frac{1}{4\pi\varepsilon_0}\frac{\mu^b_{j_b} q^a_{i_a s}}{r^2_{i_a s j_b}}\boldsymbol{e}_{j_b}\times\boldsymbol{e}_{i_a s j_b}, \tag{251}$$

and the torque on the a-molecule i_a bearing the set of point charges due to the point dipole $\mu^b_{j_b}$ on b-molecule j_b is

$$\boldsymbol{\tau}^{q\mu ab}_{i_a j_b} = \sum_s \Delta\boldsymbol{r}_{i_a s}\times\boldsymbol{F}^{q\mu ab}_{i_a s j_b}. \tag{252}$$

The torque on the point quadrupole $Q^b_{j_b}$ due to the spherically symmetric electrostatic field of the point charge $q^a_{i_a s}$ is zero, and the torque on the a-molecule i_a bearing the set of point charges due to the point quadrupole $Q^b_{j_b}$ on b-molecule j_b is

$$\boldsymbol{\tau}^{qQab}_{i_a j_b} = \sum_s \Delta\boldsymbol{r}_{i_a s}\times\boldsymbol{F}^{qQab}_{i_a s j_b}. \tag{253}$$

A.6.3 Pressure

The evaluation of the virials for pair interactions of point quadrupoles, point dipoles, two sets of point charges, and point quadrupole and a point dipole is given in Appendices A.2, A.3, A.4, and A.5.

In analogy to Equation (223), the pair virials for the interaction of point quadrupoles or point dipoles with point charges are evaluated by the means of the pair forces, i.e.

$$w^{qQab}_{i_a j_b} = \boldsymbol{r}_{i_a j_b}\sum_s -\boldsymbol{F}^{qQab}_{i_a s j_b}, \tag{254}$$

$$w^{q\mu ab}_{i_a j_b} = \boldsymbol{r}_{i_a j_b}\sum_s -\boldsymbol{F}^{q\mu ab}_{i_a s j_b}. \tag{255}$$

A.6.4 Chemical Potential

The Lennard-Jones contributions to the interaction energy ψ_{i_a} and ψ_{i_b}, cf. Equation (150), are given in Appendix A.1.4. The additive contributions due to the interaction of point quadrupoles, point dipoles, sets of point charges, and the reaction field are given in Appendices A.2.4, A.3.4, and A.4.4. The additive contributions due to the interactions of point dipole and point quadrupole are given in Appendix A.5.4. The additive contributions due to the interactions of point quadrupoles and sets of point charges or point dipoles and sets of point charges are

$$\psi_{i_a}^{qQ\mu} = \sum_{\substack{j_b=1 \\ r_{i_a j_b} < r_c}}^{N_b} \left(u_{i_a j_b}^{q\mu ab} + u_{i_a j_b}^{qQab} \right), \tag{256}$$

and

$$\psi_{i_b}^{Q\mu q} = \sum_{\substack{j_a=1 \\ r_{i_b j_a} < r_c}}^{N_a} \left(u_{i_b j_a}^{q\mu b a} + u_{i_b j_a}^{qQba} \right). \tag{257}$$

Appendix B Derivation of the Chemical Potential

The following derivations of the chemical potential start from Equation (58) in Chapter 2.4.2.

Derivation for a'-components

The evaluation of Equation (58) with Equations (49), (50), and (52) yields

$$\begin{aligned}\mu_{a'}(p,T,\boldsymbol{x}) &= -k_\mathrm{B}T\ln\left[\frac{N_{a'}!}{(N_{a'}+1_{a'})!}\cdot\frac{\langle V\rangle_{(N+1_{a'})pT}^{N_{a'}+1_{a'}}}{\langle V\rangle_{NpT}^{N_{a'}}}\cdot\frac{\Lambda_{a'}^{f_{a'}^{\mathrm{tr}}N_{a'}}}{\Lambda_{a'}^{f_{a'}^{\mathrm{tr}}(N_{a'}+1_{a'})}}\right]\\ &\quad -k_\mathrm{B}T\ln\left[\frac{Q^{\mathrm{c}}_{NpT}(N_{a'}+1_{a'})}{Q^{\mathrm{c}}_{NpT}(N_{a'})}\right].\end{aligned}\tag{258}$$

Assuming, that the volumes and the numbers of molecules in the system containing $N_{a'}+1_{a'}$ molecules of component a' and in the system containing $N_{a'}$ molecules of component a' are approximately equal, i.e.

$$\langle V\rangle_{(N+1_{a'})pT} \approx \langle V\rangle_{NpT},\tag{259}$$

$$N_{a'}+1_{a'} \approx N_{a'},\tag{260}$$

Equation (258) becomes

$$\begin{aligned}\mu_{a'}(p,T,\boldsymbol{x}) &= -k_\mathrm{B}T\ln\left[\frac{\langle V\rangle_{NpT}}{N_{a'}}\cdot\frac{1}{\Lambda_{a'}^{f_{a'}^{\mathrm{tr}}}}\right]\\ &= -k_\mathrm{B}T\ln\left[\frac{\int e^{-\beta pV}e^{-\beta U_{N+1}(\Gamma_1^{\mathrm{c}},\ldots,\Gamma_{a'}^{\mathrm{c}}\cup\gamma_{a'}^{\mathrm{c}},\ldots,\Gamma_m^{\mathrm{c}})}d\gamma_{a'}^{\mathrm{c}}\prod_a d\Gamma_a^{\mathrm{c}}dV}{\langle V\rangle_{NpT}\int e^{-\beta pV}e^{-\beta U_N(\Gamma_1^{\mathrm{c}},\ldots,\Gamma_a^{\mathrm{c}},\ldots,\Gamma_m^{\mathrm{c}})}\prod_a d\Gamma_a^{\mathrm{c}}dV}\right].\end{aligned}\tag{261}$$

The additional three position variables of the added a' molecule are represented by $\gamma_{a'}^{\mathrm{c}}$. For convenience, in Equation (261), and hereafter, all NpT-phase space variable sets are noted without NpT-index.

With the following decomposition of the potential energy U_{N+1} in Equation (261)

$$U_{N+1}(\Gamma_1^{\mathrm{c}},\ldots,\Gamma_{a'}^{\mathrm{c}}\cup\gamma_{a'}^{\mathrm{c}},\ldots,\Gamma_m^{\mathrm{c}}) = U_N(\Gamma_1^{\mathrm{c}},\ldots,\Gamma_{a'}^{\mathrm{c}},\ldots,\Gamma_m^{\mathrm{c}}) + \psi_{a'}(\Gamma_1^{\mathrm{c}},\ldots,\Gamma_{a'}^{\mathrm{c}}\cup\gamma_{a'}^{\mathrm{c}},\ldots,\Gamma_m^{\mathrm{c}}),\tag{262}$$

wherein $\psi_{a'}$ is the interaction energy of the added a' molecule with all other molecules in the mixture (cf. Appendix A for its calculation) and with

$$N_{a'} = x_{a'}N,\tag{263}$$

Equation (261) becomes

$$\begin{aligned}\mu_{a'}(p,T,\boldsymbol{x}) &= -k_\mathrm{B}T\ln\left[\frac{\langle V\rangle_{NpT}}{N}\cdot\frac{1}{\Lambda_{a'}^{f_{a'}^{\mathrm{tr}}}}\right]+k_\mathrm{B}T\ln x_{a'}\\ &\quad -k_\mathrm{B}T\ln\left[\frac{\int\left[\int e^{-\beta\psi_{a'}}d\gamma_{a'}^{\mathrm{c}}\right]e^{-\beta(U_N+pV)}\prod_a d\Gamma_a^{\mathrm{c}}dV}{\langle V\rangle_{NpT}\int e^{-\beta(U_N+pV)}\prod_a d\Gamma_a^{\mathrm{c}}dV}\right].\end{aligned}\tag{264}$$

With the position average of $e^{-\beta\psi_{a'}}$ within the volume V

$$\langle e^{-\beta\psi_{a'}}\rangle_r = \frac{1}{V}\int e^{-\beta\psi_{a'}} d\gamma^{\mathrm{c}}_{a'}, \tag{265}$$

Equation (264) becomes

$$\begin{aligned}\mu_{a'}(p,T,\boldsymbol{x}) &= -k_{\mathrm{B}}T\ln\left[\frac{\langle V\rangle_{NpT}}{N}\cdot\frac{1}{\Lambda_{a'}^{f^{\mathrm{tr}}_{a'}}}\right] + k_{\mathrm{B}}T\ln x_{a'} \\ &\quad -k_{\mathrm{B}}T\ln\left[\frac{\int V\cdot\langle e^{-\beta\psi_{a'}}\rangle_r e^{-\beta pV}e^{-\beta U_N}\prod_a d\Gamma^{\mathrm{c}}_a dV}{\langle V\rangle_{NpT}\int e^{-\beta pV}e^{-\beta U_N}\prod_a d\Gamma^{\mathrm{c}}_a dV}\right],\end{aligned} \tag{266}$$

which is Equation (59) in Chapter 2.4.2 for an a' component.

Derivation for a''-components

In order to obtain a composition dependent contribution to the chemical potential also for a''-components, a modified form $\bar{Q}^{\mathrm{id}}_{a'',NVT}$ of the ideal contribution of the NVT-partition function is used. It is independent of the factorial of the number of molecules and is, hence, defined as

$$\bar{Q}^{\mathrm{id}}_{a'',NVT} = N_{a''}!\cdot Q^{\mathrm{id}}_{a'',NVT}, \tag{267}$$

wherein $Q^{\mathrm{id}}_{a'',NVT}$ according to Equation (35). Then the ideal contribution to the NpT-partition function, cf. Equation (51), is rewritten as

$$Q^{\mathrm{id}}_{a'',NpT} = \frac{\langle V\rangle^{N_{a''}}_{NpT}}{N_{a''}!}\cdot\bar{Q}^{\mathrm{id}}_{a'',NVT}. \tag{268}$$

The evaluation of Equation (58) with Equations (49), (52), (268), and with the approximations according to Equations (259) and (260), yields

$$\begin{aligned}\mu_{a''}(p,T,\boldsymbol{x}) &= -k_{\mathrm{B}}T\ln\left[\frac{\langle V\rangle_{NpT}}{N_{a''}}\cdot\frac{\bar{Q}^{\mathrm{id}}_{a'',NVT}(N_{a''}+1_{a''})}{\bar{Q}^{\mathrm{id}}_{a'',NVT}(N_{a''})}\right] \\ &\quad -k_{\mathrm{B}}T\ln\left[\frac{Q^{\mathrm{c}}_{NpT}(N_{a''}+1_{a''})}{Q^{\mathrm{c}}_{NpT}(N_{a''})}\right] \\ &= -k_{\mathrm{B}}T\ln\left[\frac{\langle V\rangle_{NpT}}{N}\cdot\frac{1}{R_{a''}(T)}\right] + k_{\mathrm{B}}T\ln x_{a''} \\ &\quad -k_{\mathrm{B}}T\ln\left[\frac{\int\left[\int e^{-\beta\psi_{a''}}d\gamma^{\mathrm{c}}_{a''}\right]e^{-\beta(U_N+pV)}\prod_a d\Gamma^{\mathrm{c}}_a dV}{\langle V\rangle_{NpT}\int e^{-\beta(U_N+pV)}\prod_a d\Gamma^{\mathrm{c}}_a dV}\right],\end{aligned} \tag{269}$$

which is Equation (59) in Chapter 2.4.2 for an a'' component. In Equation (269) the position variables $\gamma^{\mathrm{c,tr}}_{a''}$ and orientational variables $\gamma^{\mathrm{c,rot}}_{a''}$ of the added a'' molecule are contained in $\gamma^{\mathrm{c}}_{a''}$. In Equation (269) the ideal term

$$R_{a''}(T) = \frac{\bar{Q}^{\mathrm{id}}_{a'',NpT}(N_{a''})}{\bar{Q}^{\mathrm{id}}_{a'',NpT}(N_{a''}+1_{a''})} \tag{270}$$

is analogous to the ideal term $1/\Lambda_{a'}^{f^{tr}}$ in Equation (264). Due to the rotational degrees of freedom of a'' molecules, the dimensionless expression $e^{-\beta\psi_{a''}}$ in Equation (269) is averaged over positions and orientations within the volume V

$$\langle e^{-\beta\psi_{a''}}\rangle_{\omega,r} = \frac{1}{V\cdot\Omega}\int e^{-\beta\psi_{a''}} d\gamma_{a''}^{c}, \tag{271}$$

wherein the normalizing constant Ω is the total orientational integral of the added a'' molecule

$$\Omega = \int d\gamma_{a''}^{c,rot}. \tag{272}$$

Appendix C Technical Details of Simulations

C.1 Vapor-Liquid Equilibria of 2CLJQ Model Fluids

The NpT+Test Particle Method, cf. Chapter 2.5.1, was applied to obtain the vapor-liquid equilibrium data. NpT molecular dynamics simulations with $N = 864$ particles for both liquid and vapor phases were performed. The cut-off radius r_c was set to $5.0 \cdot \sigma$, except for cold liquid phase simulations of some strongly quadrupolar fluids with $L^* = 0$, where values of r_c down to about $4.75 \cdot \sigma$ were required in order to keep the cut-off radius smaller than the half simulation box edge length. The dimensionless integration time step was set to $\Delta t^* = 0.0015$. Starting from a face centered cubic lattice arrangement every simulation run was given 10,000 integration time steps to equilibrate. Data production was performed for 100,000 integration time steps. The configurational part of the chemical potential was obtained from insertion of $2 \cdot N$ test particles in the liquid phase, and N test particles in the vapor phase per production time step. The dimensionless dynamical parameter of NpT-MD-simulations ascribed to the box membrane was set to $2 \cdot 10^{-4}$ for liquid simulations and to 10^{-6} for vapor simulations. The high value of N allowed simulations in the vicinity of the critical point, and the high number of time steps n was used in order to obtain small statistical uncertainties.

As suggested by Möller and Fischer [282], during test particle insertion, the quadrupole sites were shielded by a hard sphere of diameter $0.4 \cdot \sigma$, in order to avoid numerical problems due to divergence of the energetic contributions in the case of small intermolecular distances. This hard sphere was not active during configuration generation. For reasons of consistency, it was applied to all fluids studied here.

C.2 Vapor-Liquid Equilibria of 2CLJD Model Fluids

For most 2CLJD model fluids the simulation parameters were identical to those given for the 2CLJQ model fluids in Appendix C.1. For the lowest temperatures of four 2CLJD fluids ($L^* = 0$ with $\mu^{*2} = 12$, $L^* = 0$ with $\mu^{*2} = 16$, $L^* = 0$ with $\mu^{*2} = 20$, and $L^* = 0.2$ with $\mu^{*2} = 16$), the liquid phase simulations were performed with extended data production phase ($n = 200,000$), and the configurational part of the chemical potentials was obtained from insertion of $10 \cdot N$ test particles per integration time step.

At the lowest temperatures ($0.55 \cdot T_c^*$) of the remaining 2CLJD fluids, vapor-liquid equilibria with very low statistical uncertainties were calculated on the basis of accurate data on the configurational part of the chemical potential in the liquid phase from the gradual insertion method, cf. Chapter 2.4. Monte Carlo based NpT simulations of the liquid phases with gradual insertion were performed with $N = 864$ particles. Starting from a face centered cubic lattice arrangement, these simulations were given 5,000 Monte Carlo loops for equilibration. Data production was performed for 100,000 Monte Carlo loops. One Monte Carlo loops is defined here as N trial translations and $(2/3) \cdot N$ trial rotations

of non-fluctuating molecules, $10 \cdot N$ trial translations and $(20/3) \cdot N$ trial rotations of the fluctuating molecule, $50 \cdot N$ trial translations and $(100/3) \cdot N$ trial rotations of non-fluctuating molecules preferentially in the vicinity of the fluctuating molecule, and one trial volume change. Further simulation parameters for runs with gradual insertion were taken from [420]. Table 32 gives the definition of the seven intermediate states i for the gradual insertion of a 2CLJD molecule used in the present work. Multiplication of the 2CLJD parameters σ, ε, and μ with the scaling factors $f_{\sigma,i}$, $f_{\varepsilon,i}$, and $f_{\mu,i}$ yields the parameters of the fluctuating molecule in the intermediate state i. The point dipole is shielded as soon as it is allowed to interact, i.e. $f_{\mu,i} > 0$. The parameter L^* was kept constant for or all intermediate states.

Table 32: Intermediate states for the gradual insertion of a 2CLJD molecule.

i	$f_{\sigma,i}$	$f_{\varepsilon,i}$	$f_{\mu,i}$	Shield
1	0.0	0.0	0.0	no
2	0.408	$(1/6)^2$	1/6	yes
3	0.578	$(2/6)^2$	2/6	yes
4	0.708	$(3/6)^2$	3/6	yes
5	0.816	$(4/6)^2$	4/6	yes
6	0.912	$(5/6)^2$	5/6	yes
7	1.0	1.0	1.0	yes

Long-range corrections for the dipolar part of the 2CLJD potential model were calculated with the reaction field method, cf. Appendix A.3.

C.3 Vapor-Liquid Equilibria of Methanol

The vapor-liquid equilibrium data of methanol were obtained from the NpT+Test Particle Method, cf. Chapter 2.5.1. Vapor-phase simulations shown in the present work were Monte Carlo based, as equilibration was achieved substantially faster and more reliably than with molecular dynamics simulations. For molecular dynamics simulations of the vapor phase, that are not shown in the present work, it was assumed, that the mass distribution in the methanol molecule is $m_{CH_3} : m_O : m_H = 15 : 12 : 6$, which was also applied for the definition of the molecular center in all Monte Carlo simulations of methanol. The increased hydrogen mass helped to keep the rotational motion of the molecules numerically stable. The results were consistent with results from simulations using the physical mass distribution $m_{CH_3} : m_O : m_H = 15 : 12 : 1$, that, however, needed very small integration time steps for numerical stability.

For the model $\boldsymbol{M}_0$, the Monte Carlo based NpT simulations of the liquid phases with gradual insertion were performed with $N = 500$ particles and cut-off radius 15.75 Å. Starting from a face-centered cubic lattice arrangement, every simulation run was given 5,000

Monte Carlo loops for equilibration. Data production was performed over $n = 95,000$ Monte Carlo loops. One Monte Carlo loop is defined here as N trial translations and N trial rotations of non-fluctuating molecules, $10 \cdot N$ trial translations and $(20/3) \cdot N$ trial rotations of the fluctuating molecule, $50 \cdot N$ trial translations and $(100/3) \cdot N$ trial rotations of non-fluctuating molecules preferentially in the vicinity of the fluctuating molecule, and one trial volume change. Further simulation parameters for runs with gradual insertion were taken from [420].

The definition of the eleven intermediate states for the gradual insertion of a methanol molecule used in the present work is shown in Table 33. Multiplication of the Lennard-Jones size parameters, Lennard-Jones energy parameters, and the point charges with the scaling factors $f_{\sigma,i}$, $f_{\varepsilon,i}$, and $f_{q,i}$ yields the parameters of the fluctuating molecule in the intermediate state i. Furthermore, Table 33 contains the locations of the CH_3-, oxygen-, and hydrogen-sites relative to the center of mass in the principal axis system. All z coordinates are zero. The location of the Lennard-Jones sites and the point charges of the CH_3-group and the oxygen atom were always identical, whereas the hydrogen-site moved stepwise outward. The C-O bond length was kept constant for all intermediate states. Table 33 shows, that the point charges were activated only after the Lennard-Jones sites were grown to their full size. This strategy helps to enhance the transition between intermediate states.

The interaction of point charge $q_{i,s}$ on molecule i and point charge $q_{j,k}$ on molecule j was shielded by a hard sphere as soon as the point charges were activated, i.e. $f_{q,i} > 0$. For reasons of consistency with literature, according to a suggestion by Lísal et al. [228], the diameter of the hard sphere was set to $0.8 \cdot \sigma_{isjk}$, with $\sigma_{isjk} = (\sigma_{is} + \sigma_{jk})/2$ (the Lennard-Jones size parameter is set to zero in the case of the hydrogen site). However, without showing the results here, it was verified in the frame of the present work, that the insertion strategy listed in Table 33 does not require point charge shielding at all. Error free gradual insertion runs, also in cold, dense liquid phases were obtained without any shielding. This very satisfactory result allowed to specify the hard spheres diameter, that will start to influence the interaction energy. It was found, that hard sphere diameters $0.8 \cdot \sigma_{isjk}$ are on the edge of getting influence. For correct results, they must not be larger.

For the model $\boldsymbol{M}_0$, Monte Carlo based NpT simulations of the vapor phases were performed with $N = 500$ molecules and cut-off radius 17.5 Å. Starting from a face centered cubic lattice arrangement, every simulation run was given 40,000 Monte Carlo loops for equilibration. Data production was performed over $n = 300,000$ Monte Carlo loops. The configurational part of the chemical potential was obtained from insertion of $N = 500$ test particles per Monte Carlo loop. During test particle insertion, the above discussed hard spheres were used to shield the point charges.

For the model $\boldsymbol{M}_{\text{opt}}$, the $\boldsymbol{M}_0$ simulation conditions were applied to the liquid phase simulations, except for particle numbers N, numbers of Monte Carlo production loops n,

Table 33: Intermediate states for the gradual insertion of a methanol molecule.

i	$f_{\sigma,i}$	$f_{\varepsilon,i}$	$f_{q,i}$	$x_{i,\mathrm{CH3}}$/Å	$y_{i,\mathrm{CH3}}$/Å	$x_{i,\mathrm{O}}$/Å	$y_{i,\mathrm{O}}$/Å	$x_{i,\mathrm{H}}$/Å	$y_{i,\mathrm{H}}$/Å	Shield
1	0.0	0.0	0.0	−0.8470595	0.0	0.5775405	0.0	0.5775405	0.0	no
2	0.25	0.25	0.0	−0.8470595	0.0	0.5775405	0.0	0.5775405	0.0	no
3	0.5	0.5	0.0	−0.8470595	0.0	0.5775405	0.0	0.5775405	0.0	no
4	0.75	0.75	0.0	−0.8470595	0.0	0.5775405	0.0	0.5775405	0.0	no
5	1.0	1.0	0.0	−0.8470595	0.0	0.5775405	0.0	0.5775405	0.0	no
6	1.0	1.0	0.167	−0.8555185	$1.629740 \cdot 10^{-3}$	0.5684312	$-4.141211 \cdot 10^{-2}$	0.6229797	0.1063579	yes
7	1.0	1.0	0.333	−0.8646247	$6.946235 \cdot 10^{-3}$	0.5570511	$-8.428426 \cdot 10^{-2}$	0.6760922	0.2073925	yes
8	1.0	1.0	0.5	−0.8742784	$1.661308 \cdot 10^{-2}$	0.5428902	−0.1287077	0.7379888	0.3016878	yes
9	1.0	1.0	0.667	−0.8842961	$3.128438 \cdot 10^{-2}$	0.5253404	−0.1746527	0.8098324	0.3875294	yes
10	1.0	1.0	0.833	−0.8943874	$5.151623 \cdot 10^{-2}$	0.5037292	−0.2218975	0.8926905	0.4629362	yes
11	1.0	1.0	1.0	−0.9041495	$7.762531 \cdot 10^{-2}$	0.4773997	−0.2699474	0.9873079	0.5257966	yes

and cut-off radii $r_c = 17.5$Å. For 325 K to 405 K, they were $N = 864$, $n = 50,000$. For 445 K to 490 K they were $N = 500$, $n = 70,000$.

For vapor phase simulations of the model M_{opt}, the vapor-phase simulation conditions of the model M_0 were applied, but with data production only over 100,000 Monte Carlo loops.

Long-range corrections for the interaction of the point charges were calculated with the reaction field method, cf. Appendix A.3

C.4 Vapor-Liquid Equilibria of 2CLJQ/2CLJD Mixtures

The Grand Equilibrium method was applied for the calculation of the vapor-liquid equilibria of mixtures. For the adjustment of the binary interaction parameter ξ, $N = 864$ particles were used for NpT molecular dynamics liquid phase simulations and about 300 particles for the subsequent quasi grand canonical Monte Carlo vapor phase simulations. The cut-off radius was set to $5 \cdot \sigma$. The simulations were started from face centered cubic lattice arrangements. The liquid phase simulations were equilibrated over 10,000 time steps, and data production was carried out for 100,000 time steps (one time step ≈ 3 fs). The configurational part of the chemical potential and the partial molar volume of each component in the liquid phase were obtained from insertion of $4 \cdot N$ test particles of each component per integration time step. The vapor phase simulations were given 10,000 Monte Carlo loops for equilibration and 100,000 Monte Carlo loops for data production. One Monte Carlo loop was defined as N trial translations, $(2/3) \cdot N$ trial rotations, one trial particle insertion, and one trial particle deletion.

For most of the vapor-liquid equilibrium isotherms for binary systems shown in Chapter 6 the number of particles in the liquid phase was reduced to 500, in the vapor phase the particle number was approximately 250 and the cut-off radius was $4 \cdot \sigma$ in both phases.

Simulations of ternary mixtures were carried out with 864 particles in the liquid phase and about 300 particles in the vapor phase, the cut-off radii were $5 \cdot \sigma$ in both phases.

Long-range corrections for the dipolar part of the 2CLJD potential model were calculated with the reaction field method, cf. Appendix A.3.

C.5 Vapor-Liquid Equilibria of the Mixture Methanol + Carbon Dioxide

The Grand Equilibrium method was applied for the calculation of the vapor-liquid equilibria. During the Monte Carlo NpT simulations of the liquid phase, the configurational part of the chemical potential and the partial molar volume of both components were obtained from the gradual insertion method. The definition of one NpT Monte Carlo loop with gradual insertion and the mass distribution in the methanol molecule are described

in Appendix C.3. The intermediate states for the gradual insertion of a 2CLJQ carbon dioxide molecule in the mixture are given in Table 34. The symbols are explained in Appendix C.2, the factor $f_{Q,i}$ has got the same meaning for the point quadrupole as the factor $f_{\mu,i}$ for the point dipole.

For gradual insertion, hard sphere shielding was applied to point quadrupoles and point charges as described in Appendices C.1 and C.3. The diameters of the hard spheres that shield interactions of point charges and point quadrupoles were taken as the arithmetic mean of the diameters of the hard spheres defined for the point charges and the point quadrupoles.

All simulations were started from a face centered cubic lattice arrangement.

For the adjustment of the binary interaction parameter ξ, 864 particles were used for liquid phase simulations and about 500 particles for the vapor phase simulations. The cut-off radius was 17.5 Å. The liquid phase simulations were equilibrated over 5,000 Monte Carlo loops, data production was carried out within 45,000 Monte Carlo loops. The vapor phase simulations were given 20,000 Monte Carlo loops for equilibration in the NVT ensemble, then 70,000 Monte Carlo loops of equilibration in the μVT ensemble. Data production was done within 200,000 Monte Carlo loops.

The liquid phases at 298.15 K were simulated with $N = 500$ particles, cut-off radius $r_c = 15.75$ Å, 5,000 Monte Carlo loops for equilibration, 25,000 Monte Carlo loops for data production. At 323.15 K, these numbers were $N = 864$, $r_c = 17.5$ Å, 5,000 Monte Carlo loops for equilibration, 45,000 Monte Carlo loops for data production. At 373.15 K they were $N = 500$, $r_c = 14$ Å, 5,000 Monte Carlo loops for equilibration, 30,000 Monte Carlo loops for data production. For the quasi grand canonical Monte Carlo simulations of the vapor phases about 500 molecules were used. These simulations were equilibrated for 20,000 Monte Carlo loops in the NVT ensemble, and 70,000 Monte Carlo loops in the μVT ensemble. Data production was done within 100,000 Monte Carlo loops.

Long-range corrections for the interaction of the point charges were calculated with the reaction field method, cf. Appendix A.3.

Table 34: Intermediate states for the gradual insertion of 2CLJQ carbon dioxide in the mixture methanol + carbon dioxide. Symbols, cf. Appendix C.2.

i	$f_{\sigma,i}$	$f_{\varepsilon,i}$	$f_{Q,i}$	Shield
1	0.0	0.0	0.0	no
2	0.408	1/6	1/6	yes
3	0.578	2/6	2/6	yes
4	0.708	3/6	3/6	yes
5	0.816	4/6	4/6	yes
6	0.912	5/6	5/6	yes
7	1.0	1.0	1.0	yes

Appendix D Global Correlations

Tables 35 and 36 contain the elementary functions and their coefficients for the global correlations of the critical temperature $T_c^*(P^{*2}, L^*)$, the saturated liquid and vapor densities $\rho'^*(P^{*2}, L^*, T^*)$, $\rho''^*(P^{*2}, L^*, T^*)$, and the vapor pressure $p_\sigma^*(P^{*2}, L^*, T^*)$ for the 2CLJQ and 2CLJD model fluids, cf. Chapter 3.2.2. P^* symbolizes Q^* or μ^*. The control values below Tables 35 and 36 help to avoid mistyping of the global correlations.

Table 35: Elementary functions ψ_i, ξ_i, χ_i and their coefficients α_i, β_i, γ_i, as well as constant c for the correlations $T_c^*(Q^{*2}, L^*)$, $\rho_c^*(Q^{*2}, L^*)$, $C_1(Q^{*2}, L^*)$ to $C_3''(Q^{*2}, L^*)$, and $c_1(Q^{*2}, L^*)$ to $c_3(Q^{*2}, L^*)$. Notation: ℓ is L^*, q is Q^{*2}.

Elementary functions		Coefficients	Elementary functions		Coefficients
$T_c^*(q,\ell)$			$\rho_c^*(q,\ell)$		
c	1	$0.1507579 \cdot 10^{1}$	c	1	0.3143171
ψ_i	q^2	$0.2047231 \cdot 10^{-1}$	ψ_i	q^2	$0.2469999 \cdot 10^{-2}$
	q^3	$-0.1291671 \cdot 10^{-2}$		q^3	$-0.2422011 \cdot 10^{-3}$
ξ_i	$1/(0.1+\ell^2)$	0.3319456	ξ_i	$\ell^2/(0.11+\ell^2)$	−0.1452035
	$1/(0.1+\ell^5)$	$0.4136462 \cdot 10^{-1}$		$\ell^5/(0.11+\ell^5)$	$-0.4259098 \cdot 10^{-1}$
χ_i	$q^2/(0.1+\ell^2)$	$0.9755649 \cdot 10^{-2}$	χ_i	$\ell^2 q^2/(0.11+\ell^2)$	$-0.2700883 \cdot 10^{-2}$
	$q^2/(0.1+\ell^5)$	$-0.1715840 \cdot 10^{-2}$		$\ell^5 q^2/(0.11+\ell^5)$	$0.2785485 \cdot 10^{-2}$
	$q^3/(0.1+\ell^2)$	$-0.8173578 \cdot 10^{-3}$		$\ell^2 q^3/(0.11+\ell^2)$	$0.3007566 \cdot 10^{-3}$
	$q^3/(0.1+\ell^5)$	$0.2301229 \cdot 10^{-3}$		$\ell^5 q^3/(0.11+\ell^5)$	$-0.5084756 \cdot 10^{-3}$
$C_1(q,\ell)$			$C_2'(q,\ell)$		
c	1	0.3019549	c	1	$0.4955956 \cdot 10^{-1}$
ψ_i	q^2	$-0.3796746 \cdot 10^{-3}$	ψ_i	q^2	$0.6125793 \cdot 10^{-2}$
	q^3	$0.6745920 \cdot 10^{-3}$		q^3	$-0.1684225 \cdot 10^{-2}$
ξ_i	$\ell^3/(\ell+0.4)^3$	$-0.1608258 \cdot 10^{-1}$	ξ_i	ℓ^2	$0.7665178 \cdot 10^{-1}$
	$\ell^4/(\ell+0.4)^5$	−0.5227964		ℓ^3	$0.4320915 \cdot 10^{-1}$
χ_i	$q^2\ell^2/(\ell+0.4)$	$0.1122068 \cdot 10^{-1}$	χ_i	$q^2\ell^2$	$-0.1489510 \cdot 10^{-1}$
	$q^2\ell^3/(\ell+0.4)^7$	$-0.4523730 \cdot 10^{-2}$		$q^2\ell^3$	$-0.2119930 \cdot 10^{-2}$
	$q^3\ell^2/(\ell+0.4)$	$-0.2711606 \cdot 10^{-2}$		$q^3\ell^2$	$0.3030791 \cdot 10^{-2}$
	$q^3\ell^3/(\ell+0.4)^7$	$0.3949744 \cdot 10^{-3}$		–	–
$C_3'(q,\ell)$			$C_2''(q,\ell)$		
c	1	$0.6676718 \cdot 10^{-3}$	c	1	$0.1984681 \cdot 10^{-1}$
ψ_i	q^2	$-0.2125521 \cdot 10^{-2}$	ψ_i	q^2	$-0.3677042 \cdot 10^{-2}$
	q^3	$0.5591744 \cdot 10^{-3}$		q^3	$0.1251499 \cdot 10^{-2}$
ξ_i	ℓ	$-0.5007894 \cdot 10^{-2}$	ξ_i	ℓ^2	$-0.5941681 \cdot 10^{-1}$
	ℓ^4	$-0.7089158 \cdot 10^{-1}$		ℓ^3	$0.5235979 \cdot 10^{-1}$
χ_i	$q^2\ell$	$0.1218855 \cdot 10^{-2}$	χ_i	$q^2\ell^2$	$0.1966272 \cdot 10^{-1}$
	$q^2\ell^4$	$0.8615708 \cdot 10^{-2}$		$q^2\ell^3$	$-0.7711454 \cdot 10^{-2}$
	$q^3\ell^4$	$-0.1407562 \cdot 10^{-2}$		$q^3\ell^2$	$-0.2604483 \cdot 10^{-2}$

Table 35: continued.

Elementary functions		Coefficients	Elementary functions		Coefficients
$C_3''(q,\ell)$			$c_1(q,\ell)$		
c	1	$0.1185765 \cdot 10^{-1}$	c	1	$0.4333882 \cdot 10^{1}$
ψ_i	q^2	$0.1556412 \cdot 10^{-2}$	ψ_i	q^2	0.1503665
	q^3	$-0.4872161 \cdot 10^{-3}$		q^3	$-0.2085311 \cdot 10^{-1}$
ξ_i	ℓ	$0.4232978 \cdot 10^{-1}$	ξ_i	$\ell^2/(\ell^2+0.75)$	$-0.1870607 \cdot 10^{1}$
	ℓ^4	$-0.2872173 \cdot 10^{-3}$		$\ell^3/(\ell^3+0.75)$	-0.7103387
χ_i	$q^2\ell$	$-0.2451944 \cdot 10^{-2}$	χ_i	$\ell^2q^2/(\ell^2+0.75)$	-0.5758677
	$q^2\ell^4$	$-0.5240982 \cdot 10^{-2}$		$\ell^3q^2/(\ell^3+0.75)$	0.6802547
	$q^3\ell^4$	$0.1487717 \cdot 10^{-2}$		$\ell^2q^3/(\ell^2+0.75)$	0.1358236
	–	–		$\ell^3q^3/(\ell^3+0.75)$	-0.1916098
$c_2(q,\ell)$			$c_3(q,\ell)$		
c	1	$-0.2660590 \cdot 10^{2}$	c	–	–
ψ_i	q^2	$-0.1144385 \cdot 10^{1}$	ψ_i	q^2	-0.1059248
	q^3	0.1097780		q^5	$-0.3559731 \cdot 10^{-2}$
ξ_i	$\ell^2/(\ell+0.75)^2$	$0.1138729 \cdot 10^{3}$	ξ_i	$\ell^{0.5}$	-0.8836935
	$\ell^3/(\ell+0.75)^3$	$-0.1082939 \cdot 10^{3}$			
χ_i	$\ell^2q^2/(\ell+0.75)^2$	$0.1131664 \cdot 10^{2}$	χ_i	–	–
	$\ell^3q^2/(\ell+0.75)^3$	$-0.1732358 \cdot 10^{2}$		–	–
	$\ell^2q^3/(\ell+0.75)^2$	$-0.1609370 \cdot 10^{1}$		–	–
	$\ell^3q^3/(\ell+0.75)^3$	$0.3026670 \cdot 10^{1}$		–	–

Control values: with $Q^{*2} = 2.5$, $L^* = 0.35$, $T^* = 2.9$ the correlations yield
$T_c^* = 3.6491536$, $\rho_c^* = 0.2415375$, $\rho'^* = 0.5369483$, $\rho''^* = 0.0233367$, $p_\sigma^* = 0.0562932$.

Table 36: Elementary functions ψ_i, ξ_i, χ_i and their coefficients α_i, β_i, γ_i, as well as constant c for the correlations $T_c^*(\mu^{*2}, L^*)$, $\rho_c^*(\mu^{*2}, L^*)$, $C_1(\mu^{*2}, L^*)$ to $C_3''(\mu^{*2}, L^*)$, and $c_1(\mu^{*2}, L^*)$ to $c_3(\mu^{*2}, L^*)$. Notation: ℓ is L^*, m is μ^{*2}, $a_1 = m + 88$, $a_2 = m + 70$, $a_3 = 0.1 + \ell^2$, $a_4 = 0.1 + \ell^5$, $a_5 = 0.11 + \ell^2$, $a_6 = 0.11 + \ell^5$, $a_7 = \ell + 0.4$, and $a_8 = \ell + 0.75$.

Elementary functions		Coefficients	Elementary functions		Coefficients
$T_c^*(m,\ell)$			$\rho_c^*(m,\ell)$		
c	1	$0.1454013 \cdot 10^{1}$	c	1	0.3157828
ψ_i	$m/{a_1}^2$	$0.1363894 \cdot 10^{3}$	ψ_i	$m/{a_1}^2$	$0.9871123 \cdot 10^{1}$
	$m^2/{a_1}^3$	$0.2020243 \cdot 10^{4}$		$m^2/{a_1}^3$	$-0.1461751 \cdot 10^{3}$
ξ_i	$1/a_3$	0.3269772	ξ_i	ℓ^2/a_5	-0.1475616
	$1/a_4$	$0.4910240 \cdot 10^{-1}$		ℓ^5/a_6	$-0.4152214 \cdot 10^{-1}$
χ_i	$m/({a_1}^2 \cdot a_3)$	$0.4239005 \cdot 10^{2}$	χ_i	$m/{a_1}^2 \cdot \ell^2/a_5$	$-0.1010584 \cdot 10^{2}$
	$m^2/({a_1}^3 \cdot a_3)$	$0.6724083 \cdot 10^{3}$		$m^2/{a_1}^3 \cdot \ell^2/a_5$	$0.4105884 \cdot 10^{2}$
	$m^2/({a_1}^3 \cdot a_4)$	$0.7913876 \cdot 10^{2}$		$m^2/{a_1}^3 \cdot \ell^5/a_6$	$0.5299302 \cdot 10^{2}$

Table 36: continued.

Elementary functions		Coefficients	Elementary functions		Coefficients
$C_1(m,\ell)$			$C_2'(m,\ell)$		
c	1	0.2951644	c	1	$0.6484789 \cdot 10^{-1}$
ψ_i	$m^2/{a_2}^2$	−0.6339151	ψ_i	$m^2/{a_2}^2$	0.7301440
	$m^3/{a_2}^3$	$0.3182745 \cdot 10^1$		$m^3/{a_2}^3$	$-0.8780100 \cdot 10^1$
ξ_i	$\ell^2 \cdot e^\ell$	−0.2359527	ξ_i	$\ell^2 \cdot e^\ell$	−0.6551324
	ℓ^3	0.5466755		ℓ^3	$0.1810641 \cdot 10^1$
χ_i	$m^2/{a_2}^2 \cdot \ell^8/a_7$	$0.1449170 \cdot 10^1$	χ_i	$m^2/{a_2}^2 \cdot \ell^2 \cdot e^\ell$	$0.4808117 \cdot 10^1$
	$m^3/{a_2}^3 \cdot \ell^2/{a_7}^2$	−0.1955388		$m^3/{a_2}^3 \cdot \ell^2 \cdot e^\ell$	$0.1937455 \cdot 10^1$
	$m^3/{a_2}^3 \cdot \ell^8/a_7$	$-0.5849357 \cdot 10^1$		$m^2/{a_2}^2 \cdot \ell^3$	$-0.1320822 \cdot 10^2$
$C_3'(m,\ell)$			$C_2''(m,\ell)$		
c	1	$-0.7258204 \cdot 10^{-2}$	c	1	$-0.5486341 \cdot 10^{-2}$
ψ_i	$m^2/{a_2}^2$	−0.6215183	ψ_i	$m^2/{a_2}^2$	$0.1223952 \cdot 10^1$
	$m^3/{a_2}^3$	$0.4708560 \cdot 10^1$		$m^3/{a_2}^3$	$0.1350701 \cdot 10^1$
ξ_i	$\ell^2 \cdot e^\ell$	0.4316296	ξ_i	$\ell^2/{a_7}^2$	0.2479957
	ℓ^3	$-0.1166922 \cdot 10^1$		ℓ^8/a_7	−0.1684560
χ_i	$m/{a_1}^2 \cdot \ell^2/{a_7}^2$	$-0.2215021 \cdot 10^2$	χ_i	$m/{a_1}^2 \cdot \ell^2/{a_7}^2$	$-0.1956742 \cdot 10^2$
	$m^2/{a_1}^3 \cdot \ell^2/{a_7}^2$	$-0.7803181 \cdot 10^2$		$m^2/{a_1}^3 \cdot \ell^2/{a_7}^2$	$-0.2289032 \cdot 10^3$
	$m/{a_1}^2 \cdot \ell^8/a_7$	−0.5735507		$m^2/{a_1}^3 \cdot \ell^8/a_7$	$0.7221121 \cdot 10^3$
$C_3''(m,\ell)$			$c_1(m,\ell)$		
c	1	$0.2574709 \cdot 10^{-1}$	c	1	$0.4411718 \cdot 10^1$
ψ_i	$m/{a_1}^2$	$-0.2940407 \cdot 10^1$	ψ_i	$m/{a_1}^2$	$0.4575129 \cdot 10^3$
	$m^2/{a_1}^3$	$-0.1008706 \cdot 10^3$		$m^2/{a_1}^3$	$0.2469929 \cdot 10^4$
ξ_i	$\ell^2/{a_7}^2$	$-0.9426323 \cdot 10^{-1}$	ξ_i	$\ell^2/{a_7}^2$	$-0.2016356 \cdot 10^1$
	ℓ^8/a_7	0.1108324		ℓ^8/a_7	0.4346103
χ_i	$m/{a_1}^2 \cdot \ell^2/{a_7}^2$	$0.2543158 \cdot 10^2$	χ_i	$m^2/{a_1}^3 \cdot \ell^2/{a_7}^2$	$0.9787962 \cdot 10^3$
	$m^2/{a_1}^3 \cdot \ell^2/{a_7}^2$	$0.5987224 \cdot 10^2$		$m^2/{a_1}^3 \cdot \ell^8/a_7$	$0.2467171 \cdot 10^4$
	$m^2/{a_1}^3 \cdot \ell^8/a_7$	$-0.6511462 \cdot 10^3$		–	–
$c_2(m,\ell)$			$c_3(m,\ell)$		
c	1	$-0.2686327 \cdot 10^2$	c	–	–
ψ_i	$m/{a_1}^2$	$-0.3428826 \cdot 10^4$	ψ_i	$m/{a_1}^2$	$-0.5264689 \cdot 10^3$
	$m^2/{a_1}^3$	$-0.8720808 \cdot 10^5$		$m^2/{a_1}^3$	$0.6782756 \cdot 10^4$
ξ_i	$\ell^2/{a_8}^2$	$0.1275315 \cdot 10^3$	ξ_i	ℓ^4	0.1812550
	$\ell^3/{a_8}^3$	$-0.1393077 \cdot 10^3$		–	–
χ_i	$m/{a_1}^2 \cdot \ell^2/{a_8}^2$	$0.7248855 \cdot 10^4$	χ_i	–	–
	$m^2/{a_1}^3 \cdot \ell^2/{a_8}^2$	$0.5715498 \cdot 10^6$		–	–
	$m^2/{a_1}^3 \cdot \ell^3/{a_8}^3$	$-0.7433962 \cdot 10^6$		–	–

Control values: with $\mu^{*2} = 10$, $L^* = 0.35$, $T^* = 3.4$ the correlations yield $T_c^* = 4.3461035$, $\rho_c^* = 0.2279013$, $\rho'^* = 0.5325071$, $\rho''^* = 0.0150705$, $p_\sigma^* = 0.0416502$.

Appendix E Details on the choice of the model type

For monatomic fluids, i.e. the noble gases neon, argon, krypton, and xenon, the spherical unpolar Lennard-Jones model was used. Neglecting the only weak octupole of methane, also an unpolar Lennard-Jones model was chosen for that fluid. For these fluids the adjustment of the Lennard-Jones parameters according to Equations (132) to (134) was carried out with the vapor pressure and saturated liquid density correlations for the 1CLJ model fluid $p_\sigma^*(T^*)$ and $\rho'^*(T^*)$ from Lotfi et al. [234], as they yield slightly better results than the present global correlations for $Q^{*2} = 0$ or $\mu^{*2} = 0$ with $L^* = 0$.

For symmetric diatomic quadrupolar molecules, i.e. oxygen, nitrogen, and the halogens fluorine, chlorine, bromine, and iodine, all-atom 2CLJQ modeling was evidently a good choice.

For other symmetric quadrupolar fluids, that are the rotationally symmetric carbon dioxide, carbon disulfide, and ethyne, the planar symmetric ethene, perfluoroethene, perchloroethene, and propadiene, and also ethane and perfluoroethane, united-atom modeling was assumed. United-atom modeling means, that each of the two Lennard-Jones sites represents groups or parts of bonded atoms.

In the sense of united-atom modeling, two-center Lennard-Jones based models are also justified for fluids like tetrafluoromethane, tetrachloromethane, or sulfur hexafluoride. Quadrupolar modeling was chosen for these fluids in order to verify to which extent the quadrupole, as the polarity "closest" to the octu- or hexadecapole of these molecules, is able to account for these higher polarities.

The multipolar fluids modeled in the present work are at least both dipolar and quadrupolar, and additionally in some cases even octupolar [132]. Symmetric and unipolar 2CLJQ and 2CLJD models were developed for these fluids. The application of these symmetric unipolar molecular models to asymmetric multipolar molecules is a considerable but justifiable simplification. Despite the simplification, a physical interpretation of the model parameters is still possible, as important contributions of the molecular interactions are still accounted for. Criteria for deciding between dipolar or quadrupolar modeling are discussed hereafter.

Halogenated methane derivatives are considered first.

- *Methane derivatives with a single halogen substitute:* The halogen substitute in R41 (CH_3F), CH_3Cl, CH_3Br, and CH_3I causes di- and quadrupolarity. The dipole momentum decreases slightly from about 1.8 D for R41 to about 1.6 D for CH_3I, the quadrupole momentum increases considerably from about 0 DÅ for R41 to about 5 DÅ for CH_3I [132]. Therefore, 2CLJD modeling is reasonable for R41 and CH_3Cl. Despite the strong quadrupole, 2CLJD modeling was also used for the still considerably dipolar CH_3Br and CH_3I. The model parameter μ is not steadily decreasing for these four fluids, as it has to compensate for the lacking quadrupole, however, its value of roughly 2 D is still reasonable compared to the experimental data.

- *Methane derivatives with two identical halogen substitutes:* For these fluids (R32 (CH_2F_2), CH_2Cl_2, CH_2Br_2, CH_2I_2) parameters for the spherical Stockmayer fluid are given. It is not reasonable to apply the present 2CLJD model with $L > 0$ to these fluids, as they would require a dipole orthogonal instead of parallel to the model's elongation. Elongated 2CLJQ modeling can be reasonable for the larger molecules, i.e. CH_2Cl_2, CH_2Br_2, CH_2I_2. Indeed, as an alternative to the proposed 2CLJD model an accurate 2CLJQ model was found for CH_2Br_2, cf. Tables 9 and 10. For 2CLJQ modeling of CH_2I_2 reduced squared quadrupole momenta $Q^{*2} > 4$ would be needed. Therefore only a 2CLJD model is given in Table 10.

- *Methane derivatives with three identical halogen substitutes:* Shape and polarity of these fluids (R23 (CHF_3), $CHCl_3$, $CHBr_3$) are difficult to describe with the 2CLJD or the 2CLJQ model. Although the reduced elongation $L^* = L/\sigma$ of the 2CLJD models for these fluids are somewhat too large - one would expect more compact models - they yield a good description of the vapor-liquid equilibria.

- *The remaining methane derivatives:* These fluids are R11 ($CFCl_3$), R12 (CF_2Cl_2), R13 (CF_3Cl), R13B1 (CF_3Br), R22 (CHF_2Cl), CH_2BrCl, $CHFCl_2$, CBr_2F_2, $CBrClF_2$, and $CBrCl_3$. The size differences of the halogen substitutes makes it easy to justify united-atom modeling with two-center Lennard-Jones based models. The equal size of the Lennard-Jones sites is oviously a simplification. Again, only the dipolarity of these fluids was modeled. Typically, the molecular dipole vector will be inclined to the model's elongated axis. The axial dipole vector of the 2CLJD model is considered here as a projection of the molecular dipole vector on the model axis.

Generally, for halogenated methane derivatives 2CLJD modeling was chosen, as results from 2CLJQ modeling generally yielded less convincing results.

Next, halogenated ethane and ethene derivatives are considered.

- *Ethane/ethene derivatives with only one kind of halogen substitute:* The resulting dipole vector of molecules whose halogen substitutes are located on one side of the molecule only (R125 (CHF_2–CF_3), R134a (CH_2F–CF_3), R143a (CH_3–CF_3), R152a (CH_3–CHF_2), CH_2F–CH_3, $CHCl_2$–CH_3, CH_2Br–CH_3, $CHBr_2$–CH_3, $CHF{=}CH_2$, $CF_2{=}CH_2$, $CHCl{=}CH_2$) or whose halogen substitutes are asymmetrically distributed on both sides of the molecule ($CHCl_2$–CH_2Cl, CH_2Cl–CCl_3, CCl_3–CH_3), has an axial component that justifies 2CLJD modeling. As an exception, 2CLJQ modeling of the only weakly dipolar fluid $CCl_2{=}CHCl$ was more accurate than 2CLJD modeling. If the halogen substitutes are symmetrically distributed on both sides of the molecule (R134 (CHF_2–CHF_2), CH_2Br–CH_2Br), the axial component of the resulting molecular dipole vector disappears and, therefore, 2CLJQ modeling is reasonable. The molecules CH_2F–CH_2F, CH_2Cl–CH_2Cl, $CHCl_2$–$CHCl_2$, and $CHBr_2$–$CHBr_2$ would

fit in this latter category, but models are not given in the present work for these fluids, as, in these cases, 2CLJQ modeling would require quadrupole momenta or elongations higher than those available in the present 2CLJQ correlations.

- *Fluorinated-chlorinated ethane/ethene derivatives:* 2CLJD modeling is justified due to sufficiently high dipole momenta caused by asymmetry when i.) the halogen substitutes are found on one side of the molecule (R141b (CH_3–$CFCl_2$), R142b (CH_3–CF_2Cl)), ii) fluorine is found on one side and chlorine on the other side of the molecule (R123 ($CHCl_2$–CF_3), CH_2F–CCl_3, CHCl=CF_2), iii) fluorine is found on one side and the other side has substitutes with not more than one fluorine atom (R124 ($CHFCl$–CF_3)), iv) chlorine is located on one side of the molecule, the other side has fluorine or chlorine substitutes (CCl_3–CF_2Cl). For R115 (CF_2Cl–CF_3) it was more reasonable to choose the 2CLJQ model. As an exception, for the weakly dipolar fluid $CFCl$=CF_2 2CLJD modeling yields better results than 2CLJQ modeling. For other fluorinated-chlorinated fluids (R113 ($CFCl_2$–CF_2Cl), R114 (CF_2Cl–CF_2Cl), $CFCl_2$–CF_2Cl) dipole momenta are weak and strong quadrupole momenta can be expected, so 2CLJQ modeling was used.

- *Fluorinated-brominated ethane/ethene derivatives:* Rules similar to fluorinated-chlorinated ethane/ethene derivatives apply. In analogy to R114 (CF_2Cl–CF_2Cl), a 2CLJQ model is justified for $CBrF_2$–$CBrF_2$. Similarly to $CFCl = CF_2$, 2CLJD modeling of $CFBr$=CF_2 yields better results than 2CLJQ modeling.

- *Fluorinated-chlorinated-brominated ethane derivatives:* Rules similar to fluorinated-chlorinated ethane/ethene derivatives apply. A 2CLJD model was used for the fluid $CHClBr$–CF_3.

Overall, 2CLJD modeling was chosen for most multipolar fluids, due to the better description of thermophysical properties. This finding is supported by the fact that the lowest non-disappearing multipole momentum usually dominates the electrostatic interactions of a given molecule, cf. [305].

Appendix F Experimental Database

Table 37: Experimental database for vapor pressures p_σ, saturated liquid densities ρ', and enthalpies of vaporization Δh_v used in the present work.

Fluid	p_σ	ρ'	Δh_v	Fluid	p_σ	ρ'	Δh_v
Ne	[264]	[55]	[67]	Ar	[376]	[376]	[376]
Kr	[67]	[55]	[67]	Xe	[67]	[55]	[67]
CH_4	[354]	[354]	[354]	F_2	[264]	[55]	[67]
Cl_2	[329]	[55]	[67]	Br_2	[67]	[353]	[67]
I_2	[67]	[55]	[67]	N_2	[157]	[157]	[157]
O_2	[352]	[352]	[352]	CO_2	[87]	[87]	[87]
CS_2	[67]	[67]	[251]	C_2H_6	[115]	[115]	[115]
C_2H_4	[158]	[158]	[158]	C_2H_2	[318]	[67]	[67]
C_2F_6	[188]	[188]	[188]	C_2F_4	[329]	[67]	[67]
C_2Cl_4	[329]	[67]	[67]	Propadiene	[67]	[55]	[67]
SF_6	[67]	[67]	[67]	CF_4	[320]	[320]	[320]
CCl_4	[264]	[67]	[110]	CO	[209]	[209]	[209]
R11	[156]	[156]	[156]	R12	[258]	[258]	[258]
R13	[248]	[248]	[248]	R13B1	[67]	[67]	[67]
R22	[167]	[167]	[167]	R23	[317]	[317]	[317]
R32	[393]	[393]	[393]	R41	[145]	[145]	[145]
R113	[258]	[258]	[258]	R114	[329]	[67]	[67]
R115	[154]	[154]	[154]	R123	[444]	[444]	[444]
R124	[79]	[79]	[79]	R125	[207]	[207]	[207]
R134	[67]	[67]	[67]	R134a	[392]	[392]	[392]
R141b	[210]	[210]	[210]	R142b	[211]	[211]	[211]
R143a	[208]	[208]	[208]	R152a	[311]	[311]	[311]
R161	[67]	[67]	[67]	CH_3Cl	[329]	[67]	[67]
CH_3Br	[67]	[67]	[67]	CH_3I	[67]	[67]	[67]
CH_2Cl_2	[353]	[67]	[67]	CH_2Br_2	[67]	[67]	[67]
CH_2I_2	[67]	[67]	[67]	CH_2ClBr	[67]	[67]	[67]
$CHCl_3$	[67]	[67]	[67]	$CHBr_3$	[67]	[67]	[67]
$CHFCl_2$	[67]	[67]	[67]	CF_2Br_2	[67]	[67]	[67]
CF_2ClBr	[67]	[67]	[67]	CCl_3Br	[67]	[67]	[67]
$CHCl_2$–CH_3	[67]	[67]	[67]	$CHCl_2$–CH_2Cl	[329]	[67]	[67]
CCl_3–CH_3	[329]	[55]	[67]	CCl_3–CH_2Cl	[67]	[67]	[67]
CH_2Br–CH_3	[67]	[55]	[67]	CH_2Br–CH_2Br	[329]	[67]	[67]
$CHBr_2$–CH_3	[67]	[67]	[67]	CCl_3–CH_2F	[67]	[67]	[67]
$CHClBr$–CF_3	[67]	[67]	[67]	CCl_3–CF_2Cl	[67]	[67]	[67]
CF_2Br–CF_2Br	[329]	[67]	[67]	$CHF{=}CH_2$	[329]	[67]	[67]
$CF_2{=}CH_2$	[329]	[67]	[67]	$CHCl{=}CH_2$	[329]	[67]	[67]
$CCl_2{=}CHCl$	[329]	[67]	[67]	$CHCl{=}CF_2$	[67]	[67]	[67]
$CFCl{=}CF_2$	[329]	[67]	[67]	$CFBr{=}CF_2$	[67]	[67]	[67]
Propylene	[5]	[5]	[5]	Propyne	[329]	[55]	[67]

Appendix G Sign of the Quadrupole Momentum

For several pure fluids the sign of the momentum Q of the elongated point quadrupole in the 2CLJQ potential function, cf. Equation (183), was determined. The momentum Q is the component Q_{zz} of the quadrupole tensor $\boldsymbol{Q}$ of a symmetric elongated quadrupole. This type of quadrupole consists of the charges q, $-2q$, q at distances a along the z-axis. With the origin of the (x, y, z)-coordinate system located in the central $-2q$ charge, the charge density $\rho(x, y, z)$ of that quadrupole is given by

$$\rho(x, y, z) = q \cdot \delta(x) \cdot \delta(y) \cdot (\delta(z - a) - 2\delta(z) + \delta(z + a)), \tag{273}$$

wherein Dirac δ-functions are used, and its quadrupole tensor is [150, 305]

$$\boldsymbol{Q} = \begin{pmatrix} -\frac{1}{2}Q_{zz} & 0 & 0 \\ 0 & -\frac{1}{2}Q_{zz} & 0 \\ 0 & 0 & Q_{zz} \end{pmatrix}, \tag{274}$$

wherein

$$Q_{zz} = 4qa^2. \tag{275}$$

Equations (273) and (275) show, that $Q_{zz} > 0$ for $q > 0$, i.e. charge arrangement $+ - -+$, and $Q_{zz} < 0$ for $q < 0$, i.e. inverse arrangement $- + +-$. Consequently, the sign of Q is determined when signed values for Q_{zz} are available from experiment, calculation, or estimation.

Signed values of Q_{zz} from experiment are available from Gray and Gubbins [132] and from Stogryn and Stogryn [377] for the symmetric molecules fluorine, chlorine, bromine, iodine, nitrogen, oxygen, carbon dioxide, carbon disulfide, ethane, ethene, ethyne, and propadiene. These signs of Q_{zz} were adopted as signs of the model parameter Q for these fluids, cf. Table 8.

For the perhalogenated molecules C_2F_4, C_2Cl_4, and C_2F_6 the signs of Q_{zz} were determined with the bond dipole method [94], that yields $Q_{zz} < 0$, and thus $Q < 0$, for these three molecules. This result is physically reasonable due to the high electronegativity of fluorine and chlorine atoms. For propyne, the bond dipole method yields a negative value of $Q_{zz} < 0$, i.e. $Q < 0$.

In the case of propylene, R113, R114, R115, R134, CH_2Br_2, CH_2Br–CH_2Br, $CBrF_2$–$CBrF_2$, and CCl_2=$CHCl$, whose molecular charge distributions are asymmetric, the description of the quadrupole tensor requires two principal quadrupole momenta, for example Q_{xx} and Q_{zz}, with $Q_{yy} = -(Q_{xx} + Q_{zz})$, that can be determined by the bond dipole method. However, only a squared effective quadrupole momentum can be calculated in these cases, which is useless for the determination of the sign of Q. Therefore, the influence of the sign inversion on vapor-liquid equilibria was empirically tested at the example of propylene as described in Chapter 6, cf. also Table 28.

Appendix H CAS Registry Numbers

Table 38: CAS Registry Numbers (CAS RN) for the fluids modeled in the present work.

Fluid	CAS RN	Fluid	CAS RN
Neon (Ne)	7440-01-9	Argon (Ar)	7440-37-1
Krypton (Kr)	7439-90-9	Xenon (Xe)	7440-63-3
Methane (CH_4)	74-82-8	Fluorine (F_2)	7782-41-4
Chlorine (Cl_2)	7782-50-5	Bromine (Br_2)	7726-95-6
Iodine (I_2)	7553-56-2	Nitrogen (N_2)	7727-37-9
Oxygen (O_2)	7782-44-7	Carbon dioxide (CO_2)	124-38-9
Carbon disulfide (CS_2)	75-15-0	Ethane (C_2H_6)	74-84-0
Ethene (C_2H_4)	74-85-1	Ethine (C_2H_2)	74-86-2
Perfluoroethane (C_2F_6)	76-16-4	Perfluoroethene (C_2F_4)	116-14-3
Perchloroethene (C_2Cl_4)	127-18-4	Propadiene (CH_2=C=CH_2)	463-49-0
Sulfur hexafluoride (SF_6)	2551-62-4	Tetrafluoromethane (CF_4)	75-73-0
Tetrachloromethane (CCl_4)	56-23-5	Carbon monoxide (CO)	630-08-0
R11 ($CFCl_3$)	75-69-4	R12 (CF_2Cl_2)	75-71-8
R13 (CF_3Cl)	75-72-9	R13B1 (CF_3Br)	75-63-8
R22 (CHF_2Cl)	75-45-6	R23 (CHF_3)	75-46-7
R32 (CH_2F_2)	75-10-5	R41 (CH_3F)	593-53-3
R113 ($CFCl_2$–CF_2Cl)	76-13-1	R114 (CF_2Cl–CF_2Cl)	76-14-2
R115 (CF_2Cl–CF_3)	76-15-3	R123 ($CHCl_2$–CF_3)	306-83-2
R124 ($CHFCl$–CF_3)	2837-89-0	R125 (CF_3–CHF_2)	354-33-6
R134 (CHF_2–CHF_2)	359-35-3	R134a (CF_3–CH_2F)	811-97-2
R141b ($CFCl_2$–CH_3)	1717-00-6	R142b (CF_2Cl–CH_3)	75-68-3
R143a (CF_3–CH_3)	420-46-2	R152a (CHF_2–CH_3)	75-37-6
R161 (CH_2F–CH_3)	353-36-6	CH_3Cl	74-87-3
CH_3Br	74-83-9	CH_3I	74-88-4
CH_2Cl_2	75-09-2	CH_2Br_2	74-95-3
CH_2I_2	75-11-6	CH_2ClBr	74-97-5
$CHCl_3$	67-66-3	$CHBr_3$	75-25-2
$CHFCl_2$	75-43-4	CF_2Br_2	75-61-6
CF_2ClBr	353-59-3	CCl_3Br	75-62-7
$CHCl_2$–CH_3	75-34-3	$CHCl_2$–CH_2Cl	79-00-5
CCl_3–CH_3	71-55-6	CCl_3–CH_2Cl	630-20-6
CH_2Br–CH_3	74-96-4	CH_2Br–CH_2Br	106-93-4
$CHBr_2$–CH_3	557-91-5	CCl_3–CH_2F	27154-33-2
$CHClBr$–CF_3	151-67-7	CCl_3–CF_2Cl	76-11-9
CF_2Br–CF_2Br	124-73-2	CHF=CH_2	75-02-5
CF_2=CH_2	75-38-7	$CHCl$=CH_2	75-01-4
CCl_2=$CHCl$	79-01-6	$CHCl$=CF_2	359-10-4
$CFCl$=CF_2	79-38-9	$CFBr$=CF_2	598-73-2
Propylene (CH_2=CH–CH_3)	115-07-1	Propyne (CH≡C–CH_3)	74-99-7

Appendix I Optimization Method

The tuning of parameters of molecular models for accurate description of thermophysical properties can be a tedious task, for which methods are needed, that allow a systematic model optimization. Beyond grid search algorithms, further methods have been suggested for that purpose.

Njo et al. [304] applied the weak-coupling method for model parameter optimization. This method allows automatic optimization of model parameters during a molecular simulation run by coupling the time derivatives of these model parameters to the deviation of a thermophysical property from its specified value. Though good for fine tuning, problems occur when the considered thermophysical properties, for example the pressure, the density, the internal energy, or the chemical potential, are significantly influenced by more than one model parameter, which is generally the case. Moreover, the weak coupling method was not extended to optimization at more that one state point, and it was not yet applied to phase equilibrium states.

A robust and widely used algorithm is stochastic simplex optimization, cf. for example the work of Faller et al. [96]. Stochastic simplex optimization shows slow but stable convergence and is convenient to automatize, but, due to the stochastic advancement, it does not take advantage of the knowledge about the model. Thus, this method would not allow to make use of knowledge gained from 2CLJD/2CLJQ-modeling.

Further optimization methods rely on genetic algorithms and neuronal networks [155, 425], which are claimed to be particularly efficient for high-dimensional optimization problems.

In the present work, a method based on sensitivities, that quantify the influence of model parameters on the thermophysical properties, is used for the optimization of the parameters of the models of ethylene oxide and methanol. The present method has many similarities with that suggested by Ungerer at el. [397], that later was modified by Bourasseau et al. [27].

The optimization method relies on a least-squares minimization of a weighted fitness function $\mathcal{F}$, that quantifies the deviation of thermophysical properties calculated from a given molecular model compared to experimental data. The weighted fitness function writes as

$$\mathcal{F} = \frac{1}{d} \sum_{i=1}^{d} \frac{1}{\left(\delta A_{i,\mathrm{sim}}\right)^2} \left(A_{i,\mathrm{sim}}\left(\boldsymbol{M}_0\right) - A_{i,\mathrm{exp}}\right)^2 , \tag{276}$$

wherein the n-dimensional vector $\boldsymbol{M}_0 = (m_{01}, ..., m_{0n})$ is a short-cut notation for the set of n model parameters $m_{01}, ..., m_{0n}$ to be optimized. Equation (276) allows simultaneous adjustment of the model parameters to different thermophysical properties A (in the present work: saturated liquid densities ρ' and vapor pressures p_σ at various temperatures). The deviations of results from simulation $A_{i,\mathrm{sim}}$ to experimental data $A_{i,\mathrm{exp}}$ are weighted with the expected simulation uncertainties $\delta A_{i,\mathrm{sim}}$.

Correlations of experimental data of the saturated liquid density and the vapor pressure were used to obtain values for $\rho'_{i,\mathrm{exp}}$ and $p_{\sigma,i,\mathrm{exp}}$. The influence of the fluctuations of simulation data on the optimization process was damped by using in Equation (276) temperature dependent, smoothing correlations for ρ' and p_σ according to Equations (123) and (126), which were adjusted to the saturated liquid densities and vapor pressures from simulation.

The optimized model parameter set $\boldsymbol{M}_{\mathrm{opt1}} = (m_{\mathrm{opt1}\,1}, ..., m_{\mathrm{opt1}\,n})$ is found from minimizing the fitness function (276). For that purpose, the unknown functional dependence of the property A on the model parameters is replaced by a first order Taylor series developed in the vicinity of the initial model parameter set $\boldsymbol{M}_0$

$$A_{i,\mathrm{sim}}(\boldsymbol{M}_{\mathrm{opt}}) = A_{i,\mathrm{sim}}(\boldsymbol{M}_0) + \sum_{j=1}^{n} \frac{\partial A_{i,\mathrm{sim}}}{\partial m_j} \cdot (m_{\mathrm{opt1}\,j} - m_{0j}) \,. \tag{277}$$

The partial derivatives of A_i with respect to each model parameter m_j are the sensitivities, that indicate the influence of the model parameters on the thermophysical properties. The sensitivities are approximated by difference quotients

$$\frac{\Delta A_{i,\mathrm{sim}}}{\Delta m_j} = \frac{A_{i,\mathrm{sim}}(m_{01},..., m_{0j} + \Delta m_j,..., m_{0n}) - A_{i,\mathrm{sim}}(m_{01},..., m_{0j},..., m_{0n})}{\Delta m_j} . \tag{278}$$

With this approximation the minimization problem becomes

$$\mathcal{F}_{\mathrm{app}} = \frac{1}{d} \sum_{i=1}^{d} \frac{1}{(\delta A_{i,\mathrm{sim}})^2} \left(A_{i,\mathrm{sim}}(\boldsymbol{M}_0) + \sum_{j=1}^{n} \frac{\Delta A_{i,\mathrm{sim}}}{\Delta m_j} \cdot (m_{\mathrm{opt1}\,j} - m_{0j}) - A_{i,\mathrm{exp}} \right)^2 \overset{!}{\approx} \min. \tag{279}$$

The sensitivities are evaluated by the means of molecular simulations with n modified model parameter sets. The condition of Equation (279) is fulfilled when

$$\frac{\partial \mathcal{F}_{\mathrm{app}}}{\partial m_{\mathrm{opt1}\,j}} \overset{!}{=} 0. \tag{280}$$

Equation (280) is a system of n linear equations that yields the optimized model parameter set $\boldsymbol{M}_{\mathrm{opt}}$.

Generally, further improvement of the model parameter set $\boldsymbol{M}_{\mathrm{opt1}}$ is possible by reiterating the optimization on the basis of the model parameter set obtained from each iteration step. As the evaluation of the sensitivities by the means of molecular simulations is the time consuming step in each iteration, it would be convenient to evaluate them with the use of simulation results from previous iterations. To allow this, further iterations should, whenever possible, not be done with normal sensitivities, i.e. sensitivities due to the variation of only one model parameter, but with transformed sensitivities, i.e. sensitivities due to the simultaneous variation of all model parameters. For the case of two model parameters m_1 and m_2 ($n = 2$), this approach is explained here and illustrated

in Figure 72. In the two-dimensional parameter space, Figure 72 shows the model parameter set $\boldsymbol{M}_0$ and the two model parameter sets $\boldsymbol{M}_1$ and $\boldsymbol{M}_2$ needed for the evaluation of the normal sensitivities along the vectors $\boldsymbol{s}_1$ and $\boldsymbol{s}_2$. The model $\boldsymbol{M}_{\text{opt1}}$ resulted from the optimization of model $\boldsymbol{M}_0$ on the basis of these normal sensitivities. If the optimization of model $\boldsymbol{M}_{\text{opt1}}$ was continued on the basis of normal sensitivities, time consuming molecular simulation with the model parameter sets $\boldsymbol{M}_3$ and $\boldsymbol{M}_4$ would be required in order to evaluate the normal sensitivities along the vectors $\boldsymbol{s}_3$ and $\boldsymbol{s}_4$. In contrast, the optimization of model $\boldsymbol{M}_{\text{opt1}}$ on the basis of the transformed sensitivities along the vectors $\boldsymbol{t}_1$ and $\boldsymbol{t}_2$ reuses the results for models $\boldsymbol{M}_1$ and $\boldsymbol{M}_2$ and, thus, avoids a multitude of molecular simulations. In this case, the minimization problem is not solved in the original parameter space, but in the $(\boldsymbol{t}_1, \boldsymbol{t}_2)$ parameter space described by the vectors $\boldsymbol{t}_1$ and $\boldsymbol{t}_2$ with origin in $\boldsymbol{M}_{\text{opt1}}$. The resulting parameter set $\boldsymbol{M}^t_{\text{opt2}} = (a^t_{\text{opt2}\,1}, a^t_{\text{opt2}\,2})$ in the $(\boldsymbol{t}_1, \boldsymbol{t}_2)$ parameter space is easily transformable to the original parameter space. The superscript "t" indicates, that the parameter set is described in the $(\boldsymbol{t}_1, \boldsymbol{t}_2)$ parameter space.

It is clear from Figure 72, that in the $(\boldsymbol{t}_1, \boldsymbol{t}_2)$ parameter space, it is

$$\boldsymbol{M}^t_{\text{opt1}} = \boldsymbol{0}^t, \tag{281}$$

$$\boldsymbol{M}^t_1 = \boldsymbol{t}_1, \tag{282}$$

$$\boldsymbol{M}^t_2 = \boldsymbol{t}_2, \tag{283}$$

and the variations Δm_j of the model parameters become equal to unity. Therefore, with model parameter sets expressed in the $(\boldsymbol{t}_1, \boldsymbol{t}_2)$ parameter space, the approximated Taylor series, cf. Equations (277) and (278), becomes here

$$A_{i,\text{sim}}\left(\boldsymbol{M}^t_{\text{opt2}}\right) = A_{i,\text{sim}}\left(\boldsymbol{0}^t\right) + \sum_{j=1}^{2}\left[A_{i,\text{sim}}(\boldsymbol{t}_j) - A_{i,\text{sim}}(\boldsymbol{0}^t)\right] \cdot a^t_{\text{opt2}\,j}. \tag{284}$$

As the properties A do not depend on the choice of the model parameter space, Equation (284) can conveniently be rewritten in terms of the original model parameter space

$$A_{i,\text{sim}}\left(\boldsymbol{M}_{\text{opt2}}\right) = A_{i,\text{sim}}\left(\boldsymbol{M}_0\right) + \sum_{j=1}^{2}\left[A_{i,\text{sim}}(\boldsymbol{M}_j) - A_{i,\text{sim}}(\boldsymbol{M}_0)\right] \cdot a^t_{\text{opt2}\,j}, \tag{285}$$

wherein the new parameters $a^t_{\text{opt2}\,j}$ are in the $(\boldsymbol{t}_1, \boldsymbol{t}_2)$ parameter space. With Equation (285) the optimization problem becomes

$$\mathcal{F}^t_{\text{app}} = \frac{1}{d}\sum_{i=1}^{d}\frac{1}{\delta A_{i,\text{sim}}}\left(A_{i,\text{sim}}\left(\boldsymbol{M}_0\right) + \sum_{j=1}^{2}\left[A_{i,\text{sim}}(\boldsymbol{M}_j) - A_{i,\text{sim}}(\boldsymbol{M}_0)\right] \cdot a^t_{\text{opt2}\,j}\right)^2 \overset{!}{\approx} \min, \tag{286}$$

which is fulfilled when

$$\frac{\partial \mathcal{F}^t_{\text{app}}}{\partial a^t_{\text{opt2}\,j}} \overset{!}{=} 0. \tag{287}$$

Equation (287) is a system of linear equations that yields the optimized model parameter set $\boldsymbol{M}^t_{\text{opt}2} = (a^t_{\text{opt}21}, a^t_{\text{opt}22})$ in the $(\boldsymbol{t}_1, \boldsymbol{t}_2)$ parameter space. The parameters $a^t_{\text{opt}21}$ and $a^t_{\text{opt}22}$ are transformed to the original parameter space $\boldsymbol{M}_{\text{opt}2} = (m_{\text{opt}21}, m_{\text{opt}22})$ by

$$\begin{aligned} \boldsymbol{M}_{\text{opt}2} &= \boldsymbol{M}_0 + a^t_{\text{opt}21}\boldsymbol{t}_1 + a^t_{\text{opt}22}\boldsymbol{t}_2 \\ &= \boldsymbol{M}_0 + a^t_{\text{opt}21} \cdot (\boldsymbol{M}_1 - \boldsymbol{M}_0) + a^t_{\text{opt}22} \cdot (\boldsymbol{M}_2 - \boldsymbol{M}_0). \end{aligned} \tag{288}$$

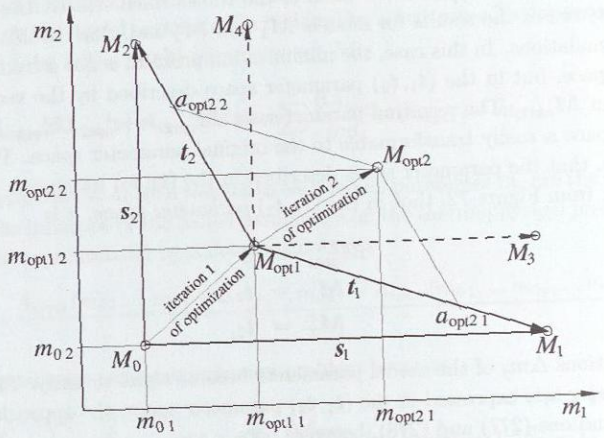

Figure 72: Optimization of two model parameters m_1 and m_2 (i.e. $n = 2$) in the original parameter space and in the $(\boldsymbol{t}_1, \boldsymbol{t}_1)$ parameter space.

The generalization of Equations (283) to (288) to the case of n model parameters is straightforward.

Note, that the optimization in the $(\boldsymbol{t}_1, \boldsymbol{t}_2)$ parameter space is only possible, when the unit vectors $\boldsymbol{t}_j$ form a complete coordinate base in the model parameter space. Otherwise, at least one new sensitivity analysis per pair of collinear vectors must be performed. Figure 72 shows such a situation after the second iteration, that yielded the model parameter set $\boldsymbol{M}_{\text{opt}2}$. The vectors pointing from $\boldsymbol{M}_{\text{opt}2}$ to $\boldsymbol{M}_1$ and to $\boldsymbol{M}_2$ are almost collinear. For continuing the optimization of $\boldsymbol{M}_{\text{opt}2}$ it is therefore advicable to evaluate for this model parameter set at least one new sensitivity in the original parameter space.

Provided that a physically reasonable model structure has been chosen and that sufficiently accurate simulation methods are available, this optimization method is good for improving coarse molecular models and for fine tuning of model parameters and can yield molecular models that describe the desired thermophysical properties with high accuracy. This method shows rapid convergence.

References

[1] Agrawal, P. M., Rice, B. M., Sorescu, D. C., Thompson, D. L., Models for predicting solubilities of 2,4,6-trinitrotoluene (TNT) and 1,3,5-trinitro-1,3,5-s-triazine (RDX) in supercritical CO_2: isothermal-isobaric Monte Carlo simulations, Fluid Phase Equilibria **187–188** (2001) 139–153.

[2] Agrawal, R., Sandler, S. I., Narten, A. H., The structure of liquid bromine .II. Theory and computer simulation, Mol. Phys. **35** (1978) 1087–1111.

[3] Allen, M. P., Tildesley, D. J., Computer Simulation of Liquids, Clarendon Press, Oxford (1987).

[4] Andersen, H. C., Molecular dynamics simulations at constant pressure and/or temperature, J. Chem. Phys. **72** (1980) 2384–2393.

[5] Angus, S., Armstrong, B., de Reuck, K. M., International Thermodynamic Tables of the Fluid State - 7 Propylene, International Union of Pure and Applied Chemistry, Pergamon Press, Oxford (1980).

[6] Barker, J. A., Watts, R. O., Monte Carlo studies of the dielectric properties of water-like models, Mol. Phys. **26** (1973) 789–792.

[7] Barley, M. H., Morrison, J. D., O'Donnel, A., Parker, I. B., Petherbridge, S., Wheelhouse, R.W., Vapour-liquid equilibrium data for binary mixtures of some new refrigerants, Fluid Phase Equilibria **140** (1997) 183–206.

[8] Barojas, J., Levesque, D., Quentrec, B., Simulation of diatomic homonuclear liquids, Phys. Rev. A **7** (1973) 1092–1105.

[9] Bembenek, S. D., Rice, B. M., Transitioning model potentials to real systems, Mol. Phys. **97** (1999) 1085–1094.

[10] Berne, B. J., Harp, G. D., On the calculation of time correlation functions, Adv. Chem. Phys. **17** (1970) 63–227.

[11] Berns, R. M., van der Avoird, A., N_2-N_2 interaction potential from *ab initio* calculations, with application to the structure of $(N_2)_2$, J. Chem. Phys. **72** (1980) 6107–6116.

[12] Berthelot, D., Sur le mélange des gas, Comptes Rendues Hebd. Séanc. Acad. Sci., Paris **126** (1898) 1703–1706.

[13] Bock, S., Bich, E., Vogel, E., A new intermolecular potential energy surface for carbon dioxide from ab initio calculations, Chemical Physics **257** (2000) 147–156.

[14] Boda, D., Chan, K.-Y., Szalai, I., Determination of vapour-liquid equilibrium using the cavity-biased grand canonical Monte Carlo method, Mol. Phys. **92** (1997) 1067–1072.

[15] Boda, D., Kristóf, T., Liszi, J., Szalai, I., A New Simulation Method for the Determination of Phase Equilibria in Mixtures in the Grand Canonical Ensemble, Mol. Phys. **99** (2001) 2011–2022.

[16] Boda, D., Liszi, J., Szalai, I., A new simulation method for the determination of the vapour-liquid equilibria in the grand canonical ensemble, Chem. Phys. Lett. **256** (1996) 474–482.

[17] Bohn, M., Lago, S., Fischer, J., Kohler, F., Excess properties of liquid mixtures from perturbation theory: results for model systems and predictions for real systems, Fluid Phase Equilibria **23** (1985) 137–151.

[18] Bohn, M., Lustig, R., Fischer, J., Description of polyatomic real substances by two-center Lennard-Jones model fluid: Fluid Phase Equilibria **25** (1986) 251–262.

[19] Böhm, H. J., Ahlrichs, R., Molecular dynamics simulation of liquid CH_2Cl_2 and $CHCl_3$ with new pair potentia Mol. Phys. **54** (1985) 1261–1274.

[20] Böhm, H. J., Ahlrichs, R., Scharf, P., Schiffer, H., Intermolecular potentials for CH_4, CH_3F, CHF_3, CH_3Cl, CH_2Cl_2, CH_3CN and CO_2, J. Chem. Phys. **81** (1984) 1389–1395 .

[21] Böhm, H. J. , Meissner, C., Ahlrichs, R., Molecular dynamics simulation of liquid CH_3F, CHF_3, CH_3Cl, CH_3CN, CO_2, and CS_2 with new pair potentials, Mol. Phys. **53** (1984) 651–672.

[22] Böttcher, C. J. F., van Belle, O. C., Bordewijk, P., Rip, A., Theory of electric polarization, Vol. 1: Dielectrics in static fields, Elsevier, Amsterdam (1973).

[23] Borówko, M., Zagórski, R., Malijevský, A., Computer simulation of the chemical potential of binary Lennard-Jones mixtures, J. Chem. Phys. **112** (2000) 2315–2318.

[24] Boulougouris, G. C., Economou, I. G., Theodorou, D. N., Engineering a molecular model for water phase equilibrium over a wide temperature range, J. Phys. Chem. B **102** (1998) 1029–1035.

[25] Boulougouris, G. C., Economou, I. G., Theodorou, D. N., On the calculation of the chemical potential using the particle deletion scheme, Mol. Phys. **96** (1999) 905–913.

[26] Boulougouris, G. C., Errington, J. R., Economou, I. G., Panagiotopoulos, A. Z., Theodorou, D. N., Molecular simulation of phase equilibria for water-*n*-butane and water-*n*-hexane mixtures, J. Phys. Chem. B **104** (2000) 4958–4963.

[27] Bourasseau, E., Haboudou, M., Boutin, A., Fuchs, A. H., Ungerer, P., New optimization method for intermolecular potentials: Optimization of a new anisotropic united atoms potential for olefins: Prediction of equilibrium properties, J. Chem. Phys. **118** (2003) 3020–3034.

[28] Bourasseau, E., Ungerer, P., Boutin, A., Fuchs, A. H., Monte Carlo simulation of branched alkanes and long chain n-alkanes with anisotropic united atoms intermolecular potential, Mol. Sim. **28** (2002) 317–336.

[29] Brown, T. S., Sloan, E. D., Kidnay, A. J., Vapor-Liquid Equilibria in the Nitrogen + Carbon Dioxide + Ethane System, Fluid Phase Equilibria **51** (1989) 299.

[30] Brooks, B. R., Bruccoleri, R. E., Olafson, B. D., States, D. J., Swaminathan, S., Karplus, M., CHARMM: A Program for Macromolecular Energy, Minimization, and Dynamics Calculations, J. Comp. Chem. **4** (1983) 187–217.

[31] Brunner, E., Hültenschmidt, W., Schlichthärle, G., Fluid mixtures at high pressures. IV. Isothermal phase equilibria in binary mixtures consisting of (methanol + hydrogen or nitrogen or methane or carbon monoxide or carbon dioxide), J. Chem. Thermodynamics **19** (1987) 273–291.

[32] Bryk, P., Patrykiejew, A., Pizio, O., Sokołowski, S., A method for determination of chemical potential of associating fluids, Mol. Phys. **90** (1997) 483–487.

[33] Burch, R. J., Low temperature phase equilibria of the gas-liquid system helium-neon-nitrogen, J. Chem. Eng. Data **9** (1964) 19–23.

[34] Burnham, C. J., Xantheas, S. S., Development of transferable interaction models for water. IV. A flexible, all-atom polarizable potential (TTM2-F) based on geometry dependent charges derived from an ab initio monomer dipole moment surface, J. Chem. Phys. **116** (2002) 5115–5124.

[35] Car, R., Parrinello, M., Unified Approach for Molecular Dynamics and Density-Functional Theory, Phys. Rev. Lett. **55** (1985) 2471.

[36] Calado, J. C. G., Chang, E., Streett, W. B., Vapour-liquid equilibrium in the krypton-xenon system, Physica **117A** (1983) 127–138.

[37] Calado, J. C. G., Staveley, L. A. K., Thermodynamics of liquid mixtures of krypton and methane, Trans. Faraday Soc. **67** (1971) 1261–1269.

[38] Canongia Lopes, J. N., Phase equilibria in binary Lennard-Jones mixtures: phase diagram simulation, Mol. Phys. **96** (1999) 1649–1658.

[39] Canongia Lopes, J. N., Tildesley, D. J., Multiphase equilibria using the Gibbs Ensemble Monte Carlo method, Mol. Phys. **92** (1997) 187–185.

[40] Canongia Lopes, J. N., Tildesley, D. J., Three-phase osmotic equilibria using the Gibbs ensemble simulation method, Mol. Phys. **98** (2000) 769–772.

[41] Carrero-Mantilla, J., Llano-Restrepo, M. Vapor-liquid equilibria of the binary mixtures nitrogen+methane, nitrogen+ethane and nitrogen+carbon dioxide, and the ternary mixture nitrogen+methane+ethane from Gibbs-ensemble molecular simulation, Fluid Phase Equilibria **208** (2003) 155–169.

[42] Carrero-Mantilla, J., Llano-Restrepo, M. Further validation of a set of quadrupolar potential models for ethylene and propylene from the prediction of some binary mixture vapor-liquid equilibria by Gibbs-ensemble Molecular Simulation, Mol. Sim. **29** (2003) 549–554.

[43] Chakraborty, A., Molecular Modeling and theory in chemical engineering, Academic Press, San Diego (2001).

[44] Chang, T.-M., Peterson, K. A., Dang, L. X., Molecular dynamics simulations of liquid, interface, and ionic solvation of polarizable carbon tetrachloride, J. Chem. Phys. **103** (1995) 7502–7513.

[45] Chapman, W. G., Jackson, G., Gubbins, K. E., Phase Equilibria of Associating Fluids. Chain molecules with Multiple Bonding Sites, Mol. Phys. **65** (1988) 1057–1079.

[46] Chapman, W. G., Gubbins, K. E., Jackson, G., Radosz, M., New Reference Equation of State for Associating Liquids, Ind. Eng. Chem. Res. **29** (1990) 1709–1721.

[47] Chen, B., Potoff, J. J., Siepmann, J. I., Monte Carlo Calculations for Alcohols and Their Mixtures with Alkanes. Transferable Potentials for Phase Equilibria. 5. United-Atom Description of Primary, Secondary, and Tertiary Alcohols, J. Phys. Chem. B **105** (2001) 3093–3104.

[48] Chen, B., Siepmann, J. I., Transferable potentials for phase equilibria. 3. Explicit-hydrogen description of normal alkanes, J. Phys. Chem. B **103** (1999) 5370–5379.

[49] Chen, J., Mi, J.-G., Chan, K.-Y., Comparison of different mixing rules for prediction of density and residual internal energy of binary and ternary Lennard-Jones mixtures, Fluid Phase Equilibria **178** (2001) 87–95.

[50] Chen, M., Guo, Z.-Y., Liang, X.-G., Molecular simulation of some thermophysical properties and phenomena, Microscale Thermophysical Engineering **5** (2001) 1–16.

[51] Cheung, P. S. Y., Powles, J. G., The properties of liquid nitrogen. IV. A compuer simulation, Mol. Phys. **30** (1975) 921–949.

[52] Cheung, P. S. Y., Powles, J. G., The properties of liquid nitrogen. V. Computer simulation with quadrupole interaction, Mol. Phys. **32** (1976) 1383–1405.

[53] Christiansen, L. J., Fredenslund, A., Gardner, N., Gas-Liquid Equilibria of the CO_2-CO and CO_2-CH_4-CO systems, Adv. Cryog. Eng. **19** (1974) 309–313.

[54] Christiansen, L. J., Fredenslund, A., Mollerup, J., Vapour-liquid equilibria of the CH_4-Ar, CH_4-CO, and Ar-CO systems at elevated pressures, Cryogenics **13** (1973) 405–413.

[55] Cibulka, I., Liquid Density Database; Prague Inst. of Chem. Technol., Prague (1990).

[56] Cieplak, P., Caldwell, J., Kollman, P. A., Aqueous Solution Free Energies of Methanol and N-Methyl Acetamide, Nucleic Acid Base, and Amide Hydrogen Bonding and Chloroform/Water Partition Coefficients of the Nucleic Acid Bases, J. Comp. Chem. **22** (2001) 1048–1057.

[57] Clark, A. M. , Din, F., Robb, J., The liquid-vapour equilibrium of the binary system argon/oxygen, Proc. Roy. Soc. London A **221** (1954) 517–534.

[58] Clausen, I., Arlt, W., A priori calculation of phase equilibria for thermal separation processes using COSMO-RS, Chem. Eng. Technol. **25** (2002) 254–258.

[59] Colina, C. M., Olivera-Fuentes, C. G., Siperstein, F. R., Lísal, M., Gubbins, K. E., Thermal properties of supercritical carbon dioxide by Monte Carlo simulations, Mol. Sim. **29** (2003) 405–412.

[60] Conrad, P. B., de Pablo, J. J., Comparison of histogram reweighting techniques for a flexible water model, Fluid Phase Equilibria **150** (1998) 51–61.

[61] Cornell, W. D., Cieplak, P., Bayly, C. I., Gould, I. R., Merz,K. M.,Jr., Ferguson, D. M., Spellmeyer,D. C., Fox, T., Caldwell, J. W., Kollman, P. A., A Second Generation Force Field for the Simulation of Proteins, Nucleic Acids, and Organic Molecules, J. Am. Chem. Soc. **117** (1995) 5179–5197.

[62] Cornell, W. D., Cieplak, P., Bayly, C. I., Gould, I. R., Merz, K. M.,Jr., Ferguson, D. M., Spellmeyer, D. C., Fox, T., Caldwell, J. W., Kollman, P. A., Additions and Corrections. A Second Generation Force Field for the Simulation of Proteins, Nucleic Acids, and Organic Molecules, J. Am. Chem. Soc. **118** (1996) 2309.

[63] Corti, D. S., Alternative derivation of Widom's test particle insertion method using the small system grand canonical ensemble, Mol. Phys. **93** (1998) 417–420.

[64] CRC Handbook of Chemistry and Physics, Lide, D. R. (ed.), 76th ed., CRC Press, Inc., Florida (1995).

[65] Cui, S. T., Cochran, H. D., Cummings, P. T., Vapor-Liquid Phase Coexistence of Alkane-Carbon Dioxide and Perfluoroalkane-Carbon Dioxide Mixtures, J. Phys. Chem. B **103** (1999) 4485–4491.

[66] Dang, L. X., Intermolecular interactions of liquid dichloromethane and equilibrium properties of liquid-vapor and liquid-liquid interfaces: A molecular dynamics study, J. Chem. Phys. **110** (1999) 10113–10122.

[67] Daubert, T. E., Danner, R. P., Physical and Thermodynamic Properties of Pure Chemicals (DIPPR-Project), Hemisphere Publishing Corporation (1989, 1991, 1992).

[68] Davalos, J., Anderson, W. R., Phelps, R. E., Kidnay, A. J., Liquid-vapor equilibria at 250.00 K for systems containing methane, ethane, and carbon dioxide, J. Chem. Eng. Data **21** (1976) 81–84, in [181].

[69] Deem, M. W., Recent contributions of statistical mechanics in Chemical Engineering, AIChE J. **44** (1998) 2569–2596.

[70] Delhommelle, J., Boutin, A., Fuchs, A. H., Molecular simulation of vapour-liquid coexistence curves for hydrogen sulfide-alkane and carbon dioxide-alkane mixtures, Mol. Sim. **22** (1999) 351–368.

[71] Delhommelle, J., Boutin, A., Tavitian, B., Mackie, A. D., Fuchs, A. H., Vapour-liquid coexistence curves of the united-atom and anisotropic united-atom force fields for alkane mixtures, Mol. Phys. **96** (1999) 1517–1524.

[72] Delhommelle, J., Millié, P., Inadequacy of the Lorentz-Berthelot combining rules for accurate predictions of equilibrium properties by molecular simulation, Mol. Phys. **99** (2001) 619–625.

[73] Delhommelle, J., Millié, P., Fuchs, A., On the role of the definition of potential models in Gibbs ensemble phase equilibria simulations of the H_2S-pentane mixture, Mol. Phys. **98** (2000) 1895–1905.

[74] Delhommelle, J., Tschirwitz, C., Ungerer, P., Granucci, G., Millié, P., Pattou, D., Fuchs, A. H., Derivation of an Optimized Potential Model for Phase Equilibria (OPPE) for Sulfides and Thiols, J. Chem. Phys. **104** (2000) 4745–4753.

[75] Del Rio, F., Ramos, J. E., McLure, I. A., Accurate effective potentials and virial coefficients in real fluids. Part II. Pure homodiatomics and their mixtures, Phys. Chem. Chem. Phys. **1** (1999) 4937–4945.

[76] de Pablo, J. J., Bonnin, M., Prausnitz, J. M., Vapor-liquid equilibria for polyatomic fluids from site-site computer simulations: pure hydrocarbons and binary mixtures containing methane, Fluid Phase Equilibria **73** (1992) 187–210.

[77] de Pablo, J. J., Escobedo, F. A., Molecular simulation in chemical engineering: Present and Future, AIChE J. **48** (2002) 2716–2721.

[78] de Reuck, K. M., Craven, R. J. B., Methanol, International Thermodynamic Tables of the Fluid State - 12, IUPAC, Blackwell Scientific Publications, London (1993).

[79] de Vries, B., Tillner-Roth, R., Baehr, H. D., Thermodynamic Properties of HCFC 124, 19th International Congress of Refrigeration, The Hague, The Netherlands, International Institute of Refrigeration, IVa:582-589, (1995), in [328].

[80] Dietz, W., Heinzinger, K., A Molecular Dynamics Study of Liquid Chloroform, Ber. Bunsenges. Phys. Chem. **89** (1985) 968–977.

[81] Dodge, B. F., Chem. and Met. Eng. **10** (1927) 622, in [181].

[82] Dubey, G. S., O'Shea, S. F., Phase equilibria of Lennard-Jones dipolar plus quadrupolar fluids by Gibbs-ensemble Monte Carlo simulation, Physical Review E **49** (1994) 2175–2183.

[83] Dubey, G. S., O'Shea, S. F., Monson, P. A., Vapour-liquid equilibria for two centre Lennard-Jones diatomics and dipolar diatomics, Mol. Phys. **80** (1993) 997–1007.

[84] Eckert, F., Klamt, A., Fast solvent screening via quantum chemistry: COSMO-RS approach, AIChE J. **48** (2002) 369–385.

[85] Eckert, F., Klamt, A., Prediction of halocarbon thermodynamics with COSMO-RS, Fluid Phase Equilibria **210** (2003) 117–141.

[86] Ely, J. F., A Predictive, Exact Shape Factor Extended Corresponding States Model for Mixtures, Advances in Cryogenic Engineering **35** (1990) 1511–1520.

[87] Ely, J. R., Magee, J. W., Haynes, W. M., Research Report-110; Gas Processors Association (1987).

[88] Ely, J. F., Magee, J. W., Haynes, W. M., NBS standard reference database 14, DDMIX, Version 9.06, NIST, Boulder, Colorado (1989).

[89] Errington, J. R., Boulougouris, G. C., Economou, I. G., Panagiotopoulos, A. Z., Theodorou, D. N., Molecular Simulation of Phase Equilibria for Water-methane and Water-ethane Mixtures, J. Phys. Chem. B **102** (1998) 8865–8873.

[90] Errington, J. R., Panagiotopoulos, A. Z., A Fixed Point Charge Model for Water Optimized to the Vapor- Liquid Coexistence Properties, J. Phys. Chem. B **102** (1998) 7470–7475.

[91] Errington, J. R., Panagiotopoulos, A. Z., A new intermolecular potential model for the n-alkane homologous series, J. Phys. Chem. B **103** (1999) 6314–6322.

[92] Errington, J. R., Panagiotopoulos, A. Z., Phase equilibria of the modified Buckingham exponential-6 potential from Hamiltonian scaling grand canonical Monte Carlo, J. Chem. Phys. **109** (1998) 1093–1100.

[93] Errington, J. R., Panagiotopoulos, A. Z., New intermolecular potential models for benzene and cyclohexane, J. Chem. Phys. **111** (1999) 9731–9738.

[94] Eubank, P. T., Estimation of Effective Molecular Quadrupole Moments, AIChE. J. **18** (1972) 454–456.

[95] Evans, M. W., Ferrario, M., Computer simulation of the molecular dynamics of liquid dichloro methane, Advances in Molecular Relaxation and Interaction Processes **24** (1982) 75–105.

[96] Faller, R., Schmitz, H., Biermann, O., Müller-Plathe, F., Automatic Parameterization of Force Fields for Liquids by Simplex Optimization, J. Comp. Chem. **20** (1999) 1009–1017.

[97] Fastowskij, W. G., Petrowskij, Ju. W., Zh. Fiz. Khim. **30** (1956) 589, in [181].

[98] Fender, B. E. F., Halsey, G. D,Jr., Second Virial Coefficients of Argon, Krypton, and Argon-Krypton Mixtures at Low Temperatures, J. Chem. Phys. **36** (1962) 1881–1888.

[99] Fermeglia, M., Ferrone, M., Pricl, S., Development of an all-atoms force field from ab initio calculations for alternative refrigerants, Fluid Phase Equilibria **210** (2003) 105–116.

[100] Fermeglia, M., Pricl, S., Molecular dynamics simulations of real systems: application to chloro-fluoro-hydrocarbons and polymers, Fluid Phase Equilibria **158–160** (1999) 49–58.

[101] Fermeglia, M., Pricl, S., A novel approach to thermophysical properties prediction for chloro-fluoro-hydrocarbons, Fluid Phase Equilibria **166** (1999) 21–37.

[102] Fermeglia, M., Pricl, S., Longo, G., Molecular modeling and process simulation: real possibilities and challenges, Chem. Biochem. Eng. **17** (2003) 19–29.

[103] Fernández, G. A., Vrabec, J., Hasse, H., Self diffusion and binary Maxwell-Stefan diffusion in simple Fluids with the Green-Kubo Method, Int. J. Thermophys. **25** (2004) 175–186.

[104] Fernández, G. A. , Vrabec, J. , Hasse, H., Self-Diffusion and Binary Maxwell-Stefan Diffusion coefficients of Quadrupolar Real Fluids from Molecular Simulation, International Journal of Thermophysics, submitted (2004).

[105] Fernández, G. A., Vrabec, J., Hasse, H., A molecular simulation study of shear and bulk viscosity and thermal conductivity of simple real fluids, Fluid Phase Equilibria **221** (2004) 157–163.

[106] Filippini, G., Gramaccioli, C. M., Simonetta, M., Application of semiempirical atom-atom potentials to crystals of acetylene, J. Chem. Phys. **73** (1980) 1376–1380.

[107] Fincham, D., Quirke, N., Tildesley, D. J., Computer Simulation of Molecular Liquid Mixtures. I. A Diatomic Lennard-Jones Model Mixture for CO_2/C_2H_6, J. Chem. Phys. **84** (1986) 4535–4546.

[108] Fischer, J., Lustig, R., Breitenfelder-Manske, H., Lemming, W., Influence of intermolecular potential parameters on orthobaric properties of fluids consisting of spherical and linear molecules, Mol. Phys. **52** (1984) 485–497.

[109] Fischer, J., Möller, D., Chialvo, A., Haile, J. M., The influence of unlike molecule interaction parameters on liquid mixture excess properties, Fluid Phase Equilibria **48** (1989) 161–176.

[110] Fluid properties from ASMW (Amt für Standardisierung, Messwesen und Warenprüfung der DDR), Berlin (1985).

[111] Frantz, D. D., Freeman, D. L., Doll, J. D., Extending J walking to quantum systems: Applications to atomic clusters, J. Chem. Phys. **97** (1992) 5713–5731.

[112] Fredenslund, A., Mollerup, J., Measurement and prediction of equilibrium ratios for the C_2H_6+CO_2 system, J. Chem. Soc., Faraday Trans. I **70** (1974) 1653–1660, in [181].

[113] Fredenslund, A., Sather, G. A., Gas-Liquid Equilibrium of the Oxygen-Carbon Dioxide System, J. Chem. Eng. Data **15** (1970) 17–22.

[114] Frenkel, D., Smit, B., Understanding Molecular Simulation, Academic Press, Elsevier, San Diego (2002).

[115] Friend, D. G., Ingham, H., Ely, J. F., Thermophysical Properties of Ethane, J. Phys. Chem. Ref. Data **20** (1991) 275–347.

[116] Galassi, G., Tildesley, D. J., Phase diagrams of diatomic molecules using the Gibbs Ensemble Monte Carlo Method, Mol. Sim. **13** (1994) 11–24.

[117] Galindo, A., Gil-Villegas, A., Whitehead, P.J., Jackson, G., Burgess, A.N., Prediction of Phase Equilibria for Refrigerant Mixtures of Difluoromethane (HFC-32), 1,1,1,2-Tetrafluoroethane(HFC-134a), and Pentafluoroethane(HFC-125a) Using SAFT-VR, J. Phys. Chem. B **102** (1998) 7632–7639.

[118] Gamba, Z., Bonadeo, H., Lattice dynamics and phase transition of acetylene, J. Chem. Phys. **76** (1982) 6215–6220.

[119] Gao, G., Wang, W., Gibbs Ensemble Monte Carlo simulation of binary vapor-liquid equilibria for CFC alternatives, Fluid Phase Equilibria **130** (1997) 157–166.

[120] Gao, G., Wang, W., Zeng, X. C., Vapor-liquid equilibria for pure HCFC/HFC substances by Gibbs ensemble simulation of Stockmayer potential molecules, Fluid Phase Equilibria **137** (1997) 87–98.

[121] Gao, G. T., Woller, J. B., Zeng, X. C., Weng, W., Vapour-liquid equilibria of binary mixtures containing Stockmayer molecules, J. Phys.: Condens. Matter **9** (1997) 3349–3360.

[122] Garzón, B., Lago, S., Vega, C., Reaction Field Simulations of the Vapor-Liquid-Equilibria of Dipolar Fluids - Does the Reaction Field Dielectric-Constant Affect the Coexistence Properties?, Chem. Phys. Lett. **231** (1994) 366–372.

[123] Garzón, B., Lago, S., Vega, C., de Miguel, E., Rull, L. F., Computer simulation of vapor-liquid equilibria of linear quadrupolar fluids. Departures from the principle of corresponding states, J. Chem. Phys. **101** (1994) 4166–4176.

[124] Garzón, B., Lago, S., Vega, C., Rull, L. F., Computer simulation of vapor-liquid equilibria of linear dipolar fluids Departures from the principle of corresponding states, J. Chem. Phys. **102** (1995) 7204–7215.

[125] Gear, C. W., Numerical initial value problems in ordinary differential equations, Prentice-Hall, Englewood Cli (1971).

[126] Gelb, L. D., Müller, E. A., Location of phase equilibria by temperature-quench molecular dynamics simulations, Fluid Phase Equilibria **203** (2002) 1–14.

[127] Gibbons, T. G., Klein, M. L., Thermodynamic properties for a simple model of solid carbon dioxide: Monte Carlo, cell model, and quasiharmonic calculations, J. Chem. Phys. **60** (1974) 112–126.

[128] Gil-Villegas, A., del Rio, F., Benavides, A. L., Deviations from corresponding-states behaviour in the vapor- liquid equilibrium of the square-well fluid, Fluid Phase Equilibria **119** (1996) 97–112.

[129] Glättli, A., Daura, X., van Gunsteren, W.F., Derivation of an improved simple point charge model for liquid water: SPC/A and SPC/L, J. Chem. Phys. **116** (2002) 9811–9828.

[130] Gotlib, I. Yu., Piotrovskaya, E. M., de Leeuw, S. W., Properties of coexisting fluid phases of a binary system methanol-ethane by computer simulation, Fluid Phase Equilibria **129** (1997) 1–13.

[131] Grausø, L., Fredenslund, A., Mollerup, J., Vapor-Liquid Equilibrium Data for the Systems C_2H_6+N_2, C_2H_4+N_2, C_3H_8+N_2, and C_3H_6+N_2, Fluid Phase Equilibria **1** (1977) 13–26, in [181].

[132] Gray, C. G., Gubbins, K. E., Theory of molecular fluids, Volume 1: Fundamentals, Clarendon Press, Oxford (1984).

[133] Gross, J., Sadowski, G., Application of Perturbation Theory to a Hard-Chain Reference Fluid: an Equation of State for Square-Well Chains, Fluid Phase Equilibria **168** (2000) 183–199.

[134] Gubbins, K.E., Applications of Molecular Simulation, Fluid Phase Equilibria **83** (1993) 1–14.

[135] Gubbins, K. E., Quirke, N., Molecular simulation and industrial applications, Gordon and Breach Science Publishers, Amsterdam (1996).

[136] Guevara, Y., Benavides, A. L., Del Rio, F., Thermodynamics of a square-well octopolar fluid, Mol. Phys. **89** (1996) 1277–1290.

[137] Guggenheim, E. A., The Principle of Corresponding States, J. Chem. Phys. **13** (1945) 253–261.

[138] Gupta, S., Olson, J. D., Industrial needs in physical properties, Ind. Eng. Chem. Res. **42** (2003) 6359–6374.

[139] Haile, J. M., Molecular Dynamics Simulation: Elementary Methods, John Wiley & Sons, New York (1992).

[140] Hall, C. D., Johnson, K. A., Burgess, A. N., Winterton, N., The structure of fluid dichlorodifluoromethane. A comparison between molecular dynamics simulations and neutron diffraction results, Mol. Phys. **76** (1992) 1061–1070.

[141] Hansen, J. P., McDonald, I. R., Theory of simple liquids, Academic Press, London (1986).

[142] Harismiadis, V. I., Koutras, N. K., Tassios, D. P., Panagiotopoulos, A. Z., How good is conformal solutions theory for phase equilibrium predictions? Gibbs ensemble simulations of binary Lennard-Jones mixtures, Fluid Phase Equilibria **65** (1991) 1–18.

[143] Harris, J. G., Yung, K. H., Carbon Dioxide's Liquid-Vapor Coexistence Curve and Critical Properties As Predicted by a Simple Molecular Model, J. Phys. Chem. **99** (1995) 12021–12024.

[144] Haselden, G. G., Holland, F. A., King, M. B., Strickland-Constable, R. F., Two phase equilibrium in binary and ternary systems. X. Phase equilibria and compressibility of the systems carbon dioxide/propylene, carbon dioxide/ethylene and ethylene/propylene, and an account of the thermodynamic functions of the systems carbon dioxide/propylene, Proc. Roy. Soc. A **240** (1957) 1–28.

[145] Haynes, W. M., Thermophysical properties of HCFC alternatives, National Institute of Standards and Technology, Boulder, Colorado, Final Report for ARTI MCLR Project Number 660-50800 (1996), in [328].

[146] Hendrix, D. A., Jarzynski, C., A "fast growth" method of computing free energy differences, J. Chem. Phys. **114** (2001) 5974–5981.

[147] Heyes, D. M., Chemical potential, partial enthalpy and partial volume of mixtures by NPT molecular dynamics, Mol. Sim. **8** (1992) 227–238.

[148] Heyes, D. M., The Liquid State - Applications of Molecular Simulations, John Wiley & Sons, Chichester (1998).

[149] S. Higashi and A. Takada, Molecular dynamics study of liquid CH_2F_2 (HFC-32), Mol. Phys. **92** (1997) 641–650.

[150] Hirschfelder, J. O., Curtiss, C. F., Bird, R. B., Molecular Theory of Gases and Liquids, J. Wiley & Sons, Inc., New York (1954).

[151] Hloucha, M., Deiters, U. K., Monte Carlo study of the thermodynamic properties and the static dielectric constant of liquid trifluoromethane, Fluid Phase Equilibria **149** (1998) 41–56.

[152] Hogan, R. J., Nelson, W. T., Hanson, G. H., Cines, M. R., Ethane-Ethylene-Acetylene System, Ind. Eng. Chem. **47** (1955) 2210–2215, in [181].

[153] Hoinkis, J., Ahlrichs, R., Böhm, H.-J., A Simple Treatment of Intermolecular Interactions: Synthesis of Ab initio Calculations and Combination Rules, Int. J. Quantum Chem. **XXIII** (1983) 821–834.

[154] Huber, M. L., Ely, J. F., A predictive extended corresponding states model for pure and mixed refrigerants including an equation of state for R134a, Int. J. Refrigeration **17** (1994) 18–31, in [328].

[155] Hunger, J., Huttner, G., Optimization and Analysis of Force Field Parameters by Combination of Genetic Algorithms and Neural Networks, J. Comp. Chem. 20 (1999) 455–471.

[156] Jacobsen, R. T., Penoncello, S. G., Lemmon, E. W., A fundamental equation for trichlorofluoromethane (R-11), Fluid Phase Equilibria **80** (1992) 45–56, in [328].

[157] Jacobsen, R. T., Stewart, R. B., Jahangiri, M., Thermodynamic Properties of Nitrogen from the Freezing Line to 2000 K at Pressures to 1000 MPa, J. Phys. Chem. Ref. Data **15** (1986) 735–909.

[158] Jahangiri, M., Jacobsen, R. T., Stewart, R. B., McCarty, R. D., Thermodynamic Properties of Ethylene from the Freezing Line to 450 K at Pressures to 260 MPa, J. Phys. Chem. Ref. Data **15** (1986) 593–734.

[159] Jedlovszky, P., Mezei, M., Computer simulation study of liquid CH_2F_2 with a new effective pair potential model, J. Chem. Phys. **110** (1999) 2991–3002.

[160] Jedlovszky, P., Pálinkás, G., Monte Carlo simulation of liquid acetone with a polarizable molecular model, Mol. Phys., **84** (1995) 217–233.

[161] Jelinek, G. E., Slutsky, L. J., Karo, A. M., Model for the lattice vibrations of a crystal of diatomic molecules - I. Frequency distributions, Debye-Waller factors, and infrared spectra, J. Phys. Chem. Solids **33** (1972) 1279–1290.

[162] Jorgensen, W. L., Transferable Intermolecular Potential Functions for Water, Alcohols, and Ethers. Application to Liquid Water, J. Am. Chem. Soc. **103** (1981) 335–340.

[163] Jorgensen, W. L., Optimized Intermolecular Potential Functions for Liquid Alcohols, J. Phys. Chem. **90** (1986) 1276–1284.

[164] Jorgensen, W. L., Madura, J. D., Swenson, C. J., Optimized Intermolecular Potential Functions for Liquid Hydrocarbons, J. Am. Chem. Soc. **106** (1984) 6638–6646.

[165] Jorgensen, W. L., Maxwell, D. S., Tirado-Rives, J., Development and Testing of the OPLS All-Atom Force Field on Conformational Energetics and Properties of Organic Liquids, J. Am. Chem. Soc. **118** (1996) 11225–11236.

[166] Jorgensen, W. L., Tirado-Rives, J., The OPLS Potential Functions for Proteins. Energy Minimizations for Crystals of Cyclic Peptides and Crambin, J. Am. Chem. Soc. **110** (1988) 1657–1666.

[167] Kamei, A., Beyerlein, S. W., Jacobsen, R. T., Application of nonlinear regression in the development of a wide range formulation for HCFC-22, Int. J. Thermophys. **16** (1995) 1155–1164, in [328].

[168] Kaminishi, G.-I., Arai, Y., Saito, S., Maeda, S., Vapor-liquid equilibria for binary a ternary systems containing carbon dioxide, J. Chem. Eng. Japan **1** (1968) 109–116.

[169] Karakorin, F. F., Foreign Petr. Techn. **9** (1941) 397, in [181].

[170] Kidnay, A. T., Miller, R. C., Parrish, W. R., Hiza, M. J., Liquid-vapour phase equilibria in the N_2–CH_4 system from 130 to 180 K, Cryogenics **15** (1975) 531–540, in [181].

[171] Kido, A., Nakanishi, K., Molecular dynamics study of nucleation in supersaturated vapor of carbon dioxide, Fluid Phase Equilibria **158–160** (1999) 79–86.

[172] Kikuchi, H., Kuwajima, S., Fukuda, M., Novel method to estimate solubility of small molecules in cis- polyisoprene by molecular dynamics simulations, J. Chem. Phys. **115** (2001) 6258–6265.

[173] Kimura, E., Fukushima, S., Vapor-Liquid Equilibria in the Cl_2-CO_2 System, J. Japan Inst. of Metals **43** (1979) 223–229.

[174] Kiyohara, K., Gubbins, K. E., Panagiotopoulos, A. Z., Phase coexistence properties of polarizable Stockmayer fluids, J. Chem. Phys. **106** (1997) 3338–3347.

[175] Kiyohara, K., Gubbins, K. E., Panagiotopoulos, A. Z., Phase coexistence properties of polarizable water models, Mol. Phys. **94** (1998) 803–808.

[176] Kiyohara, K., Spyriouni, T., Gubbins, K. E., Panagiotopoulos, A. Z., Thermodynamic Scaling Gibbs Ensemble Monte Carlo: A new method for determination of phase coexistence properties of fluids, Mol. Phys. **89** (1996) 965–974.

[177] Klamt, A., Conductor-like screening model for real solvents: a new approach to the quantitative calculation of solvation phenomena, J. Phys. Chem. **99** (1995) 2224–2235.

[178] Klamt, A., Eckert, F., COSMO-RS: a novel and efficient method for the a priori prediction of thermophysical data of liquids, Fluid Phase Equilibria **172** (2000) 43–72.

[179] Klamt, A., Jonas, V., Bürger, T., Lohrenz, C. W., Refinement and parametrization of COSMO-RS, J. Phys. Chem A **102** (1998) 5074–5085.

[180] Kleemiß, M., Thermodynamische Eigenschaften zweier ternärer Kältemittelgemische, Fortschr.-Ber. VDI Reihe 19 N 98, VDI-Verlag, Düsseldorf (1997).

[181] Knapp, H., Döring, R., Oellrich, L., Plöcker, U., Prausnitz, J. M., Vapor-Liquid Equilibria of Mixtures of Low-Boilin Substances, DECHEMA Chemistry Data Series, Vol. VI, Frankfurt/Main (1982).

[182] Kofke, D. A., Cummings, P. T., Quantitative comparison and optimization of methods for evaluating the chemica potential by molecular simulation, Mol. Phys. **92** (1997) 973–996.

[183] Kofke, D. A., Gibbs-Duhem integration: a new method for direct evaluation of phase coexistence by molecular simulation, Mol. Phys. **78** (1993) 1331–1336.

[184] Kofke, D. A., Direct Evaluation of Phase Coexistence by Molecular Simulation via Integration Along the Saturation Line, J. Chem. Phys. **98** (1993) 4149–4162.

[185] Kohler, F., van Nhu, N., The second virial coefficients of some halogenated ethanes, Mol. Phys. **80** (1993) 795–800.

[186] Kölmel, C., Ahlrichs, R., Karch, B., MD simulations of liquid CCl4 with a new pair potential, Mol. Phys. **66** (1989) 1015–1025.

[187] Kong, J., Combining rules for intermolecular potential parameters. II. Rules for the Lennard-Jones (12-6) potential and the Morse potential, J. Chem. Phys. **59** (1973) 2464–2467.

[188] Kozlov, A. D., Moscow (1996), in: REFPROP, NIST Standard Reference Database 23, Version 6.01 (1998).

[189] Kriebel, C., Mecke, M., Winkelmann, J., Vrabec, J., Fischer, J., An equation of state for dipolar two-center Lennard-Jones molecules and its application to refrigerants, Fluid Phase Equilibria **142** (1998) 15–32.

[190] Kriebel, C., Müller, A., Mecke, M., Winkelmann, J., Fischer, J., Prediction of Thermodynamic Properties for Fluid Nitrogen with Molecular Dynamics Simulations, Int. J. Thermophys. **17** (1996) 1349–1363.

[191] Kriebel, C., Müller, A., Winkelmann, J., Fischer, J., Vapour-liquid equilibria of two-centre Lennard-Jones fluids from the NpT plus test particle method, Mol. Phys. **84** (1995) 381–394.

[192] Kriebel, C., Müller, A., Winkelmann, J., Fischer, J., A Hybrid Equation of State for Stockmayer Pure Fluids and Mixtures, Fluid Phase Equilibria **119** (1996) 67–80.

[193] Kriebel, C., Winkelmann, J., Vapour-liquid equilibria for Stockmayer fluids with rigid and polarizable dipoles, Mol. Phys. **90** (1997) 297–301.

[194] Kristóf, T., Liszi, J., Szalai, I., Vapour-liquid equilibria for a model of liquid carbon disulphide, Mol. Phys. **89** (1996) 931–942.

[195] Kristóf, T., Vorholz, J., Liszi, J., Rumpf, B., Maurer, G., A simple effective pair potential for the molecular simulation of the thermodynamic properties of ammonia, Mol. Phys. **97** (1999) 1129–1137.

[196] Kristóf, T., Vorholz, J., Maurer, G., Molecular simulation of the high-pressure phase equilibrium of the system carbon dioxide-methanol-water, J. Phys. Chem. B **106** (2002) 7547–7553.

[197] Kronome, G., Liszi, J., Szalai, I., Monte Carlo simulation of some thermophysical properties of two- centre Lennard-Jones fluids along the vapour-liquid equilibrium curve, Mol. Phys. **93** (1998) 279–286.

[198] Kronome, G., Szalai, I., Wendland, M., Fischer, J., Extension of the NpT + Test Particle Method for the Calculation of Phase Equilibria of Nitrogen + Ethane, J. Mol. Liq. **85** (2000) 237–247.

[199] Kuznetsowa, T., Kvamme, B., Thermodynamic properties and interfacial tension of a model water-carbon dioxide system, Phys. Chem. Chem. Phys. **4** (2002) 937–941.

[200] Laasonen, K., Wonczak, S., Strey, R., Laaksonen, A., Molecular dynamics simulation of gas-liquid nucleation of Lennard-Jones fluid, J. Chem. Phys. **133** (2000) 9741–9747.

[201] Lago, S., Garzón, B., Calero, S., Vega, C., Accurate Simulations of the Vapor-Liquid Equilibrium of Important Organic Solvents and Other Diatomics, J. Phys. Chem. B **101** (1997) 6763–6771.

[202] Lamm, M. H., Hall, C. K., Monte Carlo simulations of complete phase diagrams for binary Lennard-Jones mixtures, Fluid Phase Equilibria **182** (2001) 37–46.

[203] Lamm, M. H., Hall, C. K., Equilibria between solid, liquid, and vapor phases in binary Lennard-Jones mixtures, Fluid Phase Equilibria **194–197** (2002) 197–206.

[204] Landolt-Börnstein, Zahlenwerte und Funktionen aus Physik, Chemie, Astronomie, Geophysik und Technik, Bd. I/2, 6. Aufl., Springer, Berlin (1961).

[205] Lee, K. H., Reardon, K. F., Proteomics: An exciting new science, but where are the chemical engineers?, AIChE J. **49** (2003) 2682–2686.

[206] Leonhard, K., Deiters, U. K., Monte Carlo simulations of neon and argon using *ab initio* potentials, Mol. Phys. **98** (2000) 1603–1616.

[207] Lemmon, E. W., Jacobsen, R. T., preliminary formulation (2002), in [328].

[208] Lemmon, E. W., Jacobsen, R. T., An International Standard Formulation for the Thermodynamic Properties of 1,1,1-Trifluoroethane (HFC-143a) for Temperatures From 161 to 450 K and Pressures to 50 MPa, J. Phys. Chem. Ref. Data **29** (2000) 521–552, in [328].

[209] Lemmon, E. W., Span, R., preliminary equation (2001), in [328].

[210] Lemmon, E. W., Span, R., preliminary equation (2001), in [328].

[211] Lemmon, E. W., Span, R., preliminary equation (2001), in [328].

[212] Lewis, K. L., Staveley, L. A. K., Excess enthalpies of the liquid mixtures nitrogen + oxygen, nitrogen + argon, argon + ethane, and methane + carbon tetrafluoride, J. Chem. Thermodynamics **7** (1975) 855–864, in [181].

[213] Li, B., Clapp, P. C., Rifkin, J. A., Zhang, X. M., Molecular dynamics calculation of heat dissipation during sliding friction, Int. J. Heat and Mass Trans. **46** (2003) 37–43.

[214] Lim, J. S., Park, J.-Y., Lee, B.-G., Lee, Y.-W., Phase equilibria of 1,1,1-trifluoroethane (HFC-143a)+1,1,1,2- tetrafluoroethane (HFC-134a), and + 1,1-difluoroethane (HFC-152a) at 273.15, 293.15, 303.15, and 313.15 K, Fluid Phase Equilibria **193** (2002) 29–39.

[215] Lim, S. Y., Tsotsis, T. T., Sahimi, M., Molecular simulation of diffusion and sorption of gases in an amorphous polymer, J. Chem. Phys. **119** (2003) 496–504.

[216] Liu, A., Calculation of chemical potentials of mixtures from computer simulations, Mol. Phys. **89** (1996) 1651–1658.

[217] Liu, A., Excess thermodynamic properties of CO_2 + C_2H_6 mixtures from MD simulations, Mol. Sim. **17** (1996) 75–81.

[218] Liu, A., Beck, T. L., Vapor-Liquid Equilibria of Binary and Ternary Mixtures Containing Methane, Ethane, and Carbon Dioxide from Gibbs Ensemble Simulations, J. Phys. Chem. B **102** (1998) 7627–7631.

[219] Lísal, M., Aim, K., Vapor-liquid equilibrium, fluid state, and zero-pressure solid properties of chlorine from anisotropic interaction potential by molecular dynamics, Fluid Phase Equilibria **161** (1999) 241–256.

[220] Lísal, M., Aim, K., Fischer, J., Vapour-liquid equilibria of dipolar two-centre Lennard-Jones fluids from a physically based equation of state and computer simulations, Mol. Sim. **23** (2000) 363–388.

[221] Lísal, M., Budinský, R., Vacek, V., Vapour-liquid equilibria for dipolar two-centre Lennard-Jones fluids by Gibbs-Duhem integration, Fluid Phase Equilibria **135** (1997) 193–207.

[222] Lísal, M., Budinský, R., Vacek, V., Aim, K., Vapor-liquid equilibria of alternative refrigerants by molecular dynamics simulations, Int. J. Thermophys. **20** (1999) 163–174.

[223] Lísal, M., Kolafa, J., Nezbeda, I., An examination of the five-site potential (TIP5P) for water, J. Chem. Phys. **117** (2002) 8892–8897.

[224] Lísal, M., Nezbeda, I., Pure fluids of homonuclear and heteronuclear square-well diatomics. I. Computer simulation study, Mol. Phys. **96** (1996) 335–347.

[225] Lísal, M., Nezbeda, I., Smith, W. R., The reaction ensemble method for the computer simulation of chemical and phase equilibria. II. The Br_2+Cl_2+$BrCl$ system, J. Chem. Phys. **110** (1999) 8597–8604.

[226] Lísal, M., Smith, W. R., Nezbeda, I., Accurate computer simulation of phase equilibrium for complex fluid mixtures. Application to binaries involving isobutene, methanol, methyl tert-butyl ether, and *n*-butane, J. Phys. Chem. B **103** (1999) 10496–10505.

[227] Lísal, M., Smith, W. R., Nezbeda, I., Molecular Simulation of Multicomponent Reaction and Phase Equilibria in MTBE Ternary Systems, AIChE J. **46** (2000) 866–875.

[228] Lísal, M., Smith, W. R., Nezbeda, I., Accurate vapour-liquid equilibrium calculations for complex systems using the reaction Gibbs ensemble Monte Carlo simulation method, Fluid Phase Equilibria **181** (2001) 127–146.

[229] Lísal, M., Vacek, V., Effective potentials for liquid simulation of the alternative refrigerants HFC-32: CH_2F_2 and HFC-23: CHF_3, Fluid Phase Equilibria **118** (1996) 61–76.

[230] Lísal, M., Vacek, V., Molecular dynamics simulations of fluorinated ethanes, Mol. Phys. **87** (1996) 167–187.

[231] Lísal, M., Vacek, V., Direct evaluation of vapour-liquid equilibria of mixtures by molecular dynamics using Gibbs-Duhem Integration, Mol. Sim. **18** (1996) 75–99.

[232] Lorentz, H. A., Über die Anwendung des Satzes vom Virial in der kinetischen Theorie der Gase, Annalen Phys. **12** (1881) 127–136.

[233] Lorrain, P., Corson, D. R., Lorrain, F., Elektromagnetische Felder und Wellen, Walter de Gruyter, Berlin (1995).

[234] Lotfi, A., Vrabec, J., Fischer, J., Vapour liquid equilibria of the Lennard-Jones fluid from the NpT plus test particle method, Mol. Phys. **76** (1992) 1319–1333.

[235] Lucas, K., Applied Statistical Thermodynamics, Springer-Verlag, Berlin (1991).

[236] Luckas, M., Lucas, K., Thermodynamic properties of fluid carbon dioxide from the SSR-MPA potential, Fluid Phase Equilibria **45** (1989) 7–23.

[237] Luckas, M., Ripke, M., Lucas, K., Prediction of the thermophysical properties of fluid methane from SSR-MPA potential, Fluid Phase Equilibria **58** (1990) 35–50.

[238] Lustig, R., Application of thermodynamic perturbation theory to multicentre Lennard-Jones molecules. Results for CF_4, CCl_4, neo-C_5H_{12} and SF_6 as tetrahedral and octahedral models, Fluid Phase Equilibria **32** (1987) 117–137.

[239] Lustig, R., Angle-average for the powers of the distance between two separated vectors, Mol. Phys., **65** (1988) 175–179.

[240] Lustig, R., personal communication (2002).

[241] Lyubartsev, A. P., Laaksonen, A., Vorontsov-Velyaminov, P. N., Free energy calculations for Lennard-Jones systems and water using the expanded ensemble method. A Monte Carlo and molecular dynamics study, Mol. Phys. **82** (1994) 455–471.

[242] Lyubartsev, A. P., Laaksonen, A., Vorontsov-Velyaminov, P. N., Determination of free energy from chemical potentials: Application of the expanded ensemble method, Mol. Sim. **18** (1996) 43–58.

[243] Lyubartsev, A. P., Martinovskii, A. A., Shevkunov, S. V., Vorontsov-Velyaminov, P. N., New approach to Monte-Carlo calculation of free energy: method of expanded ensembles, J. Chem. Phys. **96** (1992) 1776–1783.

[244] MacDowell, L. G., Menduiña, C., Vega, C., de Miguel, C., Third virial coefficient and critical properties of quadrupolar two center Lennard-Jones models, Phys. Chem. Chem. Phys. **5** (2003) 2851–2857.

[245] MacKerell, A. D.,Jr., Wiórkiewicz-Kuczera, J., Karplus, M., An All-Atom Empirical Energy Function for the Simulation of Nucleic Acids, J. Am. Chem. Soc. **117** (1995) 11946–11975.

[246] Mackie, A. D., Tavitian, B., Boutin, A., Fuchs, A. H., Vapour-liquid phase equilibria predictions of methane-alkane mixtures by Monte Carlo simulation, Mol. Sim. **19** (1997) 1–15.

[247] MacRury, T. B., Steele, W. A., Berne, B. J., Intermolecular potential models for anisotropic molecules, with application to N_2, CO_2, and benzene, J. Chem. Phys. **64** (1976) 1288–1299.

[248] Magee, J. W., Outcalt, S. L., Ely, J. F., Molar heat capacity c_V, vapor pressure, and (p, ρ, T) measurements from 92 to 350 K at pressures to 35 MPa and a new equation of state for chlorotrifluoromethane (R13), Int. J. Thermophys. **21** (2000) 1097–1121, in [328].

[249] Mahoney, M. W., Jorgensen, W. L., A five-site model for the liquid water and the reproduction of the density anomaly by rigid, nonpolarizable potential functions, J. Chem. Phys. **112** (2000) 8910–8922.

[250] Maitland, G. C., Rigby, M., Smith, E. B., Wakeham, W. A., Intermolecular Forces, Clarendon Press, Oxford (1981).

[251] Majer, V., Svoboda, V., Enthalpies of Vaporization of Organic Compounds, Blackwell Scientific Publications, London (1985).

[252] Marcelli, G., Sadus, R. J., Molecular simulation of the phase behavior of noble gases using accurate two-body and three-body intermolecular potentials, J. Chem. Phys. **111** (1999) 1533–1540.

[253] Martin, M. G., Siepmann, J. I., Predicting multicomponent phase equilibria and free energies of transfer for alkanes by molecular simulation, J. Am. Chem. Soc. **119** (1997) 8921–8924.

[254] Martin, M. G., Siepmann, J. I., Transferable potentials for phase equilibria. 1. United-atom description of *n*-alkanes, J. Phys. Chem. B **102** (1998) 2569–2577.

[255] Martin, M. G., Siepmann, J. I., Novel configurational-bias Monte Carlo method for branched molecules. Transferable potentials for phase equilibria. 2. United-atom description of branched alkanes, J. Phys. Chem. B **103** (1999) 4508–4517.

[256] Martinez-Haya, B., Rull, L. F., Cuetos, A., Lago, S., Gibbs ensemble simulation of the vapour-liquid equilibrium of square well spherocylinders, Mol. Phys. **99** (2001) 509–516.

[257] Maruyama, S., A molecular dynamics simulation of heat conduction of a finite length single-walled carbon nanotube, Microscale Thermophysical Engineering **7** (2003) 41–50.

[258] Marx, V., Pruss, A., Wagner, W., Neue Zustandsgleichungen fuer R 12, R 22, R 11 und R 113. Beschreibung des thermodynamischen Zustandsverhaltens bei Temperaturen bis 525 K und Drücken bis 200 MPa, Series 19: Wärmetechnik/Kältetechnik, No. 57, VDI Verlag, Düsseldorf (1992), in [328].

[259] McCurdy, J. L., Katz, D. L., Phase equilibria in the system ethane-ethylene-acetylene, Ind. Eng. Chem. **36** (1944) 674–680.

[260] McDonald, I. R., *NpT*-ensemble Monte Carlo calculations for binary liquid mixtures, Mol. Phys. **23** (1972) 41–58.

[261] McDonald, I. R., NpT-ensemble Monte Carlo calculations for binary liquid mixtures, Mol. Phys. **100** (2002) 95–105.

[262] McDonald, I. R., Bounds, D. G., Klein, M. L., Molecular dynamics calculations for the liquid and cubic plastic crystal phases of carbon tetrachloride, Mol. Phys. **45** (1982) 521–542.

[263] McDonald, I. R., Singer, K., An equation of state for simple liquids, Mol. Phys. **23** (1972) 29–40.

[264] Mc Garry, J., Correlation and Prediction of the Vapor Pressures of Pure Liquids over Large Pressure Ranges, Ind. Eng. Chem. Process Des. Dev. **22** (1983) 313.

[265] McLure, I. A., Ramos, J. E., del Río, F., Accurate effective potentials and virial coefficients in real fluids. 1. Pure noble gases and their mixtures, J. Phys. Chem. B **103** (1999) 7019–7030.

[266] McQuarrie, D. A., Statistical mechanics, Univ. Science Books, Sausalito, California (2000).

[267] Mecke, M., Fischer, J., Winkelmann, J., Molecular dynamics simulation of the liquid-vapor interface of dipolar fluids under different electrostatic conditions, J. Chem. Phys. **114** (2001) 5842–5852.

[268] Mecke, M., Müller, A., Winkelmann, J., Fischer, J., An Equation of State for Two-Center Lennard-Jones Fluids, Int. J. Thermophys. **18** (1997) 683–698.

[269] Mecke, M., Winkelmann, J., Fischer, J., Molecular dynamics simulation of the liquid-vapor interface: Binary mixtures of Lennard-Jones fluids, J. Chem. Phys. **110** (1999) 1188–1194.

[270] Mehta, M., Kofke, D. A., Molecular simulation in a pseudo grand canonical ensemble, Mol. Phys. **86** (1995) 139–147.

[271] Meier, K., Tillner-Roth, R., Kabelac, S., Edwards, T. J., Monte Carlo Simulations of Binary Lennard-Jones Mixtures: A Test of the van der Waals One-Fluid Model, Int. J. Thermophys. **19** (1998) 687–696.

[272] Michael, D., Benjamin, I., Molecular dynamics computer simulations of solvation dynamics at liquid/liquid interface, J. Chem. Phys. **114** (2001) 2817–2824.

[273] Miller, R. C., Kidnay, A. J., Hiza, M. J., Liquid + vapor equilibria in methane + ethene and in methane + ethane from 150.00 to 190.00 K, J. Chem. Thermodynamics **9** (1977) 167–177, in [181].

[274] Milocco, O., Fermeglia, M., Pricl, S., Prediction of thermophysical properties of alternative refrigerants by computational chemistry, Fluid Phase Equilibria **199** (2002) 15–21.

[275] Mollerup, J., Vapor/liquid equilibrium in ethylene+carbon dioxide and ethane+carbon dioxide, J. Chem. Soc., Faraday. I. **71** (1975) 2351–2360, in [181].

[276] Mon, K. K., Griffiths, R. B., Chemical potential by gradual insertion of a particle in Monte Carlo simulation, Phys. Rev. A **31** (1985) 956–959.

[277] Mountain, R. D., Morrison, G., Molecular dynamics study of liquid CCl_2F_2 and $CClHF_2$, Mol. Phys **64** (1988) 91–95.

[278] Morales, J. J, Nuevo, M. J., Path Integral Molecular Dynamics Methods: Application to Neon, J. Comput. Chem. **16** (1995) 105–112.

[279] Morales, J. J., Singer, K., Path integral simulation of the free energy of (Lennard-Jones) neon, Mol. Phys. **73** (1991) 873–880.

[280] Möller, D., Fischer, J., Vapour liquid equilibrium of a pure fluid from test particle method in combination with NpT molecular dynamics simulations, Mol. Phys. **69** (1990) 463–473.

[281] Möller, D., Fischer, J., Erratum, Vapour Liquid Equilibrium of a Pure Fluid from Test Particle Method in Combination with NpT Molecular Dynamics Simulations, Mol. Phys. **75** (1992) 1461–1462.

[282] Möller, D., Fischer, J., Determination of an effective intermolecular potential for carbon dioxide using vapour-liquid phase equilibria from NpT + test particle simulations, Fluid Phase Equilibria **100** (1994) 35–61.

[283] Möller, D., Óprzynski, J., Müller, A., Fischer, J., Prediction of thermodynamic properties of fluid mixtures by molecular dynamics simulations: methane–ethane, Mol. Phys. **75** (1992) 363–378.

[284] Murthy, C. S., Singer, K., Klein, M. I., McDonald, I. R., Pairwise additive effective potentials for nitrogen, Mol. Phys. **41** (1980) 1387–1399.

[285] Murthy, C. S., Singer, K., McDonald, I. R., Interaction site models for carbon dioxide, Mol. Phys. **44** (1981) 135–143.

[286] Murthy, C. S., Singer, K., Vallauri, R., Computer simulation of liquid chlorine, Mol. Phys. **49** (1983) 803–815.

[287] Müller, A., Winkelmann, J., Fischer, J., BACKONE Family of Equations of State: 1. Nonpolar and Polar Pure Fluids, AIChE J. **42** (1996) 1116–1126.

[288] Müller, A., Winkelmann, J., Fischer, J., Simulation studies in mixtures of dipolar with nonpolar linear molecules. II. A mixing rule for the dipolar contribution to the Helmholtz energy, Fluid Phase Equilibria **120** (1996) 107–119.

[289] Nagahama, K., Konishi, H., Hoshino, D., Hirata, M., Binary vapor-liquid equilibria of carbon dioxide-light hydrocarbons at low temperature, J. Chem. Eng. Japan **7** (1974) 323–328.

[290] Nagel, M., Bier, K., Vapour-liquid equilibrium of ternary mixtures of the refrigerants R32, R125 and R134a, Int. J. Refrig. **18** (1995) 534–543.

[291] Nagel, M., Bier, K., Vapour-liquid equilibrium of ternary mixtures of the refrigerants R125, R143a and R134a, Int. J. Refrig. **19** (1996) 264–271.

[292] Narten, A. H., Danford, M. D., Levy, H. A., Structure and intermolecular potential of liquid carbon tetrachloride derived from X-ray diffraction data, J. Chem. Phys. **46** (1967) 4875–4880.

[293] Nath, S. K., Molecular simulation of vapor-liquid equilibria of hydrogen sulfide and its mixtures with alkanes, J. Phys. Chem. B **107** (2003) 9498–9504.

[294] Nath, S. K., Banaszak, B. J., de Pablo, J. J., A new united atom force field for α-olefins, J. Chem. Phys. **114** (2001) 3612–3616.

[295] Nath, S. K., de Pablo, J. J., Simulation of vapour-liquid equilibria for branched alkanes, Mol. Phys. **98** (2000) 231–238.

[296] Nath, S. K., Escobedo, F. A., de Pablo, J. J., On the simulation of vapor-liquid equilibria for alkanes, J. Chem. Phys. **108** (1998) 9905–9911.

[297] Nath, S. K., Escobedo, F. A., de Pablo, J. J., Patramai, I., Simulation of Vapor-Liquid Equilibria for Alkane Mixtures, Ind. Eng. Chem. Res. **37** (1998) 3195–3202.

[298] Nath, S. K., Khare, R., New forcefield parameters for branched hydrocarbons, J. Chem. Phys. **115** (2001) 10834–10844.

[299] Nezbeda, I., Simple short-ranged models of water and their application. A review, J. Mol. Liq. **73, 74** (1997) 317–336.

[300] Nezbeda, I., Kolafa, J., A New Version of the Insertion Particle Method for Determining the Chemical Potential by Monte Carlo Simulation, Mol. Sim. **5** (1991) 391–403.

[301] Nezbeda, I., Lísal, M., Effect of short and long range forces on the thermodynamic properties of water. A simple short range reference system, Mol. Phys. **99** (2001) 291–300.

[302] Neubauer, B., Boutin, A., Tavitian, B., Fuchs, A. H., Gibbs ensemble simulations of vapour-liquid phase equilibria of cyclic alkanes, Mol. Phys. **97** (1999) 769–776.

[303] Neubauer, B., Tavitian, B., Boutin, A., Ungerer, P., Molecular simulations on volumetric properties of natural gas, Fluid Phase Equilibria **161** (1999) 45–62.

[304] Njo, S. L., van Gunsteren, W. F., Müller-Plathe, F., Determination of force field parameters for molecular simulation by molecular simulation: An application of the weak-coupling method, J. Chem. Phys. **102** (1995) 6199–6207.

[305] Nolting, W., Grundkurs: Theoretische Physik, 3 Elektrodynamik, Verlag Zimmermann-Neufang, Ulmen, Germany (1990).

[306] Nosé, S., Klein, M. L., A study of solid and liquid carbon tetrafluoride using the constant pressure molecular dynamics technique, J. Chem. Phys. **78** (1983) 6928–6939.

[307] Nymand, T. M., Linse, P., Ewald summation and reaction field methods for potentials with atomic charges, dipoles, and polarizabilities, J. Chem. Phys. **112** (2000) 6152–6160.

[308] Ohji, H., Morimoto, S., Fujihara, I., Murakami, S., Thermodynamic properties and structure of supercritical Stockmayer/Lennard-Jones fluid mixtures, Fluid Phase Equilibria **132** (1997) 47–60.

[309] Okumura, H., Yonezawa, F., Liquid-vapor coexistence curves of several interatomic model potentials, J. Chem. Phys. **113** (2000) 9162–9168.

[310] O'Shea, S. F., Dubey, G. S., Rasaiah, J. C., Phase transitions of quadrupolar fluids, J. Chem. Phys. **107** (1997) 237–242.

[311] Outcalt, S. L., McLinden, M. O., A modified Benedict-Webb-Rubin equation of state for the thermodynamic properties of R152a (1,1-difluoroethane), J. Phys. Chem. Ref. Data **25** (1996) 605–636, in [328].

[312] Palmer, B. J., Anchell, J. L., Molecular Mechanics Parameters for Fluorine-Substituted Methanes from ab initio Quantum Calculations, J. Phys. Chem. **99** (1995) 12239–12248.

[313] Panagiotopoulos, A. Z., Direct determination of phase coexistence properties of fluids by Monte Carlo simulation in a new ensemble, Mol. Phys. **61** (1987) 813–826.

[314] Panagiotopoulos, A. Z., Exact Calculations of Fluid-Phase Equilibria by Monte Carlo Simulation in a New Statistical Ensemble, Int. J. Thermophys. **10** (1989) 447–457.

[315] Panagiotopoulos, A. Z., Wong, V., Floriano, M. A., Phase Equilibria of Lattice Polymers from Histogram Reweighting Monte Carlo Simulations, Macromolecules **31** (1998) 912–918.

[316] Peng, D.-Y., Robinson, D. B., A New Two-Constant Equation of State, Ind. Eng. Chem. Fundamen. **15** (1976) 59–64.

[317] Penoncello, S. G., Lemmon, E. W. , Shan, Z., Jacobsen, R. T., An equation of state for the calculation of the thermodynamic properties of trifluoromethane (R-23), submitted to: Int. J. Thermophys. (2002), in [328].

[318] Physikalisch-Technische Bundesanstalt, PTB-Stoffdatenblätter, Braunschweig and Berlin (1992–1995).

[319] Pitzer, K. S., Lippmann, D. Z., Curl, R. F., Huggins, C. M., Petersen, D. E., The Volumetric and Thermodynamic Properties of Fluids. II. Compressibility Factor, Vapor Pressure and Entropy of Vaporization, J. Am. Chem. Soc., 77 (1955) 3433–3440.

[320] Platzer, B., Polt, A., Maurer, G., Thermophysical Properties of Refrigerants, Springer, Berlin (1990).

[321] Poling, B. E., Prausnitz, J. M., O'Connell, J. P., The Properties of Gases and Liquids, 5th ed., McGraw-Hill Book Company, New York (2001).

[322] Pomès, R., Eisenmesser, E., Post, C. B., Roux, B., Calculating the excess chemical potentials using dynamic simulations in the fourth dimension, J. Chem. Phys. **111** (1999) 3387–3395.

[323] Potoff, J. J., Errington, J. R., Panagiotopoulos, A. Z., Molecular Simulation of Phase Equilibria for Mixtures of Polar and Non-Polar Components, Mol. Phys. **97** (1999) 1073–1083.

[324] Potoff, J. J., Panagiotopoulos, A. Z., Critical point and phase behavior of the pure fluid and a Lennard-Jones mixture, J. Chem. Phys. **109** (1998) 10914–10920.

[325] Potoff, J. J., Siepmann, J. I., Vapor-Liquid Equilibria of Mixtures Containing Alkanes, Carbon Dioxide, and Nitrogen, AIChE J. **47** (2001) 1676–1682.

[326] Potter, S. C., Tildesley, D. J., Burgess, A. N., Rogers, S. C., A transferable potential model for the liquid-vapour equilibria of fluoromethanes, Mol. Phys. **92** (1997) 825–833.

[327] Předota, M., Nezbeda, I., Kalyuzhnyi, Y. V., Fluids of pseudo-hard bodies .II. Reference models for water, methanol, and ammonia, Mol. Phys. **94** (1998) 937–948.

[328] REFPROP, NIST Standard Reference Database 23, Version 7.0 (2002).

[329] Reid, R. C., Prausnitz, J. M., Poling, B. E., The Properties of Gases and Liquids, 4th ed., McGraw-Hill Book Company, New York (1987).

[330] Reiff, W.-E., Roth, H., Lucas, K., Phase equilibria in the binary system carbon disulfide-carbon dioxide, Fluid Phase Equilibria **73** (1992) 323–338.

[331] Rivera, J. L., Alejandre, J., Nath, S. K., de Pablo, J. J., Thermodynamic and Transport Properties of Nitrogen and Butane Mixtures, Mol. Phys. **98** (2000) 43–55.

[332] Rivera, J. L, Predota, M., Chialvo, A. A., Cummings, P. T., Vapor-liquid equilibrium simulations of the SCPDP model of water, Chem. Phys. Lett. **357** (2002) 189–194.

[333] Rodger, P. M., Stone, A. J., Tildesley, D. J., Atomic anisotropy and the structure of liquid chlorine, J. Chem. Soc., Faraday Trans. 2 **83** (1987) 1689–1702.

[334] Rodger, P. M., Stone, A. J., Tildesley, D. J., The intermolecular potential of chlorine. A three phase study, Mol. Phys. **63** (1988) 173–188.

[335] Rodríguez, I., Acevedo, A. J., López, G. E., Structure and thermodynamics of molecular nitrogen clusters, Mol. Phys. **90** (1997) 943–949.

[336] Roth, H., Peters-Gerth, P., Lucas, K., Experimental vapor-liquid equilibria in the systems R22-R23, R22-CO_2, CS_2-R22, R23-CO_2, CS_2-R23, Fluid Phase Equilibria **73** (1992) 147–166.

[337] Rowlinson, J. S., Liquids and Liquid Mixtures, Butterworth, London (1969).

[338] Saager, B., Anwendung von Computersimulationen zur direkten Stoffdatenvorhersage und zur Konstruktion einer Zustandsgleichung reiner polarer Fluide, Dissertation, Ruhr-Universität Bochum, Bochum (1990).

[339] Saager, B., Fischer, J., Construction and Application of Physically Based Equations of State: II. The Dipolar and Quadrupolar Contributions to the Helmholtz Energy, Fluid Phase Equilibria **72** (1992) 67–88.

[340] Saager, B., Fischer, J., Neumann, M., Reaction field simulations of monatomic and diatomic dipolar fluids, Mol. Sim. **6** (1991) 27–49.

[341] Sadus, R. J., Monte Carlo simulation of vapour-liquid equilibria in "Lennard-Jones + three-body potential" binary fluid mixtures, Fluid Phase Equilibria **116** (1996) 289–295.

[342] Sadus, R. J., Molecular simulation of the vapour-liquid equilibria of pure fluids and binary mixtures containing dipolar components: the effect of Keesom interactions, Mol. Phys. **87** (1996) 979–990.

[343] Sadus, R. J., Exact calculation of the effect of three-body Axilrod-Teller interactions on vapour-liquid coexistence, Fluid Phase Equilibria **144** (1998) 351–359.

[344] Sadus, R. J., Molecular simulation of the phase behaviour of ternary fluid mixtures: the effect of a third component on vapour-liquid and liquid-liquid coexistence, Fluid Phase Equilibria **157** (1999) 169–180.

[345] Sadus, R. J., Prausnitz, J. M., Three-body interactions in fluids from molecular simulation: Vapor- liquid phase coexistence of argon, J. Chem. Phys. **104** (1996) 4784–4787.

[346] Sagara, H., Arai, Y., Saito, S., Vapor-liquid equilibria of binary and ternary systems containing hydrogen and light hydrocarbons, J. Chem. Eng. Jap. **5** (1972) 339–348.

[347] Sagarik, K. P., Ahlrichs, R., Molecular dynamics simulations of liquid $CHClF_2$ with a test- particle model potential, Chem. Phys. Lett. **131** (1986) 74–81.

[348] Sage, B. H., Lacey, W. N., Am. Petrol. Inst., Project 37 (1955).

[349] Sandler, S. I., Models for thermodynamic and phase equilibria calculations, Marcel Dekker, New York (1994).

[350] Sasinovskii, V., (title in Russian not given here), cf. therein Figure 2, Trudy Moskovskogo Ordena Lenina i Ordena Oktjabrskoj Revoljuzi **364** (1979) 13–18.

[351] Schmidt, H., Das thermodynamische Verhalten des flüssigen Systems Ar-Kr, Z. Phys. Chem. Neue Folge **24** (1960) 265–274.

[352] Schmidt, R., Wagner, W., A new form of the equation of state for pure substances and its application to oxygen, Fluid Phase Equilibria **19** (1985) 175–200.

[353] Seidel, P., Basisdatenbank COMDAB, Leuna-Werke AG (1987-1993).

[354] Setzmann, U., Wagner, W., A New Equation of State and Tables of Thermodynamic Properties for Methane Covering the Range from the Melting Line to 625 K at Pressures up to 1000 MPa, J. Phys. Chem. Ref. Data **20** (1991) 1061–1155.

[355] Shatskaya, L. V., Zhirnova, N. A., Liquid-vapour phase equilibria in binary systems at low temperatures. I. Argon-methane system, Russ. J. Phys. Chem. **50** (1976) 298, in [181].

[356] Shevkunov, S. V., Martinovskii, A. A., Vorontsov-Velyaminov, P. N., Calculation of the critical sizes and properties of microdrops using the Monte-Carlo method in a generalized ensemble, Teplofizika vysokikh temperatur **26** (1988) 246–254.

[357] Shiflett, M. B., Sandler, S. I., Modeling fluorocarbon vapor-liquid equilibria using the Wong-Sandler model, Fluid Phase Equilibria **147** (1998) 145–162.

[358] Shing, K. S., Chung, S. T., Computer simulation method for the calculation of solubility in supercritical extraction systems, J. Phys. Chem. **91** (1987) 1674–1681.

[359] Simmrock, K. H., Janowsky, R., Ohnsorge, A., Chemistry Data Series, Vol. II, Part 2, DECHEMA, Frankfurt (1986).

[360] Singer, J. V. L., Singer, K., The thermodynamic properties of mixtures of Lennard-Jones (12-6) liquids, Mol. Phys. **19** (1970) 279–284.

[361] Singer, K., Monte Carlo calculations of the thermodynamic properties of mixtures of Lennard-Jones liquids, Chem. Phys. Lett. **3** (1969) 164–166.

[362] Singer, K., Smith, W., The classical and quantum-mechanical free energy of solid (Lennard-Jones) argon, Chem. Phys. Lett. **140** (1987) 406–410.

[363] Singer, K., Taylor, A., Singer, J. V. L., Thermodynamic and structural properties of liquids modelled by '2- Lennard-Jones centres' pair potentials, Mol. Phys. **33** (1977) 1757–1795.

[364] Smit, B., Karaborni, S., Siepmann, J. I., Computer simulations of vapor-liquid phase equilibria of n-alkanes, J. Chem. Phys. **102** (1995) 2126–2140.

[365] Smit, B., Williams, C. P., Vapour-liquid equilibria for quadrupolar Lennard-Jones fluids, J. Phys.: Condens. Matter **2** (1990) 4281–4288.

[366] Smit, B., Williams, C. P., Hendriks, E. M., de Leeuw, S. W., Vapour-liquid equilibria for Stockmayer fluids, Mol. Phys. **68** (1989) 765–769.

[367] Smith, W. R., Tříska, B., The reaction ensemble method for the computer simulation of chemical and phase equilibria. I. Theory and basic examples, J. Chem. Phys. **100** (1994) 3019–3027.

[368] Soetens, J.-C., Jansen, G., Millot, C., Molecular dynamics simulation of liquid CCl_4 with a new polarizable potential model, Mol. Phys. **96** (1999) 1003–1012.

[369] Somait, F. A., Kidnay, A. J., Liquid-vapor equilibria at 270.00 K for systems containing nitrogen, methane, and carbon dioxide, J. Chem. Eng. Data **23** (1978) 301–305, in [181].

[370] Song, W., Patel, N., Maroncelli, M., A 2-Site Model for Simulating Supercritical Fluoroform, J. Phys. Chem. B **106** (2002) 8783–8789.

[371] Song, W., Rossky, P. J., Maroncelli, M., Modeling alkane+perfluoroalkane interactions using all-atom potentials: Failure of the usual combining rules, J. Chem. Phys. **119** (2003) 9145–9162.

[372] Sprow, F. B., Prausnitz, J. M., Vapor-liquid equilibria for five cryogenic mixtures, AIChE J. **12** (1966) 780–784, in [181].

[373] Stapleton, M. R., Tildesley, D. J., Panagiotopoulos, A. Z., Quirke, N., Phase equilibria of quadrupolar fluids by simulation in the Gibbs ensemble, Mol. Sim **2** (1989) 147–162.

[374] Steinhauser, O., Reaction field simulation of water, Mol. Phys. **45** (1982) 335–348.

[375] Steinhauser, O., Neumann, M., Structure and dynamics of liquid carbon tetrachloride. A molecular dynamics study, J. Chem. Phys. **40** (1980) 115–128.

[376] Stewart, R. B., Jacobsen, R. T., Thermodynamic Properties of Argon from the Triple Point to 1200 K with Pressures to 1000 MPa, J. Phys. Chem. Ref. Data **18** (1989) 639–798.

[377] Stogryn, D. E., Stogryn, A. P., Molecular multipole moments, Mol. Phys. **11** (1966) 371–393.

[378] Stoll, J., Internal report, Institut für Technische Thermodynamik und Thermische Verfahrenstechnik, Universität Stuttgart (2004).

[379] Streett, W. B., Liquid-vapor phase behaviour and liquid phase density in the system neon-argon at high pressures, J. Chem. Phys. **46** (1967) 3282–3286.

[380] Streett, W. B., Jones, C. H., Liquid-vapor equilibrium in the system neon-oxygen from 63° to 152°K and at pressures to 5000 psi, Adv. Cryog. Eng. **11** (1966) 356–366.

[381] Streett, W. B., Tildesley, D. J., Computer simulations of polyatomic molecules. II. Molecular dynamics studies of diatomic liquids with atom-atom and quadrupole-quadrupole potentials, Proc. R. Soc. Lond. A **355** (1977) 239–266.

[382] Sum, A. K., Sandler, S. I., Ab initio pair potential and phase equilibria predictions for the refrigerant methyl fluoride, Mol. Phys. **100** (2002) 2433–2447.

[383] Sum, A. K., Sandler, S. I., Bukowski, R., Szalewicz, K., Prediction of the phase behavior of acetonitrile and methanol with ab initio pair potentials. II. The mixture, J. Chem. Phys. **116** (2002) 7637–7644.

[384] Sun, H., COMPASS: An ab Initio Force-Field Optimized for Condensed-Phase Applications – Overview with Details on Alkane and Benzene Compounds, J. Chem. Phys. B **102**(1998) 7338–7364.

[385] Suzuki, M., Schnepp, O., Intermolecular potential and lattice dynamics of the CO2 crystal, J. Chem. Phys. **55** (1971) 5349–5356.

[386] Tavares, F. W., Sandler, S. I., Vapour-liquid equilibria of exponential-six fluids, Mol. Phys. **87** (1996) 1471–1476.

[387] Taylor, M. P., Luettmer-Strathmann, J., Lipson, J. E. G., Structure and phase behaviour of square-well dimer fluids, J. Chem. Phys. **114** (2001) 5654–5662.

[388] Tester, J. W., Modell, M., Thermodynamics and its applications, 3. ed., Prentice-Hall, Upper Saddle River, NJ (1997).

[389] The Chemical Rubber Co., Handbook of Chemistry and Physics, 46th ed.; Cleveland, Ohio (1965).

[390] Thirumalai, D., Hall, R. W., Berne, B. J., A path integral Monte Carlo study of liquid neon and the quantum effective pair potential, J. Chem. Phys. **81** (1984) 2523–2527.

[391] Tildesley, D. J., Madden, P. A., An effective pair potential for liquid carbon disulphide, Mol. Phys. **42** (1981) 1137–1156.

[392] Tillner-Roth, R., Baehr, H. D., An international standard formulation of the thermodynamic properties of 1,1,1,2-tetrafluoroethane (HFC-134a) covering temperatures from 170 K to 455 K at pressures up to 70 MPa, J. Phys. Chem. Ref. Data **23** (1994) 657–729, in [328].

[393] Tillner-Roth, R., Yokozeki, A., An international standard equation of state for difluoromethane (R-32) for temperatures from the triple point at 136.34 K to 435 K and pressures up to 70 MPa, J. Phys. Chem. Ref. Data **25** (1997) 1273–1328, in [328].

[394] Toxvaerd, S., Equation of state of alkanes II, J. Chem. Phys. **107** (1997) 5197–5204.

[395] Trust, D. B., Kurata, F., Vapor-Liquid and Liquid-Liquid Vapor Phase Behavior of the Carbon Monoxide-Propane and the Carbon Monoxide-Ethane Systems, AIChE J. **17** (1971) 415–419.

[396] Tsang, P. C., White, O. N., Perigard, B. Y., Vega, L. F., Panagiotopoulos, A. Z., Phase Equilibria in ternary Lennard-Jones Systems, Fluid Phase Equilibria **107** (1995) 31–43.

[397] Ungerer, P., Beauvais, C., Delhommelle, J., Rousseau, B., Fuchs, A. H., Optimization of the anisotropic united atoms intermolecular potential for *n*-alkanes, J. Chem. Phys. **112** (2000) 5499–5510.

[398] Ungerer, P., Boutin, A., Fuchs, A. H., Direct Calculation of Bubble Points by Monte Carlo Simulation, Mol. Phys. **97** (1999) 523–539.

[399] Ungerer, P., Boutin, A., Fuchs, A. H., Direct calculation of bubble points for alkane mixtures by molecular simulation, Mol. Phys. **99** (2001) 1423–1434.

[400] Valleau, J. P., Density-Scaling: A New Monte Carlo Technique in Statistical Mechanics, J. Comput. Phys. **96** (1991) 193–216.

[401] van der Spoel, D., van Maaren, P. J., Berendsen, H. J. C., A systematic study of water models for molecular simulation: Derivation of water models optimized for use with a reaction field, J. Chem. Phys. **108** (1998) 10220–10230.

[402] van Leeuwen, M. E., Derivation of Stockmayer potential parameters for polar fluids, Fluid Phase Equilibria **99** (1994) 1–18.

[403] van Leeuwen, M. E., Molecular simulation of the phase behaviour of polar fluids, PhD thesis, University of Utrecht, Utrecht (1995).

[404] van Leeuwen, M. E., Smit, B., Molecular simulation of the vapor-liquid coexistence curve of methanol, J. Phys. Chem. **99** (1995) 1831–1833.

[405] van Leeuwen, M. E., Smit, B., Hendriks, E. M., Vapour-liquid equilibria of Stockmayer fluids. Computer simulations and perturbation theory, Mol. Phys. **78** (1993) 271–283.

[406] Vega, C., McBridge, C., Menduiña, C., The second virial coefficient of the dipolar two center Lennard-Jones model, Phys. Chem. Chem. Phys. **4** (2002) 3000–3007.

[407] Vega, C., Saager, B., Fischer, J., Molecular dynamics studies for the new refrigerant R152a with simple model potentials, Mol. Phys. **68** (1989) 1079–1093.

[408] Vega, E., de Miguel, E., Rull, L. F., Jackson, G., McLure, I. A., Phase equilibria and critical behaviour of square-well fluids of variable width by Gibbs ensemble Monte Carlo simulation, J. Chem. Phys. **96** (1992) 2296–2305.

[409] Vesely, F. J., Angular Monte Carlo Integration Using Quaternion Parameters: A Spherical Reference Potential for CCl_4, J. Comp. Phys. **47** (1982) 291–296.

[410] Vojta, G., Vojta, M., Teubner-Taschenbuch der Statistischen Physik, B. G. Teubner Stuttgart, Leipzig (2000).

[411] von Solms, N., Koo, K. Y., Chiew, Y. C., Mixing rules for binary Lennard-Jones chains: theory and Monte Carlo simulation, Fluid Phase Equilibria **180** (2001) 71–85.

[412] Vorholz, J., Harismiadis, V. I., Rumpf, B., Panagiotopoulos, A. Z., Maurer, G., Vapor+liquid equilibrium of water, carbon dioxide, and the binary system water+carbon dioxide from molecular simulation, Fluid Phase Equilibria **170** (2000) 203–234.

[413] Vrabec, J. Vorhersage thermodynamischer Stoffdaten durch molekulare Simulation, Fortschr.-Ber. VDI Reihe 3 Nr. 455, VDI-Verlag, Düsseldorf (1996).

[414] Vrabec, J., personal communication (2003).

[415] Vrabec, J., Fischer, J., Vapour liquid equilibria of mixtures from the *NpT* plus test particle method, Mol. Phys. **85** (1995) 781–792.

[416] Vrabec, J., Fischer, J., Vapor-liquid equilibria of binary mixtures containing methane, ethane, and carbon dioxide from molecular simulation, Int. J. Thermophys. **17** (1996) 889–908.

[417] Vrabec, J., Fischer, J., Vapour-liquid equilibria of the Ternary Mixture CH_4+C_2H_6+CO_2 from Molecular Simulation, AIChE J. **43** (1997) 212–217.

[418] Vrabec, J., Hasse, H., Grand-Equilibrium: vapour-liquid equilibria by a new molecular simulation method, Mol. Phys. **100** (2002) 3375–3383.

[419] Vrabec, J., Kedia, G. K., Hasse, H., Prediction of Joule-Thomson inversion curves for pure fluids and one mixture by molecular simulation, Cryogenics, in press (2004).

[420] Vrabec, J., Kettler, M., Hasse, H., Chemical potential of quadrupolar two-centre Lennard-Jones fluids by gradual insertion, Chem. Phys. Lett. **356** (2002) 431–436.

[421] Vrabec, J., Lotfi, A., Fischer, J., Vapour liquid equilibria of Lennard-Jones model mixtures from *NpT* plus test particle method, Fluid Phase Equilibria **112** (1995) 173–197.

[422] Vrabec, J., Stoll, J., Hasse, H., A Set of Molecular Models for Symmetric Quadrupolar Fluids, J. Phys. Chem. B **105** (2001) 12126–12133.

[423] Waldman, M., Hagler, A. T., New combining rules for rare gas van der Waals parameters, J. Comput. Chem. **14** (1993) 1077–1084.

[424] Walser, R., Mark, A. E., van Gunsteren, W. F., Lauterbach, M., Wipff, G., The effect of force-field parameters on properties of liquids: parameterization of a simple three-site model for methanol, J. Chem. Phys. **112** (2000) 10450–10459.

[425] Wang, J., Kollman, P. A., Automatic Parameterization of Force Field by Systematic Search and Genetic Algorithms, J. Comp. Chem. **22** (2001) 1219–1228.

[426] Wang, Q., Johnson, J. K., Phase equilibrium of quantum fluids from simulation: Hydrogen and neon, Fluid Phase Equilibria **132** (1997) 93–116.

[427] Wang, Z. J., Chen, M., Guo, Z. Y., Yang, C., Molecular dynamics study on the liquid-vapor interfacial profiles, Fluid Phase Equilibria **183–184** (2001) 321–329.

[428] Warshavsky, V. B., Zeng, X. C., Bulk and interfacial properties of quadrupolar fluids, J. Chem. Phys. **117** (2002) 3982–3991.

[429] Weiner, S. J., Kollman, P. A., Nguyen, D. T., Case, D. A., An All Atom Force Field for Simulations of Proteins and Nucleis Acids, J. Comp. Chem. **7** (1986) 230–252.

[430] Weingerl, U., Wendland, M., Fischer, J., Müller, A., Winkelmann, J., Backone Family of Equations of State: 2. Nonpolar and Polar Fluid Mixtures, AIChE J. **47** (2001) 705–717.

[431] Wendland, M., personal communication (2001).

[432] Wheatley, R. J., Price, S. L., A systematic intermolecular potential method applied to chlorine, Mol. Phys. **71** (1990) 1381–1404.

[433] Wichterle, I., Kobayashi, R., Vapor-liquid equilibrium of methane-ethane system at low temperatures and high pressures, J. Chem. Eng. Data **17** (1972) 9–12, in [181].

[434] Wick, C. D., Martin, M. G., Siepmann, J. I., Transferable Potentials for Phase Equilibria. 4. United-Atom Description of Linear and Branched Alkenes and Alkylbenzenes, J. Phys. Chem. B **104** (2000) 8008–8016.

[435] Widom, B., Some Topics in the Theory of Fluids, J. Chem. Phys. **39** (1963) 2808–2812.

[436] Wilding, N. B., Critical-point coexistence-curve properties of the Lennard-Jones fluid: A finite-size scaling study, Phys. Rev. E **52** (1995) 602–611.

[437] Wilding, N. B., Simulation studies of fluid critical behaviour, J. Phys.: Condens. Matter **9** (1997) 585–612.

[438] Wisotzki, K. D., Schneider, G. M., Fluid phase equilibria of the binary systems N_2 + Ethane and N_2 + pentane between 88 K and 313 K and at pressures up to 200 MPa. Ber. Bunsenges. Phys. Chem. **89** (1985) 21–25.

[439] Wojcik, M., Gubbins, K. E., Powles, J. G., The thermodynamics of symmetric two-centre Lennard-Jones liquids, Mol. Phys. **45** (1982) 1209–1225.

[440] Wu, G.-W., Sadus, R. J., Molecular simulation of the high-pressure phase equilibria of binary atomic fluid mixtures using the exponetial-6 intermolecular potential, Fluid Phase Equilibria **170** (2002) 269–284.

[441] Yamasaki, K., The crystal structure and lattice energy of halogen molecules, J. Phys. Soc. Jap. **17** (1962) 1262–1267.

[442] Yang, J., Ren, Y., Tian, A.-M., Sun, H., COMPASS Force Field for 14 Inorganic Molecules, He, Ne, Ar, Kr, Xe, H_2, O_2, N_2, NO, CO, CO_2, NO_2, CS_2, and SO_2, in Liquid Phases, J. Phys. Chem. B **104** (2000) 4951–4957.

[443] Yim, W.-L., Gong, X. G., Liu, Z.-F., Chemisorption of NO_2 on Carbon Nanotubes, J. Phys. Chem. B **107** (2003) 9363–9369.

[444] Younglove, B. A., McLinden, M. O., An international standard equation-of-state formulation of the thermodynamic properties of refrigerant 123 (2,2-dichloro-1,1,1-trifluoroethane), J. Phys. Chem. Ref. Data **23** (1994) 731–779, in [328].

[445] Zenner, G. H., Dana, L. I., Liquid-Vapor Equilibrium Compositions of Carbon Dioxide-Oxygen- Nitrogen Mixtures, Chem. Eng. Prog. Symp. Series **59** (1963) 36–41.

[446] Zhang, Z., Duan, Z., Phase equilibria of the system methane-ethane from temperature scaling Gibbs Ensemble Monte Carlo simulation, Geochimica et Cosmochimica Acta **66** (2002) 3431–3439.

[447] Zhou, J., Lu, X., Wang, Y., Shi, J., Molecular dynamics investigation on the infinite dilute diffusion coefficient of organic compounds in supercritical carbon dioxide, Fluid Phase Equilibria **172** (2000) 279–291.

Zusammenfassung

Die Entwicklung neuer Schlüsseltechnologien im 21. Jahrhundert, wie der Biotechnologie, der Nanotechnologie, den Werkstoffwissenschaften oder der Pharmakologie zwingt die Verfahrenstechnik zur beschleunigten Entwicklung neuer Verfahren für die Herstellung, Wandlung und Entsorgung einer stetig steigenden Zahl neuer Substanzen und Materialien. Dabei werden Fragestellungen wie die Suche nach optimalen Lösungsmitteln oder nach effizienteren Katalysatoren, und vor allem die zuverlässige Vorhersage von thermophysikalischen Stoffeigenschaften gehäuft unter hohem Zeitdruck zu beantworten sein. Weiterhin setzt die rechnergestützte Abbildung und Optimierung nanoskaliger Prozesse deren Verständnis auf molekularer Ebene voraus.

Nicht zuletzt aus Kostengründen kann diese Entwicklung nicht ausschließlich mit vermehrter Laborarbeit bewältigt werden. Vielmehr wird sich die Verfahrenstechnik rechnergestützter molekularer Methoden bedienen müssen, um mit dieser Entwicklung Schritt halten zu können. Die Schwerpunkte in Forschung und Lehre werden von dieser Entwicklung beeinflusst werden und verstärkt interdisziplinär orientiert sein. Im internationalen Umfeld hat diese Entwicklung bereits seit mehreren Jahren eingesetzt.

Vorgänge auf der molekularen Ebene werden mit diesen Methoden in virtueller Realität fassbar und nachvollziehbar. Sie bahnen damit den Weg zum bildlichen Verstehen von Stoffwandlungsvorgängen auf elementarer Ebene und leisten damit einen wichtigen Beitrag zur Entwicklung optimierte Modellierungsansätze für verfahrenstechnische Grundoperationen.

Weiterhin wird die Bedeutung molekularer Methoden in der Vorhersage thermophysikalischer Stoffdaten von Mischungen liegen, die für die Entwicklung und Optimierung von Gesamtverfahren unerlässlich sind.

Zahlreiche Anwendungsbeispiele aus der Industrie belegen bereits heute, dass das Potenzial molekularer Methoden erkannt ist und sie sich zu einem unverzichtbaren Werkzeug in der praktischen Anwendung entwickeln.

Die vorliegende Arbeit befasst sich mit der Vorhersage thermophysikalischer Stoffdaten realer Reinstoffe und Mischungen mit Hilfe molekularer Simulation. Üblicherweise werden zur Beschreibung der Stoffdaten von Mischungen Zustandgleichungen, wie beispielsweise die Peng-Robinson- oder die Soave-Redlich-Kwong-Zustandsgleichung oder Modelle der Freien Exzessenthalpie G^{E} verwendet, die zwar hervorragende Korrelationswerkzeuge für experimentell ermittelte Stoffdaten sind, aber bekanntermaßen Schwächen bei der Stoffdatenvorhersage zeigen. Dies gilt in besonderem Maße, wenn, wie es in der industriellen

Praxis häufig der Fall ist, nur eine schmale experimentelle Datenbasis zur Ermittlung der Modellparameter zur Verfügung steht. Die Weiterentwicklung dieser Methoden erscheint wenig aussichtsreich. Dagegen stellt molekulare Modellierung und Simulation in der Verfahrenstechnik einen vielversprechenden Weg mit hohem Entwicklungspotenzial zur zuverlässigen Stoffdatenvorhersage dar. Die molekulare Simulation ist gegenwärtig die am häufigsten angewandte molekulare Methode, die ein hohes Weiterentwicklungspotenzial mit Flexibilität bei vertretbarem Rechenzeitaufwand verbindet. Um mit Hilfe molekularer Simulation Stoffdaten quantitativ berechnen zu können, sind sorgfältig parametrierte Modelle der molekularen Wechselwirkungen von Reinstoffen und Mischungen erforderlich. Die Entwicklung solcher molekularen Modelle ist im allgemeinen ein sehr zeitaufwändiger, nicht systematisierter Prozess, so dass ein Mangel an technisch brauchbaren molekularen Modellen besteht. Im wesentlichen hierdurch wurde bislang die breitere Anwendung molekularer Simulation behindert.

In der vorliegenden Arbeit wurden molekulare Modelle für eine große Zahl von niedermolekularen Reinstoffe und Mischungen entwickelt, die die Vorhersage von thermophysikalischen Stoffdaten, insbesondere von Dampf-Flüssigkeits Gleichgewichten, mit technisch interessanter Genauigkeit ermöglichen. Zu den in dieser Arbeit modellierten unpolaren, quadrupolaren und multipolaren Reinstoffklassen gehören unter anderem Stickstoff, Sauerstoff, Ethan, Halogene, Kohlendioxid, Kohlenmonoxid und alternative Kältemittel. In dieser Arbeit wurde für viele Stoffe ein alternativer Modellierungsansatz gewählt, der von vereinheitlichten Modellklassen ausgeht und dadurch die effiziente Parametrierung molekularer Modelle für 78 Reinstoffe ermöglichte. Damit war es möglich, die für die Erstellung der molekularen Modelle erforderliche Entwicklungszeit erheblich zu verkürzen. Durch ihre Kompatibilität sind diese Reinstoffmodelle für die Modellierung von Mischungen geeignet. Zu deren Beschreibung sind einfache Kombinationsregeln ausreichend.

Die für die Modellierung dieser 78 Reinstoffe verwendeten Modellklassen sind das vierparametrige Zwei-Zentren-Lennard-Jones-Fluid mit Punktquadrupol (2CLJQ) bzw. mit Punktdipol (2CLJD). Diese Modelle haben keine inneren Freiheitsgrade. Wie die Ergebnisse der vorliegenden Arbeit zeigen, reichen in vielen Fällen die Modellgeometrie und die Polarität dieser Modellklassen aus, um die molekularen Wechselwirkungen zwar stark vereinfacht, aber ausreichend genau zu erfassen, so dass das makroskopische thermodynamische Verhalten der hier modellierten Stoffe mit sehr guter Genauigkeit beschrieben werden kann. In reduzierten Größen haben beide Modelle lediglich zwei Parameter (die Entfernung der beiden Lennard-Jones-Wechselwirkungszentren und das Quadrupol- bzw.

Dipolmoment), die die effiziente Ermittlung der thermophysikalischen Eigenschaften dieser Modellfluide als Grundlage für die Modellierung der realen Reinstoffe ermöglichten. Hierfür wurden empirische Korrelationen der Dampf-Flüssigkeits Gleichgewichte der 2CLJQ- und 2CLJD-Modellfluide in Abhängigkeit der Modellparameter und der Temperatur auf der Basis umfangreicher Simulationsdaten entwickelt. Mit Hilfe dieser Korrelationen wurden die Modellparameter durch Anpassung an experimentelle Dampf-Flüssigkeits Gleichgewichte der Reinstoffe spezifiziert. Für die modellierten Reinstoffe werden Ergebnisse aus molekularer Simulation diskutiert und mit Daten aus der Literatur verglichen.

Neben dieser für Modelle mit geringer Parameterzahl geeigneten Vorgehensweise wird in der vorliegenden Arbeit am Beispiel von Ethylenoxid und Methanol eine Methode für die Parametrierung detaillierterer molekularer Modelle diskutiert.

Auf Grundlage der in dieser Arbeit entwickelten Reinstoffmodelle wurden molekulare Modelle für eine Vielzahl binärer Mischungen entwickelt. Hierfür wurde ein binärer Wechselwirkungsparameter in den Lorentz-Berthelot-Kombinationsregeln verwendet, der nach Anpassung an einen experimentellen Zustandspunkt der Mischung eine genauere Beschreibung der thermophysikalischen Eigenschaften der Mischung erlaubt. Ergebnisse aus molekularer Simulation werden für binäre und ternäre Mischungen mit experimentellen Daten und Ergebnissen der Peng-Robinson-Zustandsgleichung verglichen.

Für die Berechnung der Dampf-Flüssigkeits Gleichgewichte von Reinstoffen wurde in dieser Arbeit die NpT + Testteilchenmethode verwendet. Dampf-Flüssigkeits Gleichgewichte von Mischungen wurde mit der Grand Equilibrium Methode berechnet, die zeitgleich am Institut für Technische Thermodynamik und Thermische Verfahrenstechnik der Universität Stuttgart entwickelt wurde. Beide Methoden werden in der vorliegenden Arbeit beschrieben. Die für diese Methoden erforderlichen molekularen Simulationen beruhten in dieser Arbeit auf der Molekulardynamik oder der Monte Carlo Methode. Für die NpT + Testteilchenmethode und die Grand Equilibrium Methode müssen die chemischen Potenziale und die partiellen molaren Volumina in der simulierten Dampf- bzw. der Flüssigphase ermittelt werden. Hierfür wurde die Testteilcheneinsetzung und in einigen Fällen die graduelle Einsetzung verwendet. Obwohl der Rechenzeitaufwand für graduelle Einsetzung sehr hoch ist gegenüber der Testteilcheneinsetzung, bietet sie gerade in schwierigen Fällen, wie etwa bei stark polaren großen Molekülen, den Vorteil, dass chemische Potenziale und partielle molare Volumina mit erheblich geringeren statistischen Unsicherheiten berechnet werden können. Die für die vorliegende Arbeit relevanten Beziehungen der statistischen Thermodynamik sowie die mathematischen Beschreibungen

der molekularen Wechselwirkungen und die daraus resultierenden Kräfte und Drehmomente werden ausführlich dargestellt.

Im folgenden werden diese einen skizzenhaften Überblick über die Arbeit verschaffenden Punkte näher erläutert.

Für 30 2CLJQ- und 38 2CLJD-Modellfluide wurden in systematischen Studien mit Hilfe der NpT + Testteilchenmethode jeweils die kritische Temperatur, die kritische Dichte, die Siede- und Taudichten, die Siede- und Tauenthalpien und der Dampfdruck ermittelt. Dabei wurden für die 2CLJQ-Fluide die reduzierten Elongationen $L^* = 0,\ 0.2,\ 0.4,\ 0.505,\ 0.6,\ 0.8$ und die reduzierten Quadrupolmomente $Q^{*2} = 0,\ 1,\ 2,\ 3,\ 4$ verwendet. Für die 2CLJD-Fluide wurden die Werte für die Elongationen auf 1 erweitert, für die Dipolmomente wurden die Werte $\mu^{*2} = 0, 3, 6, 9, 12$ verwendet. Außerdem wurden die beiden 2CLJD-Fluide mit $L^* = 0.2$ und $\mu^{*2} = 16, 20$, sowie das 2CLJD-Fluid mit $L^* = 0$ und $\mu^{*2} = 20$ hinzugezogen. Langreichweitige Korrekturen der Dipolwechselwirkungen von 2CLJD-Modellfluiden wurden mit der Reaktionsfeldmethode berechnet. Für diese 68 Modellfluide wurden Dampf-Flüssigkeits Gleichgewichte für Temperaturen zwischen 55% und 95% der jeweiligen kritischen Temperatur berechnet. Für viele der hier untersuchten 2CLJD-Fluide wurden bei der niedrigsten Temperatur durch Verwendung von gradueller Einsetzung zur Berechnung des chemischen Potenzials in der Flüssigphase die Dampfdrücke mit sehr geringer statistischer Unsicherheit bestimmt.

Diese umfangreiche Simulationsarbeit diente der Verbesserung der Datenlage, mit dem Ziel, sie als Grundlage für die Entwicklung molekularer Modelle für reale Reinstoffe zu verwenden. Die Verbesserung der Datenlage zeigt sich daran, dass die Ergebnisse aus Zustandsgleichungen für die 2CLJQ- und 2CLJD-Modellfluide aus der Literatur in vielen Fällen erheblich von den in der vorliegenden Arbeit bestimmten Simulationsergebnissen abweichen. Ursache für dieses Verhalten dieser Zustandsgleichungen ist die im Vergleich zu dieser Arbeit sehr schmale Datenbasis, die zur Beschreibung der dipolaren und quadrupolaren Beiträge in diesen Zustandsgleichungen verwendet wurde. Die Dampf-Flüssigkeits Gleichgewichte der Modellfluide aus der vorliegenden Arbeit wurden auf thermodynamische Konsistenz überprüft und stimmen innerhalb der simulationsbedingten Unsicherheit mit Daten aus der Literatur überein.

Ausgehend von den Simulationsergebnissen für die Dampf-Flüssigkeits Gleichgewichte wurden für die 2CLJQ- und 2CLJD-Modellfluide aus empirischen Ansätzen globale Korrelationsfunktionen entwickelt, die den Einfluss der Modellparameter auf die kritische Temperatur und die kritische Dichte, sowie den Einfluss der Modellparameter und der

Temperatur auf die Siede- und Taudichten und den Dampfdruck beschreiben. Diese Korrelationsfunktionen geben die Simulationsdaten mit ausreichender Genauigkeit wieder. Mit der Entwicklung dieser globalen Korrelationsfunktionen wurden die Werkzeuge geschaffen, die in der vorliegenden Arbeit die effiziente Entwicklung molekularer Modelle für reale Reinstoffe ermöglichten.

Mit Hilfe dieser globalen Korrelationsfunktionen wurden für insgesamt 78 reale Reinstoffe 2CLJQ- bzw. 2CLJD-Modellparametersätze bestimmt, indem über Fehlerquadratminimierung die kritische Temperatur und für mehrere Temperaturen die Siededichte und der Dampfdruck der Modellfluide simultan an experimentelle Daten der kritischen Temperatur, der Siededichte und des Dampfdrucks der Reinstoffe angepasst wurden. Diese 2CLJQ- (bzw. 2CLJD-) Modelle erreichen typische relative Abweichungen zwischen Modell und Experiment von 3% (4%) für den Dampfdruck, 0.5% (0.5%) für die Siededichte und 2% (3%) für die Verdampfungsenthalpie. Im Vergleich zu molekularen Modellen aus der Literatur beschreiben sie in vielen Fällen das Dampf-Flüssigkeits Gleichgewicht der Reinstoffe mit deutlich besserer Genauigkeit. Insbesondere die mittlere relative Abweichung des simulierten Dampfdrucks von experimentellen Werten ist in vielen Fällen um etwa eine Größenordnung geringer als bei molekularen Modellen aus der Literatur. Auch im homogenen Zustandsgebiet bei wesentlich höheren Drücken und Temperaturen als im Zustandsgebiet der Dampf-Flüssigkeits Gleichgewichte beschreiben die vorliegenden molekularen Modelle thermophysikalische Größen der Reinstoffe mit guter Genauigkeit. Die damit gezeigte Güte der in dieser Arbeit entwickelten 2CLJQ- und 2CLJD-Modelle macht sie für technische Anwendungen interessant.

Ein Vergleich der Modellparameter mit realen Molekülgeometrien und Polaritäten ist vor allem im Fall der hier modellierten zweiatomigen Stoffe, wie Sauerstoff, Stickstoff und den Halogenen Fluor, Chlor, Brom und Iod einfach möglich. Dabei zeigt sich eine gute Übereinstimmung zwischen realen Bindungslängen der Moleküle und der Elongation der Modelle. Auch die Quadrupolmomente der Modelle liegen im Bereich der experimentellen Daten für molekulare Quadrupolmomente. Weiterhin nehmen der Größen- und der Energieparameter des Lennard-Jones-Potenzials im Vergleich zur Molekülgröße physikalisch sinnvolle Werte an.

Aufbauend auf den Ergebnissen der Reinstoffmodellierung mit den 2CLJQ- und 2CLJD-Modellklassen wurden in der vorliegenden Arbeit für Ethylenoxid und Methanol detailliertere molekulare Modelle auf Basis von Lennard-Jones-Wechselwirkungszentren ohne innere Freiheitsgrade entwickelt. Die beiden molekularen Modelle sind mit den 2CLJQ-

und 2CLJD-Modellen kompatibel. Das Modell für Ethylenoxid mit drei Lennard-Jones-Wechselwirkungszentren und einem Punktdipole ist eine Neuentwicklung, das Modell für Methanol geht aus der Optimierung eines asymmetrischen Zwei-Zentren-Lennard-Jones-Modells mit drei Punktladungen hervor, das der Literatur entnommen wurde. Bei der Anordnung der Lennard-Jones-Wechselwirkungszentren wurden die realen Molekülgeometrien berücksichtigt. Langreichweitige Korrekturen der Dipol- bzw. der Punktladungswechselwirkungen wurden mit der Reaktionsfeldmethode berechnet. Für beide Modelle wurden jeweils drei Modellparameter so optimiert, dass die Modelle das Dampf-Flüssigkeits Gleichgewicht der Reinstoffe mit guter Genauigkeit beschreiben. Das Ethylenoxid-Modell (Methanol-Modell) erreicht eine mittlere relative Abweichung von 6.5 % (9.9 %) von experimentellen Dampfdruckdaten und von 0.17 % (0.56 %) von experimentellen Siededichtedaten. Die für beide Modelle verwendete Optimierungsmethode beruht auf einer Fehlerquadratminimierung und ermittelt mit Hilfe von Sensitivitäten iterativ und rasch konvergierend ein optimiertes molekulares Modell. Für die Optimierung des Methanol-Modells wurden sämtliche Dampf-Flüssigkeits Gleichgewichte mit Hilfe der Methode der graduellen Einsetzung mit hoher Genauigkeit ermittelt.

Mit ihrer guten Genauigkeit bei der Beschreibung thermophysikalischer Daten und der physikalisch sinnvollen Parametrierung auf molekularer Ebene sind die vorliegenden, miteinander kompatiblen molekularen Modelle von Reinstoffen für die Modellierung von Mischungen sehr gut geeignet. Daher wurden mit diesen Modellen für die Wechselwirkungen von 45 ungleichen Molekülpaaren in Mischungen molekulare Modelle entwickelt, die die quantitative Vorhersage von Dampf-Flüssigkeits Gleichgewichten von Mischungen ermöglichen.

Die Lennard-Jones-Wechselwirkung zwischen zwei verschiedenen Molekülen wurde in dieser Arbeit mit den in der Literatur häufig verwendeten Lorentz-Berthelot-Kombinationsregeln beschrieben. Vorhersagen von Dampf-Flüssigkeits Gleichgewichten allein auf Grundlage der Reinstoffmodelle und den Lorentz-Berthelot-Kombinationsregeln wurden untersucht und mit Vorhersagen aus der Peng-Robinson Zustandsgleichung und mit experimentellen Daten verglichen. Die Einführung eines anpassbaren binären Wechselwirkungsparameters in den energetischen Term der Lorentz-Berthelot-Kombinationsregeln ermöglichte eine genauere Beschreibung der Dampf-Flüssigkeits Gleichgewichte von Mischungen. In der vorliegenden Arbeit wurde dieser binäre Wechselwirkungsparameter, der im nicht angepassten Fall den Wert eins hat, für jede Mischung mit einer einfachen Methode an den Druck eines geeigneten experimentellen Zustandspunkt des Dampf-Flüssigkeits

Gleichgewichts angepasst. Angepasst liegt der binäre Wechselwirkungsparameter weiterhin nahe beim Wert eins. Simulationsergebnisse mit angepasstem binären Wechselwirkungsparameter wurden mit experimentellen Daten und mit Ergebnissen der Peng-Robinson Zustandsgleichung verglichen, deren binärer Parameter an denselben experimentellen Zustandspunkt der Mischung angepasst wurde.

Fünf technisch wichtige binäre Mischungen der quadrupolaren Komponenten Stickstoff, Sauerstoff, Kohlendioxid und Ethan wurden ausführlicher untersucht, um die Leistungsfähigkeit der molekularen Simulation im Vergleich zu Zustandsgleichungen aufzuzeigen. Besonders auffällig ist im Fall der azeotropen Mischung Kohlendioxid + Ethan, dass molekulare Simulation allein auf Grundlage der beiden Reinstoffmodelle und der Lorentz-Berthelot-Kombinationsregeln mit nicht angepasstem binärem Wechselwirkungsparameter die azeotrope Zusammensetzung vorhersagt, wohingegen die Peng-Robinson Zustandsgleichung zeotropes Siedeverhalten vorhersagt. Mit angepasstem binären Wechselwirkungsparameter und angepasstem binärem Parameter der Peng-Robinson Zustandsgleichung liefern beide Methoden eine sehr gute quantitative Beschreibung des azeotropen Dampf-Flüssigkeits Gleichgewichts. Hier wird vorweggenommen, dass sich im Fall der azeotropen Mischung Ethin + Ethan ein völlig analoges Bild der Vorhersageeigenschaften beider Modellierungsansätze ergibt. Im Fall der Mischung Stickstoff + Ethan, in der Stickstoff als überkritische Komponente enthalten ist, liefert die Peng-Robinson Zustandsgleichung auch mit angepasstem binärem Parameter eine schlechte Beschreibung der experimentellen Siedelinie, außerdem überschätzt sie die Lage des kritischen Punkts. Molekulare Simulation liefert hierfür deutlich bessere Ergebnisse. Weiterhin zeigte sich, dass die vorliegenden molekularen Modelle für Stickstoff und Ethan bei niedriger Temperatur Flüssigkeit-Flüssigkeits Gleichgewichte bilden, die bei der realen Mischung Stickstoff + Ethan experimentell nachgewiesen wurden. Bereits aus diesen Ergebnissen kann gefolgert werden, dass die Vorhersagekraft molekularer Simulationen deutlich besser ist als jene der Peng-Robinson Zustandsgleichung, wenn physikalisch sinnvolle molekulare Modelle verwendet werden.

Siededichten der fünf Mischungen werden mit molekularer Simulation zuverlässig beschrieben, was mit der Peng-Robinson Zustandsgleichung erwartungsgemäß nicht gelingt. Auch Verdampfungsenthalpien von Mischungen werden in vielen Fällen mit molekularer Simulation genauer vorhergesagt als mit der Peng-Robinson Zustandsgleichung. Vergleiche mit Ergebnissen der PC-SAFT und der BACKONE Zustandsgleichung unterstreichen, dass die in dieser Arbeit entwickelten molekularen Modelle eine sehr gute Vorhersagekraft

für thermophysikalische Eigenschaften realer Mischungen besitzen. Ergebnisse für Dampf-Flüssigkeits Gleichgewichte weiterer quadrupolarer Mischungen bestätigen dies.

Für Mischungen mit multipolaren Komponenten wurden die Ergebnisse aus molekularer Simulation mit angepasstem binären Wechselwirkungsparameter und der Peng-Robinson Zustandsgleichung mit angepasstem binärem Parameter mit experimentellen Daten verglichen. Hierzu gehören unter anderem kohlenmonoxidhaltige Mischungen und Kältemittelmischungen. Die Modellierung dieser Mischungen multipolarer Komponenten mit einfachen, nicht polarisierbaren molekularen Modellen ist besonders interessant, da einige der realen Moleküle, wie zum Beispiel CS_2, vergleichsweise stark polarisierbar sind. Es wurde gezeigt, dass auch für diese Mischungen molekulare Simulation eine sehr gute Beschreibung der experimentellen Dampf-Flüssigkeits Gleichgewichte über weite Temperatur- und Zusammensetzungsbereiche liefert. Auch die Ergebnisse der Peng-Robinson Zustandsgleichung sind in vielen Fällen sehr gut. Die Peng-Robinson Zustandsgleichung überschätzt jedoch wiederum in mehreren Fällen mit einer überkritischen Komponente die Lage des kritischen Punkts. Auch die Siede- und Taudichten dieser Mischungen werden mit molekularer Simulation genauer beschrieben als mit der Peng-Robinson Zustandsgleichung.

Mit der Modellierung der Mischung Methanol + Kohlendioxid wurde der hier verwendete vergleichsweise einfache Modellierungsansatz für reale Mischungen auf eine Mischung mit einer assoziierenden Komponente übertragen. Alle für diese Mischung erforderlichen molekularen Simulationen wurden mit gradueller Einsatzung beider Komponenten durchgeführt, wodurch die Dampf-Flüssigkeits Gleichgewichte mit sehr geringen statistischen Ungenauigkeiten ermittelt werden konnten. Damit war es auch für diese Mischung möglich, den binären Wechselwirkungsparameter der Lorentz-Berthelot-Kombinationsregeln an einen experimentellen Gleichgewichtsdruck dieser Mischung anzupassen. Die Beschreibung der Dampf-Flüssigkeits Gleichgewichte dieser Mischung mit der Peng-Robinson Zustandsgleichung mit angepasstem binärem Parameter zeigt vor allem auf der Siedelinie und im kritischen Bereich Schwächen. Mit angepasstem binärem Wechselwirkungsparameter stimmen die Ergebnisse für Dampf-Flüssigkeits Gleichgewichte aus molekularer Simulation über weite Temperatur- und Zusammensetzungsbereiche sehr gut mit experimentellen Werten überein. Auch Siededichten dieser Mischung werden mit molekularer Simulation sehr gut beschrieben. Dieser positive Befund gibt Anlass zur Vermutung, dass der in dieser Arbeit gewählte Modellierungsansatz auf weitere Mischungen mit assoziierenden Komponenten übertragbar ist.

Die molekularen Modelle für binäre Mischungen lassen sich ohne Modifikation für die Stoffdatenvorhersage ternärer Mischungen verwenden. Die Einführung ternärer Parameter oder die Neuanpassung binärer Parameter an thermophysikalische Daten ternärer Mischungen ist nicht erforderlich. Am Beispiel von fünf ternären Mischungen mit quadrupolaren und multipolaren Komponenten wurde gezeigt, dass molekulare Modelle ternärer Mischungen auf der Basis der in dieser Arbeit entwickelten molekularen Modelle binärer Mischungen die experimentellen Dampf-Flüssigkeits Gleichgewichte dieser ternären Mischungen mit guter Genauigkeit vorhersagen. Unter gleichen Voraussetzungen liefert die Peng-Robinson Zustandsgleichung in vielen Fällen hierfür deutlich schlechtere Resultate.

In der vorliegenden Arbeit wurde gezeigt, dass molekulare Simulation bereits mit vergleichsweise einfachen, zustandsunabhängigen molekularen Modellen für Reinstoffe und Mischungen eine hervorragende Vorhersagekraft besitzt. Um diese Eigenschaft molekularer Simulation ausschöpfen zu können, müssen physikalisch sinnvolle und sorgfältig parametrierte molekulare Modelle von Reinstoffen zu Grunde gelegt werden. Molekulare Modellierung stellt dann einen systematischen, für viele Stoffklassen vereinheitlichten Modellierungsansatz dar, der ein breites Spektrum thermophysikalischer Größen zuverlässig beschreiben kann. Für die verfahrenstechnische Praxis ist es wichtig, dass für die Parametrierung der molekularen Modelle binärer Mischungen jeweils nur ein einziges experimentelles Dampf-Flüssigkeits Gleichgewicht erforderlich war.

Die in dieser Arbeit dargestellten Resultate unterstreichen das hohe Entwicklungspotenzial, das die molekularen Modellierung bietet. In künftigen Arbeiten sollte untersucht werden, inwiefern der hier gewählte Modellierungsansatz auf weitere komplexe, Wasserstoffbrücken bildende Fluide und deren Mischungen übertragbar ist. Auch die Modellierung größerer Moleküle, bei denen innere Freiheitsgrade zu beachten sind, sollte in Betracht gezogen werden. Bei der Parametrierung solcher Modelle können Ergebnisse quantenmechanischer Berechnungen der Molekülinteraktionen herangezogen werden.

Abschließend sei angemerkt, dass während der Entstehung der vorliegenden Arbeit viele der hier entwickelten molekularen Modelle bereits erfolgreich zur quantitativen Vorhersage weiterer thermophysikalischer Größen, wie etwa Diffusionskoeffizienten, Oberflächenspannungen oder Henry-Konstanten verwendet wurden. Es existiert bislang kein vereinheitlichter klassischer Modellierungsansatz, der die simultane quantitative Beschreibung dieser Größen ermöglichen würde. Damit wurden außerhalb dieser Arbeit die exzellenten extrapolativen Eigenschaften der hier entwickelten molekularen Modelle bestätigt.

Online-Buchshop für Ingenieure

VDI nachrichten **BUCHSHOP**

Online-Shops

Fachliteratur und mehr - jetzt bequem online recherchieren & bestellen unter: www.vdi-nachrichten.com/buchshop

Täglich aktualisiert: Neuerscheinungen VDI-Schriftenreihen

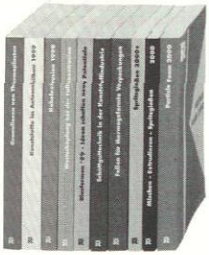

Im Buchshop von vdi-nachrichten.com finden Ingenieure und Techniker ein speziell auf sie zugeschnittenes, umfassendes Literaturangebot.

Mit der komfortablen Schnellsuche werden Sie in den VDI-Schriftenreihen und im Verzeichnis lieferbarer Bücher unter 1.000.000 Titeln garantiert fündig.

Im Buchshop stehen für Sie bereit:

VDI-Berichte und die Reihe **Kunststofftechnik:**

Berichte nationaler und internationaler technischer Fachtagungen der VDI-Fachgliederungen

Fortschritt-Berichte VDI:

Dissertationen, Habilitationen und Forschungsberichte aus sämtlichen ingenieurwissenschaftlichen Fachrichtungen

Newsletter „Neuerscheinungen":

Kostenfreie Infos zu aktuellen Titeln der VDI-Schriftenreihen bequem per E-Mail

Autoren-Service:

Umfassende Betreuung bei der Veröffentlichung Ihrer Arbeit in der Reihe Fortschritt-Berichte VDI

Buch- und Medien-Service:

Beschaffung aller am Markt verfügbaren Zeitschriften, Zeitungen, Fortsetzungsreihen, Handbücher, Technische Regelwerke, elektronische Medien und vieles mehr – einzeln oder im Abo und mit weltweitem Lieferservice

ISBN 3-18-383603-3